SZÉCHENYI ISTVÁN UNIVERSITY

DOCTORAL SCHOOL

OF MULTIDISCIPLINARY ENGINEERING SCIENCES

Numerical vehicle acoustic simulation development using SEA-based methods

Treszkai Marcell Ferenc

Doctoral dissertation

Dr. Feszty Dániel

Supervisor, Head of Department of Whole Vehicle Engineering,

Széchenyi István University

GYŐR, 2022

TABLE OF CONTENT

DECLARATION OF ORGINILATY

I hereby declare that the following thesis was written by myself, the presented results, images, and graphs are a product of my work, unless stated otherwise. Some parts of the thesis include verbatim copies of previously published, personally authored scientific articles.

ACKNOWLEDGEMENT

I would like to express my sincerest gratitude and warm appreciation to the following persons, who supported me throughout the research leading to this dissertation.

First of all, special thanks to Dr. Dániel Feszty for setting me on the way to become a researcher as well as for his advice and motivation, which helped me through the difficult times. Without these, as well as his expertise, which the completion of this study would not have been possible.

I also would like to thank Antoine Guellec, who was instrumental in creating this research group, as well as his help over the years.

I am extremely thankful to Dr. Alexander Peiffer for his assistance and expert advise in the area of Statistical Energy Analysis.

It was a privilege to work with Tamás Turcsik, who helped me with technical expertise and advice in every question, which I had during my research.

I owe a deep sense of gratitude to Zoltán Gazdagh for his help in measurement related questions.

Special thanks to all the colleagues at the Department of Whole Vehicle Development, since they helped me in the daily difficulties and struggles during my research.

I am extremely thankful to my wife for her enormous help over the years, her encouragement and her motivating words, which helped me through all the difficulties.

I am grateful for my parents for setting on me the road of higher education.

Last but not least, I would like to thank my fellow researcher and my friend, Dávid Sipos, for all his advice, help and for being a true friend over the years.

FUNDING

This research was supported by the Hungarian Academy of Sciences and Audi Hungaria Zrt. through the MTA-SZE Lendület Vehicle Acoustics Research Group. Partial funding was received by the author in 2019/2020/1 through the "Internationalization, initiatives to establish a new source of researchers and graduates and development of knowledge and technological transfer as instruments of intelligent specializations at Széchenyi István University" (EFOP-3.6.1-16-2016-00017).

ABSTRACT

For premium segment vehicles, the Noise Vibration and Harshness (NVH) characteristics are one of the most important vehicle properties. Developers work nowadays mainly with virtual models, since the 3D CAD models are available at the early phase of the development. From vibroacoustic point of view, one can distinguish three frequency ranges for vehicles: low frequency range (< 400 Hz), mid-frequency range (400-1000 Hz) and high frequency range (> 1000 Hz). The frequency below 400 Hz can be best predicted by Finite Element Method (FEM) simulations, while over 1000 Hz the so-called Statistical Energy Analysis (SEA) appears to be the most appropriate method. In the mid-frequency range (400-1000 Hz), however, neither of the classical simulation methods is appropriate, and therefore the so-called Hybrid FE-SEA method was proposed as a promising technique. This method combines the advantages of the two procedures, thus the smaller and stiffer parts are modeled as FEM, while the bigger, panel-like structures as SEA.

The results of the literature review showed that the SEA method is mainly influenced by the input parameters, such as the damping loss factor (DLF) and the coupling loss factor (CLF). On the other hand, the Hybrid FE-SEA method can be also influenced by the subdivision of the model, namely whether a given component is modeled as an FEM or as an SEA subsystem. The research described in this dissertation focused mainly on the Experimental SEA, where the DLF and CLF are obtained by measurement, as well as partly on Analytical SEA, where these parameters are accessed by analytical and/or empirical equations. Several different test cases were examined, which represent a simplified geometry of the real vehicle structure, such as plates; plates connected via various bindings; plates placed on stiff beams, and so on. These test cases were made to obtain the required parameters as well as to validate the simulations.

I proved that the damping loss factor is directly influenced by the boundary conditions of the measurements, the measurement techniques, as well as by the way how the statistical calculations are conducted. In SEA, the spatial distribution of Noise Control Treatment elements cannot be normally taken into account, but only as a percentage of coverage. I proved that the measured DLFs are influenced by the different layout of the bitumen sheets, thanks to which the different arrangements can be considered during the simulations. In order to examine the CLFs, several plate structures were designed with various binding types, as well as with different connection angles. I proved that for the combined bindings (e.g. bolting and gluing) the value of the CLF is not the simple sum of the individual CLFs, but rather a combination of

the individual junctions in terms of frequency. It has been also shown that the analytical equations can be quite accurate if the representation of the connections is appropriate or if the junction is of a simple type (such as bolting, line welding, etc.). I proved that the different binding types can reduce the vibrational response at the receiver plate, compared to a bitumen damping layer placed on the receiver plate. With the application of the structural adhesives not just the stiffness of the structure can be increased but the vibrational response can be reduced as well. I proved that in the Hybrid FE-SEA simulations the different subdivisions have an effect on the plate response velocity results, moreover it influences significantly the calculation times.

KIVONAT

A mai közútijárművek egyik legfontosabb fejlesztési szempontja – különösen a prémium szegmensben - a vibroakusztikai tulajdonságok tökéletesítése. Ez, ma már főként a virtuális térben történik, hiszen a 3D-s rajzok, már a kori fázisban a rendelkezésre állnak. Vibroakusztikai szempontból megkülönböztethető az alacsony frekvenciás (< 400 Hz), középfrekvenciás (400-1000 Hz), valamint a magas frekvenciás (> 1000 Hz) eseteket. Ezek közül az alacsony frekvenciára a Véges Elem Módszer (VEM) tud szimulációs megoldással szolgálni, valamint a magas frekvenciára a Statisztikai Energia Analízis (SEA). Az átmeneti régiót, az úgynevezett középfrekvencia tartományt a klasszikus szimulációs eljárásokkal nem lehetséges pontosan megoldani, erre a Hibrid Véges Elem – Statisztikai Energia Analízis (Hibrid VE-SEA) eljárás lehet potenciálisan alkalmas. Ez a módszer ötvözi a két metódus előnyeit, miszerint a kisebb, merevebb alkatrészek Véges Elem Módszerrel, míg a nagyobb, panelszerű komponensek Statisztikai Energia Analízissel kerülnek megoldásra.

Az doktori munka irodalomkutatásának az eredménye azt mutatja, hogy az SEA módszer főként a bemeneti paraméterekre érzékeny, úgymint a csillapítási veszteség tényező (CSVT), valamint a kapcsolási veszteség tényező (KVT). Míg a Hibrid VE-SEA módszernél az egyes alkotórészek megoldási módja befolyásolhatja főként az eredményt. Azaz, hogy az adott alkatrész VEM-mel vagy SEA-vel legyen-e modellezve, azonban ennek az érzékenységét az irodalmak nem érintik. A kutatás főként a Kísérleti SEA-t (Experimental SEA) vizsgálja, ahol a csillapítási és kapcsolási veszteség tényezők mérés által kerülnek meghatározásra. Kisebb részt az Analitikus SEA-val is foglalkozik, amelynél ezen paraméterek, empirikus és/vagy analitikus formulák alapján kerülnek meghatározásra. A mérésekhez különböző tesztesetek lettek definiálva, amelyek a járművek egyszerűsített eseteit reprezentálják, úgymint, lemezek; lemezek különböző kötési technikákkal összekapcsolva; lemezek, merev profilokra illesztve. A tesztesetek segítségével, egyrészt a szükséges paraméterek kerültek meghatározásra, másrészt a szimulációk validálására szolgáltak.

Bebizonyítottam, hogy a csillapítási veszteség tényezőt közvetlenül befolyásolja az egyes mérési peremfeltételek, a mérési eljárás, valamint a mért csillapítási paramétereken végzett statisztikai elemzéseknek is hatása van a szimulációs eredményekre. Az SEA szimulációs szoftverben a különböző zajcsillapító anyagokat lokálisan nem lehet figyelembe venni, bebizonyítottam, hogy a mért csillapítási veszteség tényezőt befolyásolja a bitumen csillapító rétegek különböző alakzatokban történő elhelyezése az alap lemezen. A kapcsolási veszteség

tényezők vizsgálatára többféle kötéssel ellátott lemezszerkezetek lettek kialakítva. Bebizonyítottam, hogy kombinált kötések esetén (pl. csavarozás és ragasztás) a KVT értéke, nem az összege az egyéni kötések KVT értékének. Továbbá, hogy az analitikus egyenletek pontos eredményeket adnak, helyes modellezés és egyszerű kötések esetén. Bebizonyítottam, hogy a strukturális ragasztók alkalmazásával a merevség növelése mellett a rezgés válaszokat is csökkenteni lehet. Bebizonyítottam, hogy a Hibrid VE-SEA szimulációban az egyes alkatrészeknek az eljárás szerinti modellezése, azaz, hogy véges elemmel, vagy statisztikai módszerrel kerül-e megoldásra a modell, nemcsak a frekvencia válaszok eredményére van hatása, hanem a futási időt is jelentősen befolyásolja.

1. INTRODUCTION

1.1. Motivation

Noise, Vibration and Harshness (NVH) research and development has become increasingly important in the vehicle industry recently. NVH deals with predicting and controlling vibroacoustics phenomenon, which can cause passenger discomfort in the form of vibrations and noise or fatigue of the car components. Therefore, the automotive sector invests lot of effort in predicting and controlling the undesired effects of vibroacoustics phenomenon. There are various trends for vibration- and noise control. One of the simplest methods is to change the mass, stiffness or damping of a component participating in the vibration or noise transfer, since these can alter the response of a system to an excitation. However, by for example adding mass, one contradicts an important aspect of modern vehicle development: the need to reduce the weight of the car due to the tightening emission standards. Another challenge nowadays is related to the NVH of electric vehicles, since the excitation due to an electric motor occurs at much higher frequencies, than for combustion engines. Also, noise sources, which have been "masked" before by the internal combustion engine, might now become important. Such noise sources include the gear noise, road noise or wind induced noise, which itself is characterized by high frequency random excitation due to the turbulent boundary layer around the vehicle. Furthermore, the heavy battery package of electric vehicles calls for the usage of new lightweight materials, such as lightweight alloys or carbon fibre composites. For such complex lightweight structures, one has to analyze the effect of high frequency excitations from structural, fatigue, failure as well as noise point of view. For this reason, electric vehicles require full car simulations, what represent a quite significant computational challenge [1].

From the frequency point of view, it is common in vehicle NVH to distinguish between low-frequency (up to 400 Hz), mid-frequency (400-1000 Hz) and high-frequency (above 1000 Hz) noise. There are quite matured methods established for predicting the low-frequency or high-frequency noise, however, there is no common approach to predict the mid-frequency range [2]. Several researchers attempted to investigate and solve this grey area in the vehicle industry, and a range of new simulation methods were developed, such as wave-based methods, wave finite element methods, energy distribution analysis methods or hybrid Finite Element-Statistical Energy Analysis methods [2].

The present work aims to use hybrid Finite Element-Statistical Energy Analysis (Hybrid FE-SEA) method to investigate the challenges of predicting mid-frequency and high-frequency vibroacoustic phenomena for vehicles. Although the main goal of the research is to enable the virtual development of vehicles, various simplified vehicle-like structures have been investigated, in order to build up a simulation know-how step-by-step from the basics. This Chapter will first describe the peculiarities of vehicle structures, followed by reviewing the state-of the-art of SEA and Hybrid FE-SEA simulations, from which the research gaps in these areas will be identified.

1.2. Specifics of vehicle structures

Vehicle chassis structures must provide comfort and safety to the passengers and must enable the desired handling qualities of the vehicle. Therefore, the vehicle chassis must fulfil multiple criteria from mass, stiffness, impact crash, strength, durability and fatigue, manufacturability as well as cost point of view. One important aspect of passenger comfort is the vibroacoustics characteristic of the vehicle. From this point of view, the goal is to create such vehicle structure, which minimizes the sound pressure level at the ear position of the passengers as well as the vibration levels at the contact points with the passengers, i.e. at the steering wheel, the floor, and the seats. In order to meet these complex challenges, modern chassis design involves the combination of strong frame elements and sheet panels as well as multiple materials, as shown in Fig. 1.

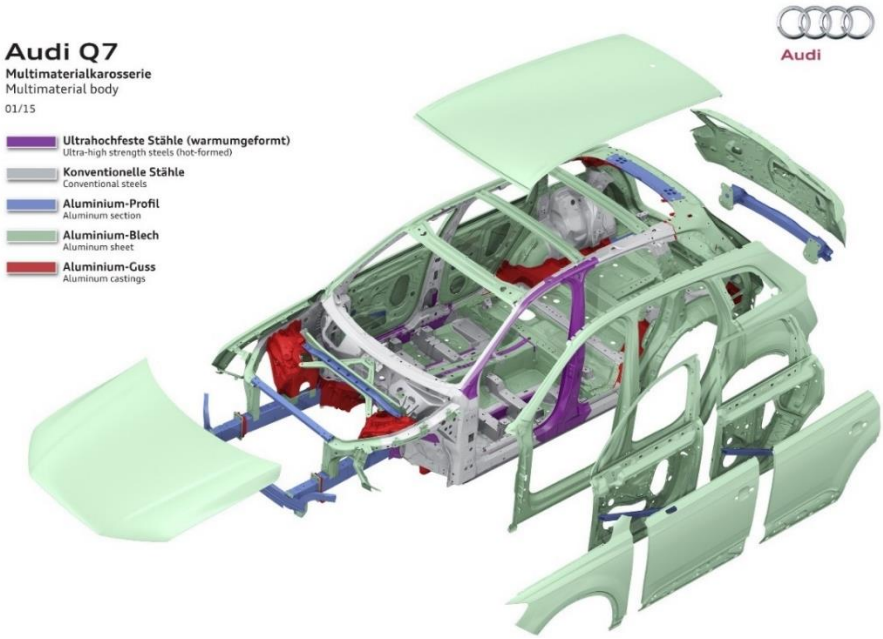

Figure 1: Illustration of the vehicle structure of the frame and panels as well as of the range of materials used in a modern chassis [3].

As a consequence of the material diversity, various binding techniques are utilized during the manufacturing process. As Fig. 2 shows, modern vehicle binding techniques include spot welding, line welding, bolting, riveting, gluing, as well as their combinations. As will be seen later, the modelling techniques for capturing the effect of junctions will appear crucial to obtain credible and accurate vibroacoustics simulation results.

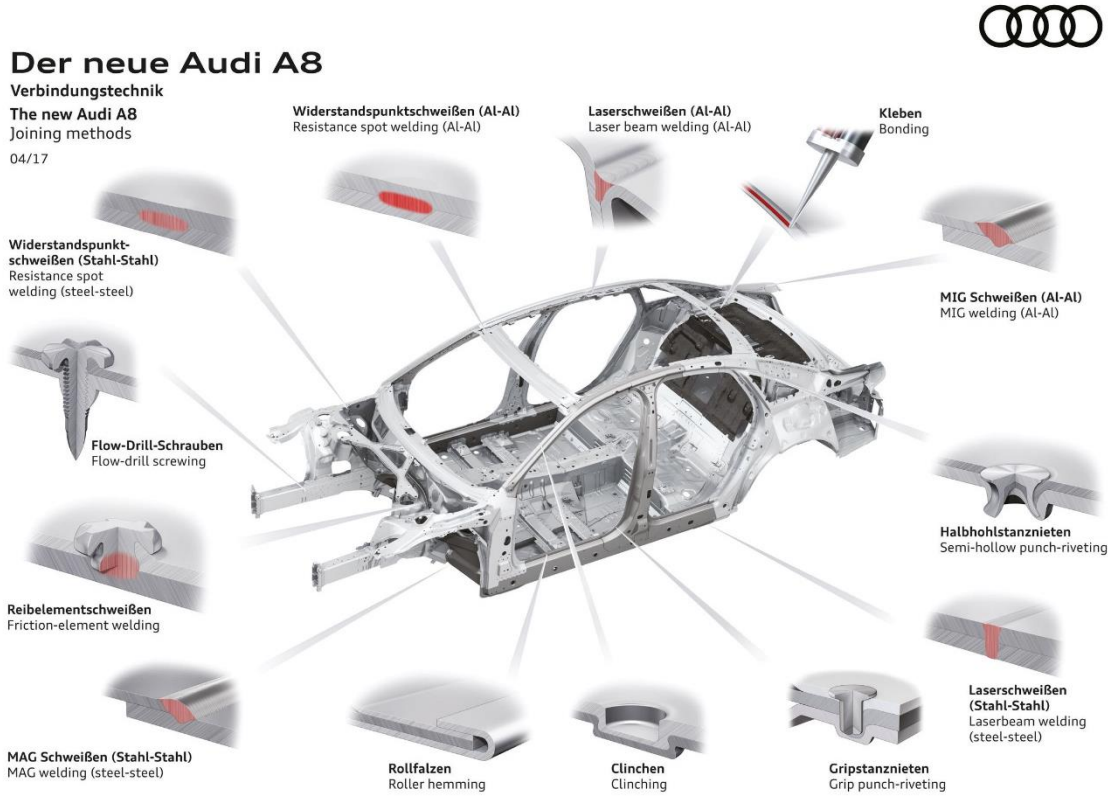

Figure 2: Various binding techniques on a passenger car [4].

In general, full vehicle structures can be subdivided into the following main elements (or "levels"):

- Stiff frames (e.g.: A-pillar, B-pillar, C-pillar, stiffeners, etc.)
- Sheet plates (e.g.: sheet metals and glasses)
- Joints (e.g.: welding, gluing, riveting, bolting, and their combinations)
- Trim materials (e.g.: foams, carpets, dashboard, seats, etc.)
- Air cavities (e.g.: air ducts, air cavity of the passenger compartment)

These elements will be used in this work to determine the various levels of validation models for the simulations. A range of simplified test apparatuses were designed to enable the detailed understanding and validation of the key parameters of simulations. The test equipment was a simplified equivalent of their full vehicle applications.

1.3. Vibroacoustics phenomenon in vehicles

As it was mentioned above, in vehicle NHV development, the main goal is to reduce the SPL level at the ear positions of the passengers as well as the vibration at the contact points between the driver and the vehicle, i.e. the steering wheel, floor, seats, etc. During a vibroacoustics measurement or simulation campaign of a vehicle, the response points (where noise or vibration data are evaluated) are therefore defined by these positions and target criteria are typically prescribed at these response points. Note though, that for methodology development and/or validation purposes, other response point locations can be considered as well.

In order to be able to control the NVH characteristics of a vehicle structure, the so called "transfer paths" between the excitation sources and the response points need to be known. Several excitations can occur on vehicles, such as the ones from engine vibrations, gearbox vibrations, the contact with the road, the turbulent boundary layer around the chassis etc., and their paths to the passenger ears and body contact points can also be diverse. From physics point of view, the transfer path can be either of "air-borne noise" or "structure-borne noise" type. While the previous one means a vibration or noise signal transmitting through air, the latter one represents a vibration signal transmitted through a solid body. Both of them occur in vehicles and therefore their accurate capturing is important for vehicle NVH simulations. From structural point of view, transfer paths between an excitation and response point can develop through several paths, i.e. a chain of chassis elements, as illustrated in Fig. 3.

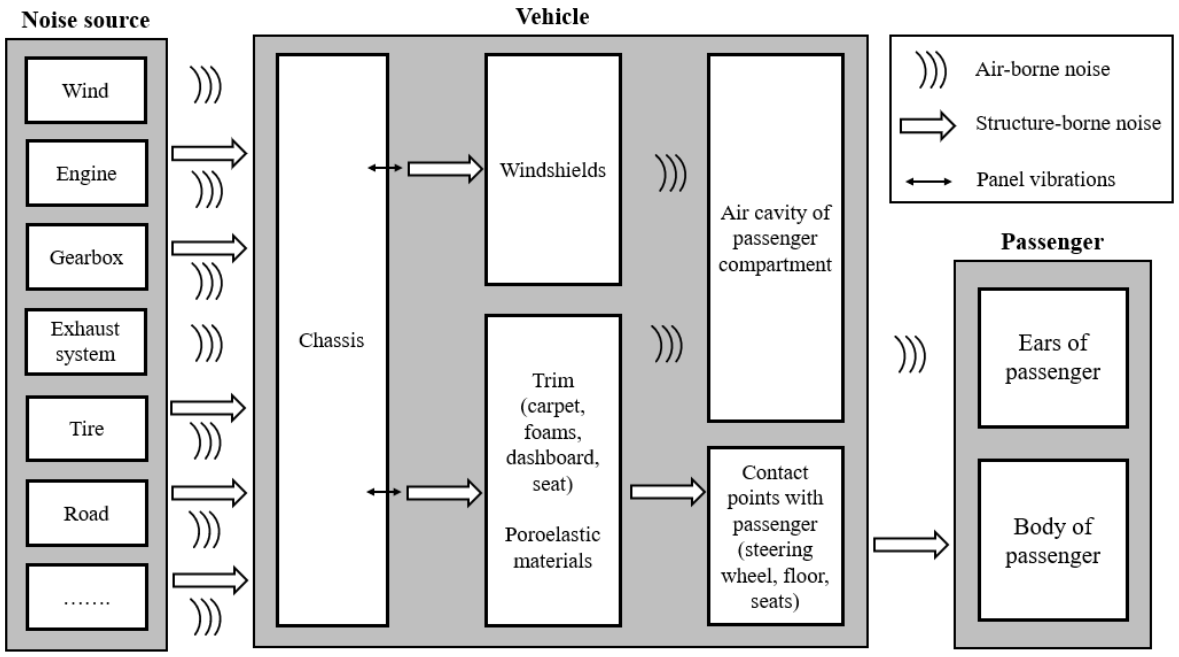

Figure 3: Typical transfer paths of a vehicle.

Consider for example the transfer path from the engine to the ear of the driver. The engine excites its mounting points in the chassis as well as the air in the engine bay. The vibrations from the mounting points are transmitted in the form of structure-borne noise all over the chassis, but also as airborne-noise in the engine compartment towards the vehicle firewall. The sum of vibrations generated in the chassis transfers into the chassis panels, such as the roof, windscreen and side windows, in the form of structure-borne noise. The chassis elements act just as membranes of a loudspeaker and transfer the signal – via airborne noise - further to the passenger ears. In parallel, the structure-borne noise propagating in the vehicle structure will transform into body vibrations of the passenger at the contact points between the passenger and the vehicle.

Finally, an important aspect of vehicle NVH analysis is the determination of the resonance frequencies and the corresponding modes shapes of the vehicle chassis. A trimmed body configuration 10.000+ of modes can be occurred up to 1000 Hz. If an excitation signal coincides with any of these, the chassis will tend to amplify the input signal and thus deteriorate the NVH characteristic of the vehicle. For example, if the chassis' first bending mode's natural frequency is close to the engine idle frequency, the body will resonate and make idling noisy. The chassis natural frequencies are a function of the mass, damping and stiffness characteristics of the chassis, thus it would be logical to modify these for improving vehicle vibroacoustics phenomenon. However, the very same parameters also define other important characteristics of the vehicle, such as the handling qualities, dynamic performance, collision safety, fuel consumption, etc, so the vibroacustics-based needs cannot be viewed separately when altering the chassis characteristics.

1.4. Principles of the simulation methods

There are several simulation methods that deal with vibroacoustic problems, such as, Boundary Element Method, Finite Element Method, Ray-tracing Method, Statistical Energy Analysis, etc. The current research focuses on pure SEA and hybrid FE-SEA methods, and for this reason the purpose of this section is to acquaint the reader with the general concepts of these methods before reviewing the literature.

At lower frequencies, the so-called "deterministic methods" (such as Finite Element Method - FEM) are capable to solve the vibroacoustic problems accurately. These methods require a detailed model of the vehicle, where the element size is dictated by the wavelength of the highest frequency to be captured, typically, about 6-8 elements need to cover one wavelength.

This on one hand necessitates high computing capacity, - thus limiting the applicability of FEM methods to higher frequencies, - while on the other hand requires a very detailed geometry of the vehicle, which is often not available at the early phases of the development process, when the geometry is far from the final one. In addition, at higher frequencies FEM is very sensitive to any deviation in the material characteristics (inhomogeneity, wall thickness changes, manufacturing inaccuracies, etc.), which can cause significant differences even in the nominally identical structures, as Fig. 4 illustrates.

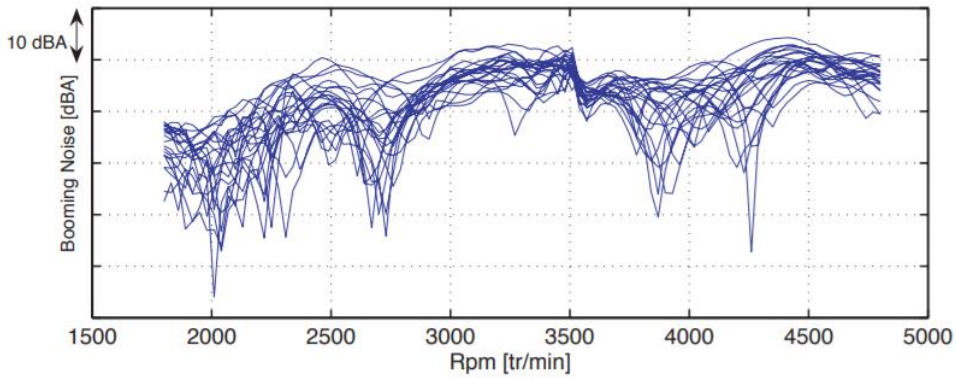

Figure 4: Vibroacoustic measurements of 20 nominally identical vehicles [5].

As a consequence, FEM is more suitable for lower frequencies, where computational costs are bearable and modal density is low. On the other hand, Statistical Energy Analysis (SEA) subdivides the vehicle model not into small elements, but rather large panels, and thus appears to be one of the most efficient methods for higher frequencies, where the modal density is sufficiently high and thus the local behavior of the structure dominates, instead of the global one (as at low frequencies) (Fig. 5).

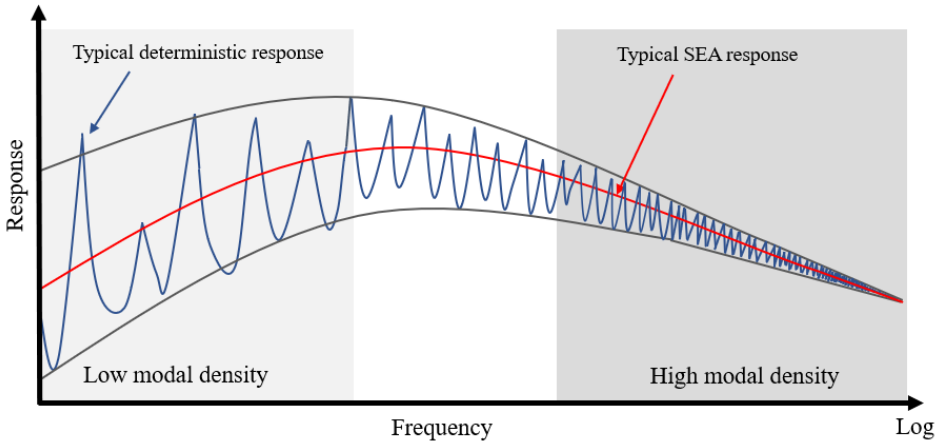

Figure 5: Deterministic methods cannot solve dense modal frequencies, while SEA predicts the ensemble average.

Since the general aim of this thesis is to develop simulation methodologies for the mid-frequency (400-1000 Hz) and high-frequency (over 1000 Hz) range, the research herein will

focus on pure SEA and hybrid FEM-SEA methods. For this reason, the purpose of the next section is to acquaint the reader with the general concepts of these methods before reviewing the literature and identifying the research gaps.

1.4.1. Statistical Energy Analysis

Statistical Energy Analysis (SEA) is a statistical method, in which results are averaged spatially as well as throughout the frequency band, therefore the method neglects most of the details of the model. The fundamental idea of SEA is to divide the geometry into subsystems, on which the governing equations are solved. Consider a single subsystem, e.g. a flat plate. The injected power equals the power loss, as the following equation shows:

$$P_{in} = \omega\, E\, \eta, \tag{1}$$

where P_{in} is the injected power, ω is the angular frequency, E is the stored vibrational energy of the subsystem, η is the Damping Loss Factor (DLF).

In the case of a coupled structure, e.g. where two subsystems are connected through a junction, the power flow can be represented as shown in Fig. 6.

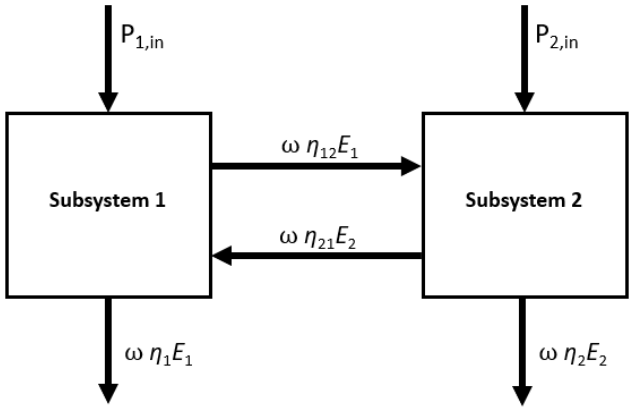

Figure 6: Energy balance between two subsystems.

The energy balance equations of the two subsystems can then be expressed as:

$$\begin{pmatrix} P_1 & 0 \\ 0 & P_2 \end{pmatrix} = \omega \begin{pmatrix} \eta_1 + \eta_{12} & -\eta_{21} \\ -\eta_{12} & \eta_2 + \eta_{21} \end{pmatrix} \begin{pmatrix} E_{11} & E_{12} \\ E_{21} & E_{22} \end{pmatrix}. \tag{2}$$

The left side of the equation is the matrix of the input power, while the right side contains the frequency, the loss matrix, and the energy matrix, respectively. The loss matrix contains the damping loss factors (η_1, η_2) and coupling loss factors (η_{12}, η_{21}) of the structure. The damping loss factor (DLF) is proportional to the subsystem damping and occurs due to the internal friction of the subsystem material, acoustic radiation loss of subsystem vibration to the environment and the energy loss caused by the boundary connection damping of the subsystem.

The coupling loss factor (CLF) defines the energy loss at a junction between two subsystems. For the case of a vehicle, the meaning of DLF and CLF can be and interpreted as shown in Fig. 7.

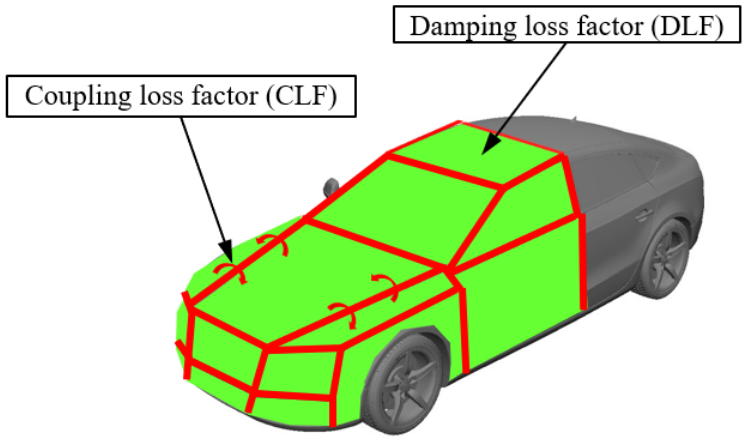

Figure 7: The front part of the vehicle is divided by SEA subsystems, the back part is the real geometry. The damping loss factor is equivalent to the damping of the subsystem while the coupling loss factor is equivalent to the energy loss between the subsystems.

The two oscillators shown in Fig. 6 are in essence an analogy to a heat transfer problem of two identical thermally conducting parts. When thermal energy is injected into the right subsystem, then one part dissipates to the environment, while the other part transfers heat energy into the left subsystem via the coupling. The modal density corresponds to the thermal capacity, the damping to radiation loss, the conductivity to the coupling loss factor and the flow of heat is similar to the flow of vibrational energy. The energy equilibrium between subsystem as well as the theory of coupling mechanisms will be introduced in more detail later, in Chapter 4.1.4.

The Loss Matrix can be obtained through the Power Injection Method. In this method, the first subsystem is excited with a certain (known or measured) injected power, while all other subsystems (response) energies are measured. Then, the next subsystem is excited, and all other subsystem's energies are measured and so on. As the Eq. 1 and Eq. 2 show the loss factors have huge importance in SEA, because they directly influence the results. Consequently, the accurate estimation of these parameters is crucial. There are three different ways to obtain DLFs and CLFs as the Fig. 8 illustrates.

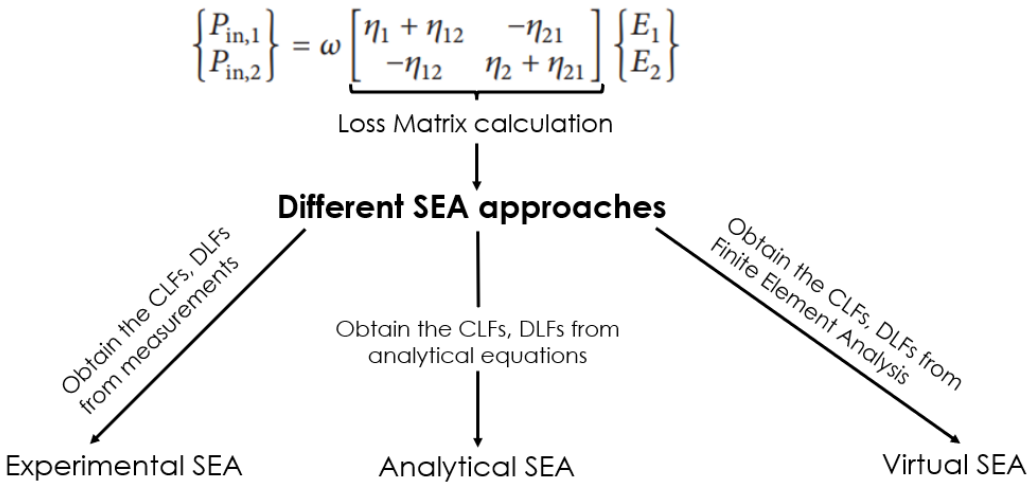

Figure 8: The 3 different approaches of SEA.

The current research will employ mainly the experimental SEA and partly the analytical SEA. Virtual SEA methods are relatively new and only a handful of publications exist in this field, with no industrial usage so far [6].

Fig. 9 illustrates the importance of using the proper damping values, since both the averaging process in the SEA simulations, as well as the different philosophies in evaluating results from FEM and SEA methods can have great influence on them. Fig. 9 shows two frequency response functions (FRF): one from an FEM simulation and the other from experimental results. Between 200-600 Hz, the FEM results are compared to the experiment without averaging, while above 600 Hz, the same FEM results are employed but by averaged in the 1/3rd octave band. Recall, that the FEM results show the exact location of the peaks as well as the magnitude of each peak, hence this method is called “deterministic” method. On the other hand, the SEA results show only the 1/3rd octave averaged results, i.e. the average magnitude of the numerous peaks in each 1/3rd octave frequency band. Thus, this “hides” the data about the individual peaks, and one cannot know anymore, where they would lie. However, it gives a good idea about their average magnitude over a certain (in this case 1/3rd octave) frequency band. Therefore, the SEA method gives information about the statistical distribution of the peaks, instead of their individual Details, hence this is termed as a “statistical” method, in contrast to FEM, which is termed as “deterministic” method.

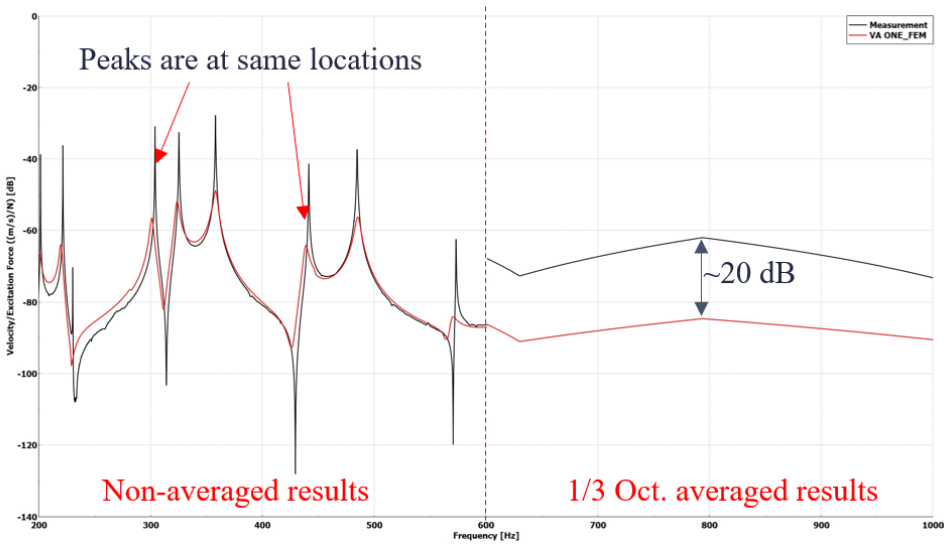

Figure 9: Comparison of FEM and experiment curves. From 200 to 600 Hz the FEM results without averaging while over 600 Hz averaged in 1/3rd octave band. As a consequence of the averaging the proper amplitudes so, damping values have significant impact to the simulation results in SEA.

Now, for the FEM analysis, the main aspect of the results is the location of the peaks i.e. the frequency differences between measurement and simulation results for the same peaks. Notice that the location of the peaks matches well, but the amplitudes do not. This is due to the errors in the damping values. However, one would be able to judge, that the FEM results match quite well the experiment, except for the amplitude. In contrast, the SEA results show much more pronounced difference from the experiment, and this is because the results are mostly influenced by the damping values due to the frequency band averaging process. Note that the two set of simulations results (FEM and SEA) are equally inaccurate with respect to experiment, yet this is much more pronounced visually in the SEA results. On the other hand, we have no information about the number or the peaks in SEA.

Although SEA in general works better at higher frequencies than FEM, the damping values can have massive effect on the results and wrong input values can literally ruin the results, as it was seen above. Consequently, entering the proper damping value in SEA is crucial for accurate simulations.

1.4.2. Hybrid FE-SEA method

SEA is ideal for panel-like structures that have a large modal density [2], [7-9]. As a rule of thumb, 3 modes/third octave band are required as a minimum for an SEA subsystem [10]. This gives a limitation to the applicability of SEA simulation methods for vehicles, where smaller subsystems or stiffer parts often cannot fulfill this requirement. Consequently, these smaller or

stiffer parts would be perfectly modelled by FEM, while the larger parts (that fulfill the SEA requirement on modal density) as an SEA subsystem. This is the main benefit of the hybrid FEM-SEA method in comparison to either pure SEA or pure FEM, since it perfectly combines the advantages of the two simulation methods. For simplified geometries, as shown in Fig. 10, the subdivision between the FEM- and SEA like subsystems is quite obvious, because it is easy to distinguish between the stiff (FEM) and panel (SEA) parts.

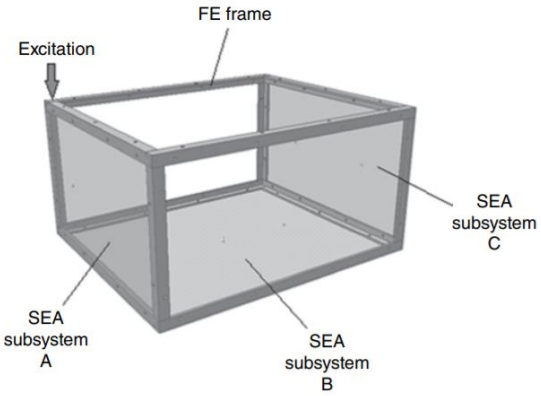

Figure 10: Ideal hybrid FE-SEA geometry with stiff parts for FEM and large panels for SEA simulations [10].

However, in vehicles the subdivision is not as straightforward as in the example above, since there are many components, which are not suitable neither for SEA nor FEM modelling. This is the real problem of the mid-frequency gap (400-1000 Hz), where some parts have too many modes to predict them accurately via FEM but they do not have enough modes to assign them as SEA subsystems [2]. These parts are then typically modelled based on the experience of the user, which can lead to accuracy problem at the end of the analysis. Fig. 11 illustrates an example of the division of the full vehicle

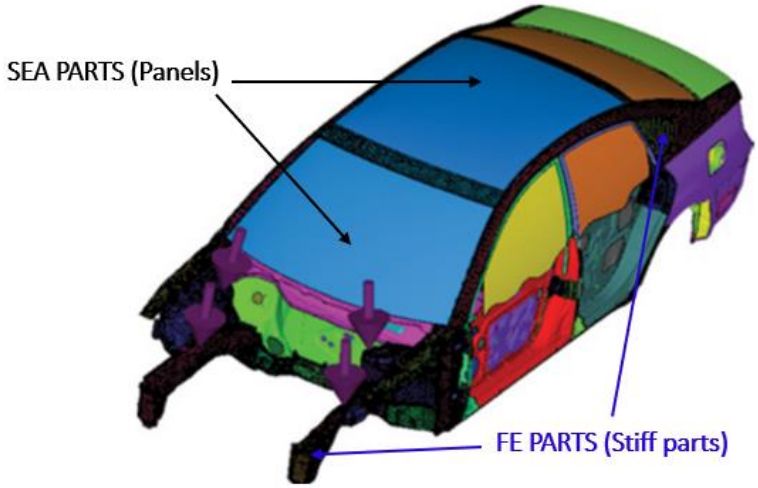

Figure 11: General philosophy of the FE and SEA division of a vehicle [11].

This Chapter highlighted the fundamental philosophy and key problems of vehicle vibroacoustic simulations in the mid-frequency and high-frequency range. In the next Chapter, we will review the state-of-the-art in these two field in detail, with the aim of identifying the concrete research gaps to be addressed in this thesis.

2. LITERATURE REVIEW

Statistical Energy Analysis (SEA) was first introduced by Lyon and co-workers [12] in the 1960s to solve complex vibroacoustic problems. Since then, SEA was applied to many other engineering problems, such as ships [13], [14], railway [15], [16], aircraft [17], [18], and there are several examples of SEA usage for household appliances as well, for example for washing machines [19] or refrigerators [20]. Although the SEA method is more ideal for large plates, which are typical of aircraft or ship structures, there are several examples for its application in the vehicle industry as well.

2.1. SEA in the vehicle industry

In 1996, Steel [21] has made a detailed investigation for a vehicle via SEA for the first time. The rubber strips around the windows as well as the door hinges were took into consideration in the virtual model. The vehicle consisted of 83 subsystems and some of them represented glass reinforced plastic material. Simulation results were compared to measurements and good agreement was found over 400 Hz. However, the simulation results overpredicted the vibration transmission at lower frequencies.

Galasso, et al., in 2004 [22] built up a detailed SEA vehicle model. Beyond the validation purposes, the goal of the study was to establish an experimental database as well as to determine the damping and coupling loss factors in assembled and disassembled configurations of the vehicle. Two different models were made a) a coarse model with 139 structural subsystems and 29 acoustic cavities; and b) a detailed model with 837 structural subsystems and 81 acoustic cavities. The final version of the vehicle model was a mixture of the coarse model functionalities and of the detailed model advantages. The results showed good agreement between the measurement and simulation results with around 3 dB error.

In 2004, Cordioli, et al., [23] summarized the main conclusions of the previous studies, which dealt with SEA in the vehicle industry. The authors described the main principles as well as the assumptions of the SEA method for vehicle development. Various excitation sources were considered, such as the tire/road noise or wind noise. The paper listed the advantages of the statistical energy analysis simulations in vehicle applications.

In 2012, Marzbanrad and Beyg [24] investigated a passenger car cabin under aerodynamic loads at high velocities. The authors compared the simulation results with experiments and considered

different viscoelastic materials. The frequency range considered was between 100-10 kHz. According to the authors, the main contributor to the sound pressure level in the cabin was the roof and a 1.4 mm thick viscoelastic layer applied to that caused around 4.3 dB reduction in the cabin.

The very same year, Musser et al. [25] have built an SEA model for a premium segment crossover. The model was validated via measurements, and among the numerous parameters evaluated they characterized the input powers, the dampings, or the absorptions of the carpets. The investigated frequency range was quite broad: between 500-6300 Hz. The SEA results were well correlated with the measurements and the model was able to predict design changes, such as the effect of laminated and nonlaminated glass.

In 2012, Xin et al. [26] investigated a car interior with SEA for a vehicle at high speed, where air-borne excitation was the main contributor to interior SPL. They investigated a highly detailed model in SEA, with proper excitations. The acceleration of the engine mounts, as well as the SPL in the engine compartment were measured at 100 km/h speed. The air-borne excitation was obtained from CFD simulations, with attention paid to the A-pillar and mirror area. The SPL at the driver's headspace was investigated from 200 Hz to 5 kHz. The comparison showed that the average deviation from the measurements was less than 3 dB (see Fig. 12).

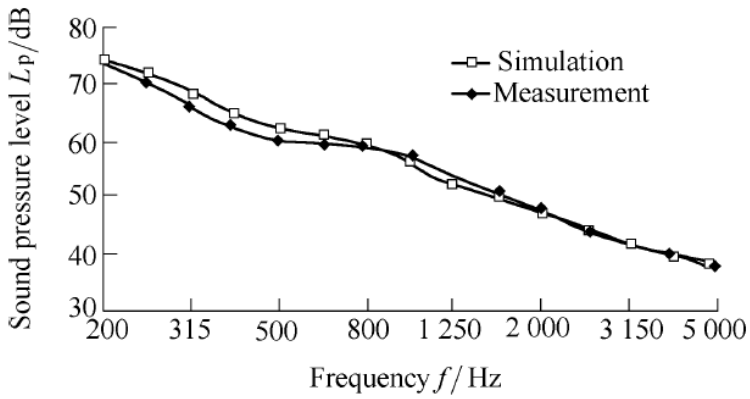

Figure 12: Comparison of SPL results for an SEA simulation of a fully trimmed vehicle according to Xin et al. Airborne noise excitation was obtained via CFD [26].

Another objective of the work was to reduce the SPL in the driver's headspace. The authors used a material database (AMDV) in order to set up different materials without measurements. There were 9 different load cases, and the results showed that they could reduce the SPL on average by 2,64 dB, except at idling condition where the SPL increased by 2,2 dB [26].

Putra et al. [27] worked out an individual method in 2014 to capture the diffuse field for the SEA in a vehicle interior. They proposed the total energy to be equal to the direct field and

reverberant field energies. For this, they removed the direct field component from the measurement and modified the DLFs and CLFs values accordingly. Fig. 13 shows the background of the analysis.

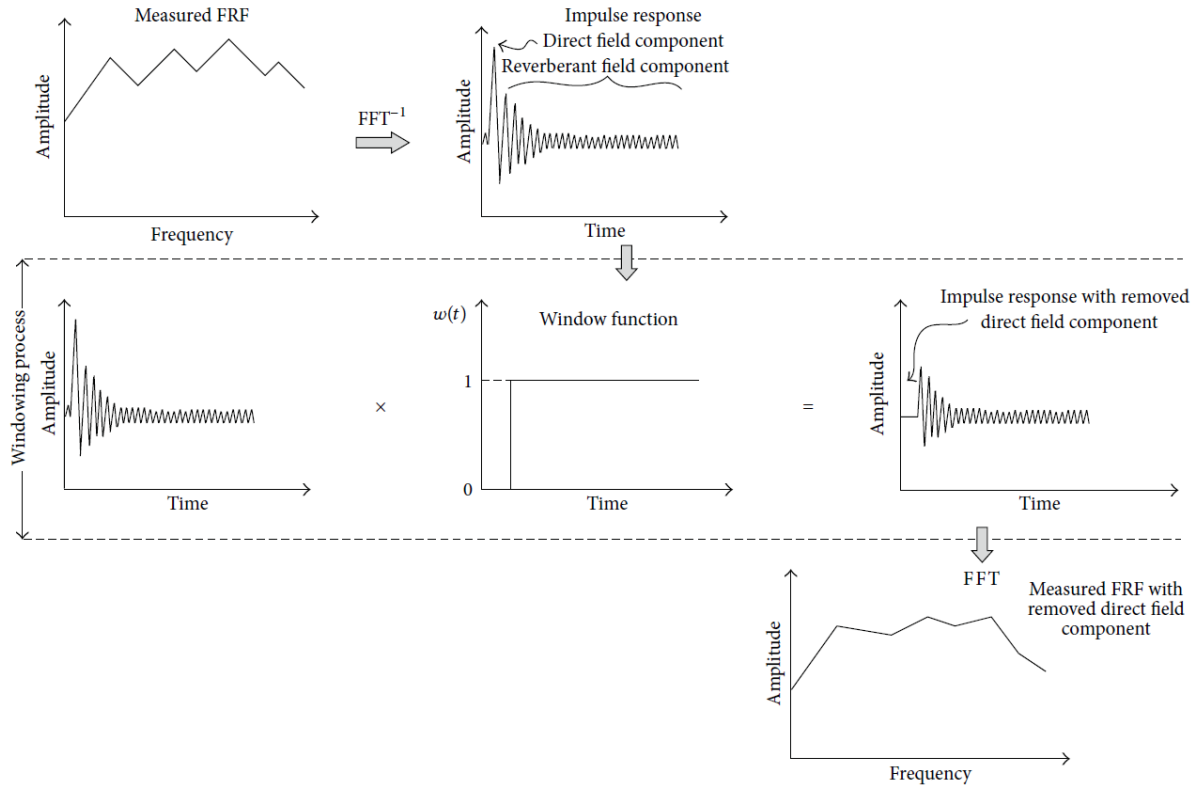

Figure 13: The direct field removing process according to Putra et al. [27].

It is interesting to note the details of the cavity substructuring. Putra et al. divided the vehicle interior into two subsystems, front and rear cabin. The front seats were the coupling between the cavities. During the measurements, a loudspeaker was used as an excitation, to inject the sound energy into the subsystem. Two cases were investigated: a) excitation from the loudspeaker, b) energy input from the engine at constant RPM. Sound intensity was measured, and the results were compared to the classical SEA as well as the corrected SEA methods. They tested a midsize vehicle in a semi-anechoic room. The corrected SEA simulations showed good correlation with the measurements, while the classical SEA overestimated the results at 1000, 2000 and 3000 RPM, as illustrated in Fig. 14 [27].

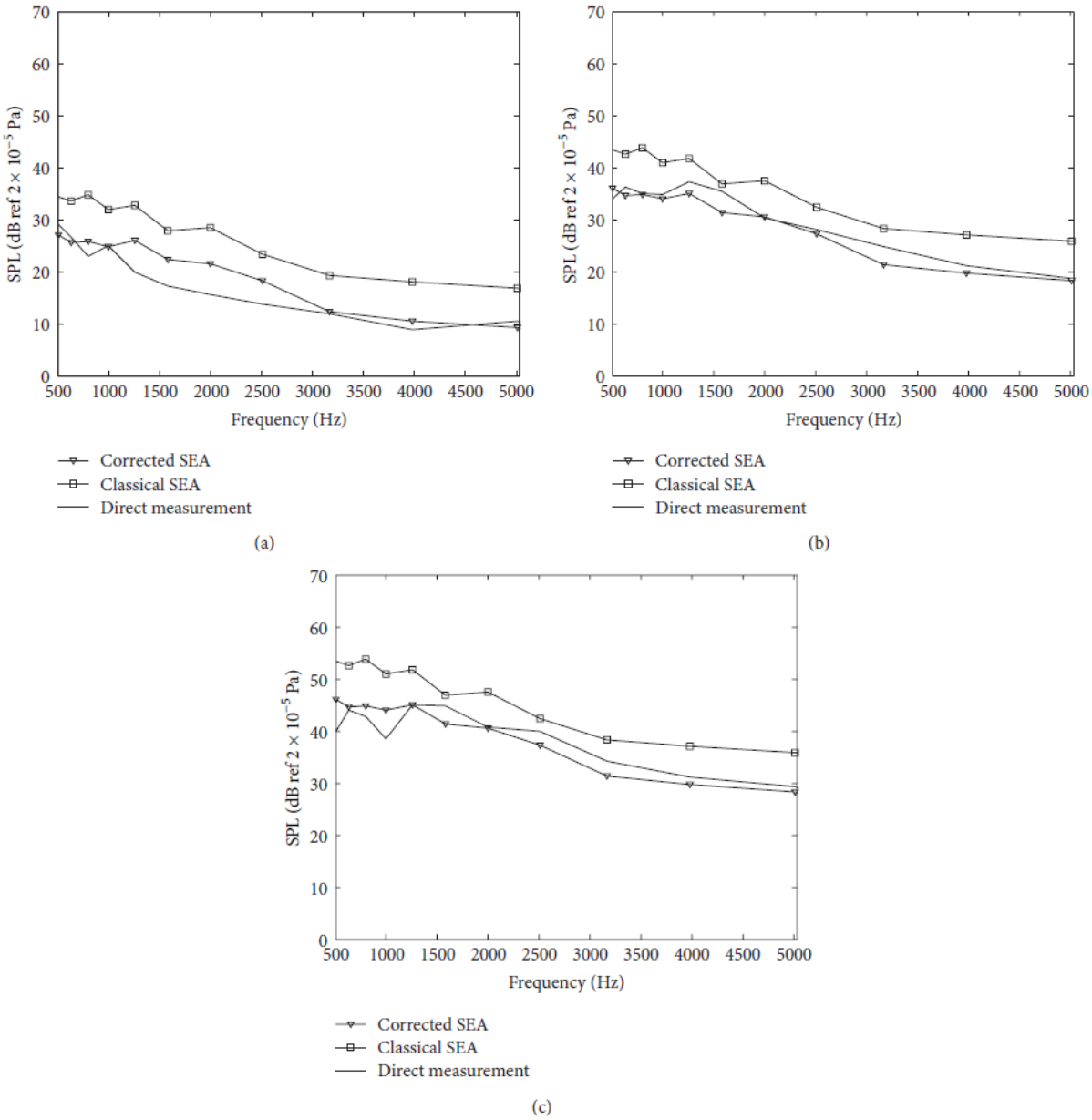

Figure 14: Results of classical and corrected SEA simulations at the three engine RPMs, according to Putra et al. [27].

Bötke et al. [28] investigated in 2015 a fully trimmed electric vehicle in SEA. They focused on the mid- and high-frequency ranges because of the high-frequency excitation. The road and the wind noise were the most dominant excitation sources, which were modelled as random signals. The authors described the limitations of FEM and explained why SEA is so powerful for these high-frequency analyses. According to Bötke et al., in the case of electric cars the location of the excitations is random, so it is required to analyse the whole vehicle and the whole sound insulation package together, which increases the model size and thus the computational costs in FEM. For the simulation model, various materials were experimentally characterized in terms of the poroelastic properties (porosity, damping loss factor, etc.) Two different test cases were

performed: a) a controlled environment in a semi-anechoic chamber, with a constant spherical sound source between 100 Hz – 10 kHz in the front and rear tire regions, using two different output nozzles; b) closed track tests at three constant speeds (10, 20, 40 km/h). The measurements were performed at the driver head as well as at the rear seat head positions with microphones. The results showed that differences of up to 10 dB could occur between the measurements and simulations. They listed the possible causes of errors, and classed them as being either dependent or independent from the actual computation.

Jang et al. [29] investigated in 2015 a mid-size truck in the commercial SEA software VA One and compared the results to measurements. They divided the truck into structural panel subsystems as well as acoustic subsystems, keeping in mind that the SEA subsystems must have at least 3 modes/bands in order to be valid. They considered the ribbing on the plate as well as the air duct in the pillars. For Noise Control Treatment definition, Biot-parameters were applied. The Transmission Loss (TL) TL for the grommets were specified analytically. If a panel was not an idealized SEA panel, they calculated it by a local FE model. Measurements were made on the road and on a 4-wheel dynamometer. The interior noise level was measured, and the structural and airborne transfer paths were investigated. According to the authors, in this case the airborne sources could be neglected below 200 Hz, while the structure-borne noise over 2 kHz. During the measurements, sound sources were placed around the vehicle and the SPL was measured at the driver and passenger headspaces. Tests were performed at multiple conditions: idle, wide open throttle for multiple gears, at constant 60, 80 km/h, as well as at steady-state conditions. It was concluded that the results correlated well, especially from 300 Hz.

In another study from the same authors, Jang et al. [30] analyzed in 2015 the air-borne noise transfer path with SEA of a truck. They optimized the sound package of the vehicle, using multi-layer poro-elastic materials. They identified the Biot-parameters of these by using an impedance tube and the FOAM-X software. The authors had two objectives: a) to improve the SPL at the driver head space at constant cost, b) to reduce the sound package cost at constant SPL. VA One has a Design Optimization Tool, which was used to optimize the performance and cost of the sound package. They measured the truck noise performance before and after the improved sound package implementation. For the beaded panels, modal correction factors were used to amend the modal densities. The truck was tested in a semi-anechoic room. In this analysis, the structure-borne sources were not considered, only the air-borne sources. The measurement was performed at 80 km/h at steady-state condition. Results showed that the

sound package was enhanced by 3 dB at no additional cost, and that the price of the sound package was reduced by 30% at same SPL.

Lafont et. al in 2016 [31] introduced a method for full vehicle SEA development, starting from the original equipment manufacturers global targets for acoustic performance down to the components target. The authors investigated the absorptions and transmission losses of the SEA panels and took into consideration the pass-through noises also. With the target cascading analysis (TCA) they managed to minimize the sound pressure level difference between the target and final model. The authors have also validated the SEA model of a B-segment vehicle and introduced a measurement process of the panel loads to identify the excitation during the simulations. The main goal of the study was to improve the acoustic transfer function at the driver's as well as the passenger's head position and they managed to reach relatively good results in this field.

In 2017, Siemens AG has issued a white paper on the challenges of vibroacoustic analysis of electric vehicles [1]. According to this, electric motors have higher excitation frequencies than internal combustion engines and thus the accessories have higher impact on the interior noise, especially at idle and low speed. Road noise and wind noise become more prominent and thus they have greater impact on the interior SPL as well. The problem with these excitation sources was that they are random and occur all around the car (Fig. 15). This implies the need for a full vehicle model with all noise control treatment.

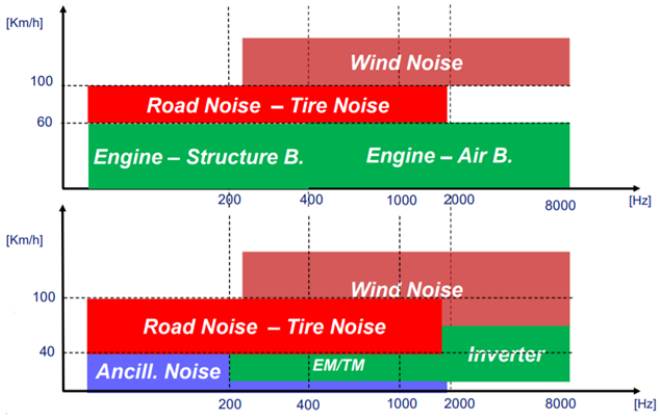

Figure 15: Contribution to interior noise for IC Engine driven vehicles (top), and Battery Electric Vehicles (bottom)according to Siemens AG [1].

The size of such model is excessive for a classical FE model. Thus, SEA simulations offer a big advantage over FEM models in a sense that they are better suited for high-frequency excitations and large models. The other issue with electric vehicles is that due to the large battery weight, weight reductions become more important. In order to design a lighter vehicle,

lot of new materials were developed, which modelling is another new challenge in vibro-acoustics. According to Siemens, an additional advantage of applying SEA analysis for electric vehicles is that the modelling of the exterior as an infinite cavity (see Fig. 16), as well as the transfer path analysis is easier in SEA than in other methods [1].

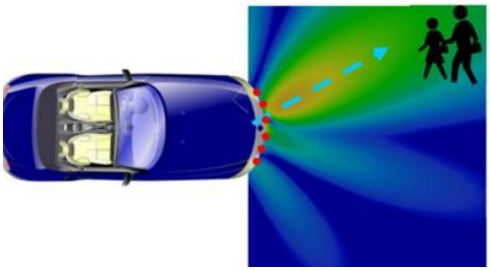

Figure 16: Exterior cavities have higher importance for electric vehicle [1].

2.2. Hybrid FE-SEA in the vehicle industry

Hauer et al. [32] wrote an article about the hybrid approach for a trimmed passenger vehicle in 2004. The hybrid method was used to identify the loss factors within and between the subsystems, by using a Power Injection Method. According to the authors, the hybrid method could calculate the tunnelling effect quite accurately, which meant that the physically not connected subsystems appeared as though coupled to each other. They investigated that how many response data were necessary in order to obtain reliable results. For internal loss factors, 5 response points were enough, while for CLFs 10 points were required. As a conclusion, the authors stated that the hybrid method was a powerful method, especially in the early stages of development, since it allowed to determine accurately the SEA model parameters for complex systems and complex junctions. Another advantage of the hybrid method was that the optimization process used only two subsystems for determining the loss factors.

Charpentier et al. in 2007 [33] used a hybrid FE-SEA method to predict the structure-borne noise in a trimmed automotive vehicle in the mid frequency range. The goal was to improve the SEA definition of the panels as well as the couplings used by the local FE models. They identified that simple structural junctions (welds, bolts) can be accurately estimated using the standard algorithms. The CLFs were described via the FE model. During the experiments, they applied a relatively large number of accelerometers, typically 10 per subsystem. Overall, 135 accelerometers were used for 15 load cases. Simulation and experimental results were found to be within 3 dB in most of the frequency bands.

Charpentier and Fukui [34] made a really detailed and advanced fully trimmed vehicle simulation via Hybrid FE-SEA in 2008. They investigated the mid-frequency domain between 200 Hz - 1 kHz. They divided the experiment to different levels: first, a subsystem analysis and then a transfer path analysis (TPA) on the rails of the chassis. In order to reduce the computational costs, they compared the various FE models with the Hybrid FE-SEA model. The authors used different excitation points and different receiver points during the investigation, and they took into account the seals, passthroughs and leakage of the vehicle. The model was able to calculate the acceleration correctly far from the excitation point during the TPA. These time-consuming tests were successful according to the authors and the results were within 2 dB. The instrument panel simulation times reduced from 20 hours to 7 hours. The difference between the models in terms of the interior noise was about 3-5 dB.

The usage of FE-SEA method in the mid-frequency range was the focus of Chen in 2011 [35]. The author made an intensive full vehicle investigation. The stiff parts of the car were modelled in FE while the flexible parts as SEA panels. The effect of the trim parts was considered as an absorption coefficient. Comparison was made at 120 km/h, the maximum absolute error was less than 3 dB(A), as Fig. 17 illustrates.

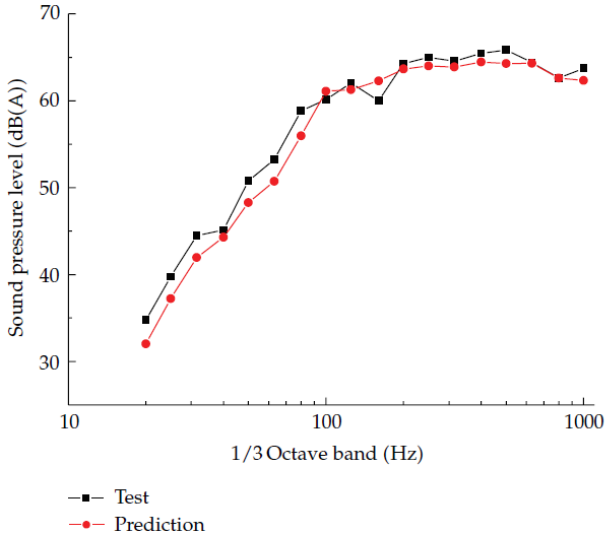

Figure 17: Simulation and measurement results of Chen for a hybrid FE-SEA method applied to a fully trimmed vehicle. No information from the trim material properties was used during the prediction [35].

Prasanth et al. [36] made a really detailed hybrid FE-SEA investigation for a trimmed full car in 2011, with the aim to reduce structure borne noise. The authors focused on the mid-frequency range, between 200-1000 Hz and used Noise Transfer Path Analysis (NTPA) to identify the main contributors of the interior noise. The receiver cavities were at the driver's headspace and

the right-rear seat headspace. Thanks to NTPA and the detailed car model, they could redesign the parts and observe the changes. For example, a modified windshield seal reduced the vibration on the windshield, which was one of the main contributors to noise. Furthermore, the headliner modification reduced the SPL too, mainly in the rear seat region. The floor and the firewall were not critical parts in this analysis. The prediction was compared to measurement and according to the article, the biggest challenge was the repeatability of the cabin noise measurement. The SPL accuracy was ±1 dB. The model was able to predict the input power within 5 dB in most of the frequency bands.

Prasanth et al. [37] used hybrid FE-SEA method in 2013 to solve the mid-frequency problem for a fully trimmed vehicle. The stiff parts were set up as an FE model, the panel-like structures as an SEA model. They used multiple sources at different locations. The sound package was modelled using a classical SEA Transfer Matrix Method and local FE models were used for each subsystem to calculate the SEA parameters. For the SEA validation, accelerometers at 40 subsystems were used, while the number of total measurement locations was 300. For the acoustic response, 40 microphones in 10 sub-cavities were applied to measure the SPL. The average difference was 3-5 dB between the measurement and the prediction. The simulation time was optimized and analysed in order to get the most accurate and reliable results as fast as possible. The fully trimmed model simulation took around 80 minutes on a regular PC.

Kurosawa [38] used hybrid SEA in 2016 to predict the SPL in a vehicle interior. His model consisted of 106 structural subsystems, of which 10 served as input subsystems. The number of acoustic cavity subsystems was 30. This model included the trims, damping materials, soundproof materials, as well as seals and leakages. Kurosawa determined the flow resistivity by Delany-Bazley's formula. The author pointed out that the flow resistivity will change if density changes. The sound absorption and sound insulation also changes. In conventional SEA model, the trim's thickness distribution is considered, and he improved it further by completing it with the density changes of the material. Measurements were carried out in a semi-anechoic room. The vehicle was measured on a chassis dynamo (CDM) as well as a test course (TC) in steady-state conditions. The difference between the two conditions was the air-borne excitation. The results of the comparison were that the SPL difference was +-2 dB in the 800 Hz – 5 kHz frequency range. This paper is one of the most comprehensive ones, including a very detailed vehicle model, as well as detailed description.

Besides full vehicle simulations, the hybrid FE-SEA method was applied on vehicles sections too. Siano, et al. [39] have made an investigation of an engine cover. The authors used the

hybrid FE-SEA method in different aspects. The geometry was modelled in FEM, while the cavity in SEA. The engine cover modelled as an FE model with very fine mesh, was able to produce modal analysis results with 100 % accuracy up to 5 kHz. They also calculated transmission loss values of the cover, but the results were not compared to measurement results.

Beigmoradi et al. [40] has performed an FE-SEA analysis of a car door in 2013. They made a clearance analysis of a B segment car door structure in order to improve the noise level in the driver's ear position. The trimmed door involved two parts: a trim panel and a pocket section. The clearance ranged between 0.1 and 6 mm, and they investigated only the worst-case scenario nodes. As a result, they improved the rattle by adding ribs or by increasing the number of connection points. Adding some ribs on the pocket increased the stiffness of the region and reduced the rattle.

A critical point, i.e. the determination of the correct Transmission Loss value between two cavities was addressed by Wu et al. in 2014 [41]. They developed a new approach to improve the Transmission Loss (TL) definition called Edge-based Smoothing FE-SEA (ES-FE-SEA). The goal was to make the stiff part of the deterministic model softer as well as to eliminate the numerical error in standard FEM. They compared the ES-FE-SEA results to a very smooth meshed FE model and a rough FE model. The second case was a dash panel and the results showed good agreement with the reference results. Also, computational efficiency was better than the reference one. The ES-FE-SEA method provided more accurate results than the traditional FE-SEA using the same mesh.

Tanner et al. [42] investigated in 2016 a vehicle floor that was excited between 0 - 3 kHz frequency. A hybrid FE-SEA method was used to solve the mid-frequency gap. The stiff beams were modelled by FE, while the panels in SEA. A new alternative model for the SEA subsystems called Discrete Flow Mapping (DFM) was also developed. The DFM result was compared to Monte Carlo FEM results, and it showed good agreement with the FEM results.

2.3. Literature review of the evaluation processes

The literature review of the full vehicle structures has showed that several important details are missing from the papers, for example that how the damping was determined, or what was the distribution of the damping values in the different frequency bands. In this subsection, the literature review focuses on these more specific questions, with detailed description of the measurements and the evaluation process.

2.3.1. Damping determination

As it was emphasized in Chapter 1, the proper damping determination is crucial from the simulation accuracy point of view. There have been numerous papers published on the experimental determination of damping loss factor, but the measurement methods used were quite diverse. Table 1. shows an overview of the literature related to determining the damping parameters for simplified systems or plates

Table 1: Review of the literature related to damping determination via experiments.

Paper	Examined structure	DLF determination method	DLF statistics	Measurement sensitivity study	SEA simulation comparison
J. Petrik, et al., 2016 [43]	Plywood plate	Impact test, DRM	Yes	No	No
M. Bustamante, et al., 2016 [44]	Steel, Aluminum plate, Beam	Shaker test, HPBM, PIM	Yes	Yes	No
M.B. Mandale, et al., 2015 [45]	Metal and Composite plates	Impact test, HPBM	No	No	No
A.A. Jadhav, et al., 2015 [46]	Glass plate	Impact test, HPBM	No	Yes	No
R. Cherif, et al., 2015 [47]	Aluminum and composite plates	Shaker test, LDV; PIM, HPBM, DRM, IWCM	No	Yes	No
M. Jaber, et al., 2014 [48]	Composite plate	Shaker test, Laser Vibrometer; PIM, HPBM	Yes	Yes	No
L. Zoghaib, et al., 2013 [49]	Aluminum plate	Acoustic excitation, Laser Vibrometer; DRM	Yes	Yes	No
N. Schiller, et al., 2010 [50]	Composite cylinder	Shaker test, Laser Vibrometer; DRM	Yes	No	Yes
R. Cabell, et al., 2009 [51]	Curved, stiffened sidewall	PIM, Manual DRM, Automated DRM	Yes	No	No
N.K. Mandal, et al., 2004 [52]	Steel plates, damping layers	Shaker test, accelerometer HPBM	No	No	No
M. Iwaniec, 2003 [53]	Loudspeaker, shaker test; DRM	Loudspeaker, shaker test; DRM	Yes	Yes	No
P.R.Mantena, 1996 [54]	Polyester, Epoxy, Aluminum, Graphite	Impact test, Eddy current probe; HPBM	No	No	No

Beyond this, only a few papers comment on the statistical distribution of the DLF values or investigate the effect of the experimental results in simulations. In addition, none of the papers makes a correlation between the way how the boundary conditions are realized or their effect

on DLF. In summary, no prior literature has investigated the following parameters simultaneously: 1) the correlation between the measurement boundary conditions and the change of DLFs, 2) the statistics of the damping values, 3) comparison of simulation with the obtained DLF values to the experiment results.

2.3.2. Damping layer application

In the vehicle and aircraft industry, the application of damping layers is one of the most efficient ways to find the optimal balance between noise reduction and added mass. Noise reduction is crucial from customer satisfaction point of view, while the added mass increases the weight of the vehicle, which consequence can be an increased CO_2-emission. Since this is a important field in the industry, lot of papers have investigated constrained and unconstrained damping layers. Wodtke and Lamancusa [55] optimized the distribution of an unconstrained damping layer for a circular plate, with the goal to reduce the radiated sound power for a given frequency band. Ege et al. [56] have achieved good results in the determination of the frequency dependent complex modulus of a polymer core layer, in a three-layered sandwich composite plate. Arenas and Hornig [57] applied an unconstrained damping layer onto a rectangular plate and estimated the sound power radiation numerically. Beldar and Kushare [58] compared the DLFs of different beams, such as that of undamped, free layer, and they applied different damping materials on the structure, then they compared the FEM results to experiments. Fan et al. [59] developed and measured new damping materials (e.g. bitumen-based, water-based and butyl rubber) for railway carriages. They applied these materials in free-layer and constrained-layer form too. They have proposed that the measure of loudness should be used to assess reduction effect. Sanliturk [60] developed a multi-layered isotropic composite finite element method to assess its damping capability. Cherkasov et al. [61] examined the damping of sandwich beams two steel sheets connected by self-adhesive bitumen-rubber mastic with the focus of investigating the effect of the thickness of the viscoelastic layer and the temperature change to the damping properties in the -40°C to +80°C temperature range. Ruijiao et al. [62] inspected a full vehicle with SEA and introduced the influence of the different parameters to the results, such as the leakage, the loss factors and the acoustic materials. Consequently, all of these parameters directly affected the simulation results. Yanninan et al. [63] investigated a Fiber Reinforced Plastics (FRP) material for yachts and accessed its loss factors by PIM and impulse response decay method (IRDM). The results showed that for FRP plate the PIM is a better way to calculate the loss factor.

2.3.3. Coupling loss factor determination

Numerous methods exist for obtaining the CLF. The main ones are the modal approach [8], the energy ratio method [64] or the Power Injection Method (PIM) [18],[65],[66]. Several papers deal with the experimental determination of CLFs. Sablik [67] measured the transmission coefficient and CLF for beams in L-shape joints. Mandale, et. al [68] measured L-shape structures with different plate materials, such as steel, copper, acrylic, etc. connected by screwed and bolted junctions. They used the energy level difference method to calculate the CLF values. Mandale, et. al [69] in a later study investigated L-shaped structures with different materials and various junction types, such as screwed, bolted and riveted junctions with different joining lengths. The effect of the tightening torque on bolted junction is also investigated. Jintao and Meiping [64] improved an energy ratio method to estimate CLFs for three shell cylinders. Le Bot, et al. [70] examined three rectangular plates with random resonators, the coupling parameter is estimated by SEA equations and compared to a semi-analytical method. Patil and Manik [71] performed a sensitivity analysis of two right angle coupled plates connected along welded and bolted joints. Panuszka, et al. [72] measured the SEA parameters experimentally and compared the results to analytical formulas. The test cases were L-shape structures with different type of junctions and different thickness ratios of the plates. The DLF is estimated from the reverberation time, while the CLF is obtained from the power balance equation. Bosmans, et al. [73] examined theoretically an L-junction with varying plate dimensions and varying orthotropic stiffness of the plate material. Cuschieri and Sun [74] determined the dissipation and coupling loss factors for a rotating machinery structure, based on measurements of the energy ratios between the subsystems. Wester and Mace [75] investigated two edge-coupled simply supported, rectangular plates from coupling strength and modal overlap point of view, while Wöhle, et al. [76] calculated the CLFs at rectangular slab junctions, by assuming springs at the coupling points and the possible energy losses. In a subsequent publication, the same authors have also examined the structure-borne sound transmission created by forced bending wave [77].

2.4. Research gap

The literature review above aimed to provide an overview about the state-of-the-art of pure SEA as well as hybrid FE-SEA simulations related to vehicle vibroacoustic simulations, including the works related to mid-frequency range applications. The literature review focused on the vehicle application and the cornerstones of the two methods. It became clear that one of

the most important features of the SEA method is the proper definition of the subsystems and of the values of the Coupling Loss Factors (CLF) and Damping Loss Factors (DLF) for them. For this reason, in Chapter 2.3. the literature review focused on the evaluation process mainly for simplified geometries. As a summary of the literature survey, the following conclusions can be made:

- Several important parameters of the SEA simulations were not described even in the most detailed papers. These include the effect of the damping loss parameters on the results, how the boundary conditions influenced the damping values during the measurements, or the frequency response results. Most of the papers did not deal with the statistic behavior of the measured values as well.

- The representation of the damping layers in SEA simulations is not trivial, since in most cases the damping layers are not covering the full subsystem and their distribution is somewhat random. Due to the very nature of SEA it is not possible to represent the damping materials locally. The current literature lacks information on how to represent the distribution of damping layers in SEA.

- The proper evaluation of the CLF values is a key to achieve accurate simulation results. The various junction types have different CLF values and therefore the measurement of these parameters is one of the most important elements of the SEA simulations. However, the literature related to vehicles does not specify the details of the junction types used or how the CLFs were determined during the simulations.

- In the full vehicle hybrid FE-SEA simulation a critical point is unclear: the current literature does not describe that along what logic were the FE parts and SEA subsystems divided or investigated as well as that how these choices influenced the results, if the proportion of the FE and SEA parts were changed.

3. AIMS OF THESIS

Based on the above, one of the most important cornerstones of SEA-based simulations is the logic of substructuring of the vehicle as well as the accurate determination of the values of DLF, CLF and the modal parameters of the structures. To answer the gaps in the literature identified in Sec. 2.4., the following specific research goals were set for this Thesis:

1) To formulate guidelines for the determination of the damping for typical SEA panels. The specific goal is to derive these guidelines for an extremely sensitive, lightly damped plate in the frequency range up to about 1000 Hz, with simultaneous consideration of the a) effect of the realization of the boundary conditions, b) the statistics of the measured data and c) the comparison between SEA simulations and experiments.
2) To propose a method for taking into account the spatial distribution of the damping layer on an SEA subsystem.
3) To examine the effect of binding technique between the subsystems. The specific goal is to investigate all binding types occurring in vehicle structures as well as to investigate the effect of the connection angle between them.
4) To examine the effect of the relative size of the SEA and FEM-like subsystems for the hybrid FE-SEA method.

In order to achieve these goals, a set of test apparatuses – with increasing complexity - were designed, which will be introduced in one of the next Chapters. However, since their design was driven by SEA-based criteria, first, the theory of SEA will be reviewed in detail.

4. THEORETICAL BACKGROUNDS OF THE SIMULATION METHODS

4.1. Statistical Energy Analysis

The main philosophy behind Statistical Energy Analysis was introduced in Chapter 1.4. This chapter, on the other hand, will introduce more details to enable later the understanding of the contributions of this thesis. The description below is based on Refs. 8 and 10, unless otherwise indicated.

Statistical Energy Analysis is suitable for high frequency problems, where the peaks in the frequency domain results occur so densely, so that it is hard to distinguish between them and therefore they are managed on a statistical basis rather than individually (or deterministically). It means, that the method uses average response values for the structure spatially as well as in the frequency band. The *Energy* refers on the main variable of interest. The idea behind SEA is to so divide the structure to subsystems, - which are groups of similar modes, - so that they have nearly equal vibrational energy. In complex systems, the model is based on energy equilibrium and power flow between the subsystems. The subsystems can store, dissipate and transmit energy and can be of beam, plate or acoustic type. One of the main challenges of the method is to determine that how can complex structures be divided into groups of similar modes. In SEA, the main variable is the vibrational energy. At higher frequencies, where the modal density is high, the average of the kinetic and potential energies are equal to each other. The total energy of a subsystem of the structure is then given by the following expression:

$$E = m < v^2 >, \tag{3}$$

where, E is the vibrational energy of the subsystem, m is the mass of the subsystem, $< v^2 >$ is the spatially averaged squared vibration velocity of the subsystem. The acoustic subsystem energy is [78]:

$$E_i = \frac{p_i^2 \, V_i}{\rho_i \, c_i^2}, \tag{4}$$

where, p_i is the root-mean-square sound pressure level (SPL) in the acoustic cavity, marked as V_i. The continuum density is ρ_i and the c_i is the wave speed in the continuum.

Consider a single subsystem – e.g. a flat plate – into which power is injected via excitation. This subsystem will store some of the vibrational energy, while the rest will be dissipated (see Fig. 18). The following equation describes this phenomenon:

$$P_{i,diss} = \omega\, \eta_i\, E_i, \tag{5}$$

where, $P_{i,diss}$ is the dissipated power, ω is the circular frequency, η_i is the damping loss factor and E_i is the stored energy in the subsystem.

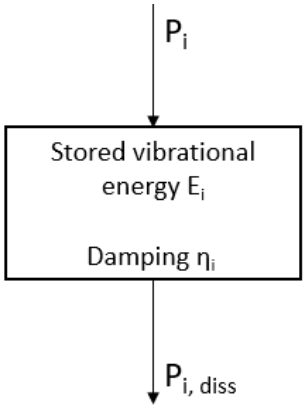

Figure 18: Power equilibrium of one subsystem.

For coupled structures, at subsystem connection the energy conservation can be written as:

$$P_{i,in} = P_{i,diss} + \sum_{j=1,\neq i}^{k} P_{ij}, \tag{6}$$

where: $P_{i,diss}$ is the dissipated power and equals with Eq. (1), P_{ij} is the power dissipation at the connections, $P_{i,in}$ is the injected power into subsystem i.

Every numerical method has limitations, or is based on assumptions, which have to be taken into account in order to get reliable results in the simulations. There are several publications, where the effect of these assumptions on the simulation results were investigated [70], [79] The theory of SEA was derived by applying the following four assumptions:

- High modal density, i.e. large number of modes
- Uncorrelated excitation, e.g. rain-on-the-roof excitation
- Light damping
- The coupling between the subsystems needs to be weak

4.1.1. Modal parameters

In SEA the actual frequency of any resonance peak and the corresponding mode shape are not as important information as the mode count, since this embodies the number of resonant modes accessible to receive and store energy in a subsystem.

The mode shape for a simply supported homogenous, isotropic plate can be written as:

$$\psi_{n,m} = 2 \sin\frac{n\pi x}{L_1} \sin\frac{m\pi y}{L_2}, \tag{7}$$

where L_1 and L_2 are the lengths of the system, the m and n are the mode numbers along the edges and are therefore integers. The resonance frequencies can then be expressed:

$$\omega_{n,m}^2 = \left[\left(\frac{n\pi}{L_1}\right)^2 + \left(\frac{m\pi}{L_2}\right)^2\right]^2 \kappa^2 c_L^2, \tag{8}$$

where κ is the radius of gyration and c_L is the longitudinal wave speed.

The wavenumber of a mode in a rectangular plate with the length L_1 and L_2 (see Fig. 19) is given by:

$$k_{m,n} = \sqrt{\left[(m-\delta_1)\frac{\pi}{L_1}\right]^2 + \left[(n-\delta_2)\frac{\pi}{L_2}\right]^2}, \tag{9}$$

where δ_1, δ_2 are correction terms dependent on the boundary conditions.

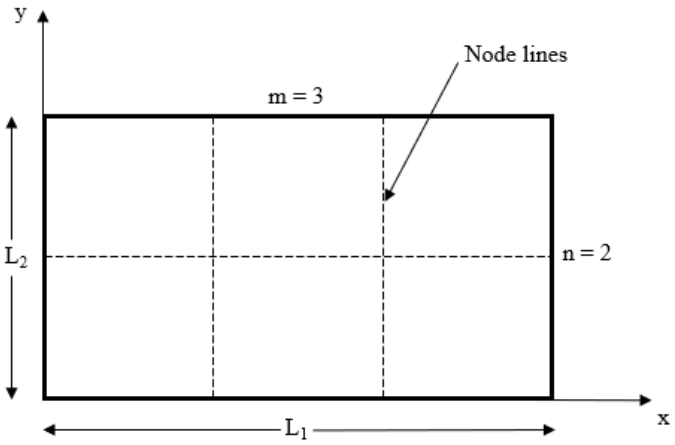

Figure 19: Node lines of a simply supported plate.

According to Eq. (9) each point represents a mode in the wavenumber lattice, while the distance from the origin gives the resonance frequency of mode ω_n, as illustrated in Fig. 20. As a consequence of this sorting, the calculation of the modes will resonate in any given frequency band.

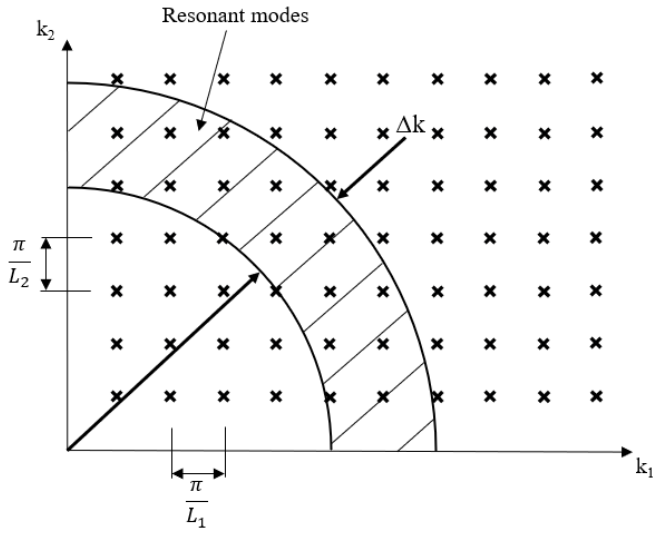

Figure 20: Wavenumber lattice for rectangular plate: represents the number of resonant modes in a frequency band.

The modal density in terms of wavenumber can be expressed as:

$$n(k) = \frac{\pi k \Delta k}{2\Delta A_k \Delta k} = \frac{\pi k}{2\Delta A_k}, \tag{10}$$

where ΔA_k is an area in the wavenumber lattice, A_p is the area of the plate, Δk is the changes of the wavenumber, which determines a new area, consequently new modes. The modal density in units of Hertz for a homogenous plate would then be the following:

$$n(f) = n(\omega)\frac{d\omega}{df} = \frac{2\pi^2 \omega A_P}{4c_p^2 \pi^2} = \frac{A_p}{2\kappa c_l} = \frac{\sqrt{3}A_p}{hc_l}, \tag{11}$$

where cp is the phase velocity, κ the radius of gyration, h the thickness of the plate, and c_l the longitudinal wave velocity. As can be seen in Eq. (11) in this instance the modal density is independent of the frequency. Next, the modal density of an acoustic volume is given by [78]:

$$n(f) = \frac{4\pi f^2 V}{c_0^3} + \frac{\pi f S}{2c_0^2} + \frac{L}{8c_0}, \tag{12}$$

where V is the volume, S is the surface, L is the total length of all edges and c_0 is the speed of sound in the fluid. The modal density in a certain frequency band can be expressed as:

$$n(f) = \frac{N}{f_2 - f_1}, \tag{13}$$

where N is the number of modes within the frequency range, which is determined by f_1, f_2. Finally, the modal overlap factor M, characterizes the adequacy of SEA for a given system in a certain frequency range. It is expressed as [80]:

$$M = \omega \eta n(f). \tag{14}$$

When M<<1 the modes can be clearly identified, when M>>1 the modes can be difficult distinguish.

4.1.2. Injected power into the system

The various types of excitations for vehicles were introduced in Chapter 1.3. As a starting point for an SEA analysis, one needs to know the injected power into the system. This can be calculated from the force acting on the structure as:

$$P = \frac{1}{2}|F|^2 \, Re\{Y\}, \tag{15}$$

where Y is the mechanical point mobility at the point where the load was applied, and it is defined by:

$$Y = \frac{v}{F} = \frac{1}{Z}, \tag{16}$$

where Z is the mechanical impedance of the structure. The excitation can be described also from a velocity source as:

$$P = \frac{1}{2}|v|^2\{Z\}, \tag{17}$$

or, alternatively, as an acceleration source:

$$P = \frac{|a|^2}{2\omega^2} Re\{Z\}, \tag{18}$$

where $|a|$ is the amplitude of acceleration. The way of calculating the input power in experiments requires to use of a force gauge as well as an accelerometer at the location of the excitation. From simulation point of view the excitation must be random, uncorrelated white noise, leading to the so-called rain-on-the-roof excitation. Moreover, the external force distribution must be statistically independent in order to excite all modes of the system. Generally, this means that with increasing the number of excitations more modes can be excited, and that the statistical parameters of the experiment are increasing. In practice, at least 3 different excitation points are preferred during the measurement process. According to Lafont [81] if the field is not diffuse, it can become a diffuse one by increasing the number of excitation points, no matter what the damping or the frequency band was. This is a favorable condition from Statistical Energy Analysis point of view, consequently the rain-on-the-roof excitation is advantageous for energy equipartition.

In the case that the input power comes from sound pressure excitation the way of power calculation would be the following:

$$P = IS = \frac{p^2}{\rho_0 c}, \tag{19}$$

where I is the sound intensity and S is the area. The sound pressure can be determined by measurement or Computational Fluid Dynamics simulations.

4.1.3. Damping loss factors

In Statistical Energy Analysis simulations, the Damping Loss Factor (DLF) is an especially important input parameter, since the response results depend directly on the damping value. Eq. (5) shows the basic formulation of the Power Injection Method (PIM), which is the foundation for statistical simulation methods. Damping converts the kinetic and potential energy into heat, and it contains several mechanisms:

$$\eta = \eta_s + \eta_{rad} + \eta_j, \tag{20}$$

in which η_s, η_{rad}, η_j, are the structural damping (including material damping), damping due to acoustic radiation, and damping due to joint friction, respectively. In simulations DLF is expressed as an average value in every frequency band. There are several methods to determine the DLF experimentally, from which the three most commonly used ones are: the Power Injection Method (PIM), the Decay Rate Method (DRM), and the Half Power Bandwidth Method (HPBM) [43] [48]. Note that all these methods are suitable for lightly damped structures.

The Power Injection Method is based on the Statistical Energy Analysis's power-balance equations. According to the definition, the DLF is equal to the ratio of the input power and of the product of the total energy of the subsystem and of angular frequency. For simple oscillators is expressed as:

$$\eta = \frac{1}{2\pi} \frac{Energy\ dissipated\ per\ cycle\ of\ oscillation}{Maximum\ energy\ storing\ during\ the\ cycle}. \tag{21}$$

In a particular subsystem, the averaged value of η in a frequency band is the following:

$$\eta = \frac{P_{in}}{\omega E}. \tag{22}$$

This method requires the input power identification during the measurement, thus the input force and the input velocity, must be simultaneously measured. For shaker excitation the usage

of an impedance head is required, while for impact excitation an accelerometer close to the hammering point is necessary. To identify the total energy of the subsystem, one must consider several spatial averaging over randomly located response points on the structure.

The second method is the Half Power Bandwidth Method, in which the DLFs are determined from the resonance peaks of the individual modes. It is related to the modal behavior of the structure. In order to reduce the experimental error during the estimation of the DLF, the averaging over several excitation and response points is required. This method uses the Frequency Response Function (FRF) directly to calculate the 3 dB drops from the resonance peaks, as shown in Fig. 21.

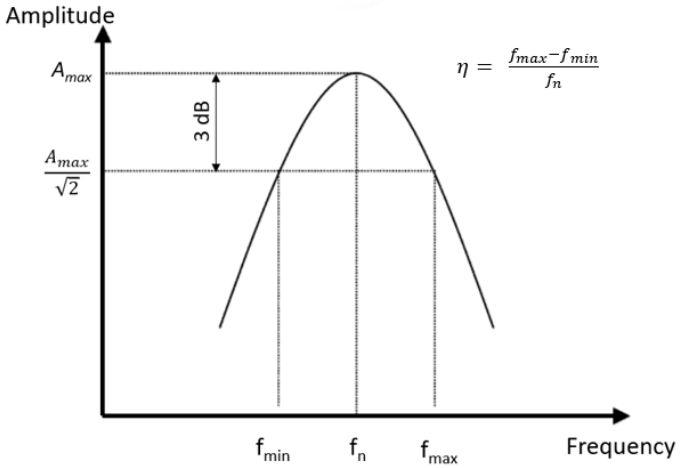

Figure 21: DLF determination from half-power bandwidth from the resonance peak.

Since this method is based on the individual peaks, the modal density must be taken into account. If this is too high, the peaks are getting too close to each other and make impossible the use of this method. Eq. (23) provides a guideline for choosing the Δf that represents the minimum distance of the two modes next to each other:

$$\Delta f < 3\,\eta\,f. \tag{23}$$

If the modes are too close to each other, one should determine the DLF in another way, such as the third method, the Decay Rate Method (DRM). This method is commonly used for broad-band damping estimates. This is based on evaluating measurement data in the time domain. In general, the excitation comes from impulse source such as a hammer hit, gun shot, noise burst, etc., and the resultant slope of the decay – termed the Decay Rate (DR) – is measured in dB/s. Fig. 22 illustrates the measurement graphically.

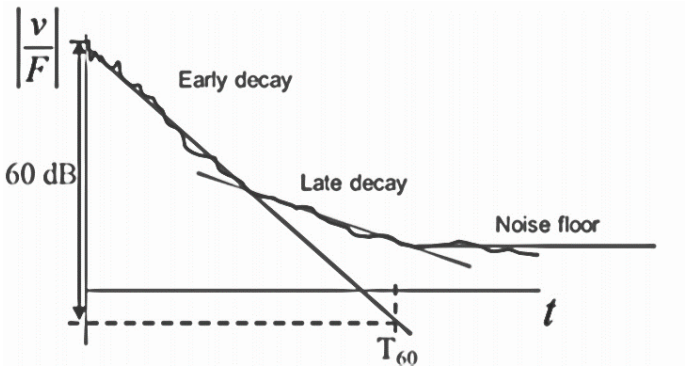

Figure 22: Theoretical background of the Decay Rate Method [43].

The damping loss factor from the decay rate will then be the following:

$$\eta = \frac{2.2}{f\,T_{60}}, \tag{24}$$

where f is the frequency center of the band and T_{60} is the time for early decay to drop by 60 dB. Several excitation and response points should be applied over the structure, to obtain the spatial average over different mode shapes.

In case of acoustic cavities, the damping loss factor is expressed as the acoustic absorption coefficient:

$$\eta = \frac{A\,c_0}{8\,\pi\,f\,V}\bar{\alpha}, \tag{25}$$

where V and A is the cavity volume and surface area, respectively, c_0 is the sound velocity, f is the frequency, $\bar{\alpha}$ is the average surface sound absorption. Note that the determination of the DLF of an acoustic cavity will not be used in this Thesis.

4.1.4. Coupling loss factors

As it was introduced in Chapter 1.4. the Coupling Loss Factors (CLF) are represented between the subsystems, and it is related to the transmitted power from subsystem *i* to subsystem *j*. CLF can be determined from analytical formulas or measurements. One of the most commonly used measurement process to obtain the loss matrix is the Power Injection Method. In this method, all subsystems are excited in one after the other and the injected powers are recorded, while all the subsystem's energies are calculated. So, as the first subsystem is excited, all subsystem's responses are measured Then, the next subsystem is excited, and the responses are measured again for all subsystems and so on. Consider a structure with two coupled subsystems as illustrated in Fig. 23.

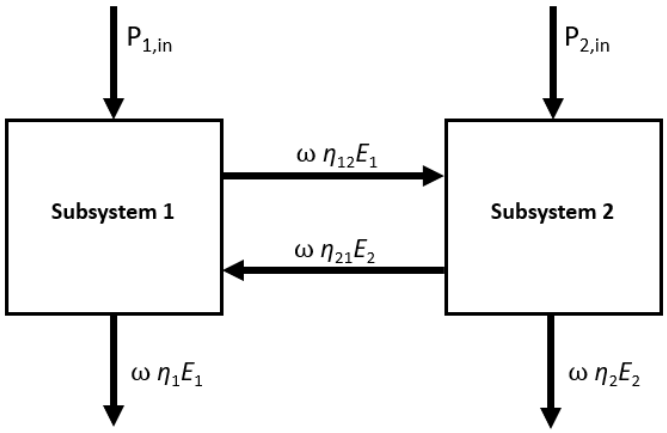

Figure 23: Energy balance between two subsystems.

The power balance equation can then be expressed as:

$$P_1 = \omega\eta_1 E_1 + \omega\eta_{12} E_1 - \omega\eta_{21} E_2. \tag{26}$$

In this instance the power balance equations can be expressed in a matrix form as:

$$\begin{pmatrix} P_1 & 0 \\ 0 & P_2 \end{pmatrix} = \omega \begin{pmatrix} \eta_1 + \eta_{12} & -\eta_{21} \\ -\eta_{12} & \eta_2 + \eta_{21} \end{pmatrix} \begin{pmatrix} E_{11} & E_{12} \\ E_{21} & E_{22} \end{pmatrix}, \tag{27}$$

where the left side of the equation is the vector of input powers, while the right side contains the frequency, the loss matrix, and the energy vector, respectively.

The reciprocity relation is given by:

$$n_1\eta_{12} = n_2\eta_{21}, \tag{28}$$

where: n_1, and n_2 are the modal densities of subsystem 1 and 2, respectively. The reciprocity is a principle that applies to systems composed of linear, passive and bilateral elements.

When *n* subsystems are connected to each other, then the Power Injection Method equation can be written in matrix form in the following way:

$$\omega \begin{bmatrix} \eta_{11} & \cdots & -\eta_{n1} \\ \vdots & \ddots & \vdots \\ -\eta_{1n} & \cdots & \eta_{nn} \end{bmatrix} \begin{bmatrix} E_{11} & \cdots & E_{n1} \\ \vdots & \ddots & \vdots \\ E_{1n} & \cdots & E_{nn} \end{bmatrix} = \begin{bmatrix} P_1 & \cdots & 0 \\ \vdots & \ddots & \vdots \\ 0 & \cdots & P_n \end{bmatrix}, \tag{29}$$

where: η_{11} and η_{nn} are the Damping Loss Factor of the 1^{th} and n^{th} subsystem, respectively, η_{1n} and η_{n1} are the Coupling Loss Factors, which represent the energy loss at the junctions.

Two different approaches are distinguished when deriving CLFs for junctions: a) modal approach and b) wave approach. In the modal approach the coupling parameters are based on the differences in the modal energies of the subsystems. On the other hand, the wave approach is based on the wave behavior of the vibration that propagates in the structure and it reflects and transmits at a junction. This approach supplies an effective way to determine the CLFs.

The assumption of weak coupling does not necessarily refer to the physical property of the junction, that means the transmitted power from a subsystem to the other should be much less than the dissipated power in the transmitting subsystem. Consequently, the damping loss factor should be higher compared to the coupling loss factor:

$$\eta_i \gg \eta_{ij}. \tag{30}$$

There are many different types of junctions, however in this study the analytical calculation of the three main types will be introduced, which are represented in Fig. 24.

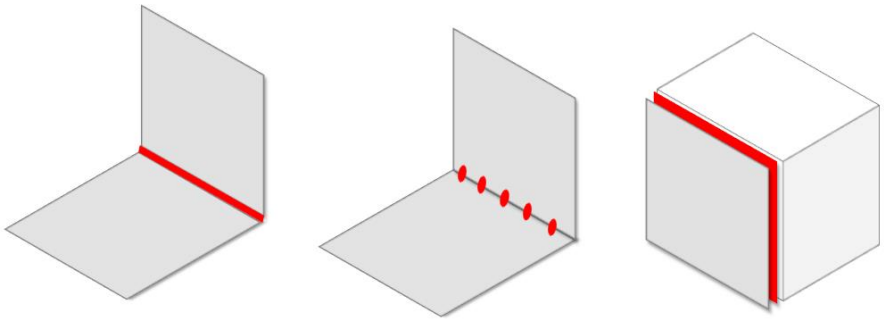

Figure 24: The junctions are signed with red color. Plate to plate connection: line and point junctions. Plate to cavity: area junction.

4.1.4.1. Line junction

Langley [82] assumed that the entering bending wave irradiates from an infinite edge under angle φ leading to a projected wavenumber k_x. This can be best illustrated visually as shown in Fig. 25. The incoming wave ($k_{B,in}$) is transmitted into plate 2 and reflected back to plate 1 by the joint. The waves in each plate can be decomposed into a bending (k_B), a longitudinal (k_L) and a shear wave(k_S). Thus, six transmission coefficients have to be considered in general. Because of the fact that the bending wave speeds are much higher than the in-plane wave speeds, therefore the in-plane (i.e. the longitudinal and shear) waves are neglected.

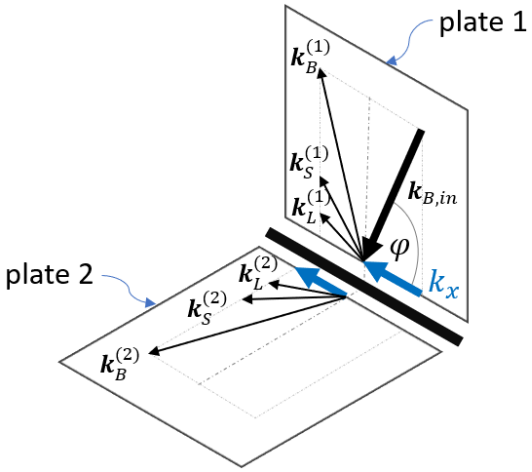

Figure 25: Transmitted and reflected waves at the junction.

In contrast to this, the calculation of the edge response requires the determination of the radiation stiffness of all wave-fields of both plates. The transmission coefficient follows finally from the power per length ratio of transmitted and incoming bending wave:

$$\tau(\varphi) = \frac{\Pi_{trans}}{\Pi_{in}}. \tag{31}$$

Note, that the angle of the transmitted wave is a function of the plate properties. The relationship between the CLF and the transmission coefficient follows from the assumptions for energy and radiated power from the reverberant bending wave field on the source plate. Langley derived this diffuse field transmission coefficient from plane-wave transmission theory as:

$$< \tau >= \frac{1}{2}\int_0^{\pi} \tau(\varphi) \sin\varphi \, d\varphi. \tag{32}$$

The transmission coefficient τ follows from the transmission and reflection of plane bending waves impinging with angle φ.

Several analytical equations exist for the case, that a plate structure is connected through a line junction, for which CLF can be calculated in the following way [83]:

$$\eta_{ij} = \frac{k_i L_c}{2\pi^2 n_i(\omega)\omega} < \tau_{ij} >= \frac{c_{gi} L_c}{\omega \pi A_i} < \tau_{ij} >, \tag{33}$$

where: k_i is the number of waves in subsystem i, A_i is the area of the source subsystem, $n_i(\omega)$ is the modal density, L_c is the length of the junction, $<\tau_{ij}>$ is the diffuse transmission coefficient and c_{gi} is the group speed, given by [83]:

$$c_{gi} = 2c_b = 2\sqrt{\omega \kappa c_l} = 2\sqrt{\frac{\omega h c_l}{2\sqrt{3}}}, \tag{34}$$

where, c_b is the wave phase velocity, κ is the bending radius of gyration, h is thickness of the plate, c_l is longitudinal wave velocity. The latter one can be expressed as [83]:

$$c_l = \sqrt{\frac{E_i}{\rho\,(1-\nu^2)}}, \tag{35}$$

where E_i is the energy of the subsystem i, and ν is the Poisson's ratio. In Eq (33), for plates form the same materials but of different thicknesses, τ_{ij} would be [84]:

$$\tau_{ij} = \frac{2}{\sigma^{-\frac{5}{4}} + \sigma^{\frac{5}{4}}}, \tag{36}$$

$$\sigma = \frac{h_j}{h_i}, \tag{37}$$

where, σ is the thickness ratio, h_j and h_i are the plate thicknesses of subsystem i and j, respectively. Rearranging Eq (33) and CLF of a line junction is the following:

$$\eta_{ij} = \frac{4}{\sqrt[4]{3}\pi}\sqrt{\frac{E_i}{\rho\,(1-\nu^2)}}\frac{L_c\sqrt{\omega h}}{\omega\,A_i\left(\sigma^{-\frac{5}{4}}+\sigma^{\frac{5}{4}}\right)}. \tag{38}$$

This is the analytical formula, on which basis the calculation of CLF in commercial SEA software is typically done.

4.1.4.2. Point junction

Langley presents in Ref. 82 the theory of wave transmission coefficients of point junctions. Similarly, to the line junction theory, the transmission depends on the radiation stiffness of point connections as well as the specific wave field. In the literature, there are limited information about point junction calculations. An analytical formula was introduced by Muller [85] for plates with the same materials. In the case when the $\lambda_b < l$ the coupling loss factor is the following:

$$\eta_{ij}^{*} = \frac{3.5Nh_ic_{li}}{\sqrt{3}\omega A_i}\frac{h_i^2h_j^2}{\left(h_i^2+h_j^2\right)^2}, \tag{39}$$

where λ_b bending wavelength of the plate, l is the point spacing, N is the number of points at the junction, A_i is the area of subsystem i; c_{li} is the longitudinal wave speed at subsystem i, hi and h_j is the thickness of the plates, respectively. When the $\lambda_b > 1.5l$ the coupling loss factor is calculated as [85]:

$$\eta_{ij}^{\circ} = 4\sqrt{\frac{2}{3}}\frac{l}{A_i}\sqrt{\frac{h_jc_{li}}{\omega}}\frac{h_i^{\frac{3}{2}}h_j^{\frac{3}{2}}}{\left(h_i^{\frac{3}{2}}+h_j^{\frac{3}{2}}\right)^2}. \tag{40}$$

In the occurrence of $l < \lambda_b < 1.5l$ an averaged value is estimated as the following [85]:

$$\eta_{ij}^{*\circ} = 0.5\left(\eta_{ij}^{*} + \eta_{ij}^{\circ}\right). \tag{41}$$

4.1.4.3. Area junctions

Area junctions are interpreted between the panel and cavity or between two cavities. The coupling loss factors between structural subsystems and acoustic cavity can be expressed as [86]:

$$\eta_{sc} = \frac{\rho_0 c \sigma}{\omega \rho_s}, \tag{42}$$

where ρ_0 is the fluid density, σ is the sound radiation coefficient, c is the sound speed, ρ_s is the area density of structure. The coupling loss factor from cavity to structural subsystem can be depicted as [86]:

$$\eta_{cs} = \frac{\sigma\ \rho_0 c\ n_s}{\omega\ \rho_s n_c}, \tag{43}$$

where n_s is the modal density of structural subsystem and n_c is the modal density of air cavity. In the case when two cavities are connected directly e. g. passenger cavity and trunk cavity, the CLF can be written as:

$$\eta_{ij} = \frac{c\ S}{8\pi\ f\ V_i}\tau, \tag{44}$$

where S is the area of the connection, f is the frequency, τ is the transmission coefficient, V_i the volume of the receiver cavity, namely the acoustic subsystem i.

4.2. Finite Element Method

Since this Thesis will deal with hybrid FE-SEA simulation as well. this section introduces the basic theory and equations of the dynamic finite element simulations according to the Nastran User's Guide [87]. Dynamic analysis in Finite Element Method is based on the equations of motion, that defines the equilibrium condition of a system at each time instant and takes into account the forces, which act on the structure as:

$$[\mathbf{M}]\ddot{x}(t) + [\mathbf{C}]\dot{x}(t) + [\mathbf{K}]x(t) = F(t), \tag{45}$$

where $x(t)$, $\dot{x}(t)$, $\ddot{x}(t)$ are the displacement, velocity and acceleration, respectively. **M** is the mass matrix, **K** is the matrix of springs and **C** matrix of dampers, $F(t)$ is the applied force vector. At the left-hand side of the equation the internal forces are found, namely inertia force, viscous damping, and elastic force. The inertia force is proportional to the mass and acceleration. Viscous damping represents an energy dissipation mechanism, which converts the kinetic energy into heat, hence reduces the vibration. It is a function of a dissipation constant and of

the velocity. The third component is the elastic resistance in the system, the so called spring force and it is a function of the displacement and stiffness of the system. At the right-hand side of the equation the applied load is defined. The load is independent from the structure or from where it is applied.

4.2.1. Modal parameter computation

As it can be seen from Eq. (45), the structure is represented by a theoretical collection of springs and masses. The first step in dynamic analysis is to obtain the natural frequencies and mode shapes of the structure without damping. This will characterize the dynamic behavior of the structure and indicate that how the structure will respond to dynamic loading, given by the reduced form of the equation of motion:

$$[\mathbf{M}]\{\ddot{u}\} + [\mathbf{K}]\{u\} = 0. \tag{46}$$

Eq. (46) above assumes a harmonic solution of the form:

$$\{u\} = \{\phi\} \sin \omega t, \tag{47}$$

where $\{\phi\}$ is the mode shape. The form of the numerical solution was chosen to be of harmonic form, since this is related to the physics of vibrations too. Harmonic motion of a structure means that all degrees-of-freedom of the structure move synchronously and that the basic shape of the motion is the same, and only the amplitudes vary. After the differentiation, the assumed harmonic solution is executed and substituted into the equation of motion, leading to the so-called eigenequation:

$$-\omega^2[\mathbf{M}]\{\phi\} \sin \omega t + [\mathbf{K}]\{\phi\} \sin \omega t = 0, \tag{48}$$

$$([\mathbf{K}] - \omega^2[\mathbf{M}])\{\phi\} = 0. \tag{49}$$

This is a set of homogeneous algebraic equations for eigenvectors and the eigenvalues, resembling in an eigenvalue problem in linear matrix algebra. There are two possible solution forms for Eq. (49), first is the trivial solution, which does not give an information about the mode shapes since it represents the case of no motion, and is given by:

$$\det([\mathbf{K}] - \omega^2[\mathbf{M}]) \neq 0, \tag{50}$$

$$\{\phi\} = 0. \tag{51}$$

The non-trivial solution, where $\{\phi\} \neq 0$ is expressed as:

$$\det([\mathbf{K}] - \omega^2[\mathbf{M}]) = 0. \tag{52}$$

The condition, that the determinant is zero is only met when a set of discrete eigenvalues ω_i^2 and $\{\phi_i\}$ corresponding to each eigenvalue fulfils the following criterion:

$$\left[\mathbf{K} - \omega_i^2 \mathbf{M}\right]\{\phi\} = 0. \tag{53}$$

The solution of the equitation defines the free vibration mode of the system, so the i^{th} eigenvalue is related to the i^{th} natural frequency where the structure shape is defined by the i^{th} eigenvectors. The number of possible eigenvalues and eigenvectors is determined by the number of degrees of freedom of the structure.

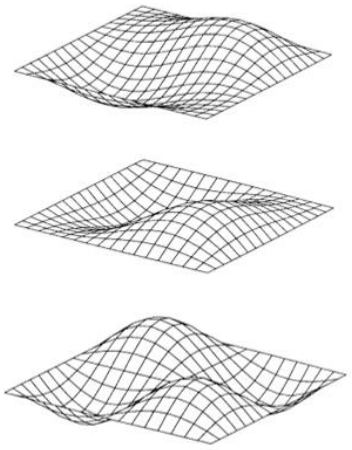

Figure 26: Mode shapes of a flat plate [87].

4.2.2. Frequency response analysis

After the calculation of the natural frequencies the next step is to solve the response of the structure when dynamic load excites it. Various excitations may act on the structure, for example a rotational excitation would correspond to unbalanced tires or turbine blades, etc.

In frequency response analysis, the results can be the displacements, velocities, accelerations of nodes, as well as forces and stresses of the elements. The calculated responses have magnitude and phase regarding the applied force so they are complex numbers with real and imaginary components, as can be seen in Fig. 27.

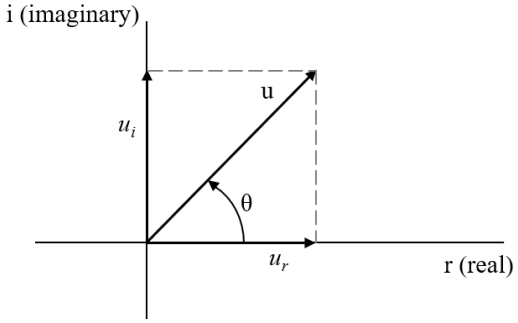

Figure 27: Real part and imaginary part of a complex number.

In frequency response analysis, the real and imaginary components can be expressed as $u_r = u$ cosθ and the imaginary component $u_i = u$ sinθ, respectively. The magnitude u and phase θ can be expressed as:

$$u = \sqrt{u_r^2 + u_i^2}, \tag{54}$$

$$\theta = \tan^{-1}\left(\frac{u_i}{u_r}\right). \tag{55}$$

In frequency response analysis two numerical methods can be used a) direct method where the coupled equations of motion are solved in terms of forcing frequency; and b) modal method where the mode shapes of the structure are used to reduce and uncouple the equations of motion. In this case, the solution for a particular forcing frequency is expressed by the summation of the individual modal responses.

In order to introduce the direct method, recall that the matrix form of the equations of motion can be written as:

$$[\mathbf{M}]\{\ddot{x}(t)\} + [\mathbf{B}]\{\dot{x}(t)\} + [\mathbf{K}]\{x(t)\} = \{P(\omega)\}e^{i\omega t}, \tag{56}$$

where the excitation is a complex vector, which is advantageous form mathematical solution point of view. The harmonic solution is then given by:

$$\{x\} = \{u(\omega)\}e^{i\omega t}, \tag{57}$$

where {u(ω)} is a complex displacement vector. Taking the first derivative of allows to obtain a complex velocity vector, while the second derivate a complex acceleration vector, as:

$$\{\dot{x}\} = i\omega\{u(\omega)\}e^{i\omega t}, \tag{58}$$

$$\{\ddot{x}\} = -\omega^2\{u(\omega)\}e^{i\omega t}. \tag{59}$$

Rearranging Eq. (56) and using the above expressions leads to:

$$-\omega^2[\mathbf{M}]\{u(\omega)\}e^{i\omega t} + i\omega[\mathbf{B}]\{u(\omega)\}e^{i\omega t} + [\mathbf{K}]\{u(\omega)\}e^{i\omega t} = \{P(\omega)\}e^{i\omega t}. \tag{60}$$

One can simplify this by dividing it by $e^{i\omega t}$:

$$[-\omega^2\mathbf{M} + i\omega\mathbf{B} + \mathbf{K}]\{u(\omega)\} = \{P(\omega)\}. \tag{61}$$

In order to solve the equation, the forcing frequency is inserted into the equation of motion and then at each input frequency the system of equations is solved, similarly to a statics problem.

In modal frequency response analysis uses, one the mode shapes of the structure to reduce the size of the problem and to make the numerical solution more efficient. At first, the physical coordinates $\{u(\omega)\}$ are transformed to modal coordinates $\{\xi(\omega)\}$ as:

$$\{x\} = [\boldsymbol{\phi}]\{\xi(\omega)\}e^{i\omega t}. \tag{62}$$

Eq. (62) represents an equality if all modes are used, which is mostly not the case so the equation usually represents an approximation. Let us temporarily ignore all damping, resulting in the undamped equation for harmonic motion:

$$-\omega^2[\mathbf{M}]\{x\} + [\mathbf{K}]\{x\} = \{P(\omega)\}, \tag{63}$$

where ω is the forcing frequency. Rearranging Eq. (63) with modal coordinates and dividing by $e^{i\omega t}$, one can obtain the coupled equation of motion as:

$$-\omega^2[\mathbf{M}][\boldsymbol{\phi}]\{\xi(\omega)\} + [\mathbf{K}][\boldsymbol{\phi}]\{\xi(\omega)\} = \{P(\omega)\}. \tag{64}$$

Multiplying Eq. (64) by $[\boldsymbol{\phi}]^T$, the uncoupled equation can be obtained as:

$$-\omega^2[\boldsymbol{\phi}]^{\mathrm{T}}[\mathbf{M}][\boldsymbol{\phi}]\{\xi(\omega)\}+[\boldsymbol{\phi}]^{\mathrm{T}}[\mathbf{K}][\boldsymbol{\phi}]\{\xi(\omega)\} = [\boldsymbol{\phi}]^{\mathrm{T}}\{P(\omega)\}, \tag{65}$$

where $[\boldsymbol{\phi}]^{\mathrm{T}}[\mathbf{M}][\boldsymbol{\phi}]$ is the modal generalized mass matrix, $[\boldsymbol{\phi}]^{\mathrm{T}}[\mathbf{K}][\boldsymbol{\phi}]$ is modal generalized stiffness matrix, $[\boldsymbol{\phi}]^{\mathrm{T}}\{P\}$ is the modal force vector. The generalized mass and stiffness matrices are diagonal matrices, so they do not have off-diagonal terms that couple the equations of motion. The uncoupled modal equations of motion are expressed as a set of uncoupled single degree-of-freedom systems as:

$$-\omega^2 m_i\xi_i(\omega) + k_i\xi(\omega) = p_i(\omega), \tag{66}$$

where m_i is the i^{th} modal mass, k_i is the i^{th} modal stiffness, p_i is the i^{th} modal force. The modal form is much faster to compute compared to a direct method, since it is a series of uncoupled single DOF systems. Once the individual modal responses are calculated, the physical responses are recovered as the summation of the modal responses using Eq. (62). The responses are in complex form such as magnitude/phase or real/imaginary.

When damping [**B**] is taken into account the orthogonality property of the modes does not diagonalize the generalized damping matrix:

$$[\boldsymbol{\phi}]^{\mathrm{T}}[\mathbf{B}][\boldsymbol{\phi}] \neq diagonal. \tag{67}$$

When structural damping is applied the orthogonality property does not diagonalize the generalized stiffness matrix:

$$[\boldsymbol{\phi}]^{\mathrm{T}}[\mathbf{K}][\boldsymbol{\phi}] \neq diagonal, \tag{68}$$

where $K = (1+iG)[K]+i\sum G_E[K_E]$. Consequently, if matrix [**B**] or a complex stiffness matrix occur, the model frequency approach solves the coupled problem in terms of modal coordinates using the direct frequency approach, given by:

$$[-\omega^2[\boldsymbol{\phi}]^{\mathrm{T}}[\mathbf{M}][\boldsymbol{\phi}]+i\omega[\boldsymbol{\phi}]^{\mathrm{T}}[\mathbf{B}][\boldsymbol{\phi}]+[\boldsymbol{\phi}]^{\mathrm{T}}[\mathbf{K}][\boldsymbol{\phi}]\{\xi(\omega)\} = [\boldsymbol{\phi}]^{\mathrm{T}}\{P(\omega)\}. \tag{69}$$

The difference between Eq. (61) and Eq. (69) is that the latter one is expressed in terms of modal coordinates. The number of modes is much less than the number of physical variables, therefore using the coupled solution of the modal equations is more effective. If damping is applied to each mode individually the uncoupled equations of motion can be used. When modal damping is applied, each mode has a damping of $b_i = 2\ m_i\ \omega_i\ \xi_i$, and the equations of motion can be used in the uncoupled form for each mode, as the following:

$$-\omega^2 m_i\xi_i(\omega) + i\omega b_i\xi_i(\omega)+k_i\xi_i(\omega) = p_i(\omega). \tag{70}$$

The modal responses can be computed as:

$$\xi_i(\omega) = \frac{p_i(\omega)}{-m_i\omega^2 + ib_i\omega + k_i}. \tag{71}$$

In this study the responses of the structures were computed by the modal frequency response analysis.

4.3. Hybrid FE-SEA method

This section is based on Ref 2, which describes the hybrid method in detail and illustrates it on different case studies. The concept of the hybrid FE-SEA method is to combine the strengths of the FE and SEA methods. Thus, some part of a subsystem is modelled in FE while the rest in SEA. The part modelled in FE has well defined physical properties, which values are equal over a part. On the other hand, the SEA subsystem has random physical parameters, such as density or geometry, etc. For this reason, the hybrid model contains enough random, or so-called statistical parameters, which make the system response more realistic. The general guideline for dividing the system is the following: stiffer parts are modelled in FE, since they have small modal density at higher frequencies (for example, the A-pillar of a vehicle). Larger panels, or plates with high modal density are, on the other hand, considered as SEA subsystems (for example, the roof or windows). The coupling of the two methods is achieved via the diffuse field reciprocity relation as can be seen at Fig. 28. The hybrid method's main advantage is on

one hand the model size, which is logically smaller compared to a pure FEM model and on other hand the ability to deal with higher frequency band for large panels. Thus, the method promises to be suitable for the mid-frequency range. In addition, the hybrid model is much faster for a fully trimmed vehicle then the pure FEM, and it gives an opportunity to monitor the noise transmission paths in the model [34]. Different hybrid solutions are being considered, since both acoustic and structural components can be included in the model [36].

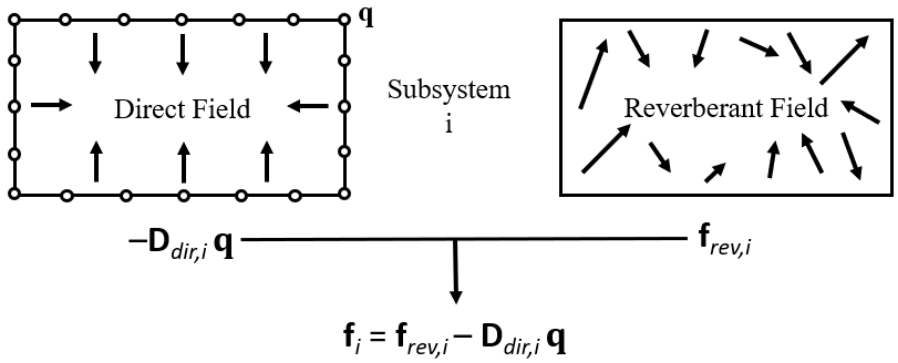

Figure 28: Direct and reverberant fields of subsystem i.

As the first step in FE-SEA method, the equation of motion is calculated for the FE subsystem, that can be obtained with the following equation:

$$\mathbf{f} = \mathbf{D}\mathbf{q}, \tag{72}$$

where **f** is the external forces at the boundary of subsystems, **D** is the frequency-dependent dynamic stiffness matrix, *q* is the degree of freedom of the subsystem, e.g. that represents the modes of the FE part without the SEA subsystems and it uses that as the basis function. Then the SEA subsystems are added to the system and the boundary forces can be split into direct field and reverberant field, because the vibration from the boundaries goes through the SEA subsystems and reflected repeatedly at the boundaries. Thus, so the boundary forces can be written as:

$$\mathbf{f} = \mathbf{f}_{rev} - \mathbf{D}_{dir}\mathbf{q}, \tag{73}$$

where $\mathbf{f}_{rev}$ is the reverberant force vector, $\mathbf{D}_{dir}\,\mathbf{q}$ is the direct field forces. The connection between FE and SEA subsystems are expressed by the cross spectrum of the reverberant forces:

$$\mathbf{S}_{ff,rev,i} \equiv \mathrm{E}\left[\mathbf{f}_{rev,i}\,\mathbf{f}_{rev,i}^{T}\right] = \left(\frac{4\,E_i}{\omega\pi n_i}\right)\mathrm{Im}\{\mathbf{D}_{dir,i}\}, \tag{74}$$

where $\mathrm{E}[\mathbf{f}_{rev,i}\,\mathbf{f}_{rev,i}^{T}]$ is the average energy of the ensemble of SEA subsystems, n_i is the modal density of the subsystem *i*, E_i is the energy of subsystem *i*. The energy balance equation of the random subsystems can be expressed as:

$$\omega(\eta_i + \eta_{d,i})E_i + \sum_j \omega\eta_{ij}n_i\left(\frac{E_i}{n_i} - \frac{E_j}{n_j}\right) = P_{in,i}^{ext} + P_{in,i}. \tag{75}$$

These equations are based on the original SEA equations supplemented with two additional parameters. The additional terms are referred to the presence of the FE subsystems. The first one, $P_{in,i}^{ext}$ is a power that comes from the applied forces on the FE subsystem, and it can be expressed by analytical formulas as a function of the cross-spectral matrix of the loading on the FE system:

$$P_{in,j}^{ext} = \left(\frac{\omega}{2}\right)\sum_{r\,s} \mathrm{Im}\{D_{dir,rs,j}\}\left(\mathbf{D}_{tot}^{-1}\mathbf{S}_{ff}\mathbf{D}_{tot}^{-1*T}\right)_{rs}. \tag{76}$$

The second one is an extra loss factor that is associated with the dissipated power in the FE subsystems, namely $\eta_{d,i}$ and analytically can be obtained as the following:

$$\omega\eta_{d,j} = \left(\frac{2a_k}{\pi n_j}\right)\sum_{r\,s} \mathrm{Im}\{D_{d,rs}\}\left(\mathbf{D}_{tot}^{-1}\mathrm{Im}\{\mathbf{D}_{dir,j}\}\mathbf{D}_{tot}^{-1*T}\right)_{rs}. \tag{77}$$

In hybrid FE-SEA simulations, the damping loss factors, and the modal densities are obtained in the same way as in SEA, however the coupling loss factors are calculated by the dynamic stiffness matrices, as:

$$\omega\eta_{jk}n_j = \left(\frac{2a_k}{\pi}\right)\sum_{r\,s} \mathrm{Im}\{D_{dir,rs,j}\}\left(\mathbf{D}_{tot}^{-1}\mathrm{Im}\{\mathbf{D}_{dir,\mathrm{i}}\}\mathbf{D}_{tot}^{-1*T}\right)_{rs}, \tag{78}$$

where α_k is a correction factor in the case when the wave field is not diffuse. The total response of the hybrid system is derived from the equation of motion:

$$\mathbf{D}_{tot}\mathbf{q} = \mathbf{f} + \sum_k \mathbf{f}_{rev,i}, \tag{79}$$

$$\mathbf{D}_{tot} = \mathbf{D}_d + \sum_k \mathbf{D}_{dir,i}, \tag{80}$$

where $\mathbf{f}$ is the forces that is applied on the FE system, $\mathbf{D}_d$ is the dynamic stiffness matrix associated with the deterministic part supplemented with the number of SEA subsystems in the model. The response of the deterministic system can be calculated once Eq. (75) has been solved for the SEA subsystem energies. Then the cross-spectrum of the deterministic response is expressed as:

$$\mathbf{S}_{qq} = \mathbf{D}_{tot}^{-1}\left[S_{ff}\sum_{i}\left(\frac{4E_i}{\omega\pi n_i}\right)\mathrm{Im}\{\mathbf{D}_{dir,i}\}\right]\mathbf{D}_{tot}^{-1*T}. \quad (81)$$

This bring us to the end of the description of the numerical methods, which will be used for addressing the research gaps in this Thesis. In Chapter 6, the test cases will be described, along with the validation strategy.

5. VALIDATION PROCESS AND DATA ACQUISITION

Recall, that this Thesis deals with simulation methodology development via Statistical Energy Analysis (SEA) as well as via Hybrid FE-SEA. The key parameters of the SEA method, namely the Damping Loss Factor (DLF) of each subsystem as well as the Coupling Loss Factor (CLF) between the subsystems, will be obtained either from measurements or from analytical formulas. In addition, an essential part of simulation methodology development is validation, i.e. the comparison of simulation results with experiments, in order to assess the accuracy of the simulation methods. For this reason, specific measurements needed to be conducted as part of the research and the purpose of this Chapter is to describe the applied vibroacoustic measurement methods.

5.1. Basic philosophy of vibroacoustic measurements

Structural vibration testing and analyses in general are conducted with the purpose of identifying unwanted vibrations as well as to determine the efficiency of vibration reduction techniques experimentally. Beside this, it is often used to validate a simulation or to obtain various input parameters for simulations. Vibration measurements are often called modal analysis, since the modal behavior of the structure can be determined from it. Modal analysis can be used to assess the resonant frequencies and the corresponding mode shapes, as well as the damping of the examined object. The principle of vibroacoustic tests is quite simple: the structure is excited with a known (i.e. measured) excitation force, while the response of the structure is also measured at specific response points in terms of displacement, velocity or acceleration. From these measured parameters can one determine the so-called Frequency Response Function (FRF).

In practice, many types of input excitations and response outputs can be used to calculate an experimental FRF, such as [88]:

- Mechanical systems: input signals in terms of force while output signals in terms of acceleration (typically expressed in g's); velocity (m/s) or displacement.
- Acoustical systems: input signals in terms of Volume Acceleration (typically denoted as Q in vibroacoustics) and outputs in Sound Pressure Levels (SPL)

Fig. 29 shows the schematic diagram of a vibrational measurement. In principle, the input force spectrum (X) should be ideally constant with frequency in order to excite all frequencies

equally. The peaks in the response (Y) represent the resonant frequencies of the structure, since the FRF is normalized by the input signal. There will be a phase delay between the input and output, and with the help of the phase the mode shapes can also be plotted by using the imaginary part of the FRFs. In modal analysis, two common types of signals are used: FRF and coherence. These will be explained later.

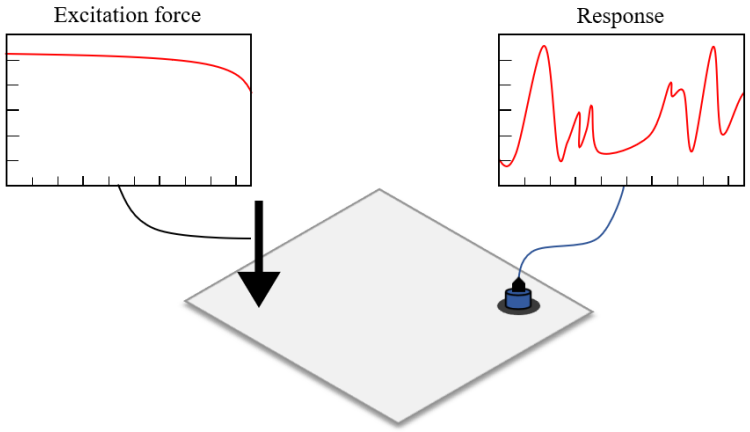

Figure 29: Schematic illustration of the vibrational measurement.

In mechanical systems the most commonly used excitation methods are the impact hammer and the electromagnetic shaker. The key aspects of these are:

- Impact hammer is often used for simple structures, because of the easy to apply behavior, as well as it does not change the stiffness and damping properties of the structure. A force sensor is placed in the hammer, so during the test, the force is directly measured. Different types of impact tips exist, and each one is suitable for a certain frequency range. With the change of the tips, the excitation frequency range can be changed. Typically, a soft rubber tip is suitable for low frequency measurements, while a hard metal tip for high frequency ranges.
- Electromagnetic shakers are used in complex structures and for complex investigations, since they allow various options for injecting the excitation signal into the structure. The user can change the driving force or acceleration in order to get a good level of response during the test. The shaker is usually driven by dynamic signal analyzer (DAC), which converts the digital signal into analog one, as it will be seen later in this chapter. The type of the excitation profile can also be selected, typical profiles include the sine wave, sine sweep, random (white noise), pseudo random, burst random, chirp, etc. Between the shaker and the structure, a thin metal rod called stinger is placed. At the end of the stinger an impedance head is placed. This is connected directly to the structure and it measures the input force as well as the acceleration at the driving point.

Additional component of the measurements:

- Accelerometer: an electronic sensor that converts electronic signal into acceleration. Two types are available a) uniaxial accelerometers, which can measure in only one axis; b) tri-axial accelerometers, which can measure in all three axes simultaneously.
- Dynamic Signal Analyzer (DSA): measures electronic signals with an analog front end, It may contain signal conditioning, such as sensor power supply and transducer electronic data sheets (TEDS), that read the calibration and other information from a chip embedded in the sensor. Basically, the input force sensor and all the acceleration sensors are connected into DSA. The device can record different kind of data including time, frequency, amplitude and statistical data. The DSA calculates among other signals the cross-power spectrum, auto and cross correlation, impulse response, histograms, octave analysis, etc.
- Analog Digital Converter (ADC): converts the analog signal to a digital format. When the signal is digitized, the system processes it with a digital signal processor (DSP). The ADC produces the electronic signals that are then amplified and converted into the excitation signals.
- Digital Signal Processor (DSP): a minicomputer, which is responsible for rapid mathematical calculations such as additional filtering, computation of time and frequency measurements, etc. The DSP is connected via interfaces to a PC.
- Computer (PC): is used for the setup, display and management of all the parameters of the measurements and measurement results.

5.2. Frequency Response Function

FRF is basically a transfer function, and it is calculated from two signals, such as the response (output) and excitation (input). The schematic diagram of transfer function is shown in Fig. 30 where the input is X, output is Y and H is the transfer function or frequency response function.

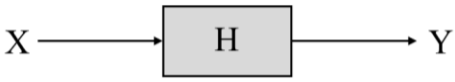

Figure 30: H represents the FRF between input X and output Y.

The FRF is then calculated as [88]:

$$H = \frac{S_{XY}}{S_{XX}}, \tag{82}$$

Where, *Sxx* is the autopower: the complex conjugate (*a-ib*) of the input spectrum, multiplied by itself (*a+ib*), Thus, it is a real function, without phase information. *Sxy* is the cross-power, the

complex conjugate of the output spectrum, multiplied by the input spectrum. It contains both amplitude as well as phase information.

The FRF can be calculated also via the Fourier Transformation of Eq. (45):

$$\{X(j\omega)\} = [\mathbf{H}(j\omega)]\{F(j\omega)\}, \tag{83}$$

where $X(j\omega)$ is the displacement vector in the frequency domain, $F(j\omega)$ is equivalent with $F(t)$ applied force vector in the frequency domain. $\mathbf{H}$ $(j\omega)$ is the FRF matrix with n × n dimension. In a damped system the FRF is given by [89]:

$$[\mathbf{H}(j\omega)] = \sum_{r=1}^{N} \frac{j2\omega_r Q_r \{\vartheta\}_r \{\vartheta\}_r^t}{(\theta_r^2 + \omega_r^2 - \omega^2) - 2\theta_r j\omega}, \tag{84}$$

where ω_r is the natural frequency of mode r, θ_r is the damping factor and controls the amplitude of the response when the system is close to a resonance frequency $\omega \approx \omega_r$, ϑ_r is the mode shape of mode r, Q_r is a constant factor and N is the number of modes.

The frequency response function is a complex function, since it contains amplitude as well as phase data. The latter shows the phase shift of the response relative to the input. The real part of the FRF will equal zero at resonant frequencies while the imaginary part can have positive or negative amplitudes, which indicates the resonant frequencies. The direction of the peaks can be used to determine the mode shape associated with the resonant frequency. FRFs can contain thousands of data and for this reason, the graphical format is the most obvious one. Visual inspection is usually sufficient to determine the similarities or dissimilarities between two FRFs. A complex function such as FRF, can be plotted on a Bode or on a Nyquist diagram.

- Bode diagrams (see Fig. 31) can show both the magnitude/phase as well as te real/imaginary variation with frequency.
- Nyquist diagrams (see Fig. 32) show the FRF in real/imaginary plane. This kind of plot gives important information such as the Nyquist stability criterion or detailed information around a resonance, such as the frequency resolution. In this study the investigation of the Nyquist plot from the proper frequency resolution point of view was used.

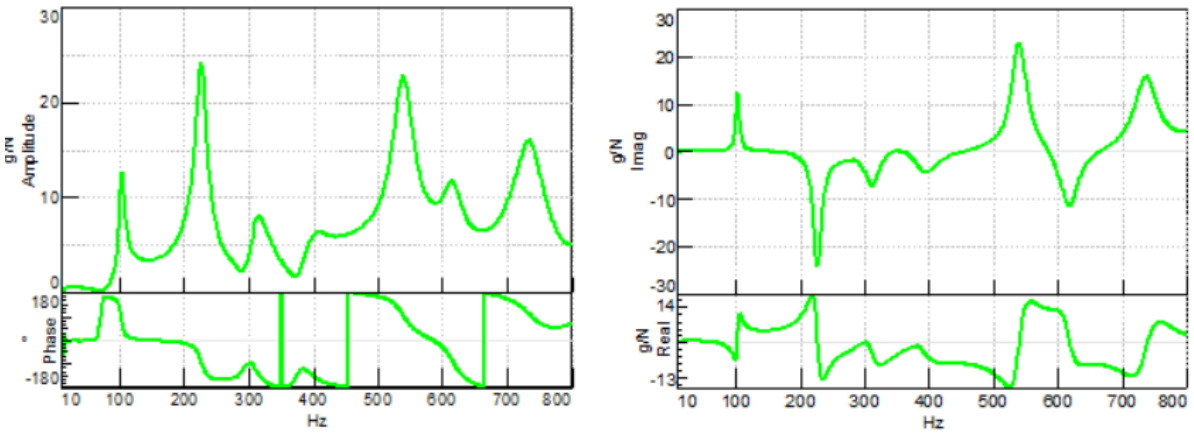

Figure 31: Left: Bode-diagram with the amplitude and phase data of the FRFs. Right: Nyquist-diagram with the real and imaginary data of the FRFs [88].

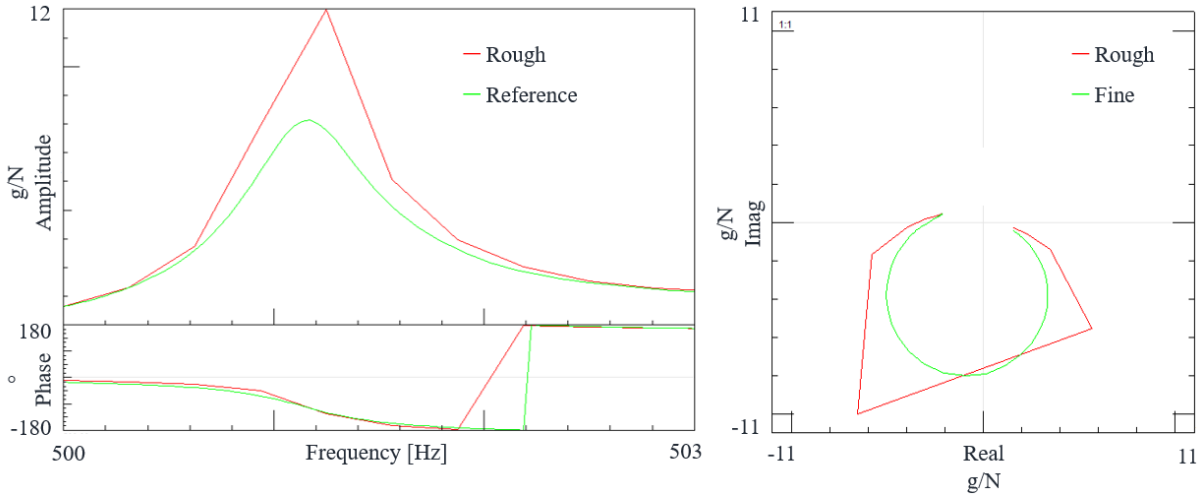

Figure 32: Bode (left) and Nyquist(right) diagram of the same FRF curves in the same frequency range.

In an experiment, one can get important information about the structure by simple comparisons, such as:

a) linearity check: FRFs are measured while the excitation is changed;

b) reciprocity check: FRFs are measured then, switching the input and output points;

c) effect of a change in the system: FRFs are calculated before and after a modification in the system;

d) FRFs measured for different geometries and levels of damping;

e) measurements of the FRFs before and after a data reduction that is purposed to eliminate the noise and the linearly-related redundant information.

5.3. Additional measurement adjustments

5.3.1. Averaging

FRF data is computed from one block of time data. Every data contains some random noise that can influence the resonant frequencies and mode shapes. By averaging, the uncorrelated random noise will be reduced, however, the instrument noise is not eliminated by it. Averaging improves the quality of the measurement and makes the signal smoother. In the case of impact hammer measurements, typically 4-8 averages are required, while in shaker test cases, about 32-64 averages are employed.

5.3.2. Frequency resolution

As it was introduced earlier, FRFs are built up from a number of data points. With increasing the data point number, the FRF curve will become more accurate, however, on the other side, the measurement process will be more time-consuming as well as the size of the data to be handled will increase as well. Basically, the frequency resolution is defined by the number of points in the chosen time frame: more points in the time block will result in finer resolution in the frequency domain spectrum. The frequency resolution is important, since it influences the frequency, the amplitude and the damping of the FRF peaks.

5.3.3. Overload

Overload happens, when a strong impact signal generates higher voltages than what was setup, so the input channel will overload. In general, the signal analyzer detects the overload and gives an alarm, because the measured data, which comes from an overloaded signal, will be classified as invalid, so it will be rejected. In order to avoid the overload, the input force should be reduced, or a lower sensitivity accelerometer and force sensor should be used.

5.3.4. Windowing

Any signal can be captured in a periodic or non-periodic manner, depending on the chosen measurement time. As an example, despite the measured signal being a sine wave, the captured signal can be only a smaller portion of it, if the frame size defined for the acquisition is too small. On the other hand, if the captured signal is repeated end-to-end, then the captured signal is periodic. If the repeated signal is not the same, then due to the acquisition time the captured signal is non-periodic. In the second case, spectral leakage from zero Hz to the full bandwidth can occur within the FFT. This phenomenon can be seen in Fig. 33.

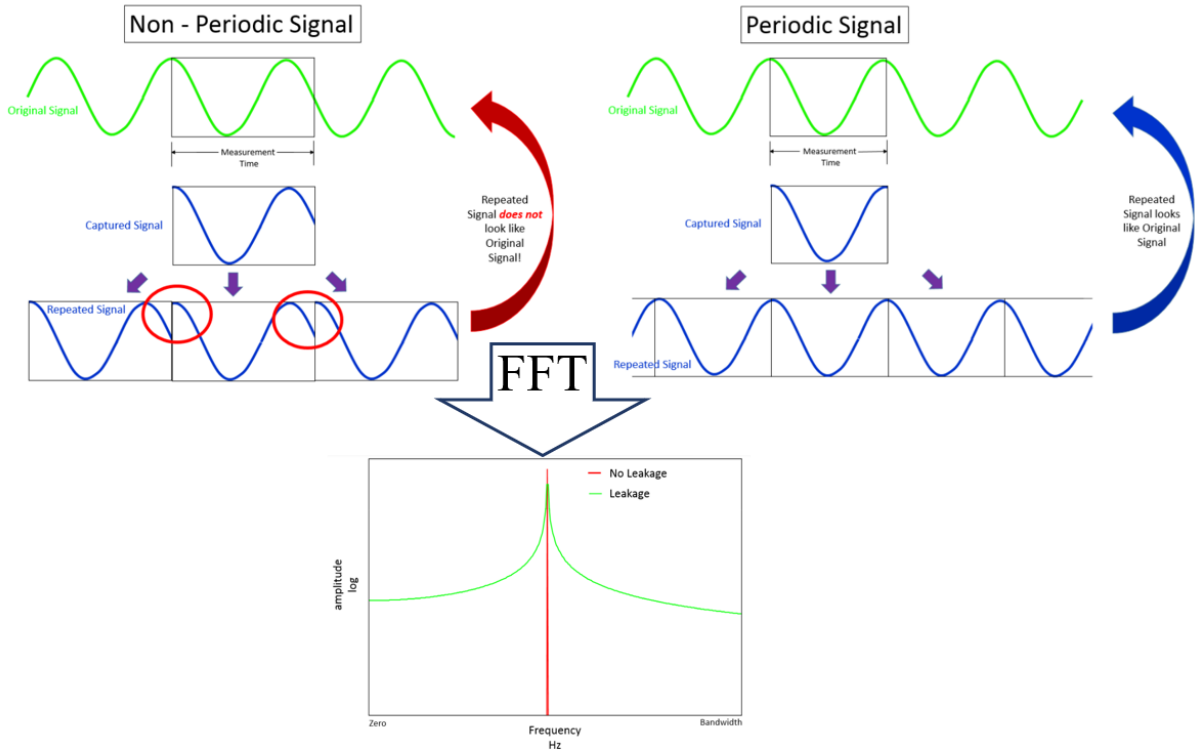

Figure 33: Leakage during the measurement [90].

Note that in the non-periodic capturing, the signal energy is smearing out over a wide frequency range because of the leakage. To reduce the leakage, various windowing techniques exist. Typically, the windows are shaped as functions that start at zero, move to a value of one, and then return to a value of zero within one frame. As a consequence, the sharp transients are reduced and smoothed, the broadband frequency of the spectral leakage is also reduced. The main advantage of windowing is that the leakage is limited in a narrower frequency range rather than the whole frequency bandwidth of the measurement. Fig. 34 shows the concepts of the windowing and its effect. There exist several kinds of windowing techniques, such as hamming, hanning, exponential, flattop, tukey, etc.

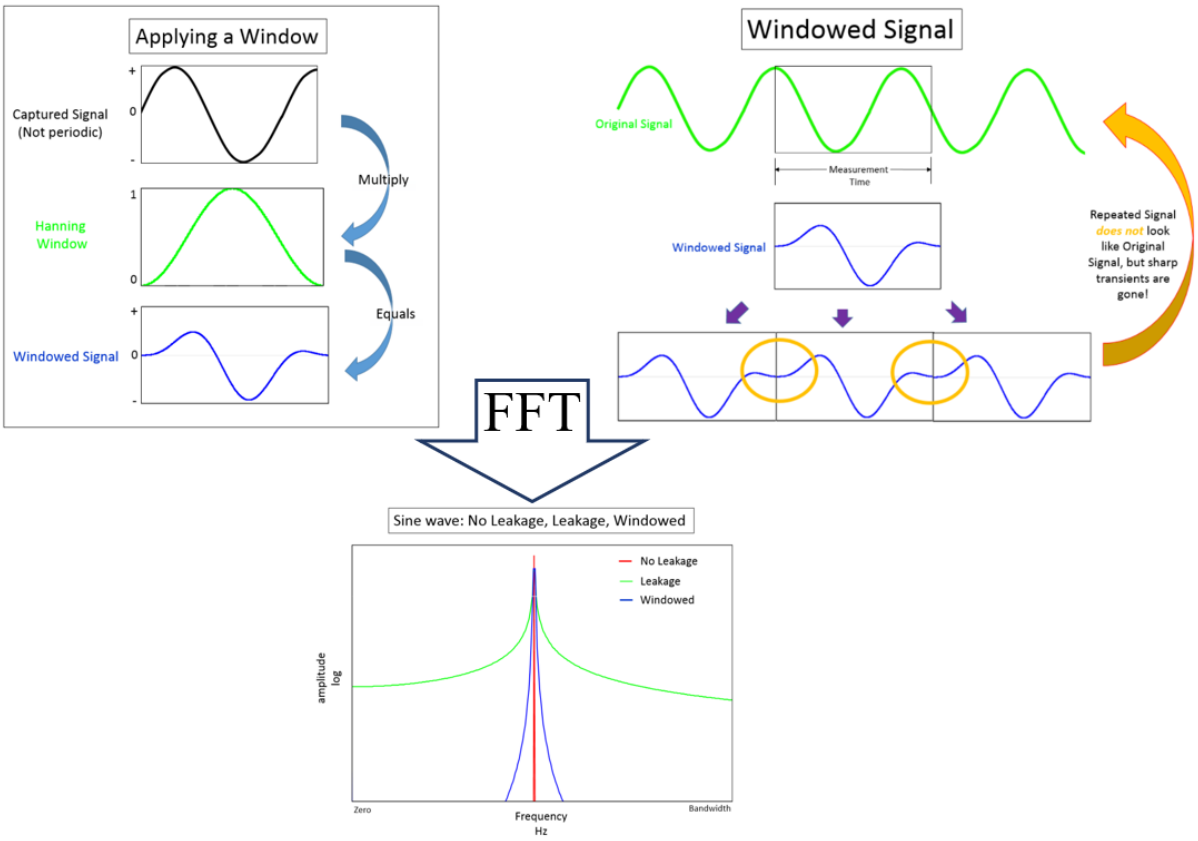

Figure 34: Theory of the windowing technique [90].

Windowing in general is needed, when a shaker is used to excite the system with broadband random noise. In the case of an impact hammer, the time block length can be adjusted, so that after the excitation, the measured response totally dissipates. This means, that, in the pre-trigger phase the signal shall be zero and after the impact it shall end once again at zero, so that no windowing is required. It will be shown later that this method will result in the most accurate amplitude and damping measurements.

5.3.5. Double hit

Double hit occurs only in impact testing when the hammer knocks the structure and the structure bounces back to the hammer tip. In this case, the second impact is usually smaller, and since it happens right after the first hit, it is hard to identify it on the diagram. This may cause invalid data and therefore it is advisable to discard such measurement and to repeat the impact. Double hit can be seen by analyzing a time trace of the impact force or the signal analyzer can detect it and inform the user.

5.3.6. Triggering

Triggering is a function in the measurement system, which helps during an impact test to automatically start the data acquisition and processing only after a knock. It is possible to set a

trigger level for launching the data acquisition. A pre-trigger can also be adjusted so that some data points are caught right away before the trigger is activated in order to get the entire impact waveform in one time frame.

5.3.7. Estimators

Estimators are used for calculating the correct amplitude ratio of the input to output of FRFs. Three main FRF estimators are commonly used: H1, H2 and HV.

The most used estimator is the H1-estimator. It assumes that there is no noise on the input and consequently all inputs (X) are accurate. On the other hand, all noise (N) is presumed to be on the output side only (Y), as Fig. 35 shows it.

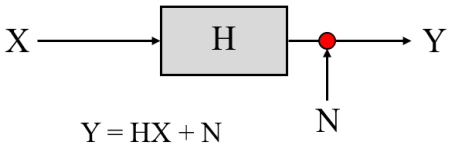

Figure 35: H1 Estimator for FRF measurement [88].

Due to its nature, H1 is sensitive to the noise on the input, and in this case, it tends to underestimate the FRF. This estimator produces the best results when the inputs are uncorrelated. H1 estimates the anti-resonances better than the resonances, as Fig. 36 illustrates it.

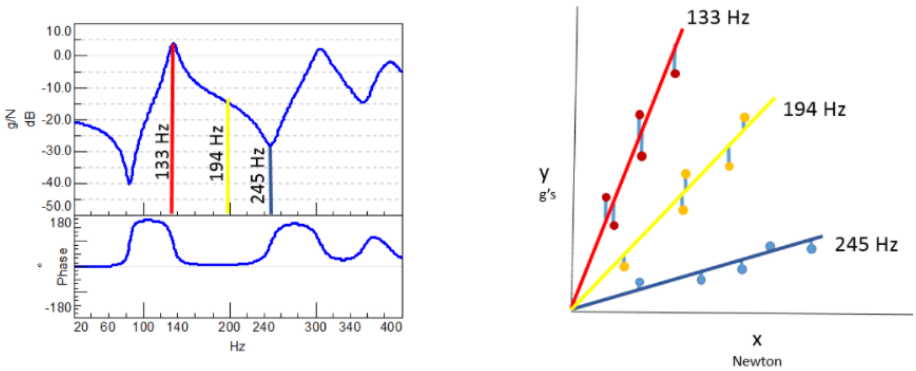

Figure 36: Left: FRF curve. Right: Y only correction of 5 separate measurements [88].

The H2 estimator assumes that there is no noise on the output and that all the noise (M) is assumed to be only on input (see Fig. 37).

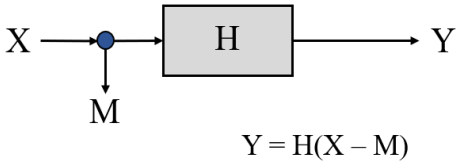

Figure 37: H2 Estimator for FRF measurement [88].

This can overestimate the FRF when the noise is on the output. It estimates the resonances better than the anti-resonances as can be seen in Fig. 38.

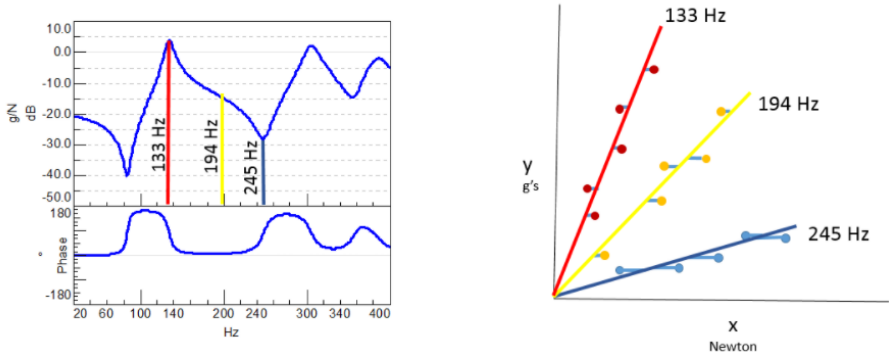

Figure 38: Left: FRF curve. Right: X only correction of 5 separate measurements [88].

Lastly, an HV estimator gives the best estimate of the FRFs since it assumes that noise is on both the input and output sides (see Fig. 39). It combines the advantages of the previous two estimators i.e. that H2 estimates better the resonances while H1 estimates better the anti-resonances (see Fig. 40).

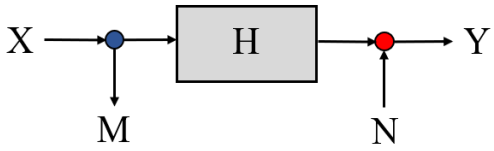

$$Y - N = H\,(X - M)$$

Figure 39: Hv Estimator for FRF measurement [88].

The drawback of the HV estimator is that it requires more computational time than the other two.

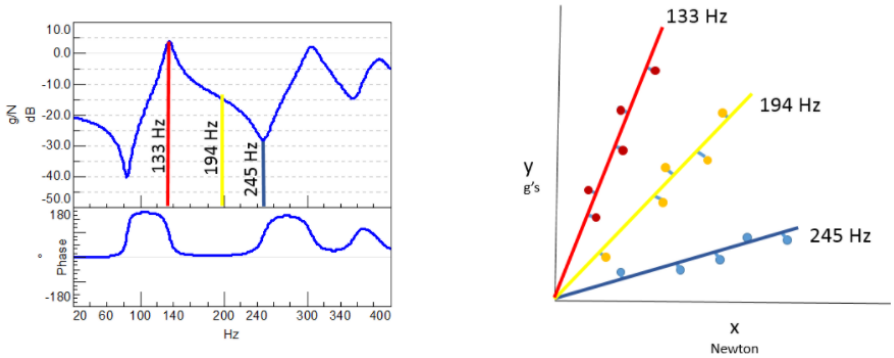

Figure 40: Left: FRF curve. Right: X and Y correction of 5 separate measurements [88].

5.4. Coherence

In vibrational measurements, one of the main indicators is the coherence function. Coherence tells that what portion of the output signal comes from the input signal, i.e. to what level is the vibrational response correlated to the excitation force. The definition of the coherence is [91]:

$$\gamma_{xy}^2(f) = \frac{\left|S_{xy}(f)\right|^2}{S_{xx}(f) \times S_{yy}(f)}, \tag{85}$$

where *x* is the signal at the input, *y* is the signal at the output, $S_{xx}(f)$ is the auto-spectrum of *x*, $S_{yy}(f)$ is the auto-spectrum of *y*, and the $S_{xy}(f)$ is the cross-spectrum of the *x* and *y* signals. Therefore, the perfect relationship between input and output would give the coherence value of 1. The coherence must be reasonable in order to get clear FRF curves, so if the signal is too noisy then the FRF would be inaccurate to identify the proper DLF values. Coherence should be monitored during the measurements to make sure that the data is valid, i.e. it is in essence the first step to investigate the signal quality. Coherence is a function of frequency, and it is interpreted between 0 and 1. The value of 1 means that the FRF amplitude and phase are repeatable from measurement to measurement, so the goal is to keep the value close to one over the whole frequency range. The value of 0 means that the measurements are inconsistently repeatable. In some cases, it is normal for the coherence to drop close to 0 due to resonance and/or anti-resonances or when the vibration responses are very low. When the coherence is close to 0 in the whole frequency range, it is an early indication of an error in the measurement setup, which could occur due to some other sources of vibration, or noise, for example that the hammer is not exciting the entire frequency range, poor boundary conditions.

6. TEST CASES

In this section, the test apparatuses used for the research are introduced. The research is conducted on a set of test cases, which start from very simple „academic" test cases and gradually increase in complexity. For this, a set of test cases of various complexity were defined. The major requirements for these were that:

- they should range from very simple to complex structures,
- they should feature characteristics (i.e. materials, thickness, joints, etc.) typical of vehicle chassis structures.

With these requirements in mind, set of Test Apparatuses have been developed by the research group (see Tab. 2 and Fig. 41).

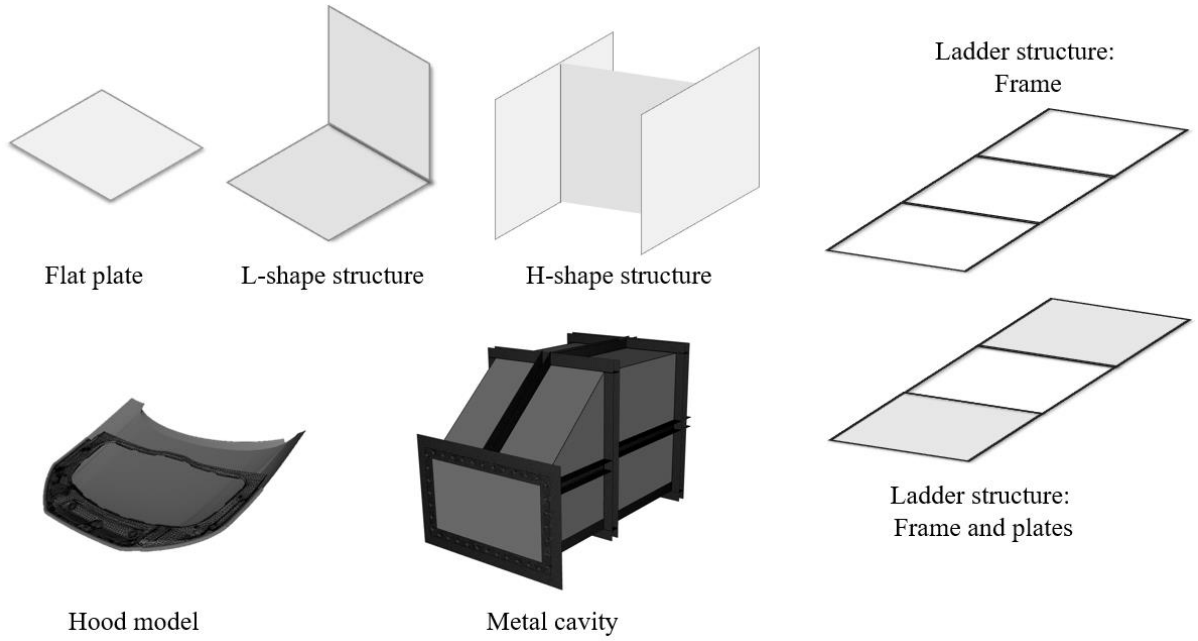

Figure 41: Test apparatuses.

The main purpose of using test apparatuses is to validate the simulation results with experiments. A major challenge was to create such structures, which can be used for validation with the SEA simulations as well. This requires such modal density, so that minimum 3 modes are contained in one-third octave. In order to satisfy this criterion, all test apparatuses were simulated via FEM and SEA software to make sure that the required modal density is achieved. All test apparatuses have been designed in-house and custom manufactured for the MTA-SZE Lendület Vehicle Acoustics Research Group. This author was personally responsible for designing test Apparatuses level 1, 2 and 3 from Tab. 2.

The design of the two cavities was especially challenging. Here, the design requirement was to have minimum 3 fluid modes in each octave above 400 Hz in order to fulfill the assumptions made for SEA simulations, with which validation was also targeted. Both cavities were modeled and simulated in FEM to make sure that the right combination of size and wall thickness is applied. The criteria for choosing the cavity size were to have the minimum total number of modes for the 400-1000 Hz range, but with a modal density of minimum 3 modes/third octave at 400 Hz. At the top of the complexity, a "rigid" (made of concrete) as well as a "soft" (made of steel) cavity has been created to be able to analyze the differences between the finite and infinite volumes [92].

Table 2: Details of the test apparatuses.

Test case name	Level	Validation methods	Simulation methods	Goal of the study
Flat plate	1	Laser doppler vibrometer, Shaker testing, Impact testing	SEA	Comparison of the measurement techniques. Determination of the damping parameters. Investigation of the influencing factors of the damping loss factor during the measurement process.
Flat plate + bitumen layer	1b	Impact testing	SEA	Comparison of the different damping treatment layups and they implementation into the simulation software.
L-shape structures	2	Impact testing	SEA	Comparison of the different binding techniques (19 variants), riveting, bolting, glueing, point welding, line welding and one reference structure without any junction, only bended. Comparison of the two different connection angles: 60° and 90°. Comparsion of the measured CLFs to the analytical values.
H-shape plate	3	Impact testing	-	Highlight the difficulties of the experimental PIM.
Ladder structure: Frame	4a	Impact testing	FEM	Comparison of the different simulation methods.
Ladder structure: Frame and plates	4b	Impact testing	FEM, Hybrid FE-SEA	
Ladder structure: Frame, plates and foams	4c	Impact testing	FEM, Hybrid FE-SEA	
Hood model	5	-	FEM, SEA, Hybrid FE-SEA	Comparison of the different simulation methods.
Metal cavity	6	Shaker testing	FEM, Hybrid FE-SEA	Investigation of 5 different hybrid subdivisions. Comparison of the calculation times as well as the velocity results at the response locations.

Every additional detail of the apparatuses such as sizes, material properties, etc. will be introduced directly in their sections.

7. PURE SEA TEST CASES

7.1. Flat plate

7.1.1. Motivation

The damping loss factor is one of the most important parameters in SEA simulations, hence its accurate definition is crucial from simulation accuracy point of view. In this section, the effect of the measurement procedure, as well as of the evaluation process on the DLF values will be investigated. Note, that although there are different methods for obtaining DLF, in this section only the HPBM will be used, since it is best suited for statistical analysis of the DLF values of a plate due to the large amount of data involved in the evaluation.

7.1.2. Measurement setup

The considered test case was a rectangular plate with the size of 650 x 550 x 2 mm. Theoretically, all modes should be excited to get the correct DLF of a structure. For this reason, 16 response points were used per excitation. However, in order to avoid too much added mass to the plate, only 4 accelerometers were used per measurement at any given time [93]. Thus, one excitation point was measured four times. In terms of avoiding extra weight, the Laser Doppler Vibrometer could have been the best choice for the measurement, however, its spectral lines did not correspond to the amount required for a slightly damped plate. For this reason, only shaker and hammer excitations with accelerometers were applied.

The sources of the excitations were: a) an electromagnetic shaker with a periodic chirp signal and b) an impact hammer. Fig. 42 represents the schematic diagram of the measurement setup.

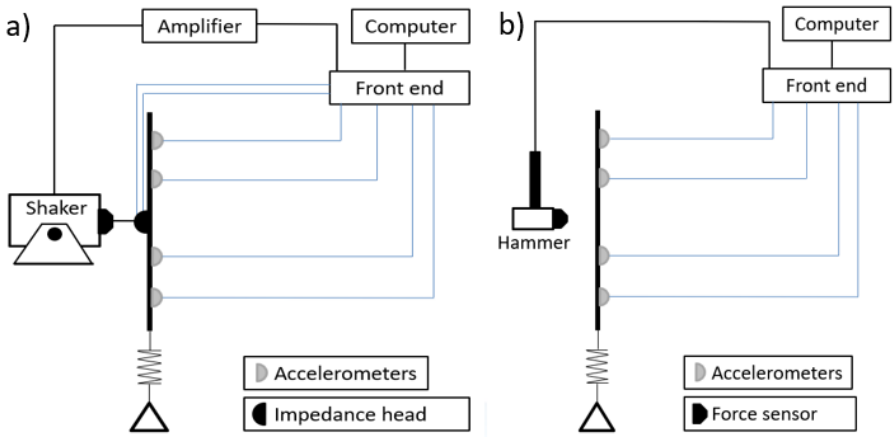

Figure 42: Schematic diagram of the measurement system: a) shaker testing, b) impact testing.

In all measurements, three different excitation points were used to get a large number of DLF samples and thus to reduce the experimental error [8]. Free-free boundary conditions were applied and to ensure these, the plate was hanged on a bungee cord with silicone inserts. The investigated frequency range was the mid-frequency range (400 Hz – 1 kHz). The measurement was performed with the Siemens LMS measurement system. The response was measured by lightweight ICP accelerometer sensors (piezo-electric, B&K, Type 4519-003) weighing 1.5 grams each. The impedance head was PCB Piezotronics, Type 3321. The impact hammer was PCB Piezotronics (Model Number: 086C03) with hard rubber head.

The shaker excitation range was between 282 – 1280 Hz. The frequency resolution of the measurement was 0.039 Hz, and Hamming windowing technique was applied. In the impact measurement case, the pre-trigger time was adjusted to about 0.02 sec, while the trigger force was 20 N. The impact force spectrum was capable to achieve up to 1.8 kHz.

Note that the considered plate is extremely sensitive to every little change in the boundary conditions, for example the room temperature or dismantling and installing the structure between two measurements.

7.1.3. Validity of the damping evaluation method

In this method, the DLFs are determined from the resonance peaks of the individual modes. It is related to the modal behavior of the structure. In order to reduce the experimental error during the estimation of the DLF, the averaging over several excitations and response points is required. This method uses the Frequency Response Function (FRF) directly to calculate the 3 dB drops from the resonance peaks, as it was shown in Fig. 21.

However, note that according to Eq. (23) the modal overlapping over a certain frequency makes this method unsuitable. Interestingly, although the structure exhibited some close peaks in the last third octave band (891 – 1122 Hz), the method appeared to remain still valid for this plate. The highest frequency in the last band is 1122 Hz, and the average damping value (in this band) was η ~9.6e-4. Thus, in this case the Δf should be around 3.2 Hz. Note that there were some peaks close to each other, the two closest ones can be seen in Fig. 43. All other peaks had a larger distance between them than the minimum required Δf. For this reason, this method was still feasible in this frequency range.

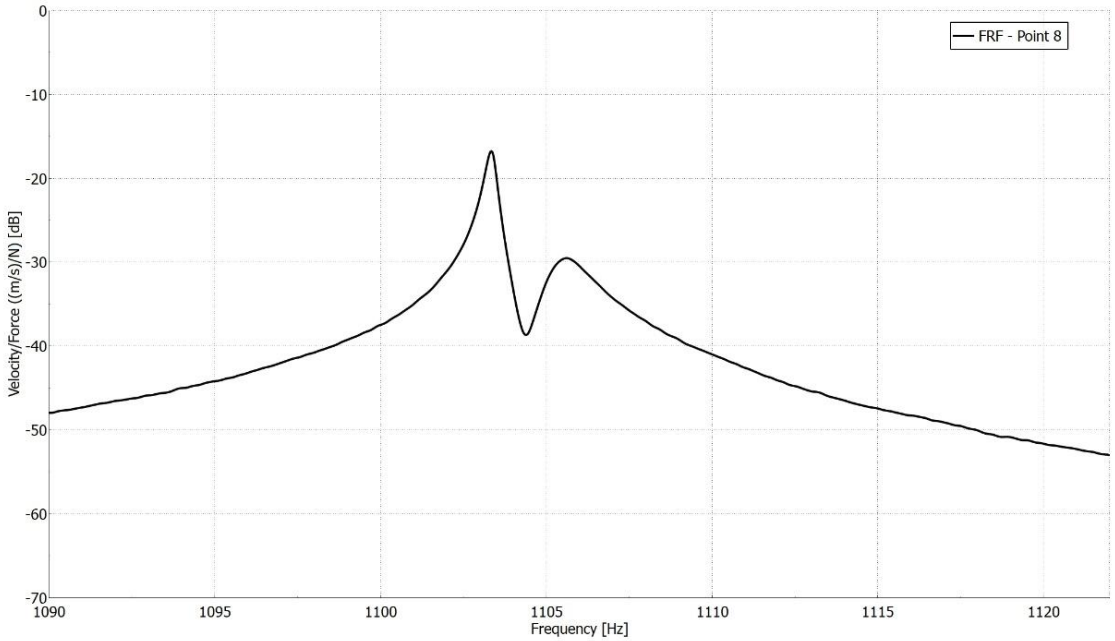

Figure 43: The closest peaks at the last third octave band. The Δf between the neighboring peaks is 2.5 Hz, while the ideal should be 3.2 Hz.

7.1.4. Electromagnetic shaker testing

An electromagnetic shaker can provide smooth and repeatable excitation signals, and therefore was used for investigation of the main measurement parameters.

7.1.4.1. Coherence

A flexible suspension is not appropriate to get a good coherence curve, because of the metal-metal friction between the hook and the washer. In order to eliminate this phenomenon, silicone inserts were used (see Fig. 44), which had a quite significant impact on the coherence curves, as illustrated in Fig. 45.

Figure 44: Silicone insert was used between the hook and washer to avoid the metal-metal friction.

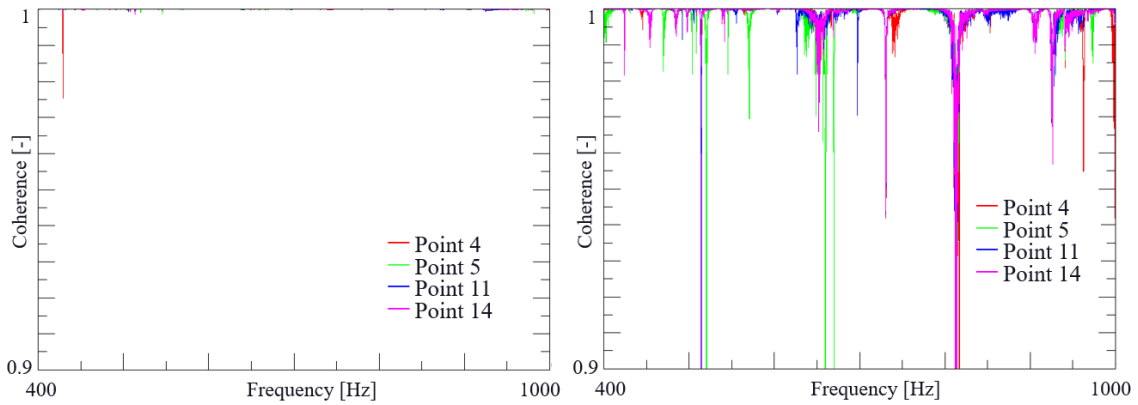

Figure 45: Coherence curves of the same measurement points. Left: with the silicone inserts; right: without the silicone insert.

7.1.4.2. Input force level

Although this structure is a linear system, under a certain excitation force the input signal can become too low compared to the noise level. This can also cause a problem at the output side, because the responses can be out of the sensitivity range of the accelerometers. This should be taken into consideration when conducting measurements, because this can have significant effect on the FRF curves, as shown in Fig. 46.

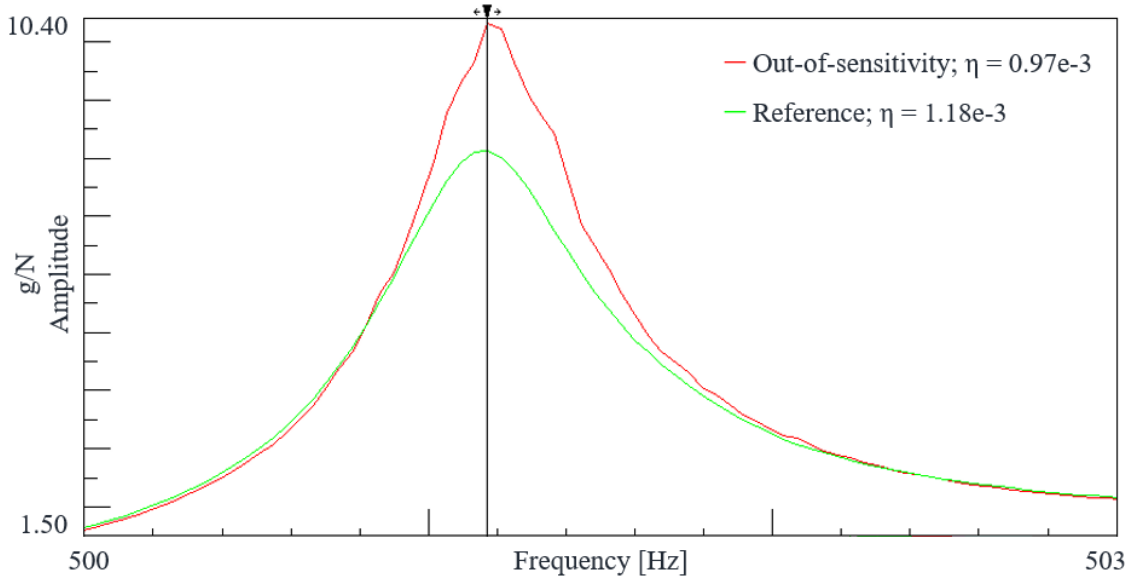

Figure 46: Effect of sensor sensitivity on the DLF values at 501.17 Hz. Green curve: reference measurement with appropriate excitation force. Red curve: low input force, the sensor sensitivity is out of its sensitivity range. Top right shows the DLF values, the difference is 18%.

As Fig. 46. shows, the amplitude of the resonance peaks is overestimated if the input force is smaller than the ideal one. The red curve contains more noise than the green one, moreover its damping value has also changed.

7.1.4.3. Frequency resolution

In order to get smooth response curves and accurate damping values, the resolution of the resonance peak is a key factor. In order to determine the proper DLF value with the Half Power Bandwidth Method, the frequency resolution must be appropriate. According to Lyon et al. [8] the following equation can be used to determine the required sample points:

$$N > \frac{20}{\eta}, \tag{86}$$

where N is the number of the sample points per channel, and η is the DLF value.

During the measurements, most of the DLF values were around η = 0.0008, which requires at least 25,000 sample points, while in the fine measurement case 32,000 spectral lines were used. The problem is that it is difficult to know a-priori the expected DLF value, so it might be required to perform a preliminary-measurement to check the Nyquist circle. If the frequency resolution is not satisfactory, the Nyquist-circle will be angular instead of circular. The aim would be to get a perfectly rounded circle. In the fine case, the frequency resolution was well-resolved, with 0.039 Hz. As a comparison, a coarse resolution case was applied with an order of magnitude larger frequency resolution i.e. 0.39 Hz. Fig. 47 shows the Nyquist diagram of the FRFs for the fine and the coarse frequency resolutions at a resonance peak around 501 Hz.

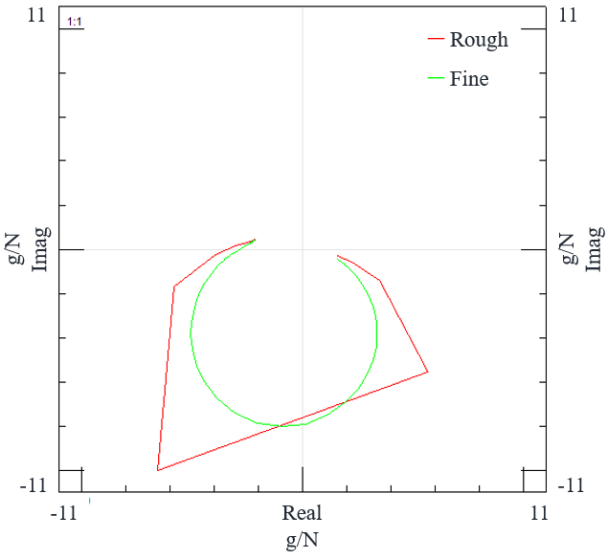

Figure 47: Nyquist diagram for one resonance peak at 501 Hz. Green curve is the fine resolution (0.039 Hz), red curve is the coarse frequency resolution (0.39 Hz).

The same resonance peaks are visualized in Fig. 48 in an Amplitude-Frequency diagram with DLF values at 501 Hz. As one can see, the frequency of the peak is shifted, and the amplitude of the peak is also changed by the frequency resolution. Consequently, the DLF value has also changed when the frequency resolution was coarse.

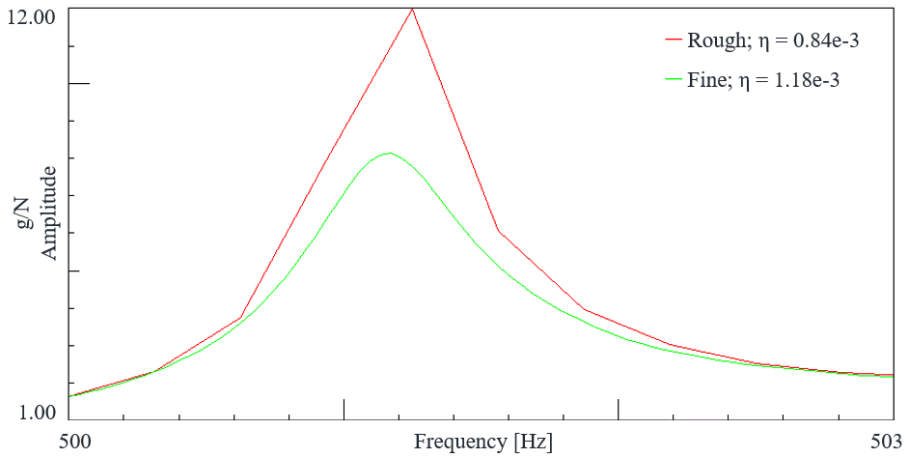

Figure 48: FRF curves with the DLF values around 501 Hz. Green curve represents the reference case with fine frequency resolution (0.039 Hz), while the red curve the coarse frequency resolution (0.39 Hz). Top right corner shows the DLF values. The peak of the green curve has at 501.16 Hz while the red curve has at 501.25 Hz.

7.1.5. Impact testing

During the impact test all parameter setups, such as the excitation, the response points, as well as the boundary conditions were the same as in the shaker excitation case. The only difference was the way of the excitation.

Although during the shaker test every important parameter was taken into consideration, due to the connection of the shaker it gave too much additional damping to the system. To avoid this phenomenon, the damping values were measured by impact testing. At lower frequencies, this effect is not too conspicuous, but over 500 Hz the amplitude of the resonance peaks was changed and shifted, as depicted in Fig. 49.

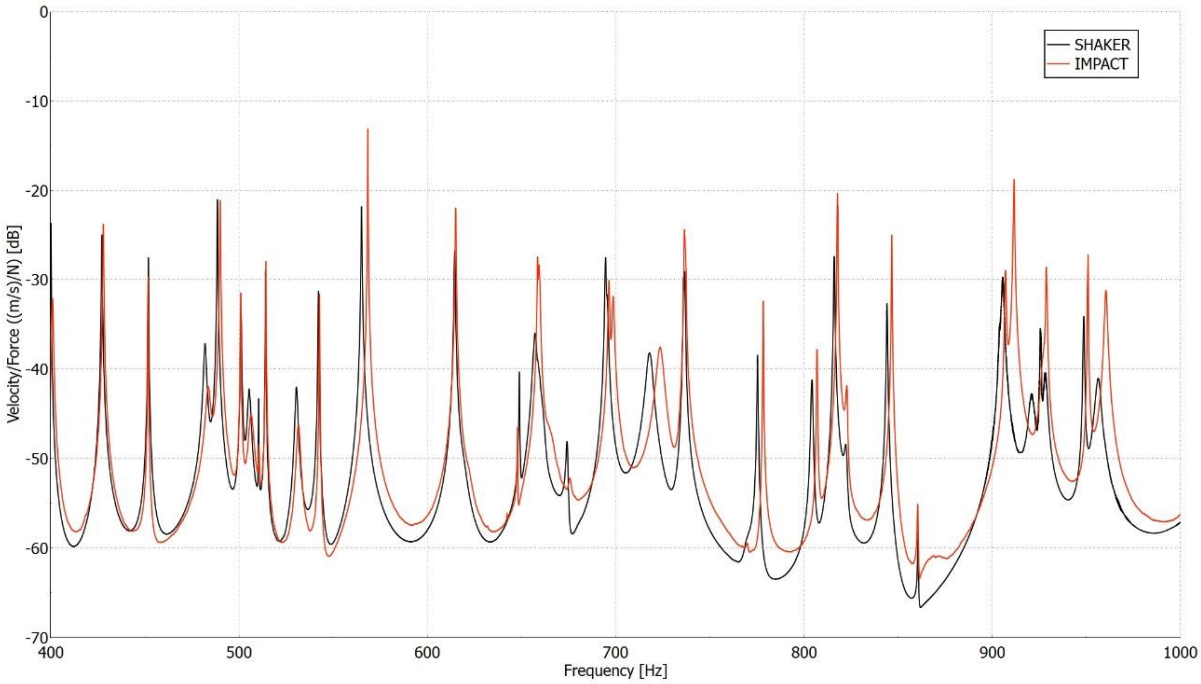

Figure 49: RMS average of 16 response points for shaker and impact excitation cases. The excitation point and the response points were at the same locations for both cases.

7.1.5.1. Coherence

Note that the impact is generated manually by a human and thus the position of the hitting points as well as the direction of the impact force will never be exactly the same during the four averaging. Hence, the coherence of the impact tests will never be as clear as for the shaker cases, and thus the coherence curves contain lot of collapses, as illustrated in Fig. 50.

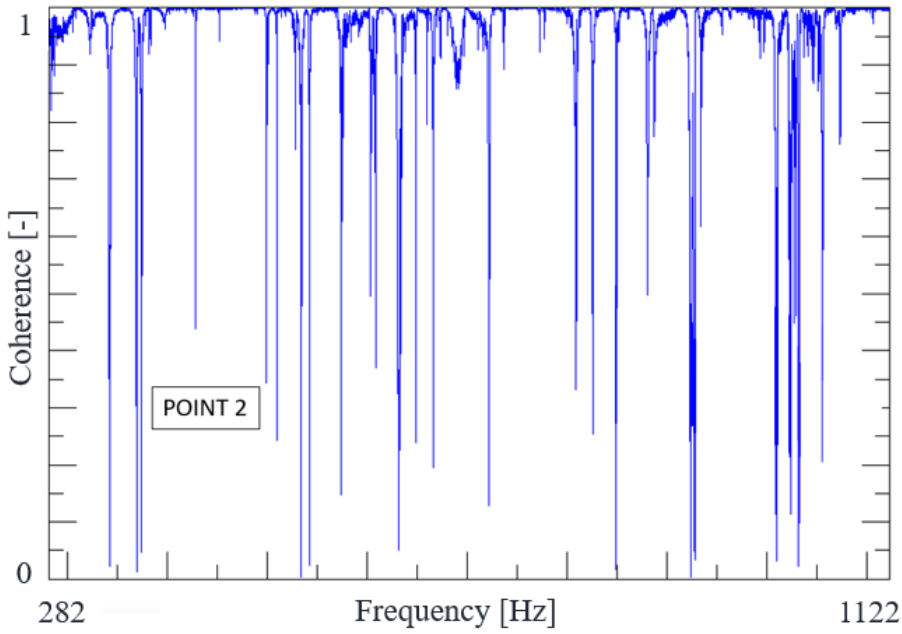

Figure 50: Coherence curve from impact excitation at Response Point 2.

One consequence of the imperfect coherence curves is that the FRF curves are not as smooth as it was for the shaker excitation case. This can be seen in Fig. 51, which shows the resonance peak at around 501 Hz for the impact hammer excitation case and at around 502 Hz at the shaker excitation case.

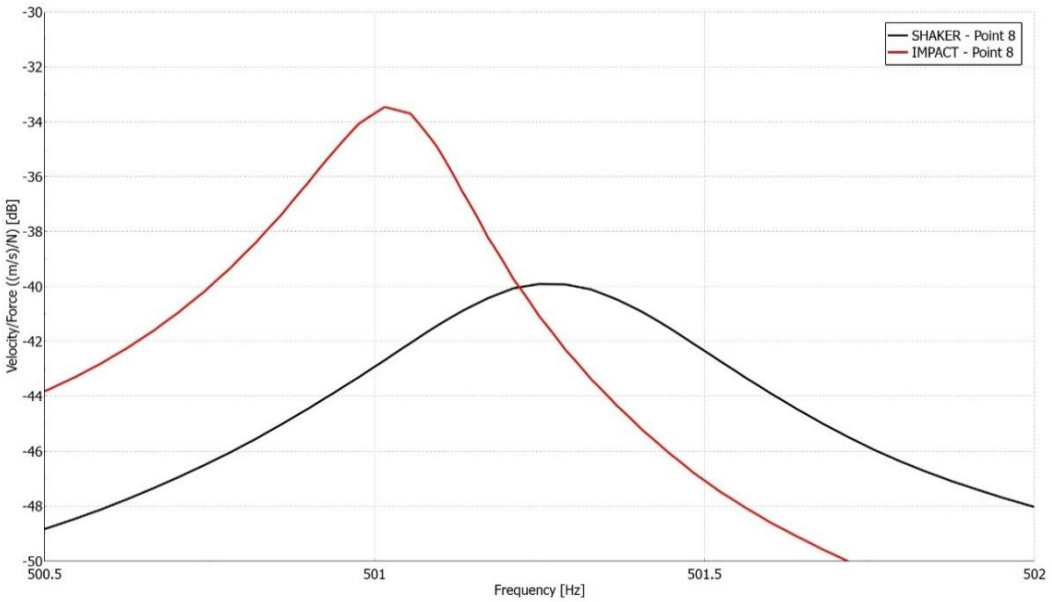

Figure 51: FRF curve of the impact hammer and shaker excitation cases in Point 1.

7.1.6. Statistics of the damping values

Recall, that three different excitation points and 16 response points were used, so in total 48 FRF curves were investigated. From these curves the DLF values were calculated for each frequency band. Fig. 52 shows the average DLF values in every third octave band, with deviations.

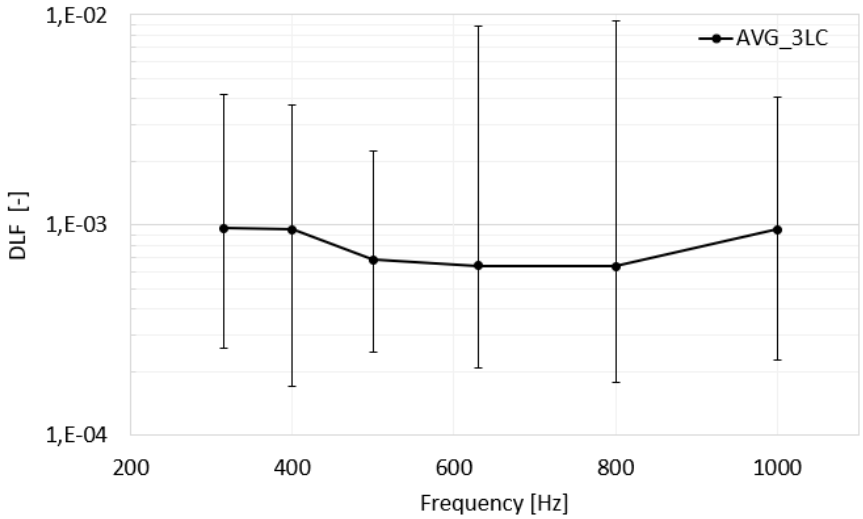

Figure 52: Average of the DLFs with deviations. Note that 16 response points were considered for each excitation, in all 3 impact positions.

The number of the samples is clearly sufficient to characterize the given frequency band. Note that the 400 Hz third octave band included the smallest number of samples, but still with as much as 130 datasets. In order to evaluate such large dataset, a statistical approach was used. The distribution of the data was investigated by plotting the histograms of each third octave bands. The Kolmogorov-Smirnov (K-S) goodness test of fitting data to theoretical distribution was performed. The histograms showed that the samples were skewed, thus lognormal distribution was assumed in the K-S test. The statistics calculated can be expressed as [50]:

$$D_n = \sup|F_n(x) - \phi(x)|\,; -\infty < x < \infty. \tag{87}$$

In case of $D_n \geq D_{crit}$, the null hypothesis can be rejected. The K-S test of fitting the data to the theoretical distribution showed that the null hypothesis – stating that the data shown by Fig. 53 come from a lognormal distribution – cannot be rejected at 95% significance level [43].

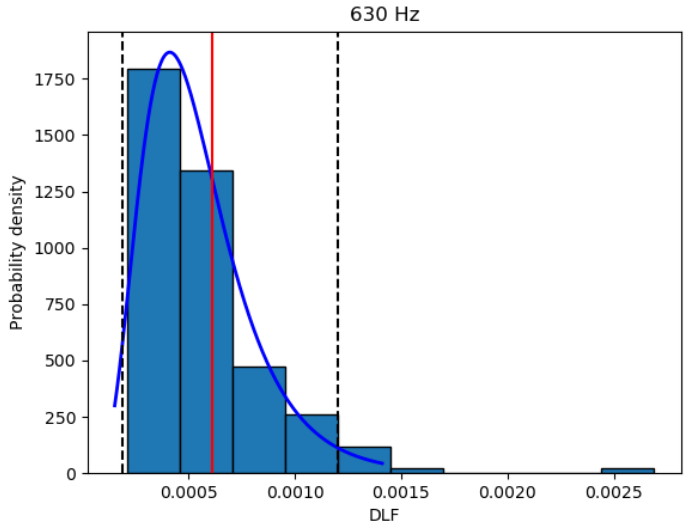

Figure 53: Histogram of samples at 630 Hz third octave band, probability density function of the fitted lognormal distribution (blue line), expected value (red line) and the 95% confidence intervals (black dashed lines) of the fitted distribution function.

The histogram of the other third octave bands showed similar trends. Thus, the confidence intervals and the expected values were calculated from the fitted lognormal distributions. The differences between log-normal expected values and arithmetic averages can be seen at Fig. 54.

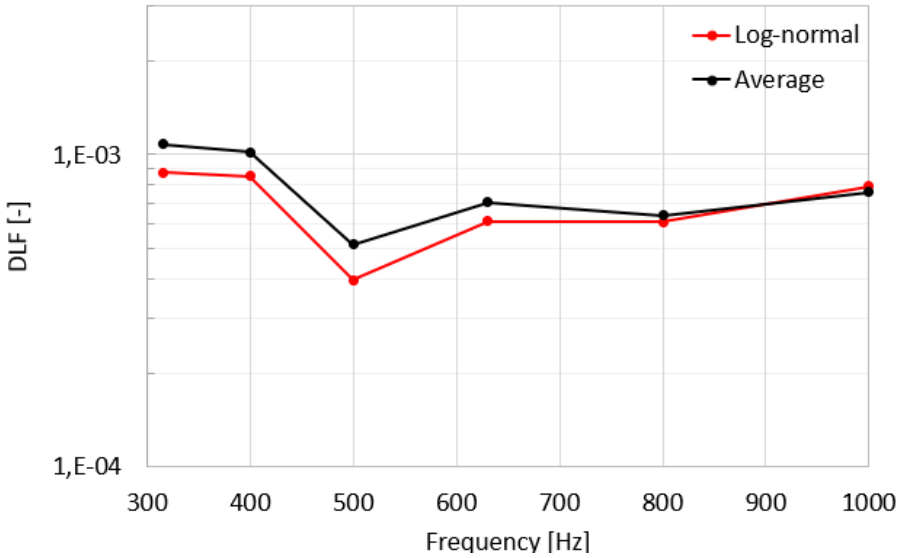

Figure 54: Log-normal vs. average mean value comparison.

Differences can be seen only at the lower frequencies, but this might be associated with the fact, that the test case was a very sensitive and lightly damped plate.

7.1.7. Simulations

Simulations were run by the ESI VA One commercial software. During the simulations, a 1 N point force was applied as the excitation. Every important parameter, such as the sizes, the mass and the material, were the same as for the real structure. The simulation was run with the expected DLF values from the log-normal distribution as well as the arithmetical averaged of the damping values. The modes in band values of the plate structure are represented in Fig. 55.

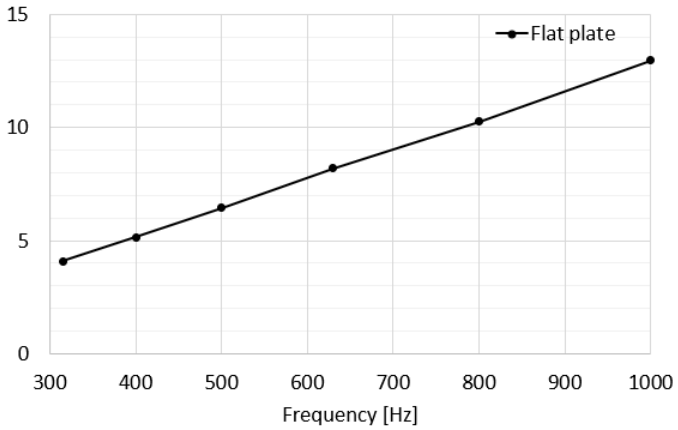

Figure 55: Modes-in-band of the test case. The required 3 modes/third octave band are already fulfilled in 315 Hz band.

The measurement curve was obtained from the RMS average of all response curves. The third octave band averages of the curves were considered. Fig. 56 shows the simulation results with

the expected values of the log-normal distribution compared to the experiment while Fig. 57 shows the simulation with the averaged DLF values compared to the experimental results.

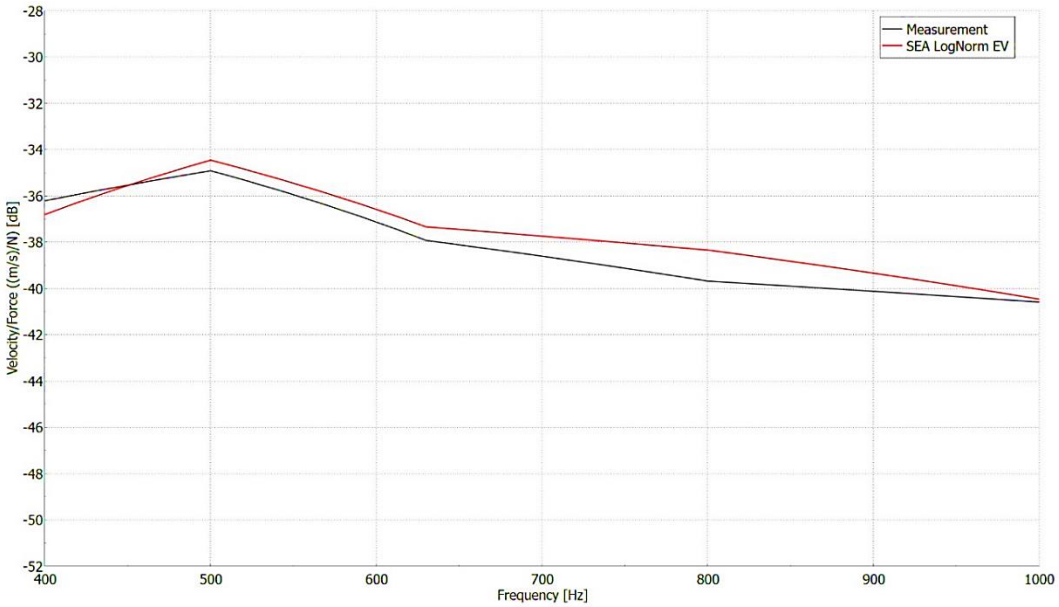

Figure 56: Comparison of the velocity/force results for the simulation and experiment results. DLF values are the expected value of the log-normal distribution.

As it can be seen on Fig. 56 the characteristics of the simulation curve are similar to the experimental curve. The maximum deviation occurred at around 800 Hz and it is about 1.5 dB.

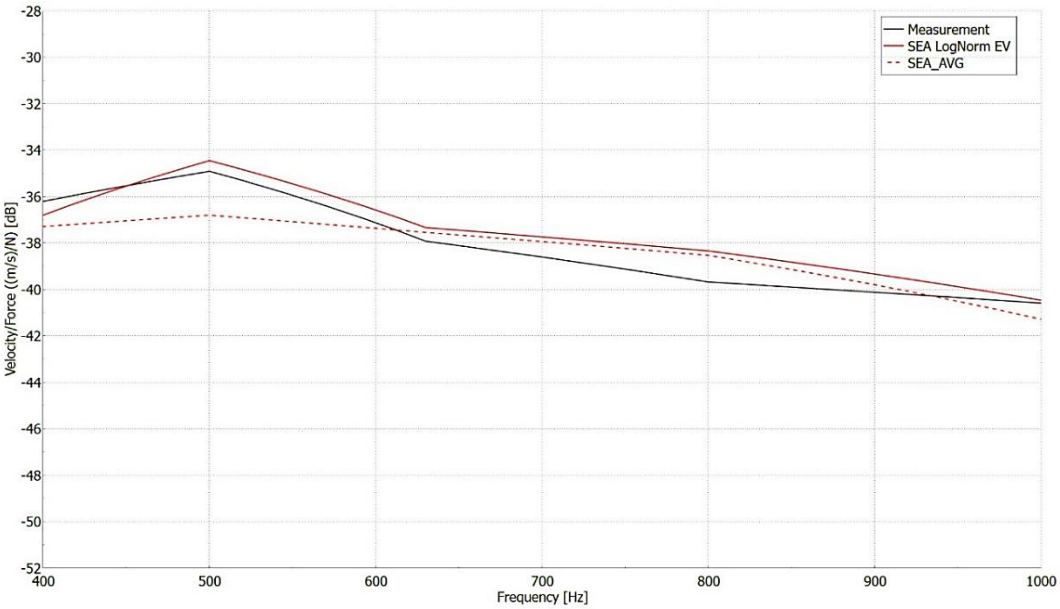

Figure 57: Comparison of the velocity/force results for the simulation and experiment results. During the simulations two different DLFs were used: a) log-normal expected values; b) average mean value.

Both simulation results showed good agreement with the measurements. The maximum difference between the simulation (by considering average DLF) and the experiment was around 2 dB at 500 Hz. According to these results, the calculation of average DLF values could be sufficient since the log-normal calculation requires an additional script to calculate the expected values. In order to illustrate the uncertainty of the DLF values, the maximum and minimum values were taken into account in all third octave bands and compared to the experiment, as shown in Fig. 58.

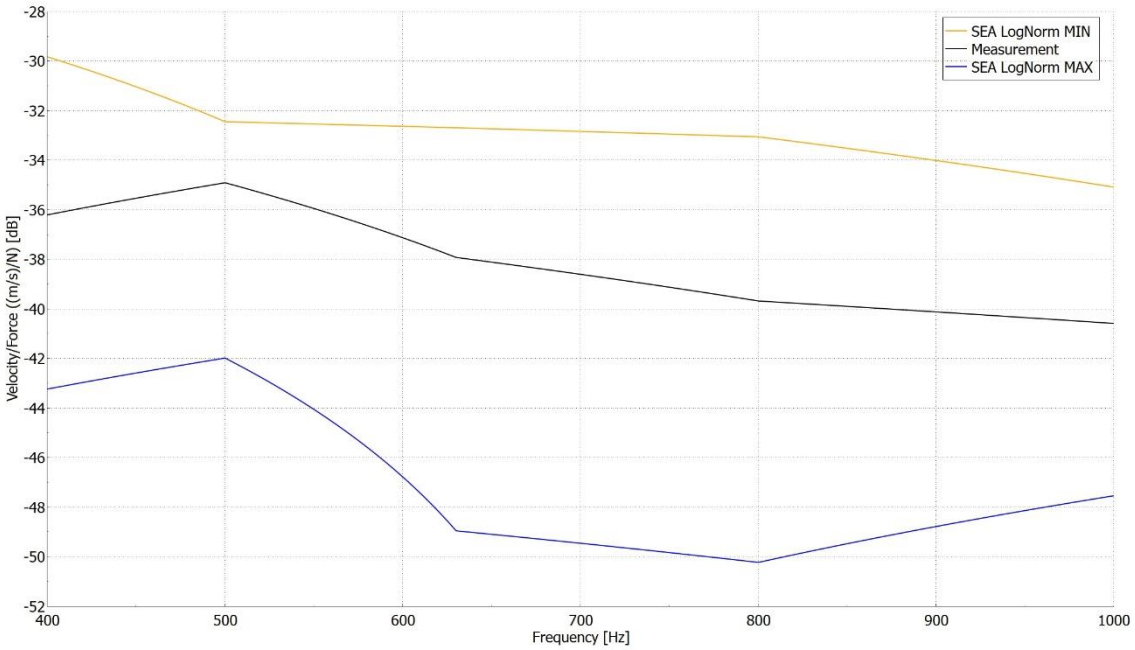

Figure 58: Comparison of the velocity/force results for the measurement and simulation with applying the extreme values of the DLFs from the measurement data in Fig.13.

As one can see, using the minimum and maximum extremes of the DLF can highly influence the results. The difference between the two extremes can be very large, for example as much as 17 dB at 800 Hz. Since the DLF values follow log-normal distribution, the maximum and minimum values of the 95% confidence level were also taken into account and compared to the experiment, as shown in Fig. 59.

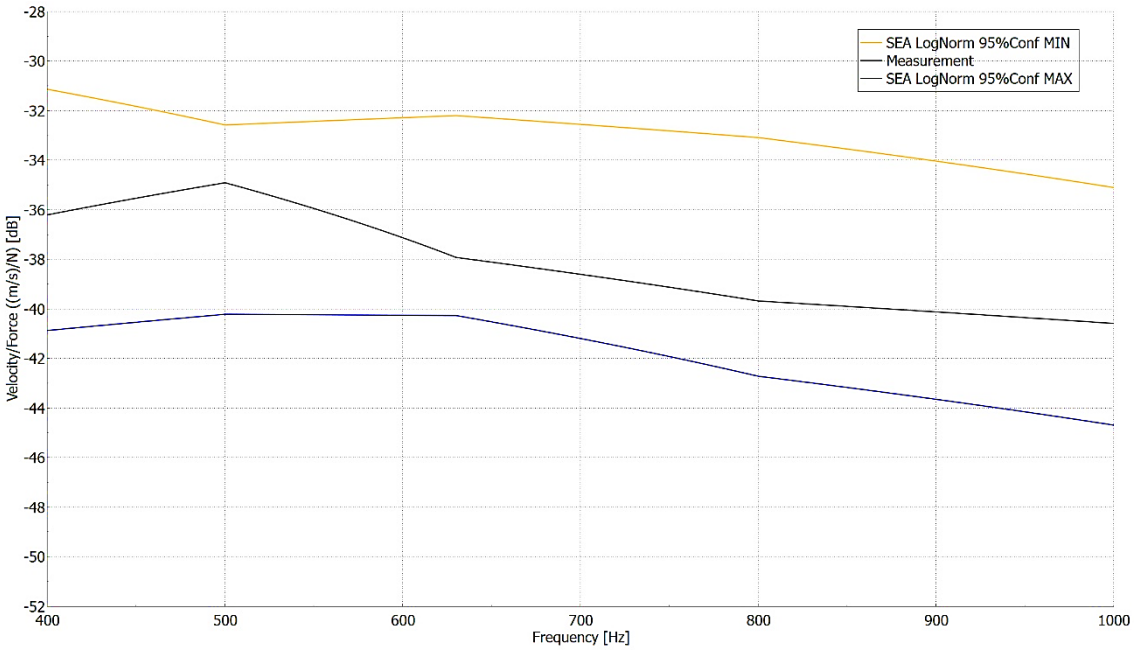

Figure 59: Comparison of the velocity/force results for the measurement and simulation with applying the 95% confidence intervals of the DLFs from the measurement data as shown in Fig. 14.

As one can see, the difference can still be significant, with the maximum deviation around 11 dB at 800 Hz.

7.1.8. Conclusions

As the examples showed, the value of measured DLF is highly influenced by the quality of the FRFs. All the parameters (such a coherences, frequency resolution, etc.) must be taken into account in order to achieve proper damping results, especially for such an extremely lightly damped plate, which was examined in this section. Small changes in the setup can cause large differences in the damping. Therefore, it is recommended to ensure that the right ratio of the excitation force and of the noise level is applied, as well as that the frequency resolution of the setup is sufficiently fine. After the first measurement, one needs to check the results from frequency resolution as well as coherence point of view, because these parameters can affect the DLF significantly. The shaker excitation ensures nearly perfect coherence curves and smooth FRFs, but its connection could add damping, mass and stiffness to the system. On the other hand, the hammer excitation is free of these effects, but inherently lead to less coherent FRFs than for the shaker case. Consequently, for a lightly damped plate the impact hammer excitation could be a better solution, if it is feasible. The capability of the half power bandwidth method is based on the individual resonance peaks. For this reason, the modal overlapping must be checked at higher frequencies. If the peaks are too close to each other, the method is unable

to determine the damping loss factor, and another damping determination method must be found. The DLF determination by HPBM required huge amount of work to calculate the damping from each individual peak, but as the results show, when the method is combined with the statistical analysis of a large number of samples, it is capable to obtain good results for a very sensitive structure. The expected value of log-normal distribution resulted in a good correlation between simulation and experiment. Also, the character of the experimental curve was correctly depicted by the log-normal distribution. The arithmetic average calculation of the DLF values gave a good simulation result in all investigated frequency bands compared to the experiments although in the 800 Hz band a 2 dB deviation can be observed. All in all, in this case the arithmetic average is the better choice from accuracy point of view, since the difference between log-normal and average is not significant, however the calculation of the log-normal is much more complicated.

7.1.9. Thesis No. 1

I formulated a novel procedure for the accurate determination of the damping for SEA panels. The procedure was deduced from a systematic approach and appears to provide relatively accurate Damping Loss Factor values in every frequency band, when compared to other method. I investigated the effects of the boundary conditions on the results, such as those of the coherence, the driving force or the type of the excitation. In addition, the method of data processing was also examined with log-normal distribution as well as through arithmetical average. The approach was validated on a rather sensitive, lightly damped flat plate, and the acquired data were implemented in SEA simulations, yielding minimal deviation (less than 1.5 dB) compared to the experiment results [I], [J].

7.2. Flat plate with damping layer

7.2.1. Motivation

In SEA simulations, the whole subsystem has one damping value for a frequency band. In addition, the noise control treatments can only be considered as a percentage of coverage in the simulation software. If noise control treatment is applied on the structure, such as it is common to apply bitumen sheets on flat plates in vehicles, the position of these sheets is expected to have a significant impact on the damping of the system. The goal of this section is to examine, whether the spatial distribution of such damping layers can be represented in SEA.

7.2.2. Measurement setup

The considered test case was the previously used rectangular steel plate of 650 × 550 × 2 mm size. Sixteen (16) randomly located response points were introduced and 3 load cases applied. In order to avoid too much added mass on the plate, only 4 accelerometers were used in each measurement at any given time. Thus, one excitation point was measured four times. Hence, five channels were used, one for a force sensor and four for the accelerometers. Free-free boundary conditions were applied, and to ensure these, the plate was hanged on a bungee cord with silicone inserts. The source of the excitations was an impact hammer. Fig. 60 depicts the schematic diagram of the measurement setup.

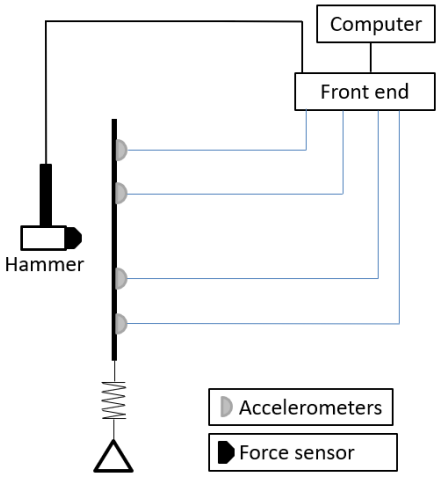

Figure 60: Schematic diagram of the measurement system.

Measurements were performed with the Siemens LMS measurement system. The response was measured by lightweight ICP accelerometer sensors (piezo-electric, B&K, Type 4519-003), weighing 1.5 grams each. The impact hammer was PCB Piezotronics (Model Number: 086C03), with hard rubber head. The pre-trigger time was adjusted to ~0.02 s, and the trigger force was 20 N. The impact force spectrum was capable of up to 1.8 kHz frequency. The investigated frequency range was between 282 – 1122 Hz, since these are the lower and upper border of the investigated third octave bands (315 – 1000 Hz). The frequency resolution was 0.39 Hz.

7.2.3. Damping layer application

In NVH, the noise level reduction is a key factor. One of the best ways to reduce the vibrational energy is to employ viscoelastic damping treatments on the component. In Section 7.1 a bare plate was examined, which damping was very low. This can be enhanced by employing viscoelastic damping layers on the structure.

Free layer damping treatments effectively reduce the bending motions of the structure, since higher strain levels can be reached [8]. Fig. 61 shows a simple free layer damping treatment on a bare plate.

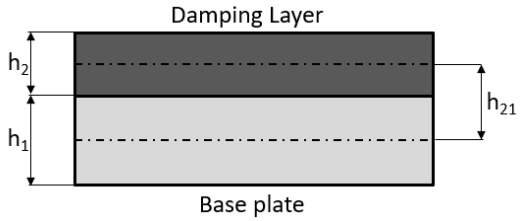

Figure 61: Free layer damping treatments.

As Fig. 61 shows, the damping layer is placed away from the neutral axis of the base plate. For this reason, the higher strain level effectively reduces the bending motion of the plate and as a consequence, the damping value will be higher. Eq. 88 represents the effective damping value of the free layer damping treatments for bending motion, when the stiffness of the damping layer is smaller, compared to the base plate ($K_{2r} << K_{1r}$) [8]:

$$\eta_B = \eta_1 + \frac{\eta_2 K_{2r}(\kappa_2^2 + h_{21}^2)}{K_{1r}\,\kappa_1^2}, \tag{88}$$

where η_1 is the damping loss factor of the base plate, η_2 is the damping loss factor of the damping material, κ_1, κ_2 are the bending radius of gyration of the cross-section of the base plate and of the damping material, respectively. The value h_{21} represents the distance between the neutral axis of the base plate and between the damping material.

The total coverage of the bitumen layer was around 20% when related to the full area of the plate and it consist of 8 bitumen sheets with the size of 50 × 100 × 1,6 mm each. Two different applications were used: a) the bitumen layer was at the middle of the plate, b) the bitumen sheets were randomly around the plate. Both of them used the same amount of the damping layer, and the added weight was 214 grams, that is 3.8 % of the bare plate weight. Fig. 62 shows the two bitumen layer application cases.

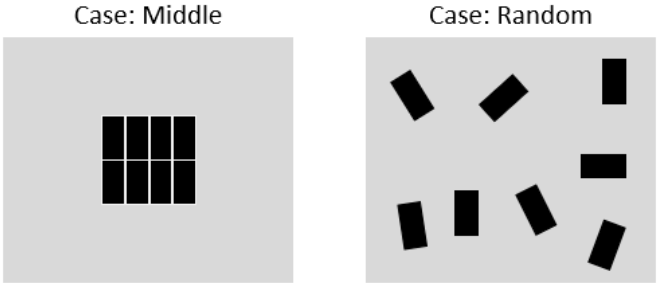

Figure 62: Two different damping layer applications: a) middle of the plate, b) placed around the plate randomly.

Fig. 63 represents the results of the DLF values at the two bitumen layer application cases.

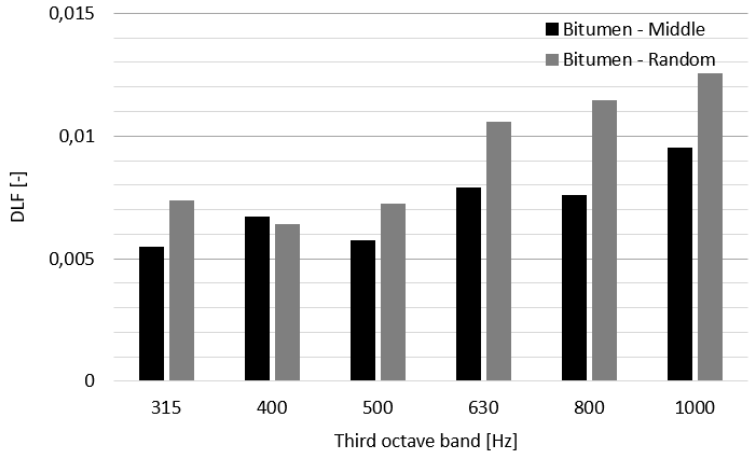

Figure 63: DLF values of the two different bitumen layer application cases.

As the results show, at higher frequencies the randomly located bitumen sheets have higher impact on the DLF values. For a comparison, Fig. 64 illustrates the differences between the bare plate and the bitumen damped plate.

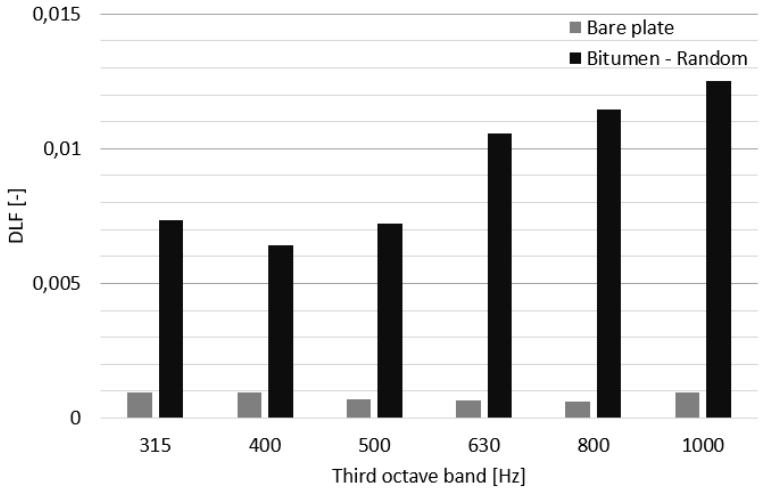

Figure 64: The DLF values of the bare and the bitumen layer application when the random location was applied.

As the results shows, at higher frequencies the differences were increased, with the maximum differences being one order of magnitude higher with damping layers than for the bare plate.

7.2.4. Results

Since SEA simulations average the results in space and in frequency, the method is unable to take into consideration the location of the bitumen sheets. The goal of the random distribution of the bitumen sheets was to investigate, how does the location of these sheets can be taken into account in the simulations, since in the software the only adjustable parameter is the coverage

of the bitumen layer. In the simulation, every parameter was the same in both cases, the only thing that was modified was the DLFs according to Fig. 62 DLF of the two different layers.

In the simulation software, the added damping layer was specified as a Noise Control Treatment, with the correct DLF values and coverage of the plate. There was no difference between the simulation and the real weight of the investigated damped plate. Fig. 65 represents the comparison results of the bitumen damped plate simulation and the measurement, when the bitumen sheets were at the middle of the plate. Fig. 66 illustrates the results for the case that they were randomly placed over the plate, while on Fig. 67 all the curves are illustrated in one diagram.

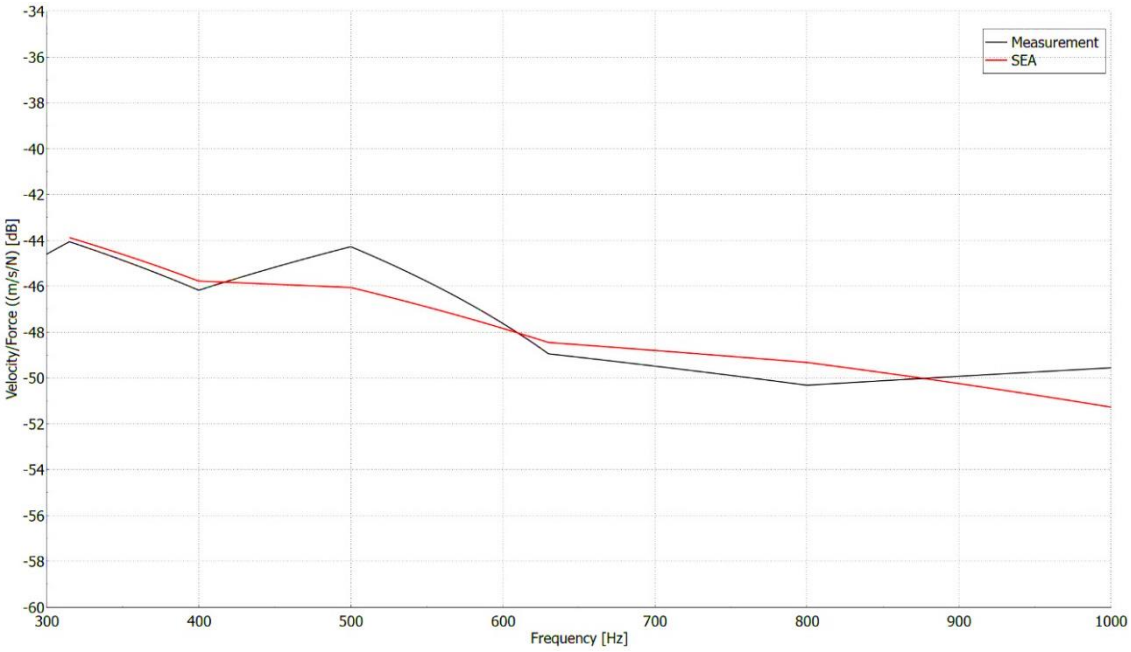

Figure 65: Simulation and measurement comparison, when the bitumen layer was at the middle of the plate. The Velocity/Force results were compared.

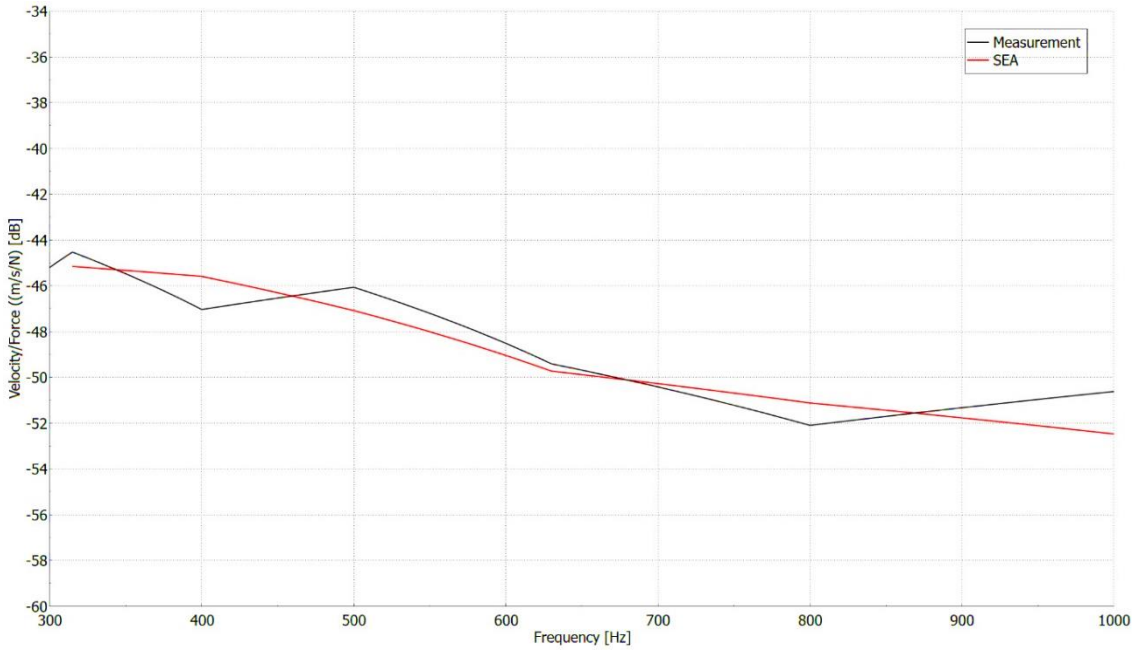

Figure 66: Simulation and measurement comparison when the bitumen sheets were randomly placed over the plate. The Velocity/Force results were compared.

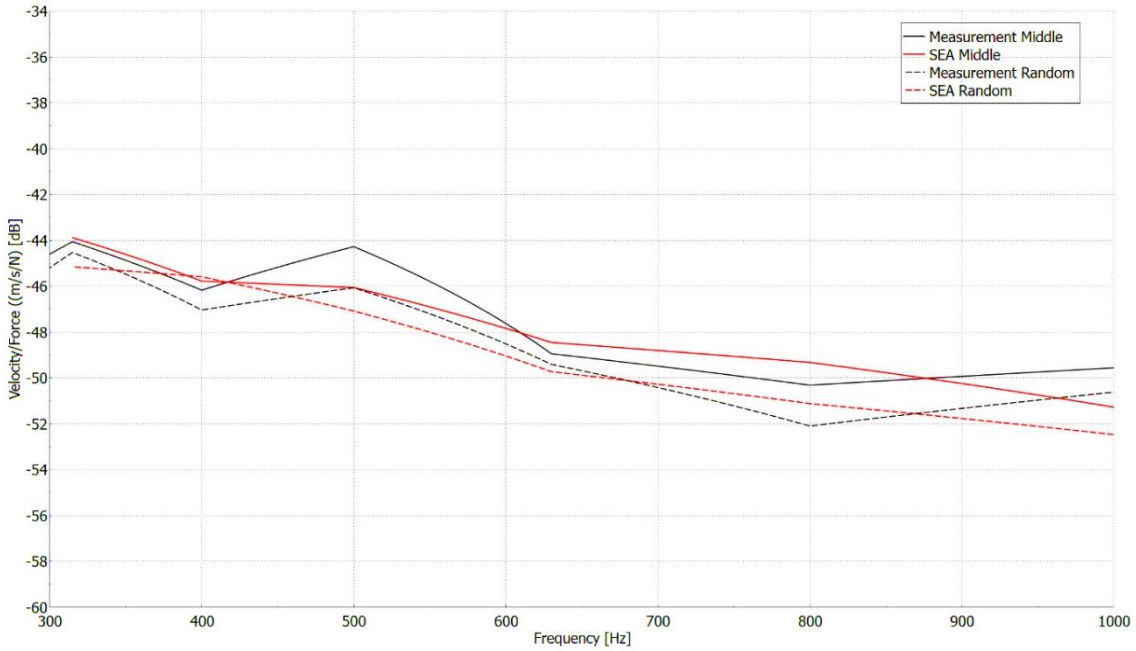

Figure 67: The two damped cases at one diagram. The solid curves are the middle bitumen location results, while the dashed lines are the random locations of the damping layers. The Velocity/Force results were compared.

As the results show that both simulations have good agreement with the experimental results. The maximum deviation was around 1.8 dB in both cases. For a better visualization of the differences, the two cases are illustrated jointly in Fig. 12. Thus, one can state, that the

simulations represent the experiments quite well. The middle location of the bitumen layers resulted in higher response in both the experiment and the simulation.

7.2.5. Conclusions

The determination of the DLFs with half power bandwidth method have some limitation, which should be taken into account (e.g. coherences, closeness of the peaks). As the results showed, the DLF determination in the bare plate and the two damped plate cases was successful. The three excitation points and the 48 response points gave enough samples of the damping values in order to get a statistically representative value in every third octave band. The comparison processes were the same when a damped layer was used on the plate. The damping layers increased the DLF values by around one order of magnitude, despite their weights being only 3.8% of the base steel plate. The random distribution of damping layers appears to be a better solution, since it generated lower responses. This trend is perfectly seen also in the simulation results. The half-power bandwidth method was capable to determine the DLF results in the bitumen cases too and helped for a better description of the structure in different bitumen application cases.

7.2.6. Thesis No. 1.b

In SEA simulations, the Noise Control Treatments are considered as a coverage on the surface and there is no information about the spatial distribution of them.

I proved that the different distributions of the damping layers can be taken into account during the SEA simulations if the panel damping is obtained during the measurements [G].

7.3. Two plates system with different junction types

7.3.1. Motivation

In vehicles, various binding types are employed, and they have a significant effect on the stiffness of the structure as well as on its vibroacoustic behavior. In this study, different binding types were investigated and compared, with the main focus being the energy loss through the various junctions, as well the effect of the modelling techniques on the simulation accuracy. The latter is really important in complex vehicle structures, where the CLF determination is not feasible, and hence the proper modelling technique is a key factor from simulation accuracy point of view.

7.3.2. Measurement setup

The main goal of the experiment was to ensure repeatability and comparability of the different connection types. Thus, the same size and material was applied for all considered test structures, and only the type of the junction was changed. The considered structures consist of two rectangular steel plates: Plate 1 with the size of 650 ×550 ×2 mm and Plate 2 with 655 × 550 × 2 mm. Fig. 68 shows the background of the experiment, illustrating that 4 excitations/plate and 16 response points/plate were applied. At once, only four response points are measured per plate to minimize the added mass to the plates. Fig. 69 illustrates the connection of the plates and the difference between Plate 1 and Plate 2, which will have quite significant effect as will be seen later. All the structures were made out of 2 mm thick cold rolled steel material without any surface treatment. They were cut to size via laser. The material property of the base S355 steel plate is the following: density of 7850 kg/m^3, Young's modulus of 200 GPa and Poisson's ratio of 0.3. Tab. 3 shows all the test cases in detail.

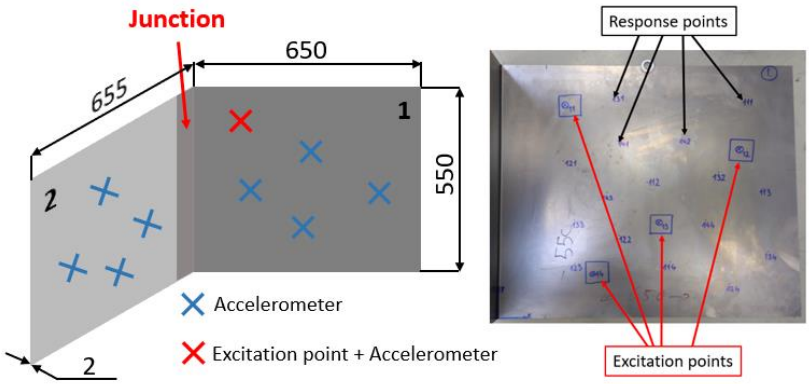

Figure 68: Illustration of the measurement concept (left) and the location of the excitation and response points (right).

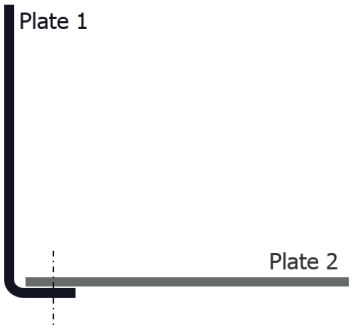

Figure 69: Detail of the plate's connection: Plate 1 is overlapped with Plate 2 in a 90° and 60° bend depend on the angle of the connection. This connection will be seen at all structures except the bended structure, since in that case there is no junction.

Both plates' responses were measured at 16 points, but with only 4 accelerometers/plate at once. This was done to reduce the mass added to the subsystems. An additional accelerometer is placed on the excited plate, because of the driving point measurement at the excitation point. The response is measured by the same lightweight ICP piezoelectric accelerometers from B&K, as described in Section 7.2. The plate is excited at four points on each plate, performed by an impact hammer. The impact hammer was PCB Piezotronics with a hard rubber head. The excitation and response points were at the same locations on every measured structure. Free-free boundary conditions were used during the experiment. In order to cover the investigated frequency range (400–1600 Hz third octave band) properly, the measured frequency range was set between 178 and 1778 Hz. During the measurements, the frequency resolution was 0.07 Hz.

7.3.3. Investigated junction types

Five types of joints – typical for vehicle chassis structures – in 19 different combinations were investigated: line welded, point welded, riveted, bolted, and glued. There are special junction types, such as the pure bended case, where obviously no joining technology was necessary between the subsystems (see Fig. 70). This case represented the "perfect" junction and served for comparison purposes. In addition, mixed junctions, such as the combined gluing and bolting, were also examined, since this binding technique is typical for the vehicle industry. Tab. 3 contains all the test cases in detail.

Table 3: The measured structures and their descriptions.

Number of the case	Name - Type of the junction	Connection angle of the plates	Description of the structure
1	Bended	90°	No junction, only one plate bended
2	Line welded	90°	Tungsten Inert Gas welding along the line, with 20 mm overlap
3	Point welded	90°	Manual point welding machine, ~5 mm points, 90 mm spacing, in all 5 connection points, 20 mm overlap
4	Point welded	90°	Manual point welding machine, ~5 mm points, 50 mm spacing, in all 10 connection points, 20 mm overlap
5	Bolted	90°	M5 bolts, 90 mm spacing, in all 5 connection points, 30 mm overlap
6	Bolted	90°	M5 bolts, 50 mm spacing, in all 10 connection points, 30 mm overlap
7	Riveted	90°	Rivets d=4.8 mm, 90 mm spacing, in all 5 connection points, 30 mm overlap
8	Superglued	90°	Superglue (Loctite 454), 30 mm overlap, pressure and drying: 4 hrs
9	Realistic - Glued	90°	Vehicle industry like glue (Loctite 3450), 30 mm overlap, pressure and drying: 12 hrs
10	Superglued	90°	Superglue (Loctite 454), 30 mm overlap, pressure and drying: 4 hrs, thickness of Plate 2: 1.5 mm
11	Superglued	90°	Superglue (Loctite 454), 30 mm overlap, pressure and drying: 4 hrs, thickness of Plate 2: 2.5 mm
12	Riveted +superglued	90°	Rivets d=4.8 mm, 90 mm spacing and Loctite 454, pressure: the rivets, 30 mm overlap
13	Bolted + superglued	90°	M5 bolts, 50 mm spacing and Loctite 454, pressure: the bolts, 30 mm overlap
14	Point welded	60°	Manual point welding machine, ~5 mm points, 90 mm spacing, in all 5 connection points, 20 mm overlap
15	Point welded	60°	Manual point welding machine, ~5 mm points, 50 mm spacing, in all 10 connection points, 20 mm overlap
16	Bolted	60°	M5 bolts, 90 mm spacing, in all 5 connection points, 30 mm overlap
17	Bolted	60°	M5 bolts, 50 mm spacing, in all 10 connection points, 30 mm overlap
18	Riveted	60°	Rivets d=4.8 mm, 90 mm spacing, in all 5 connection points, 30 mm overlap
19	Superglued	60°	Superglue (Loctite 454), 30 mm overlap, pressure and drying: 4 hrs

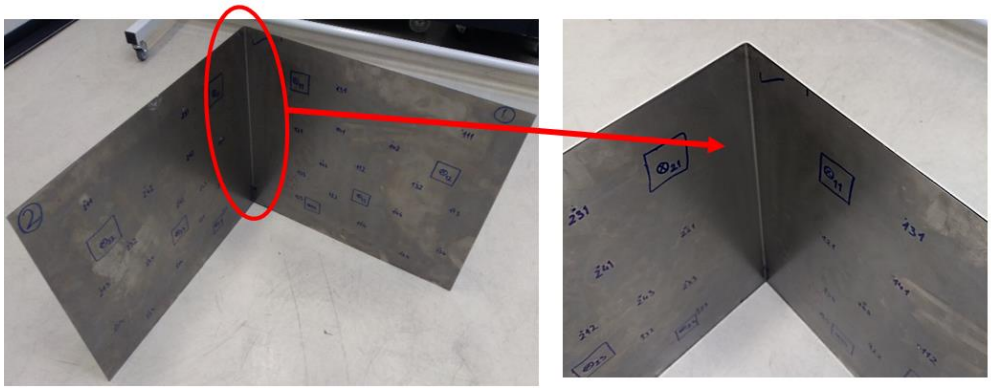

Figure 70: Bended structure, it contains no junction. It represents the perfect connection.

Not only the different junction types were measured, but also that how the angle of the connected plates affect the CLF values. Also, the point-like junctions were examined in two different patterns, as shown in Fig.71. For this reason, 90° and 60° connection angles were considered too.

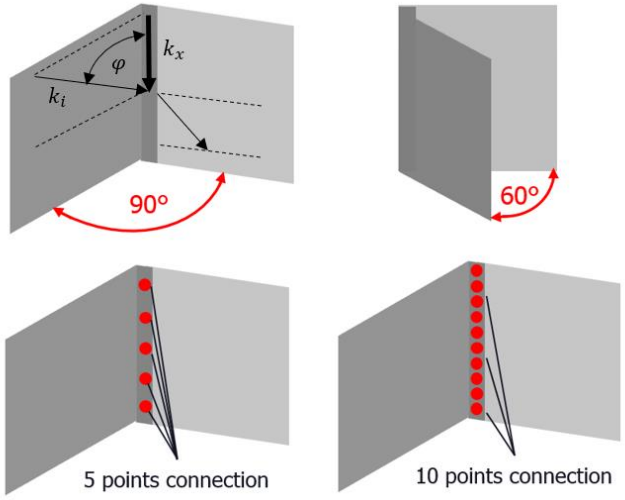

Figure 71: Two types of connection angles and point densities.

7.3.4. Coupling loss factors of different junction types

The results of the SEA simulations for complex structures depend on the CLFs. In simple cases, they can be analytically calculated. However, in more complex cases or when the connection contains different junction types, such as riveted, glued, or welded joints, the analytical determination might not be possible. Therefore, experiments are needed to obtain them accurately. In this section, the coupling loss factors of the different junction types are compared to each other.

Firstly, the modal parameters of the structures are introduced. It is important to note that these test cases do not necessarily constitute a proper SEA subsystem below the 250 Hz third octave band, since the modal density in this band is lower than the minimum 3 assumed by SEA.

Firstly, Fig. 72 shows the number of modes in each 1/3 octave band for the bended structure (Test Case 1 in Tab. 3).

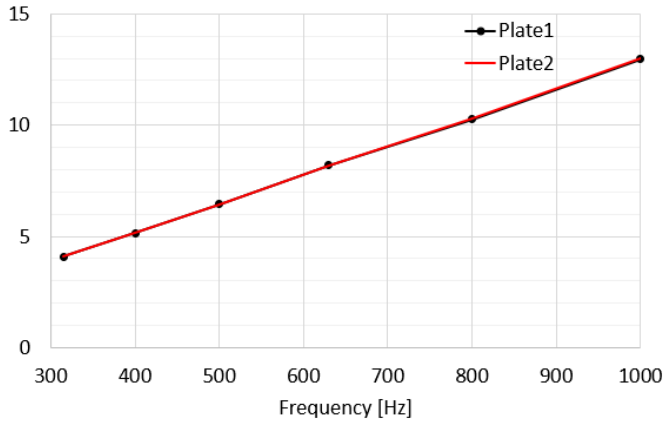

Figure 72: Modes in Band curve of the Bended structure.

As can be seen, for the 400 Hz third octave band, there are around 5.25 modes. Note that SEA normally assumes at least 3 modes per third octave band [7].

Next, the reciprocity relationship is examined, as illustrated in Fig. 73. This represents the coupling loss factor values from Plate 1 to Plate 2 and vice versa. The coupling must be conservative between the subsystems [8],[82]. Note that the modal densities of the two subsystems are very similar, because of the close similarity in the size and shape of the subsystems. For this reason, only the η_{12}, η_{21} will be illustrated, according to Eq. (28). Fig. 73 represents these values for the Bended and Riveted (90°,5 pts) cases. The results show that for the structures the reciprocity assumption of the statistical energy analysis is fulfilled, because η_{12} and η_{21} are closely the same.

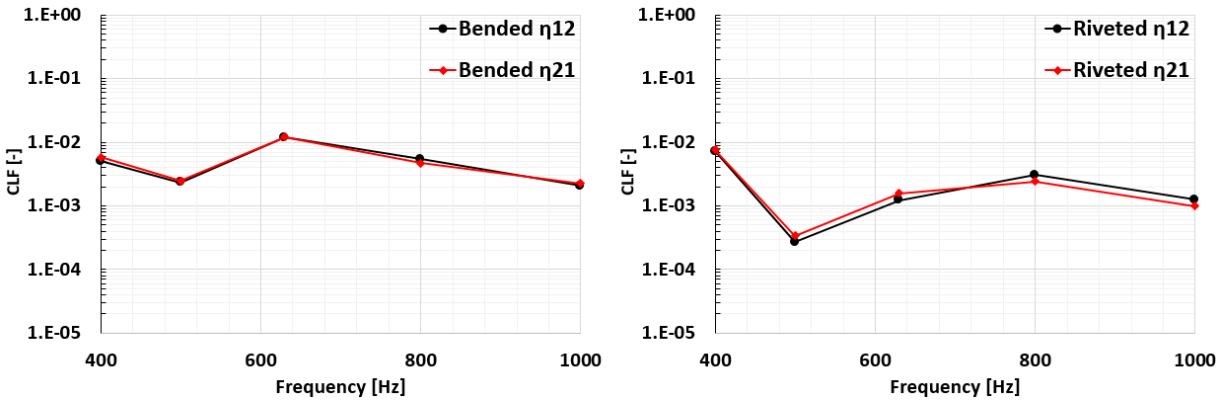

Figure 73: Reciprocity of the Bended and Riveted structures (Number 1 and 7 case according to Tab. 3).

In the experiments, four load cases were applied, so both plates were excited 4 times in different locations. Fig. 74 shows the average CLF values of the 4 measurements, and its minimum and

maximum values. As can be seen, the range between the maximum and minimum values is decreased with increasing frequency. In the frequency range between 400 – 600 Hz, there is more than two orders of magnitude difference between the maximum and minimum values, while around 1 kHz, this difference is less than one order of magnitude. This further emphasizes the well-known fact that SEA is better suited for high-frequency applications, since according to Yap and Woodhouse [94], at low modal overlap the CLFs are sensitive to small damping changes. This might be especially true for the lightly damped structure, where the CLF values have high variance about the mean value. With the increase of the frequency, the uncertainty of the measured values is decreasing, so during the simulations these parameters could be used with higher reliability at higher frequencies.

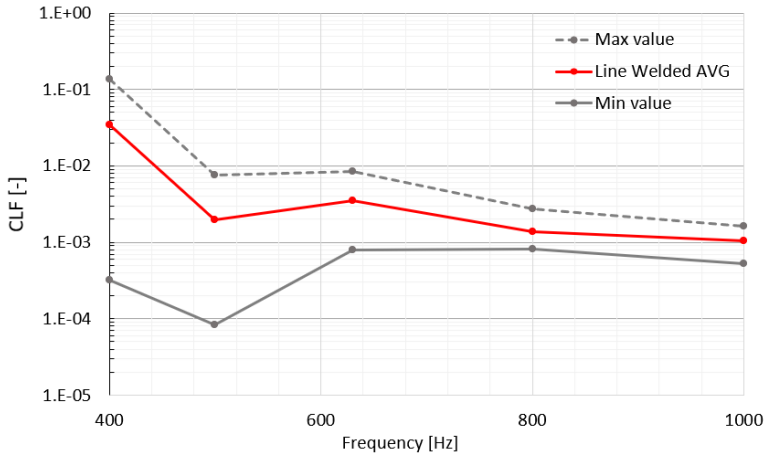

Figure 74: The CLF average of four measurements of the Line welded joint and its minimum and maximum results in the frequency range. With increasing frequency, the deviation from the average value decreases.

Fig. 75 shows the CLFs for different connection types for the right-angle configurations. For a better overview, only a few selected binding types are visible. As can be observed, the Bended case (Test Case 1 according to Tab. 3) has the highest CLFs in this frequency range, with only the superglued structure exceeding this between the 400 -500 Hz range. These two junction types have the highest CLFs from all junction types. Overall, the Point Welded 5 pts structure has the highest energy loss at the connection, about one order of magnitude less compared to the Bended case. Below the 630 Hz band the Line Welded structure has lower coupling values than the Superglued structure. These results agree with the results of Panuszka [72]. Next, the riveted structure has the highest CLF value, followed by the screwed and point welded ones, while the spot welded had the lowest CLF value. In this case the values are closer to each other and overlapped in some bands but in general the same phenomenon can be seen. However, one can observe that in some cases the binding type curves overlap and makes it difficult to

distinguish them. Mandale [68] made the same observation, for him the different connection type results had very close CLF values, in some bands overlapped. The results in Fig. 75 show the importance of taking into consideration the individual connections in much more detail, than just by assuming them to be point or line types, as often is in SEA software. Furthermore, these results can help to make a decision about the most effective design of structures, namely that which joint type is the most suitable in a particular vibrational condition.

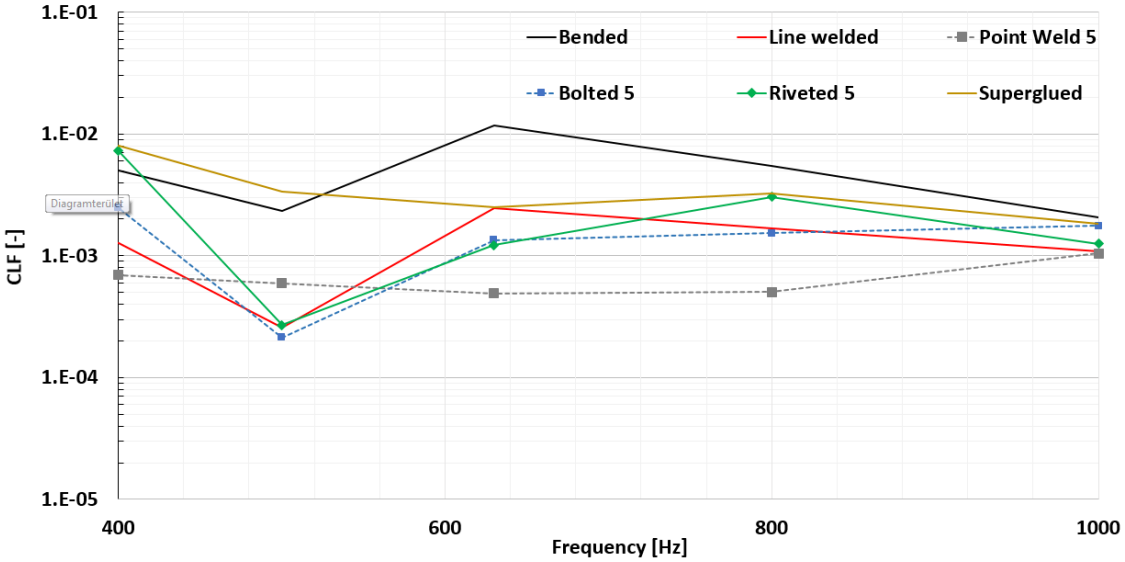

Figure 75: CLF values of the right-angle structures. The different junction types have different coupling values and as can be seen most of the bonding types overlapped.

Fig. 76 shows the influence of the number of connection points on the values of CLFs. Two different layouts were investigated: point welded and bolted structure. Two different connection points were examined: 5 points and 10 points spotwelding along the connection line, with 90 mm and 50 mm spacing, respectively. The difference between them is small: in the point welded case the CLFs of the 10 points connection is clearly higher for most of the bands, while in the bolted case the difference is negligible. Higher differences occur only at the 400 Hz and 500 Hz bands, where the reliability of the measured CLF values is lower.

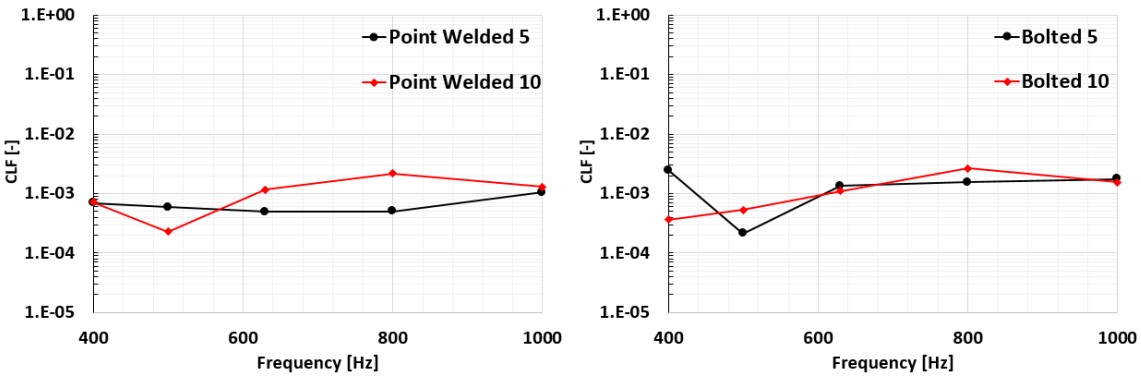

Figure 76: The influence of the density of the points along the junction to the CLF value.

Fig. 77 depicts the change of the CLFs in terms of angle of the connected plates. In this case the difference is more apparent and as it is shown, only in one frequency band is the CLF value higher than for the right-angle, (the Superglued structure), than for the 60 degrees case. Consequently, with smaller connection angle, the coupling value is increased. It means, that with sharper connection angle the energy loss is smaller.

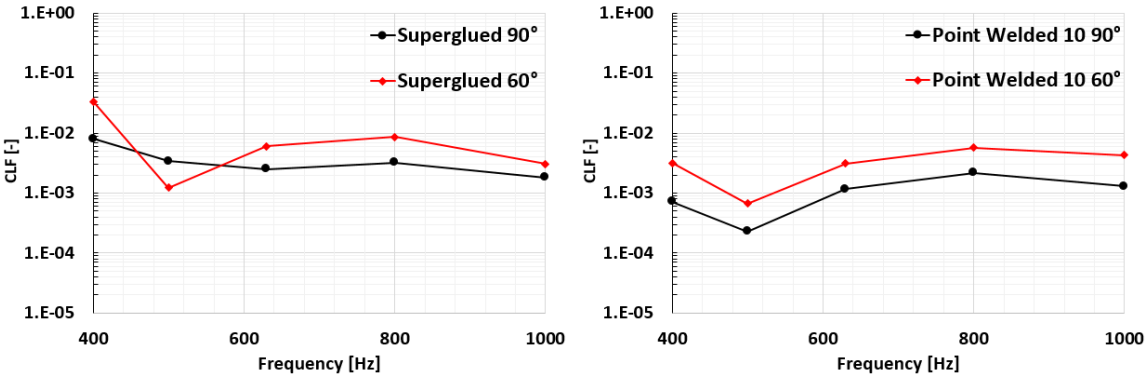

Figure 77: The influence of the connection angle to the CLF value, two angles are measured: 90° and 60°. Left side: superglued (Loctite 454), right side: point welded structure.

Fig. 78 illustrates the combined joints, such as riveting and supergluing, as well as bolting and supergluing, with 5 and 10 connection points, respectively. Combined structures were not investigated in the literature earlier, so these are quite unique results. It is interesting to observe that the combined CLF values are not the linear sum of the individually values. Also, they do not match in the whole frequency range with the connections producing the highest CLF value (i.e. the Superglued). Instead, the combined junction CLFs are rather a mixture of the two individual junction CLFs in both cases.

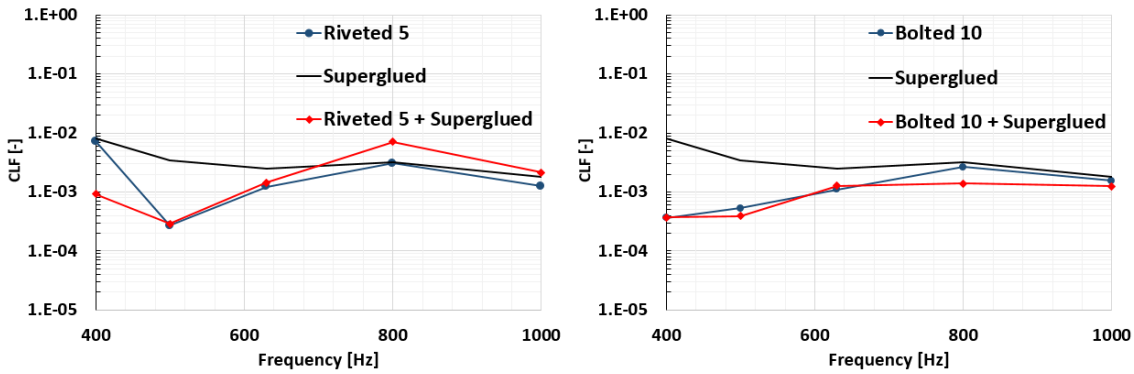

Figure 78: CLF values of the combined joints and the individual joints. Both cases a right-angle configuration. Left side: riveted joints with 90 mm spacing combined with Loctite 454, right side: bolted joint with 50 mm spacing combined with Loctite 454.

For Superglued connection case, the structure is measured with three different thicknesses of Plate 2. This meant that not only a 2 mm thick plate was connected to Plate 1, but also a 1.5 mm and 2.5 mm one. In this way, the effect of the thickness ratio of the connected plates can be examined. As Fig. 79 illustrates, the thickness ratio can cause notable differences in the CLFs, especially at the frequency range between 400-1000 Hz. As can be clearly seen, the case when the thickness of Plate 2 equals with Plate 1, the CLF has the highest value, while in other cases the CLF values are lower. These results are also unique, since none of the literature presented earlier analyzed a comparison for the different connection plate thicknesses.

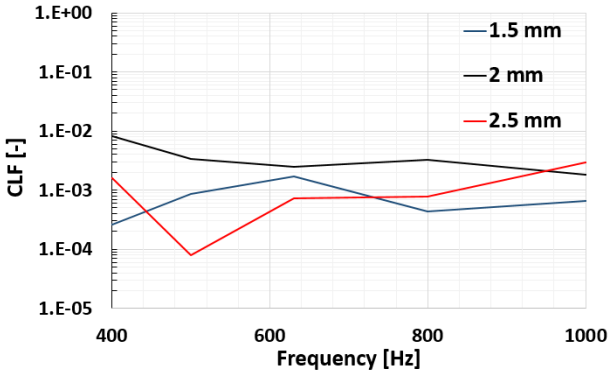

Figure 79: Influence the thickness ratio of the connected plates to the CLF.

7.3.5. Effect of the adhesive type on the CLF value

As Tab. 3. Shows not only the type of the junction was changed, but also the type of the adhesive. Two different glues were examined, a) the Loctite 454, which is a superglue with 20.9 N/mm^2 shear strength [95]; and b) the Loctite 3450, which is similar to the ones used in car structures with 25 N/mm^2 shear strength [96].

In vehicle production technology, bonding (or often called gluing) techniques gain increasing importance, since it can replace or complement some of the welding and riveting. One of the main advantages of bonding is, that structural adhesives can be applied between different materials, for example a composite and a metal part. With the application of the structural adhesives, the number of welding points can be reduced by 10-20%, which also reduces the weight and cost but increases the structural stiffness. Also, it can be used, where smooth and even surface is required from appearance or streamlining point of view. In addition, gluing can be used where the welding robot is not able to reach an area. Fig. 80 illustrates the extent of the structural adhesives used in a vehicle nowadays [97].

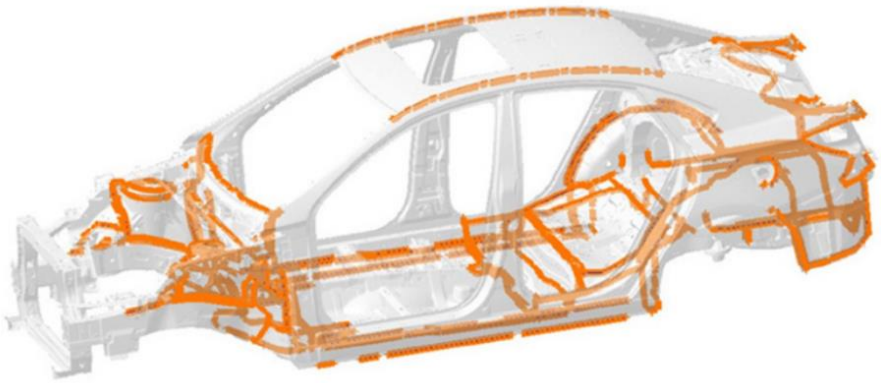

Figure 80: Structural adhesives in a vehicle chassis [97].

The last comparison is shown in Fig. 81, where the two different adhesive types are compared. Superglue (Loctite 454) forms a very thin layer between the plates and creates a massive connection, while the Loctite 3450 is similar to the glues used in the vehicle industry, by creating a thicker layer between the plates and also a massive connection. As the results show, the Loctite 454 has lower energy loss at the junction, while the Loctite 3450 has higher loss, as a reason for the higher thickness as well as the higher flexibility of the glue. The Loctite 3450 is a better choice if the vibrational energy reducing is the main aspect in a connected plate structure.

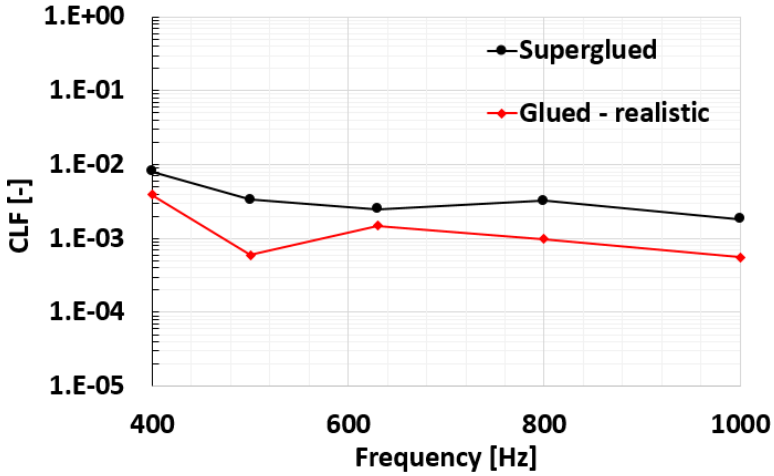

Figure 81: Comparison of the CLFs of the two different glues.

7.3.6. Effect of the modeling techniques to the analytical CLFs

The main advantage of using SEA simulations would be to apply them in the early stages of vehicle development, i.e. before prototyping takes place. However, SEA simulation results depend on several parameters, such as the DLF or CLF values. These parameters in experimental SEA come from the real structural measurements. This problem is contradictory, since in the early stage of the development neither a real structure nor a prototype is available

to determine the required parameters. Therefore, in this section the validity of analytical CLF's will be investigated in the ESI VA One software. Three steps are applied to investigate the analytical coupling loss factors in the simulations and to reduce the role of the measurements, which are summarized in Table 4. The three steps differ in the way how the DLF values are determined, while extracting the CLF values from the analytical formulas in the VA One software. Note that in the 2nd option, the DLF values come from a previous study of the authors [98], where a pure flat plate of the same size as Plate 1 and 2 is measured in uncoupled form.

Table 4: Different investigation steps to examine the analytical coupling loss factors in VA One and reduce the role of the measurement.

Number of the step	Damping loss factor	Coupling loss factor
1	From PIM measurement	From analytical formula in VA One
2	From uncoupled flat plate	From analytical formula in VA One
3	Set as a constant value	From analytical formula in VA One

All the simulations assumed the same conditions, i.e. the geometry and material of the subsystems are setup just as for the real structure. The DLFs and CLFs are calculated from power injection method, and the excitation force was 1 N. The comparison of the results was in the frequency range of 400-1600 Hz. The goal of this investigation was to examine how to change the simulation results, if the DLF or CLF values come from different sources, as well as to examine, how accurate the result can be without any prior measurement?

In the following, the experimental CLFs are compared to the analytically calculated ones, with the latter ones obtained from a simulation software. The line type junctions are obvious in the simulation software, but the point-like connections could take into account other joint types as well, e.g. line, point, or short line types, as Fig. 82 represents.

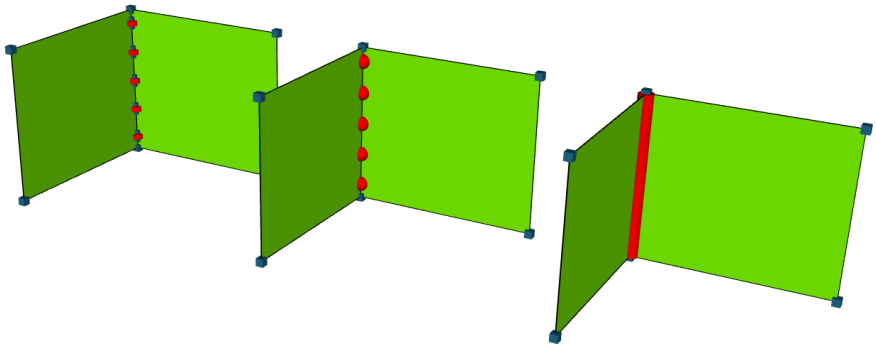

Figure 82: Three different modeling ways of the joints. Left: short line junction, 5 mm length, 90 mm spacing. Middle: point junction, 90 mm spacing. Right: line junction.

In the simulation software, the analytical coupling loss factors were adjusted and then the different types were compared to the measured values. Fig. 83 illustrates the comparison of the binding variances in terms of the modeling.

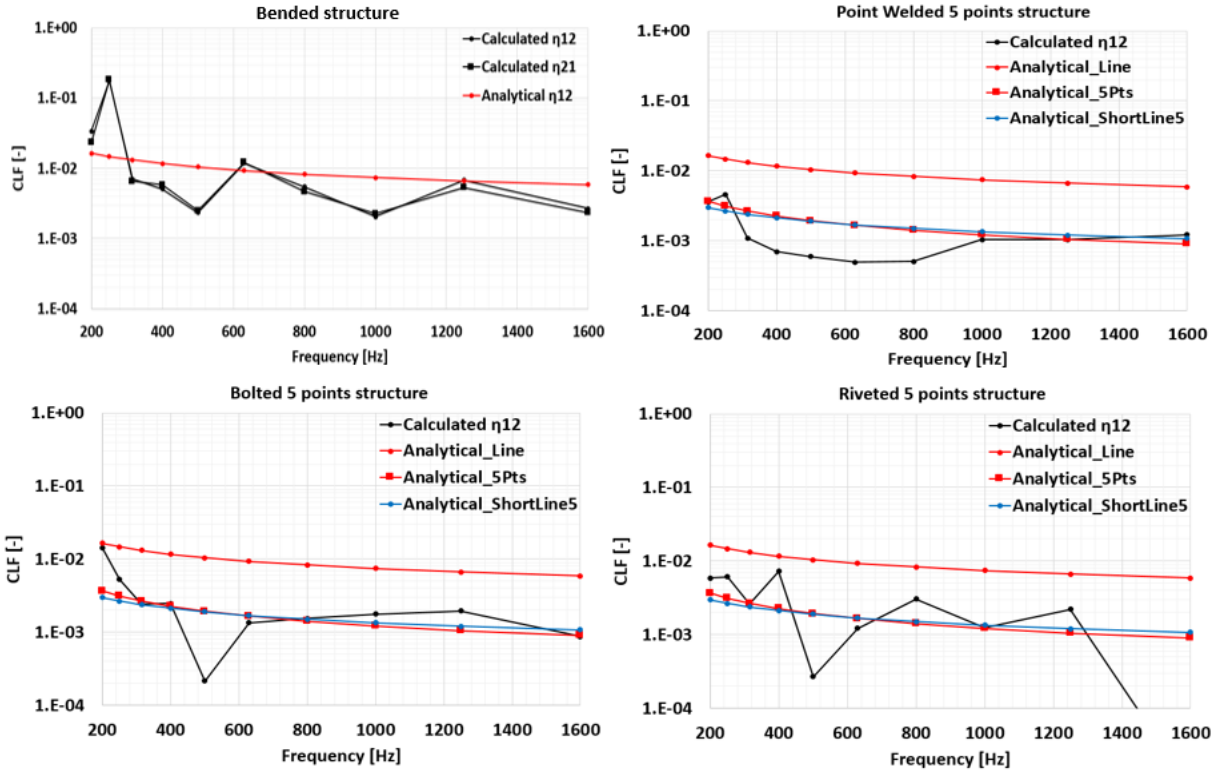

Figure 83: Comparison of the analytical and experimental coupling loss factor values regarding the different binding techniques such as bended (top, left), point welded (top, right), bolted (bottom, left), riveted (bottom, right).

As can be seen in Figure 7, in the bended case the analytical line junction gave good agreement with the experimental results, while for the other structures these type of modeling is not acceptable. The short line and point like junction modeling basically produced the same results, although the point junction is an easier modeling method, so it is a better choice. The analytical point junctions had a good coincidence with the point-like bindings, the only exception is the riveted structure at the 1600 Hz frequency band, where there was some measurement uncertainty.

7.3.7. Simulation results

At the *Bended* structure, where the plate is only bended and the connection is de facto perfect between the two subsystems, the analytical coupling loss factors worked well, in fact gave better results in some bands than the CLFs calculated from the PIM (see Fig. 84).

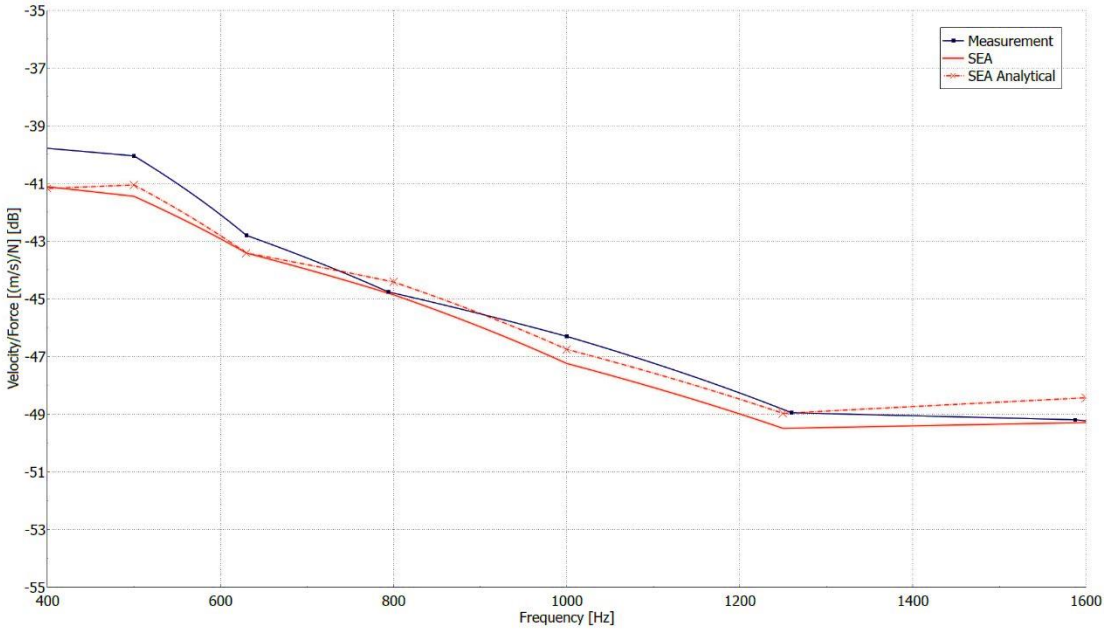

Figure 84: Comparison of the Bended structure measurement and simulations results (Number 1 case according to Tab. 4). The Plate 1 is excited, the response is examined at Plate 2. The solid, black curve is the experiment, the solid, red curve is the SEA result with the measured CLFs and DLFs values. The dashed, red curve with the crosses is the SEA result with the measured DLFs and the analytical CLFs, which is calculated by the simulation software.

The *Point Welded (5 pts, 90°)* results are very similar. In this case, the junction is not perfect, there are only 5 connection points along the line. As the diagram in Fig. 85 shows, the analytical point CLFs match the experimental results very well. Moreover, at lower frequencies the results compare better to the measured values.

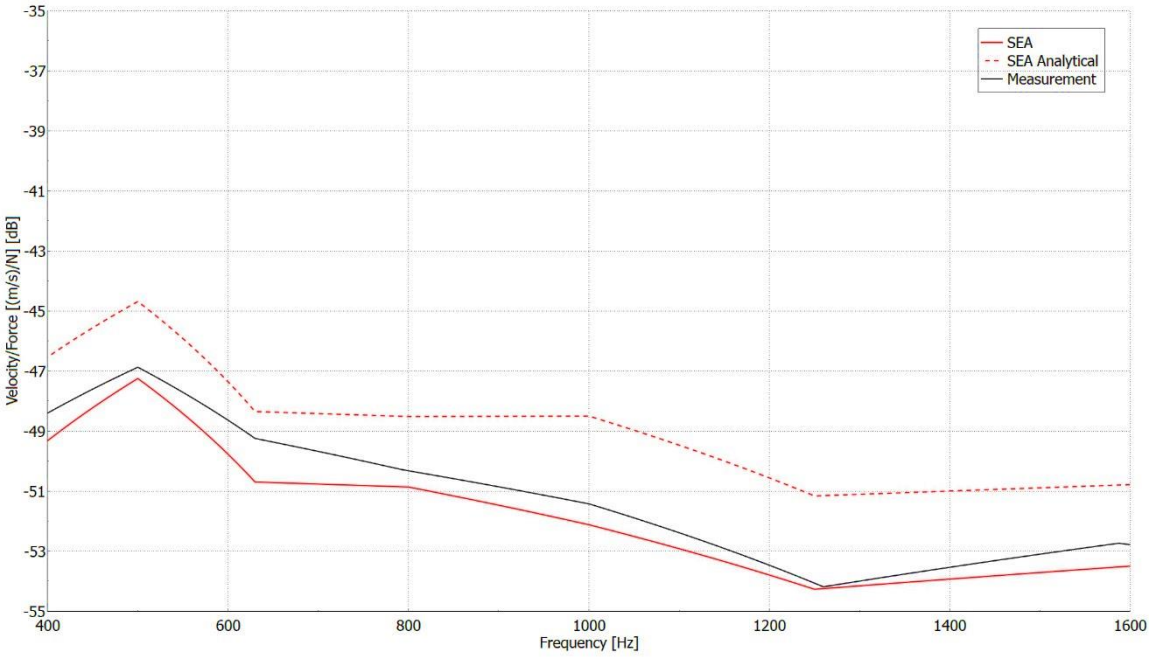

Figure 85: Comparison of the Point welded structure measurement and simulations results (Number 3 case according to Tab. 4). The Plate 1 is excited, the response is examined at Plate 2. The solid, black curve is the experiment. The solid, red line is the SEA result with the measured CLFs and DLFs values. The dashed, red line with the crosses is the SEA result with the measured DLFs and the CLFs are adjusted as analytical point junction in the simulation software with 5 points along the connection line (see Fig. 82 right).

Secondly, the Step 2 is introduced where a previous study by the authors [98] are used. In that work the damping of an uncoupled flat plate is examined. During the simulations, these uncoupled plate DLFs are set to Plates 1 and 2, while the coupling data come from an analytical formula available in VA One. This example represents a case, when data for an isolated subsystem are available for all important measurement parameters, such as mass, damping, etc. and then another equivalent subsystem is connected to it. As the results show in Fig. 86, the maximum deviation compared to the *Bended* structure measurement results is up to 3 dB, which although is not a perfect agreement, but in this situation, it could be an acceptable deviation, since the simulation parameters came from an equivalent uncoupled subsystem result. This simulation is compared to the *Point Welded (5 pts, 90°)* structure measurement results, and the maximum deviation is observed to be around 9.5 dB at 500 Hz. That, however, is a significant deviation between the simulation and measurement and is caused by changing the connection type from an idealized line welding to a non-ideal point welding. This suggests, that for real connections, such as riveted, spot welded, etc. the approach of using measured damping of an equivalent, uncoupled subsystem might not be the right approach to achieve good simulation

results. The analytical couplings are changed with the connection type, so in this case the only possibility to reach good accuracy with the simulations is to change the damping value as well with the different connection types.

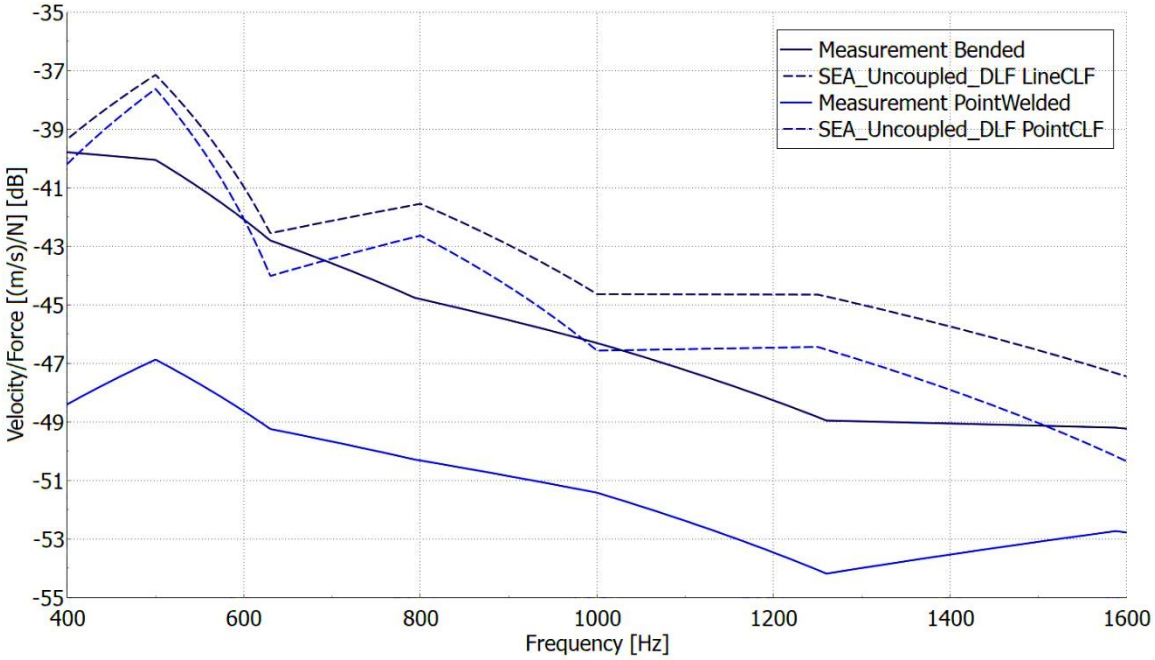

Figure 86: Comparison of the experiment and simulation results. Plate 1 is excited, and Plate 2 examined is measured. The solid, black curve is the Bended structure measurement result (Number 1 case according to Tab. 4), the blue, solid curve is the Point welded structure experiment results (Number 3 case according to Tab. 4). Black, dashed curve with the crosses is the simulation results with the measured, uncoupled flat plate damping and analytical line coupling was calculated by the simulation software. The blue, dotted curve with the boxes is the simulation results with analytical line coupling was adjusted in the software and the damping was measured at uncoupled form.

In SEA simulations, the results are highly influenced by the DLFs, as it is shown in Ref. 94. In complex structures, they also play an important role, since although the analytical coupling values could work well, but they are independent of the damping values and therefore cannot take into consideration the different joint types, such as bolting, riveting or spot welding.

The last level of this study, Step 3, involved the strategy of applying the coupling values from analytical formulas, while the damping values are set to constant values, despite the damping of real structures not being constant over a certain frequency range. Thus, the damping was set to 0.1 % for the *Bended* structure, which is a commonly used value for such steel plates. As the comparison in Fig. 87 shows, the DLF values were again not perfect, but even so the maximum

deviation between the experiments and simulations were only around 3 dB at 1250 Hz band without any measurements.

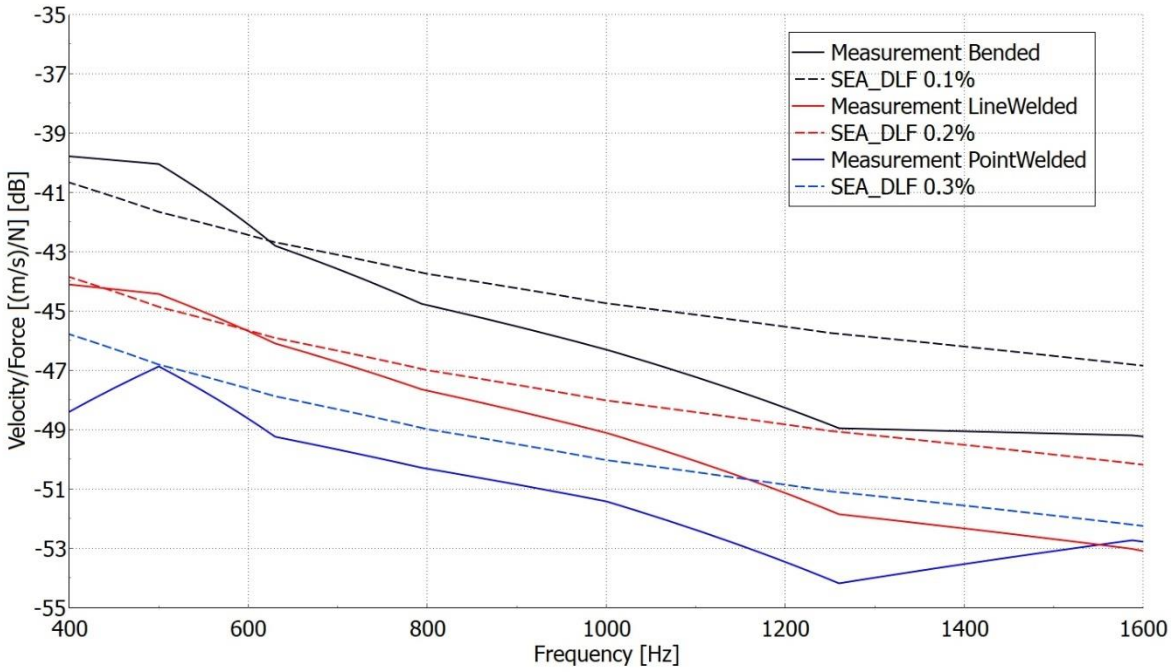

Figure 87: Comparison of the different structures measurement and simulation results (Number 1, 2, 3 cases according to Tab. 4). All case the Plate 1 is excited and the response is examined at Plate 2. The solid lines are the experiment results. The dashed lines are the SEA results with constant DLFs and analytical line CLFs are adjusted in the simulation software.

As Fig. 86 and Fig. 87 show, the analytical couplings varied slightly as a function of the different connections, e. g. point welding, line welding, no junction, but the extent of this is not enough to achieve the experimental results. Consequently, the damping must be changed to the different structures in order to estimate the experiments, and this phenomenon will be introduced in detail in Section 7.4.

7.3.8. Conclusions

In SEA simulations, the most important parameters are the DLFs and CLFs and they can be determined from experiment through the Power Injection Method. In this Section, different types of junctions and connection angles were investigated, in order to obtain the CLF values as well as to compare them to each other. As the results showed, in the mid-frequency range these values are varying due to the fact that the various joints are overlapped, and they did not separate from each other clearly. The *Bended* and *Superglued* structures had the highest coupling values while the *Point Welded* the lowest ones.

The simulation results agreed well with the experiment, when the DLFs and CLFs parameters came from the PIM. The study partly focused on decreasing the role of the experiments in the simulation parameters determination. For this reason, the DLFs remained the measured values, while in the simulation software the analytical couplings are adjusted. This proved to be a good option in the case when no measurement data for the CLFs is available. At junctions, such as *Bended, Glued, Combined* or *Line welded* structures, then the analytical line junction is the good setting. When the plates are connected along points, such as *Riveted, Bolted* or *Spot welded* then the analytical point coupling is the right setting. These analytical formulas in some cases could give a better result as the measured values.

In the case, when the damping is measured for an uncoupled subsystem, such as the pure flat plate, and analytical coupling is adjusted at the junctions, the results did not fit well with the experiments, especially when any real connection occurs between the plates. The results are satisfying only at the *Bended* structure.

It is difficult to determine the parameters, such as the DLF or CLF values without any measurements. In some cases, the constant damping and analytical coupling values could be a good solution, when the measurement is not possible. For a flat, steel plate, the 0.1 % damping loss factor is reasonable, and combined with the analytical coupling loss factor in VA One at the junction has led to quite good results if there is no physical joint between the subsystems, for instance in the *Bended* case. The situation was different when the structure contained some real junction, because the response highly depended on the damping value of the plates and this in turn depended on the type of the junction. As the outcomes showed most of the bond types can be describe well with the analytical couplings, but the damping of the plates could be also determined somehow without measurements. The main issue is how one can describe the damping level variation as a function of the different connection types. Of course, in this study the damping values were available, but when they were not, for instance at the early stages of the development, when no prototype or real structure is available, the measurement of the damping values is not an option. In this occurrence, the function of the damping changing in terms of the bonding type could be crucial.

The study introduced the importance of the damping and coupling loss factors. The main conclusion of the investigation is the following:

- In the investigated frequency range (400 – 1000 Hz) the CLF values are varying, moreover at lower frequencies the deviation between minimum and maximum values can reach more than 2 order of magnitude.

- The Bended and Superglued structures had the highest coupling values while the Point Welded the lowest ones.
- The results showed that the CLF values increased proportionally with the number of connection points
- While the CLF values decreased with the higher connection angle.
- In the combined joint cases, the CLFs could not be clearly defined: it was a mixture of the properties of the two base joints and they were in the same order of magnitude as the base joints were.
- The results of the two different glue types is obvious: the Loctite 3450 had lower coupling loss in all frequency bands, which means the energy loss higher on it.
- The second part of the paper deals with the statistical energy analysis simulations and measurement comparison. In addition, it examined the opportunity of the reducing the role of the measurement so the measured parameters were compared to the analytical results. The conclusions and interesting observations this part of the study was the following:
- The simulation results agreed well with the experiment, when the DLFs and CLFs parameters came from the measurement.
- In the case, when the DLF was measured and the CLF was adjusted as analytical: the simulation results showed good agreement with the experimental results, so it could be a good option in the case when no measurement data for the CLFs is available.
- In the case, when the damping was measured for an uncoupled subsystem, such as the pure flat plate, and the CLF was adjusted as analytical, the results did not fit well with the experiments, especially when any binding occurs between the plates.

7.3.9. Thesis No. 2

Different bindings yield different CLF values, that can significantly influence the simulation results. In addition, in the numerical method only a few types of junctions exist and for this reason the reliability of the analytical formulas for CLFs is a key factor from accuracy point of view for complex cases.

In relation to this, I proved that [F]:

- The connection angle has an impact on the CLF values and this might require modification to the analytical CLF formulas to include this effect.
- The type of the adhesive has an impact on the CLF values.

- At combined junctions, such as simultaneous riveting and gluing, the CLF is not a summation of the individual binding CLFs, but rather a combination of them, namely: $CLF_{rivet} + CLF_{glue} \neq CLF_{rivet+glue}$
- Analytical equations can be used with high precision for common cases, if the modelling technique is reliable.

7.4. Panel vibration reduction via binding technique design

7.4.1. Motivation

In vehicles, the chassis is exposed to various excitations and the vibrations propagate through the structure. The larger panels radiate vibrational energy into the passenger compartment, such as the firewall, floor, side panels, or roof, as can be seen in Fig. 88. In this case, the panels are essentially working just as a membrane of a loudspeaker. In order to reduce their vibration – and consequently the noise generated by them inside the passenger compartment – several solutions are applied, such as locally placed viscoelastic damping layers on the panels, reinforced plates, bead plates, etc. These designs improve the stiffness of the structure as well as the NVH performance of the car, but the damping layers add extra mass to the vehicle. This is nowadays disadvantageous, since it contradicts the main goal of the vehicle industry: to save as much weight as it is possible. Therefore, this Section of the work poses the question, whether instead of the panel alterations, could the bindings (or joints) at the edges of the panels so altered, so that they lead to the simultaneous reduction of weight as well as the vibrational response of the panels.

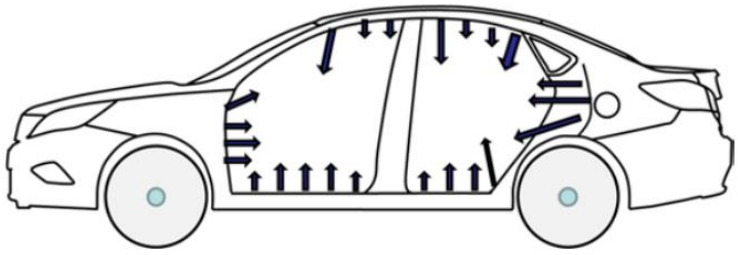

Figure 88: Vibration propagation in the chassis and radiation into the passenger cavity [97].

The sound radiation energy of a panel depends on its vibrational velocity. The various panels have different contribution to the sound radiation into the passenger cavity, but the reduction of a panel vibration is one of the main goals in the vehicle industry. By analyzing the transfer functions between the velocity responses and the input force, methods for controlling the panel vibration can be obtained. In SEA, the relationship between the input and output can be taken

by the loss matrix, which consists of the DLF and CLF values. Both parameters can reduce the vibrational response of a system, for this reason similar plate structures will be examined.

In this section, the different bindings versus damping layers will be compared to each other from panel vibration reduction point of view, as well as from stiffness and mass point of views. Moreover, the contribution of the CLF and DLF to the vibrational responses will be also analyzed in the structures.

7.4.2. Measurement setup

The same test cases were used as in Section 7.3, supplemented with a new additional test case. The following bindings were investigated of the L-shape structures: a) Bended; b) Bended with bitumen layer; c) Line welded; d) Point welded with 5 points; e) Structural adhesive. Recall, that the considered structures consist of two rectangular plates: Plate 1 with size 650 x 550 x 2 mm and Plate 2 with 655 x 550 x 2 mm. They were cut to size via laser. The material properties of the base S355 steel plate were the following: density of 7850 kg/m^3, Young's modulus of 200 GPa and Poisson's ratio of 0.3. In all cases, 16 response points were applied per subsystems, however at once only 4 response points were applied on each plate. An additional accelerometer was placed on the excited plate, because of the driving point measurement at the excitation point. Lightweight ICP piezoelectric accelerometers were used from B&K during the experiments. The plates were excited at four points on each, performed by an impact hammer (PCB Piezotronics) with a hard rubber head. The excitation and response points were at the same locations on every measured structure. Free-free boundary conditions were used during the experiment. The investigation focused on the 400-1000 Hz frequency range and the frequency resolution was 0.07 Hz during the measurements. In Section 7.2.3, Fig. 69 illustrated the overlapping of Plate1 and Plate2, which, as will be seen later, will have quite significant effect on the results later.

Fig. 89 represents the bended structure with the randomly placed bitumen sheets at Plate 2. The weight of the added damping layer was calculated in such manner, so that it is the same for the whole bended construction with the bitumen as well as the point welded structure. The weight difference between the two systems was only 2 grams.

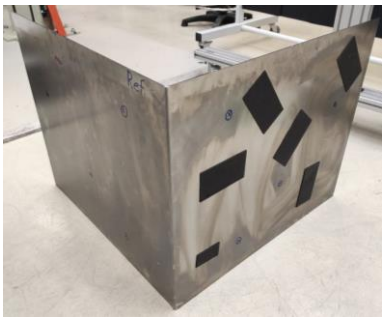

Figure 89: Bended structure with the randomly placed bitumen sheets at Plate 2.

7.4.3. Results

In this case the vibrational responses were examined only in Plate 2 and the excitations were on the Plate 1, as Fig. 90 illustrating the transmitter and receiver plates.

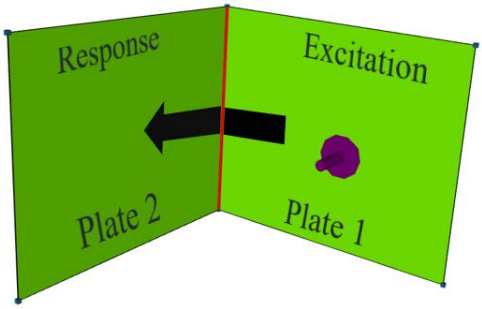

Figure 90: Illustration of the study concept, Plate 1 is the transmitter plate while Plate 2 is the receiver later.

Firstly, the DLFs of the subsystems were investigated. As reference, the results for the bare bended structure were considered, since this was the case with neither binding between the plates nor a damping layer on Plate 2. As Figure 91 shows, the damping layer has a huge impact to the DLF values and not just for the plate where it was applied, but also to the connected plate as well. The damping of Plate 2 for the point welded structure was also increased, while Plate 1 remained nearly similar as the reference bare bended plate. This phenomenon is likely the consequence of the connection type. For the point welded, line welded and structural adhesive cases, Plate 1 is curved to implement the connection of Plate 2, which is flat as can be seen in Fig. 69. As a result of the curvature of Plate 1, the damping is just slightly changed, while the damping of Plate 2 is increased by a factor of about three in the point welded case, compared to the bare bended structure.

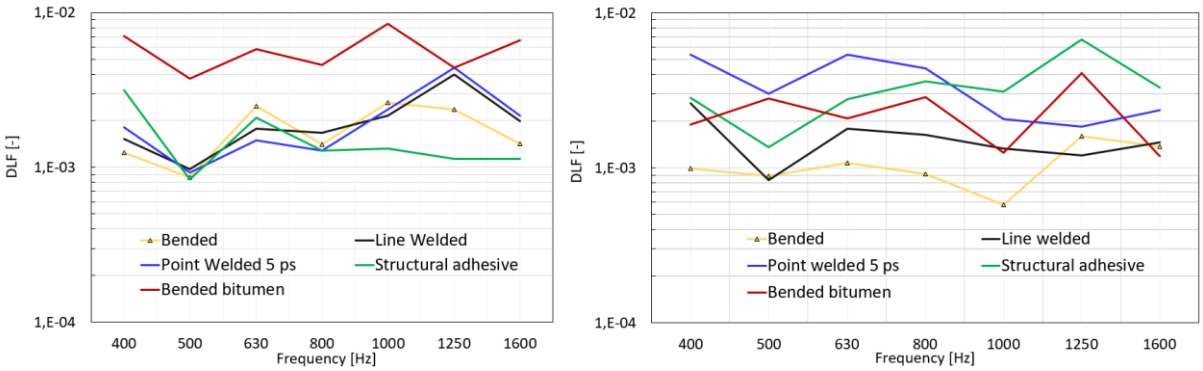

Figure 91: Effect of joint type on the plate's DLFs. Left: DLF of Plate 1, right: DLF of Plate 2.

The higher damping will reduce certainly the vibrational response at the receiver plate, but this information alone is not enough to identify the contribution to vibrational response reduction for the whole system. The other investigated parameter was the CLF between Plate 1 and 2. As Fig. 92 illustrates, the bituminous structure has the highest CLF values compared to the others. However, note the scale of the difference: there is more than one order of magnitude deviation between the point welded and bituminous bended structure.

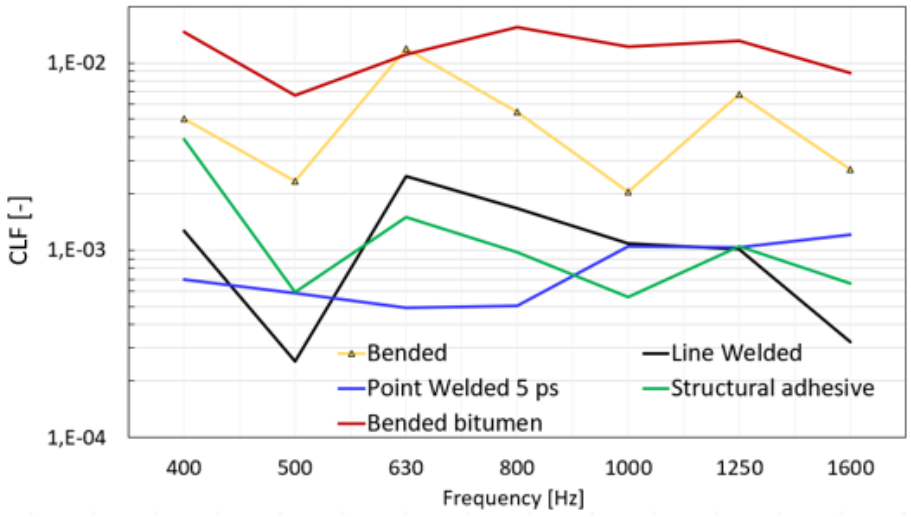

Figure 92: The changing of the CLF between the subsystems in terms of the different structures.

The smaller value of the CLF means that the energy loss is higher at the connection, so in this case the point welded structure lets through the smallest vibrational energy to the receiver plate. As the damping results show, while the bitumen layer reduces the vibrational energy on both subsystems, the coupling of this structure is actually increased, so in overall, the influence of the damping layer was not as high as expected. Structural adhesive was advantageous both from

DLF and CLF point of view, particularly at higher frequencies, since it had the highest DLF value at Plate 2 over 800 Hz and it had low CLF value over 500 Hz. These properties are useful when the goal is to reduce the vibrational response on a certain part. Fig. 93 shows the velocity results on Plate 2, when Plate 1 is the excited subsystem.

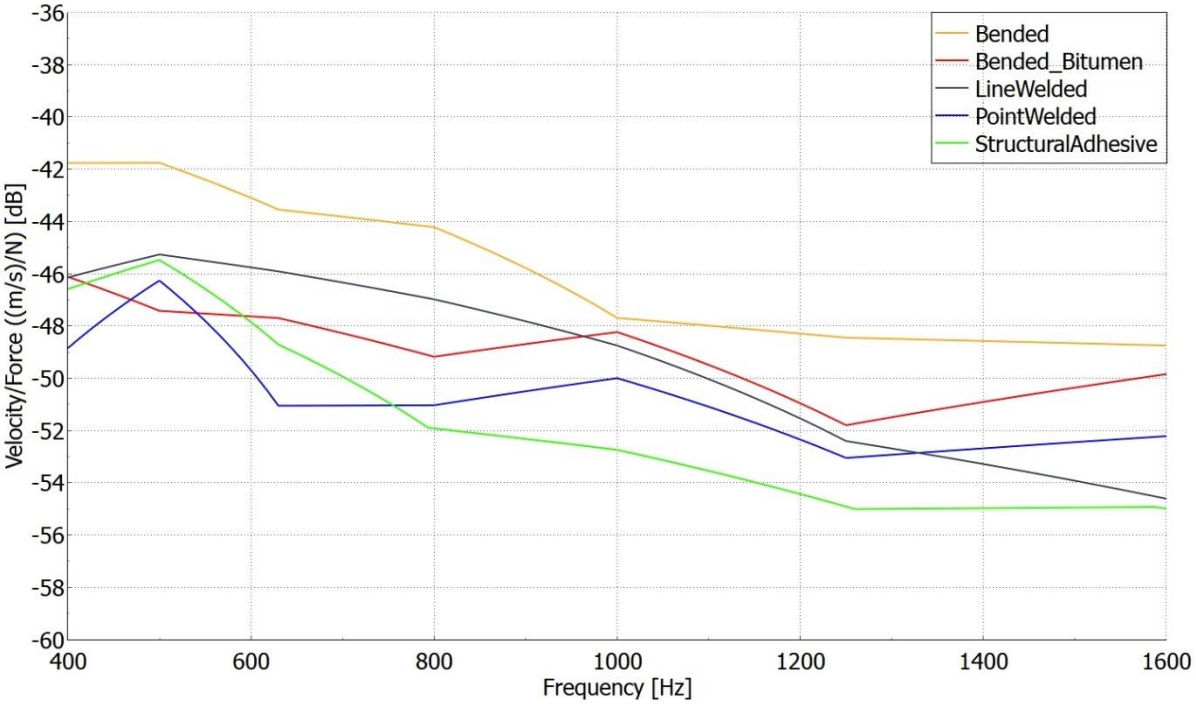

Figure 93: Velocity results of Plate 2 when Plate 1 is excited.

According to these results, a proper junction could be effective in reducing the vibrational response at the receiver plate. This is a consequence of the type of the connection, because in this case, the damping of Plate 2 is increased, and the internal friction in the real junction reduces the coupling values at the junction. Although the damping layer increases the DLFs of the plates, it also increases the CLFs, which is disadvantageous if the goal is to reduce the vibrational response.

The joints have significant influence not just on the energy absorption, but also the stiffness of the structure. For this reason, the subsystem stiffness due the various joining technologies should also be investigated. In vehicles, if the stiffness of the body panels I are strong but the junctions between them are weak, the overall stiffness will be still weak. The body frame stiffness determines the modal shapes and frequencies of the body, hence the first natural frequency gives information about the stiffness of the structure. If the first natural frequency is increasing, the stiffness of the structure is also increasing and it is also true backwards [97], [99]. The first natural frequency of the 5 different structures can be seen in Fig. 94. The results

show that the point welded structure has the lowest stiffness while the bended structure with bitumen layup has the highest.

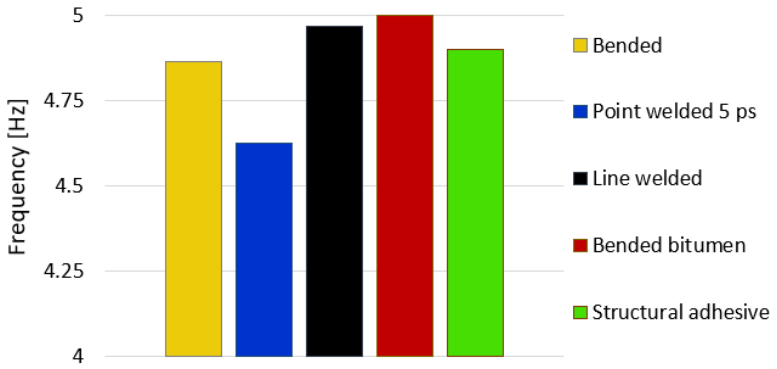

Figure 94: First natural frequency of the structures.

Beside the stiffness properties, the weight of the structure is also crucial in vehicle industry, so for this reason that was investigated as well, Fig. 95 shows it. According to the results the bended structure with bitumen treatment has the highest weight, while the bare bended structure has the lowest.

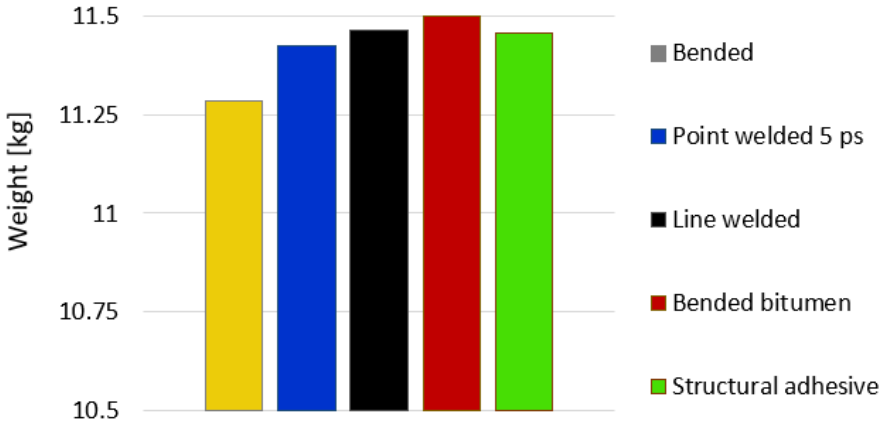

Figure 95: Weight of the different structures.

7.4.4. Conclusions

One of the most challenging tasks in vehicle industry is to reduce the sound pressure level efficiently inside the vehicle. The main contributors of the overall SPL level in the passenger compartment are the vibration propagated by the chassis and radiated by the larger panels. In this Section, the frequency response reduction was investigated as a function of the various binding techniques and bitumen layer. Results showed that the lowest panel vibrations (in terms of panel velocity) were achieved by the adhesive binding, while the highest stiffness and lowest weight belonged to the bended structure with the bitumen layup and the bare bended structure, respectively. All in all, the adhesive or the line welded bindings are the best choice from all considered points of view. Strictly speaking, the adhesive binding had the lowest frequency

response velocity over 800 Hz, so from the response reduction aspect this is the most efficient junction type.

The main conclusion of this Section is that the binding technology can reduce a panel vibration more effectively, than following the traditional logic of adding additional, heavy damping foils on the receiver plate in order to reduce the vibration. In other words, the junctions are a necessity to connect different parts, but with a conscious design, these binding techniques can also be used to improve the NVH performance of the vehicle. For the manufacturers it is worth to invest in the development of such structural adhesives, that increase the stiffness as well as the NVH performance of the vehicle at the same time.

7.4.5. Thesis No. 3

For vehicle NVH characteristics, the main goal is to reduce the vibration of the panels that radiate noise into the passenger compartment. Traditionally, the vibrational energy of the panel is controlled locally on the panel by adding viscoelastic damping material to it, which in turn adds mass to the system.

> I proved that the adhesive binding technique can more effectively reduce the vibrational response of a panel, than a viscoelastic damping layer applied directly on the receiver plate. While this leads to reduced vibration on the plate, the stiffness of the system remains unchanged, as well as the mass of the system could be reduced in comparison to a classical solution of adding viscoelastic damping layer to the plate [E], [B].

7.5. A note on the limitation of Power Injection Method

In this Chapter, virtually all results were obtained by the Power Injection Method, applied for 2 subsystems. In this section, we would like to elaborate on the question, whether this method would be practical to be used for full vehicles. To assess the complexity of the method for a full vehicle, let us consider a simple academic test case with 5 subsystems, an H-shape structure composed of flat plates. This is not very complicated, but it adequately represents the challenges of using experimental PIM. It contains three different steel plates with the sizes: Plate 1 and Plate 3: 1100 × 550 × 2 mm; Plate 2: 650 × 550 × 2 mm, which can be divided into 5 subsystems in the SEA world, as depicted in Fig 96.

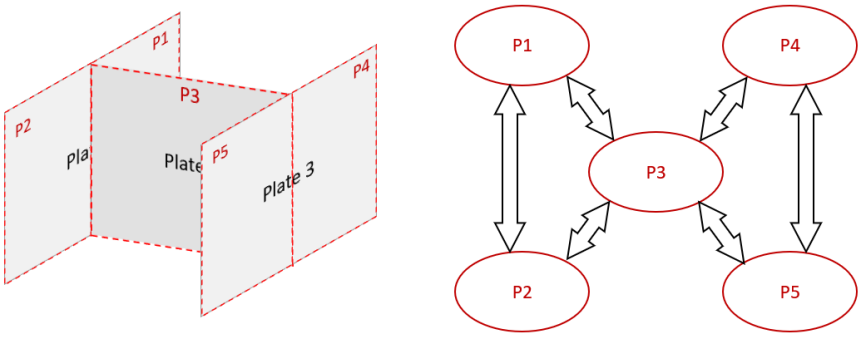

Figure 96: Left: H-shape structure consists of 3 plates and it divided into 5 subsystems (dashed line); right: energy exchange between the subsystems.

Recall that in the Power Injection Method (PIM), one subsystem is excited, and the responses are measured on all other subsystems. Then, the second subsystem is excited, and the same procedure is repeated and so on. In the particular case of the H-structure, this mean that if 4 excitation points/plate, and 10 response points/plate were used on the subsystems – in order to achieve statistically relevant samples of the subsystem – the result would be 1000 FRFs. From these curves shall the input powers and the vibrational energies of the subsystems be calculated. Then, these data would allow to calculate the loss matrices as well. In this case, the loss matrix is a 5×5 matrix in a certain frequency band, which does not require an excessive computational demand. However, for more complex structures, the Power Injection Method could be really time consuming, and the data handling grueling.

Consequently, the assessment of the DLFs and CLFs for a vehicle is not trivial, since the measurements of these parameters can result in thousands of FRFs, which the user should post-process in order to get good and reliable values for the DLFs and CLFs. One alternative option to replace this rather cumbersome experimental procedure would be the usage of Virtual SEA, in which the PIM is executed on a FEM-based simulation. This method is rather new but gains more and more attention nowadays [6].

8. HYBRID FE-SEA STRUCTURES

As it was described in Section 1.4.2, the Hybrid FE-SEA method combines the advantages of two methods in a way that rigid parts are modelled by FE while the larger panels by SEA. In this section, more complex structures will be investigated with the hybrid method, and it will be compared to pure individual models of SEA and FE models. In order to define the simulation models validity, experiments were completed for the new, more complex structures.

8.1. Ladder structure

8.1.1. Motivation

In vehicles, one of the most complex and most expensive part from development point of view is the platform. Usually, one vehicle platform belongs to several vehicle models. From vibrational viewpoint, the frame is responsible for the overall body stiffness of the vehicle and all the other components are connected to it, such as the doors, the engine hood, and the trims. The suspension, as well as the engine mount is connected to the floor and it has a direct contact to the passenger seats (Fig. 97), so its role is really important for the customers.

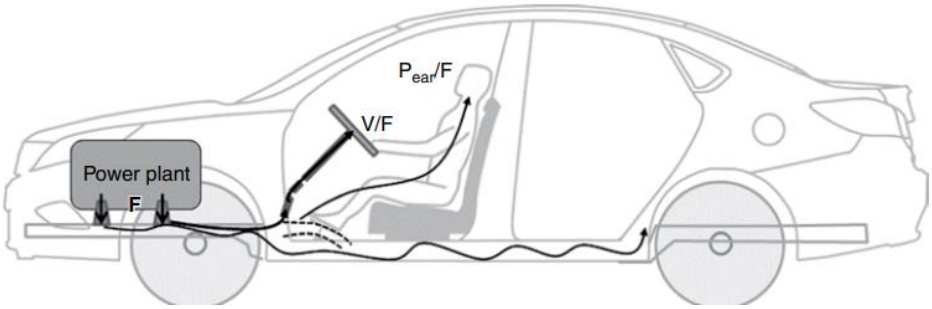

Figure 97: Wave propagation through the platform [97].

There are several principles that have to be considered during the design phase of the body layout, such as: a) the frame structure should be closed loop; b) the number of frames and the distances between them must meet the body stiffness requirements; and c) the frame resonance frequencies should not match the typical external excitation frequencies [97]. The floor structure of a vehicle is illustrated on Fig. 98 and Fig. 99.

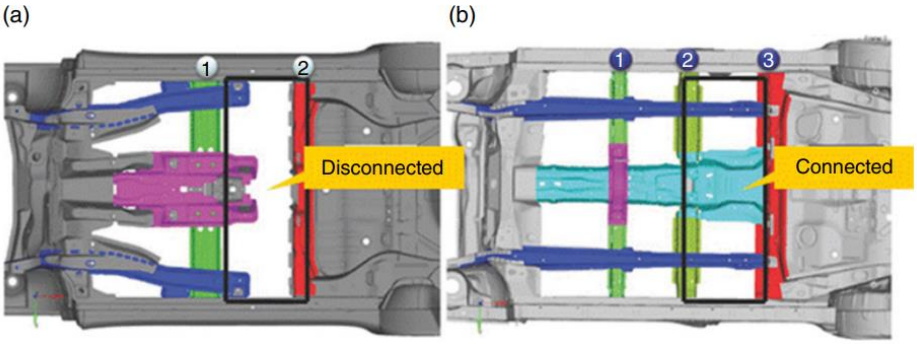

Figure 98: Typical floor structure: a) open loop; b) closed loop [97].

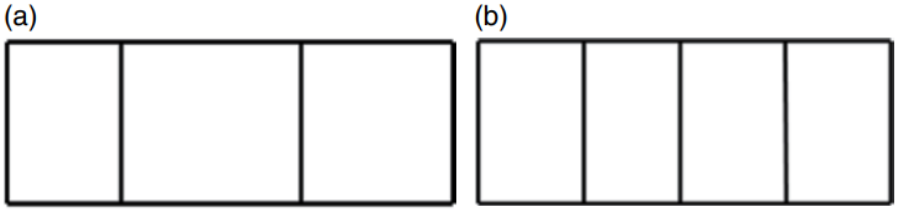

Figure 99: Simplified geometry of the floor structure: a) two cross members, b) three cross members [97].

According to Fig. 98 and Fig. 99, a vehicle floor structure inspired the ladder structure test apparatus, but in a simplified way. The main goal of this test case is to build up such a simulation campaign, in which the combination of a strong frame and of flat plates can be examined, in in increasing complexity. Three different levels were investigated (see Fig. 100): Level A: a pure frame with stiff beams; Level B: a frame with two plates; Level C: a frame with two plates and a foam material on the plates.

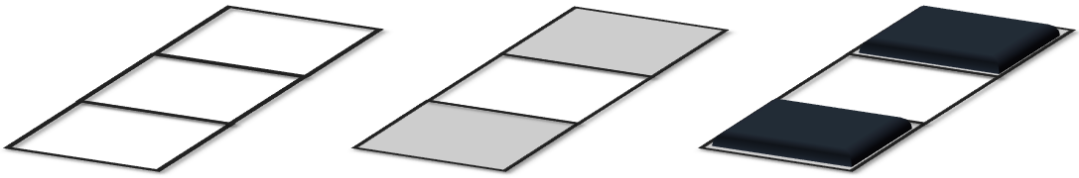

Figure 100: Ladder structure test apparatuses. Left: Level A – stiff frame only; middle: Level B – frame and two plates; right: Level C – frame and two plates covered with foam materials.

8.1.2. Measurement setup

All structures were measured in the same setup and in the same conditions. The first level was the frame structure only without any plates in it. Three response points were measured at each corner and one corner was the driving point, as Fig. 101 shows it. The second case was the frame and two plates in it: there were four accelerometers on the frame and 17 around the plate farther from the excitation, at once only 4 accelerometers were on the plate in order to avoid adding too much mass to the system. The third test case was measured exactly the same way as

second case was, but the foams were laid on the plates and the accelerometers were placed on the lower surface.

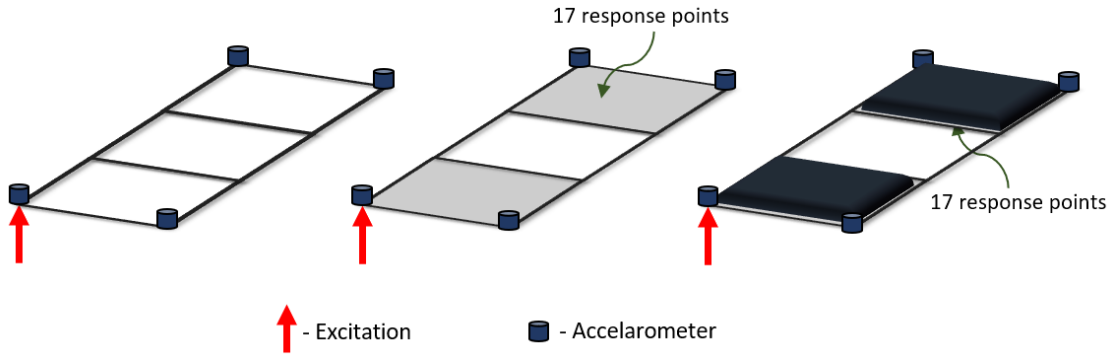

Figure 101: Excitation and response locations at the different types of the ladder structures.

The frame structures were made out of 10 × 10 mm closed section and its thickness was 1.5 mm. The enclosing size was 670 × 1690 mm, and the plates were 2 mm thick with the size of 550 × 650 mm, both had the following properties: density of 7850 kg/m^3, Young's modulus of 210 Gpa and Poisson's ratio of 0.3. The accelerometers on the frame were three-axial, the accelerometers on the plate were uniaxial. All the accelerometers were ICP piezoelectric type, from B&K. The excitation was applied by an impact hammer, with metal tip from PCB Piezotronics. Free-free boundary conditions were used. The measured frequency range was up to 4150 Hz. During the measurements, the frequency resolution was 0.07 Hz.

8.1.3. Level A test case results

In this level, only FEM simulation was performed, since the structure consisted only of stiff elements. The goal of the study was to ensure, that the measurement and the simulation method is appropriate to predict the resonant frequencies and modes of the structure. During the simulation, 5 mm large quad elements and constant 0.1% damping loss factor was used. Thus, the model consisted of a total of 24 400 quad elements. The excitation force was 1 N -in the whole frequency range and was placed at top left corner. The response point was located at the opposite, right bottom corner of the frame, as shown in Fig 102.

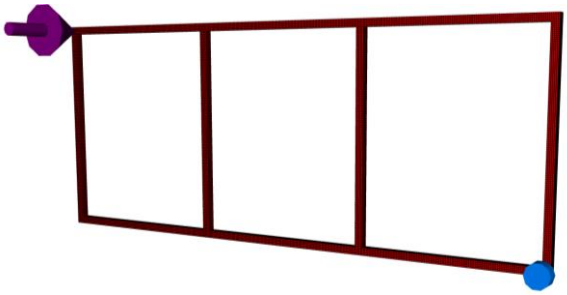

Figure 102: Simulation model of the stiff frame, excitation is on the top left corner, the response sensor is on the bottom right corner.

The modal basis calculation, as well as the frequency response simulation was performed in the VA One FEM software, where the solver itself is Cosmic Nastran. Based on its size, and the wavelength of a vibration in steel, the 5 mm cell size was able to capture vibrations up to 9000 Hz. Fig. 103 shows the second resonance mode shapes while Table 5 represents the eigenfrequencies of the structure.

Table 5: First eight flexible modes of the stiff frame.

Flexible modes	Experiment [Hz]	VA One FEM [Hz]
1	34.6	33.77
2	36.24	36.22
3	72.41	70.56
4	76.88	75.85
5	78.16	76.65
6	94.53	94.26
7	131.55	131.17
8	149.13	147.86

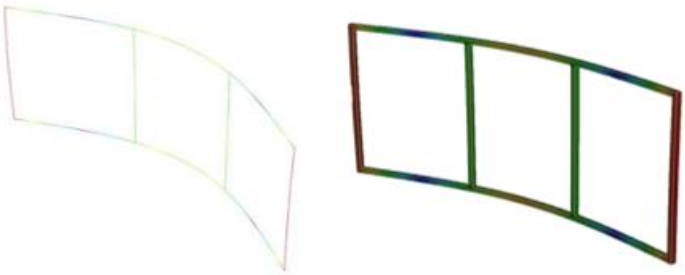

Figure 103: Second eigenmodes of the test case; left: experiment, right: simulation results.

As the results show, the deviation between the simulation and measurement is minor, one can see some difference only between 70 – 80 Hz. The next step was the frequency response simulation up to 4 kHz. Fig. 104 shows the results only up to 1 kHz while Fig. 105 shows the entire frequency range up to 4 kHz.

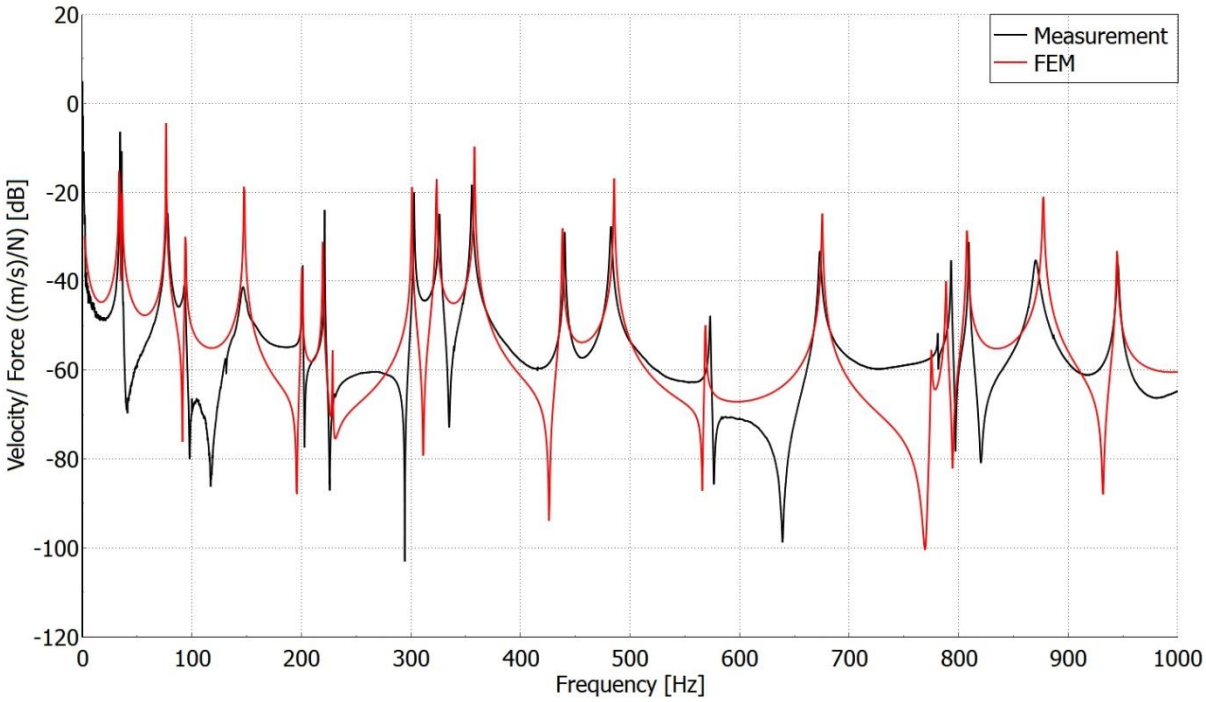

Figure 104: Results comparison up to 1000 Hz. The correlation between simulation and experiment is close to the perfect.

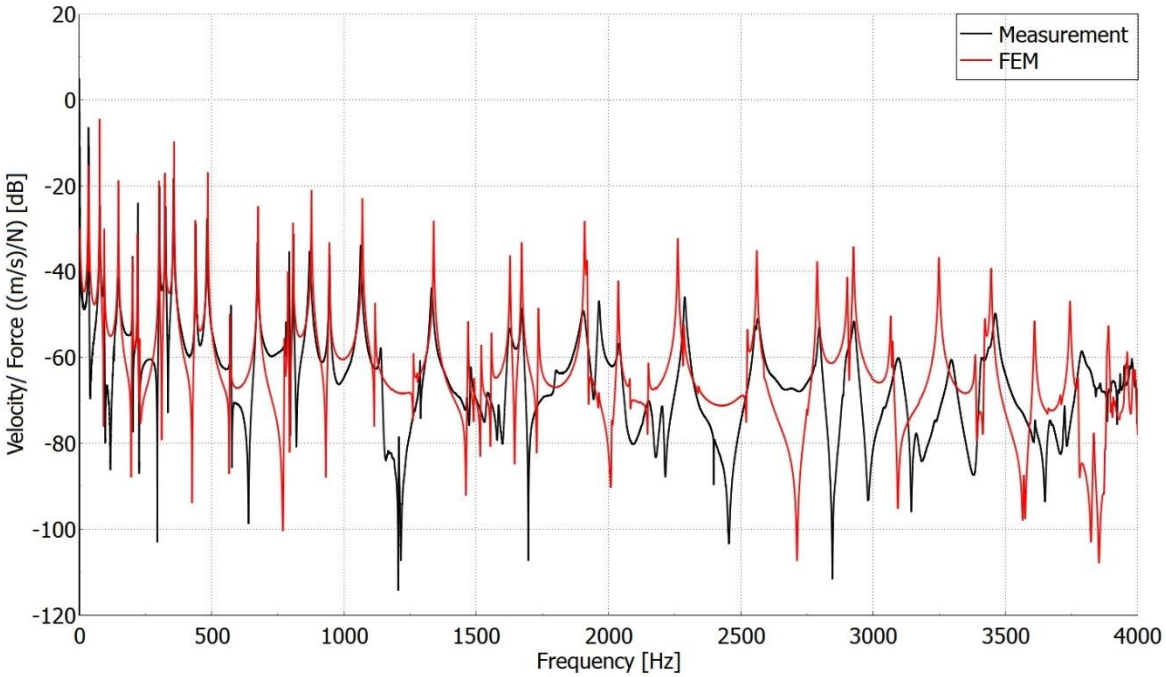

Figure 105: Results comparison up to 4000 Hz. The agreement is really good up to 3 kHz, over 3 kHz nor the frequency of the peaks nor the amplitudes are the same, but in general they are similar.

As the results show, up to 1 kHz the peaks perfectly match each other while the amplitude of the peaks is largely the same, which means that the damping value is reasonable. Over 1 kHz the peak locations lie moreless in the same frequencies, but the amplitude of the peaks is not at

the same level: ergo the damping value is not a constant value, but likely increases with the frequency. Over 3 kHz, especially at 3500 Hz, the experimental curve deviates more significantly compared to the simulation.

8.1.4. Level B results

The second level is the frame structure with the plates, and this it is a perfect academic test case for studying the capabilities of the hybrid FE-SEA method. The stiff part (frame) and the panel-like parts (plates) are clearly separated from each other, so the subdivision is straightforward, as illustrated in Fig. 106. In order to compare the different simulation methods, as well as to ensure the validity of the hybrid method, the structure was examined by pure FEM as well.

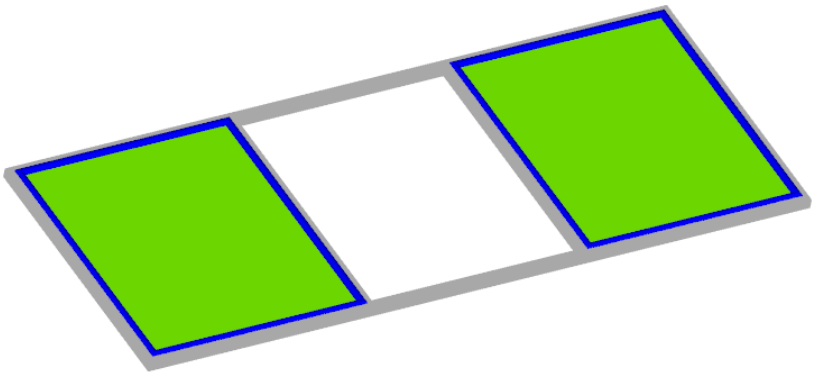

Figure 106: Hybrid FE-SEA model of the structure. The green panels are SEA subsystems, the grey frame is modelled by FEA, the blue lines are the hybrid line junction between them.

The FE model was meshed with 5 mm length quad elements and the frame consisted of 24400 elements, while the two plates contained 27560 elements in total. The mesh was valid up to 9000 Hz. The response points were in the same locations as they were at the experiment as the Fig. 107 illustrates.

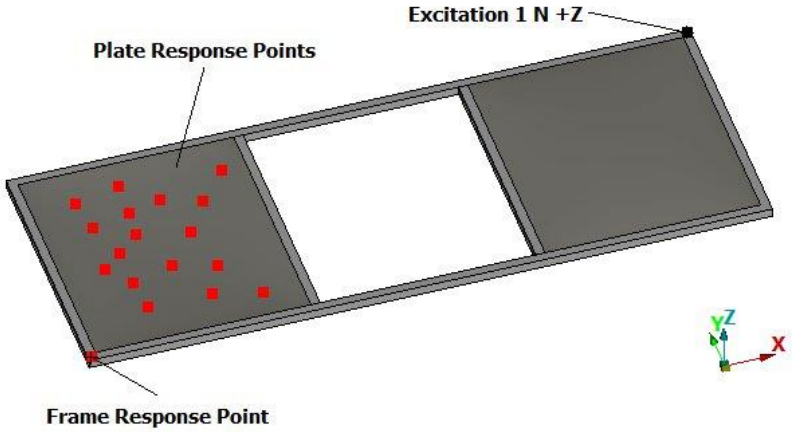

Figure 107: Excitation and response points in the finite element model.

In the real geometry, the plates were welded into the frame along as the blue line shows on Fig. 106. However, as a result of this process, the plates suffered a massive heat load during the manufacturing, which has lead to deformation as well as residual stress in the materials. Fig. 108 shows the nominally identical flat plates after the welding process.

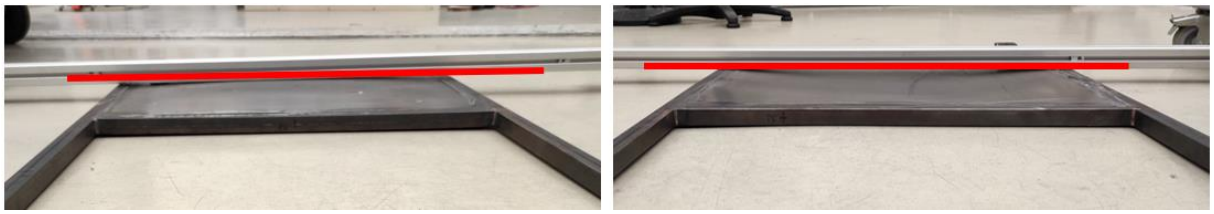

Figure 108: Results of the welding process. One plate is bent upwards, the other is bent downwards.

These curvatures added further stiffness to the system, so the eigenfrequencies and mode shapes also change, when compared to the identical flat plate case [100]. Consequently, in the simulations a curved model was also made (see Fig. 109), in which both plates curvature followed the real experiments. The simulation was run up to 4000 Hz with 1 N excitation force. All part had a constant 0.1% damping loss factor.

Figure 109: Modified simulation model, one plate is downwards curved, the other is upwards curved with 10 mm.

According to Ref. 100, the curvature does have an effect at lower frequencies, under 100 Hz. This study, however, focuses on the mid- and high-frequency range between 250 Hz and 4000 Hz, where the effect of the curvature is less significant. In order to prove this statement a comparison was made between the *Flat* and *Curved* plates. The results were analyzed at the Response plate according to Fig. 107. Fig. 110 shows the FEM simulation with the *Flat* model, while Fig. 111 represents the *Curved* model compared to the experimental result.

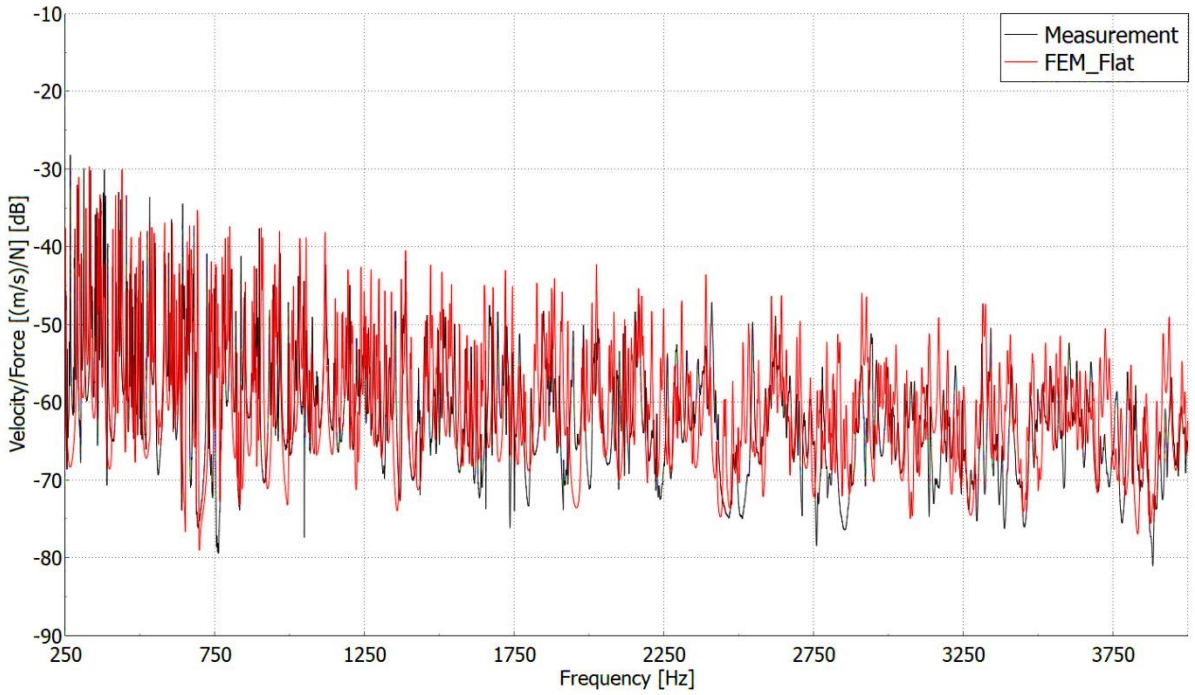

Figure 110: Velocity/force results of the Flat model.

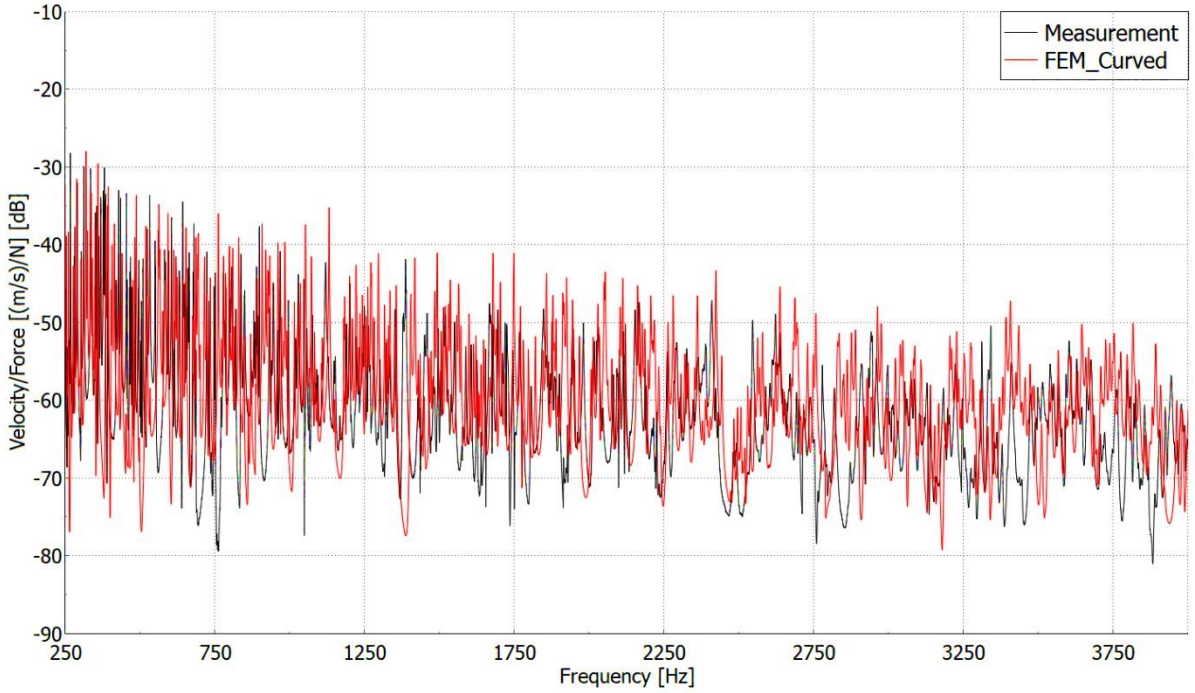

Figure 111: Velocity/force results of the curved model.

As the diagrams show, the two models agree well with the experiments. The *Curved* model gave a better approximation of the experiment around 2400 Hz where a small hiatus can be observed. However, the *Flat* model was better around 3400 Hz compared to the experiment. In order to check the differences from another aspect the third octave results will be introduced in Fig. 112.

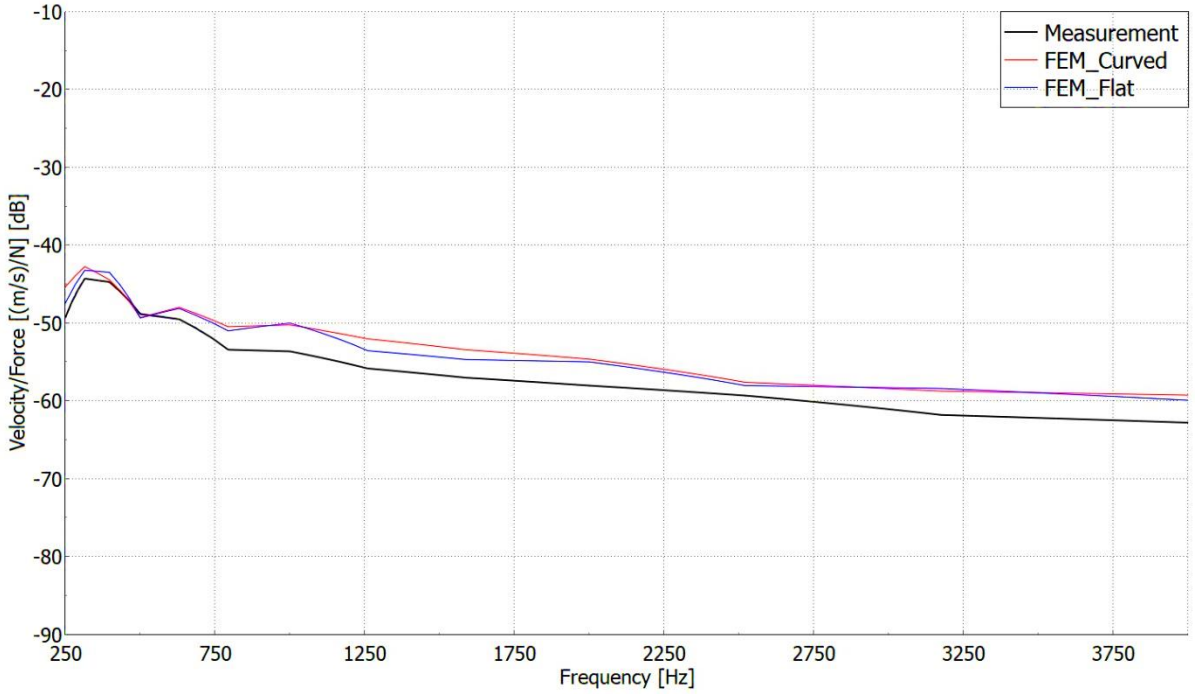

Figure 112: Velocity/Force results of the Response plates.

In the light of the results, the difference between the two different variations are negligible and for this reason, the *Flat* model will be used in the followings.

8.1.4.1. Results and discussions

For Level B test case, only the frequency response functions were compared to each other. The resonant frequencies and resonant modes were not examined, since the simulation method and the experiment validity were proved at frame investigation. Both simulations were run with flat plates and Fig. 113 represents the FEM result at the sensor location on the frame while at Fig. 114 illustrates the plate result supplemented with the hybrid result.

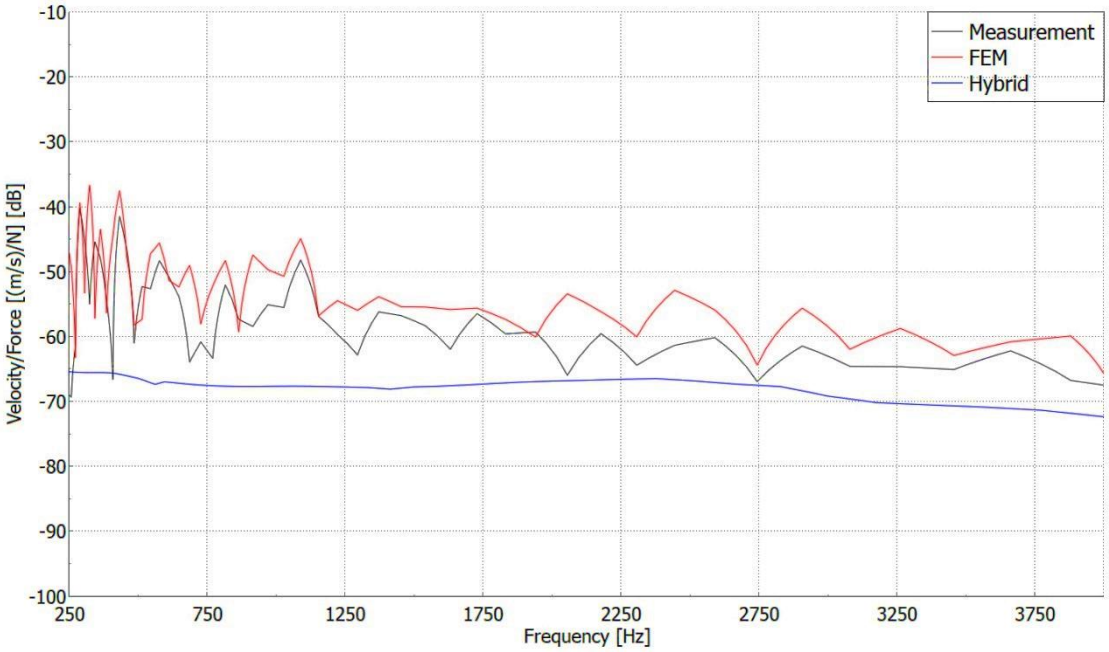

Figure 113: Velocity/Force results of the ladder and plates model at the sensor location on the stiff frame.

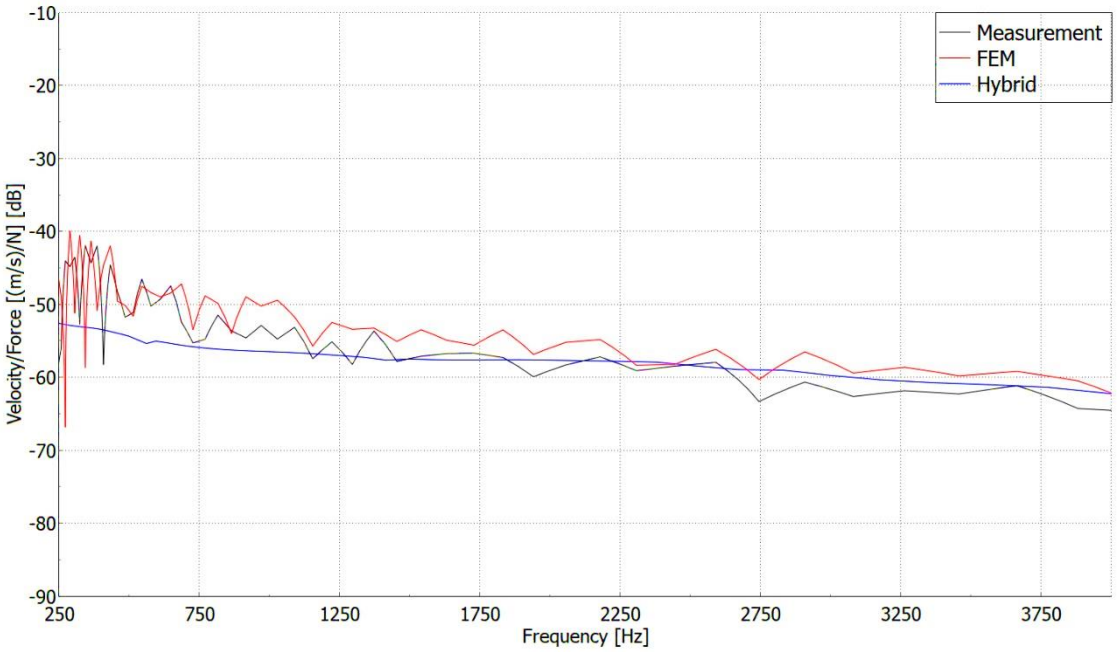

Figure 114: Plate results with averaged of 17 response points up to 4000 Hz in 1/3rd octave band average.

As the results in Fig. 113 show, the curves are averaged in the 1/12th octave band since the hybrid simulation was run with that bandwidth. FEM and experimental curves have similar characteristics, as well as the order of magnitudes are the same. The Hybrid model had a bad agreement with the experimental results in the sensor location on the stiff frame. In Fig. 114, the curves are averaged, and as it can be seen, the FEM curve is close to the experiment in the

lower frequency bands. The agreement is really good between the two curves both in terms of characteristics and the order of magnitude. The hybrid curve is close to the experiment over 1 kHz, the two curves match almost perfectly and that is a proof that the hybrid simulation is working better at higher frequencies as well as those the applied damping values are appropriate.

8.1.5. Level C results

In Level C, the ladder structure was equipped with foam materials on its plates, covered the full plates. The foams were only laid on the plates without any gluing, taking advantage of the gravity alone. The material properties of the foam are summarized in Tab. 6.

Table 6: Material properties of the foam.

Property	Value and unit
Young's modulus	200000 MPa
Poisson's ratio	0.2
Density	60 kg/m^3
Damping Loss Factor	25%
Flow resistivity	200000 Ns/m^4
Porosity	0.93
Tortuosity	1.7
Viscous characteristic length	0.000015 m
Thermal characteristic length	0.0001 m

The FE model with foam treatment is illustrated on Fig. 115. Note that the foam is modeled in a simplified way with a percentage of coverage rather than modelling it directly as the real implementation of a Poroelastic Material (PEM) with sizes and with area junction between the structure and foam.

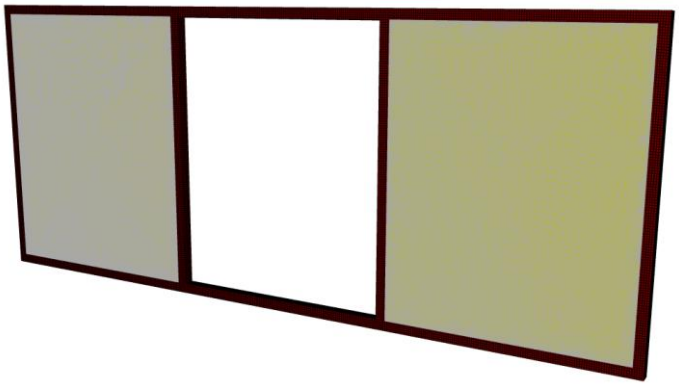

Figure 115: Ladder, plates and foam model. The foam material is considered in the model as a noise control treatment, not a real model of the poroelastic material.

At this incident, only the *Flat* model was used. The frame results are shown in Fig. 116 while the plate results are in Fig. 117. The FEM and experimental results are not averaged since the effect of the foam reduced the number of peaks and the curves can be distinguished easily. The Hybrid results are shown in the 12th octave band average.

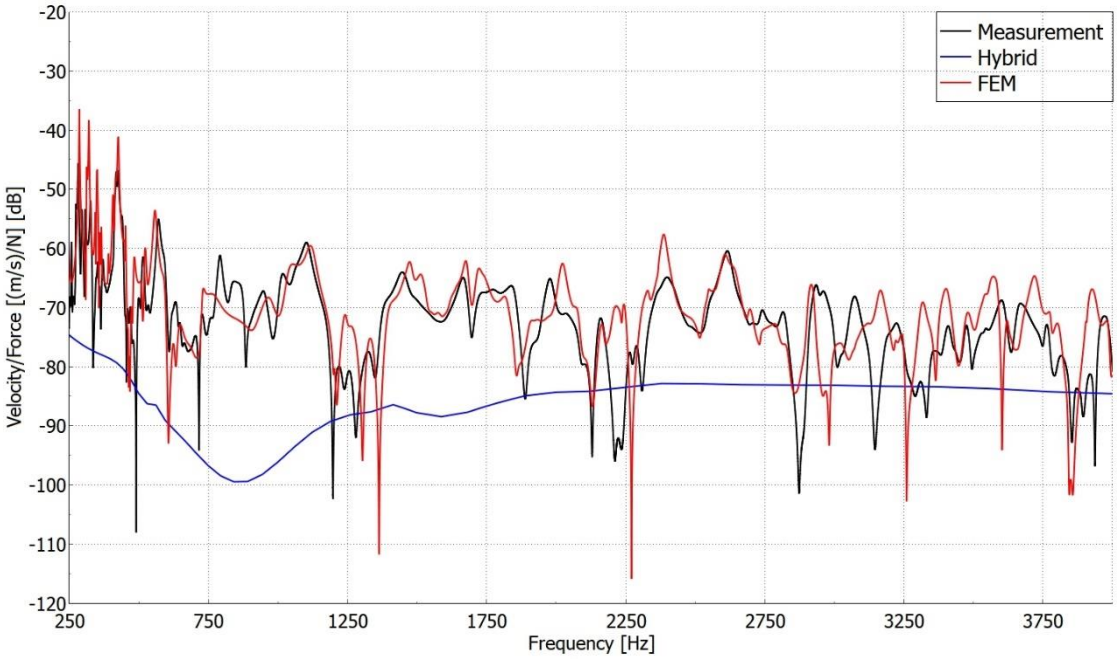

Figure 116: Velocity/Force results of the ladder, plate and foam model at the sensor location on the stiff frame.

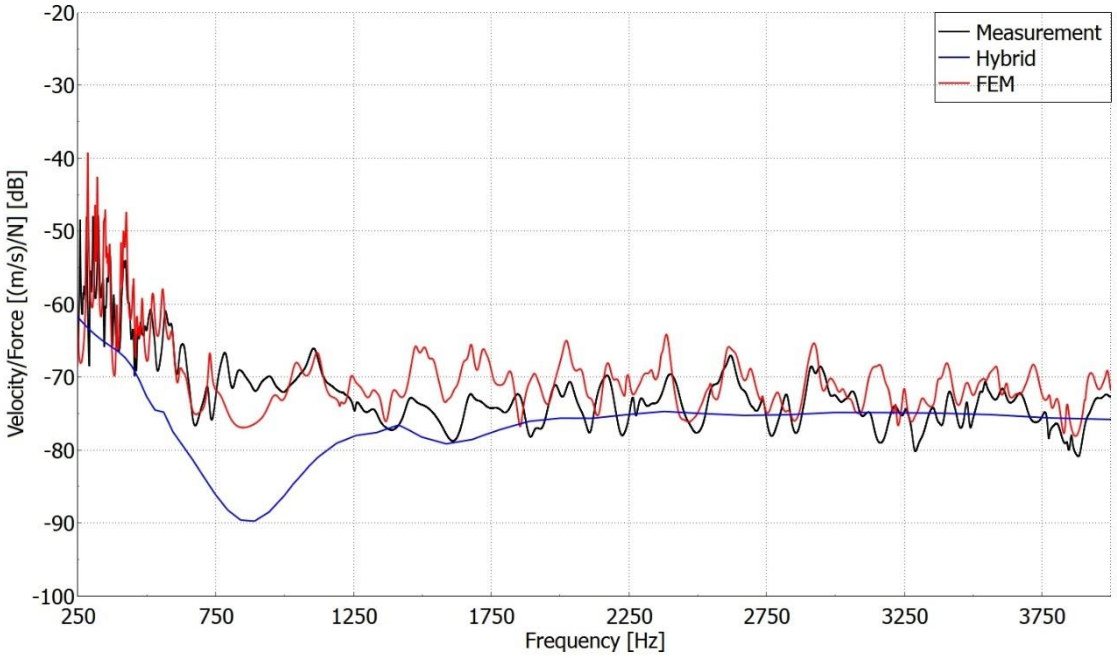

Figure 117: Velocity/Force results of the frame, plate and foam structure at the response plate.

As can be seen, at the sensor locations the FEM simulation produced really good agreement with the measurement, while the Hybrid FEM-SEA simulation underestimated the measurement. This is in line with what was observed in Fig. 113. The plate results showed that both simulations captured well the experiments. The FEM perfectly matches the measurement in the whole frequency range, while the Hybrid method only in the higher frequencies over 1300 Hz. Between 600 – 1250 Hz, the Hybrid results exhibit a dip of around 20 dB, followed by a recovery to the level around the experimental curve. This is likely caused by the damping value changing in the given frequency range. This is confirmed by plotting the DLF as a function of frequency, as shown in Fig. 118. Despite the fact, that the plate's damping loss factor is set as constant 0.1%, and the foam's damping loss factor is also set as a constant 25%, the cumulative damping loss factor is changing in terms of frequency.

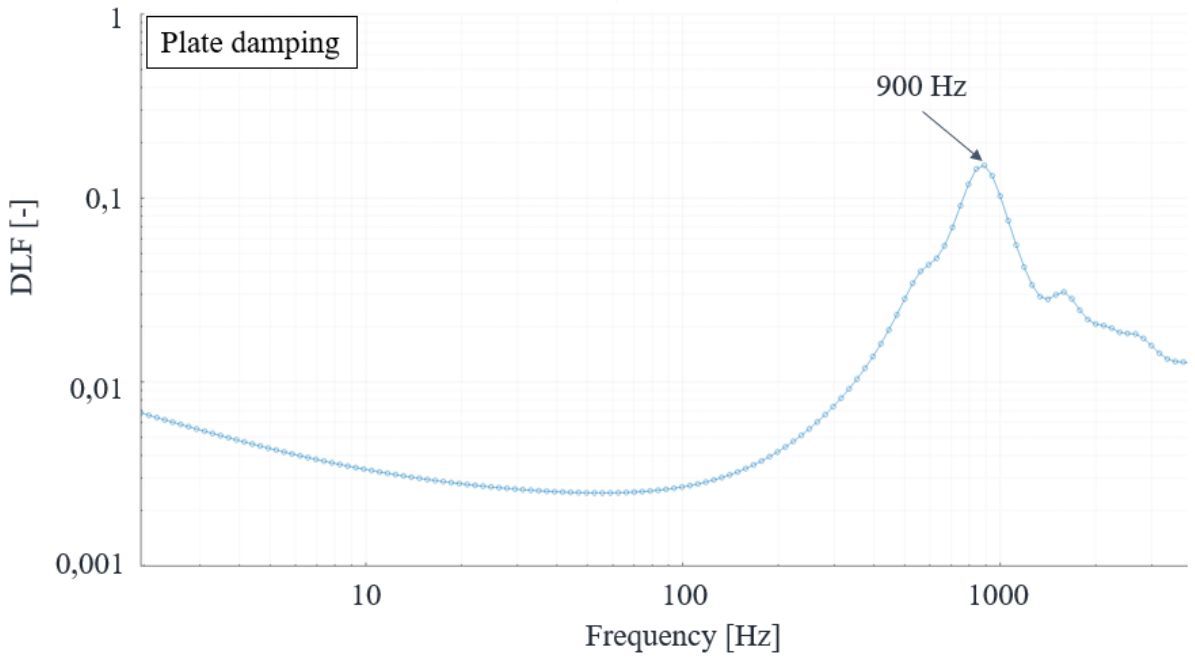

Figure 118: Damping loss factor of the plate after the simulation.

In simulations, the contact between the plate and the foam usually the bottleneck problem of modelling. For this reason, different airgaps were applied such as: a) 1 mm; b) 0.1 mm; c) 0.001 mm. The results of the airgaps are shown at Fig. 119.

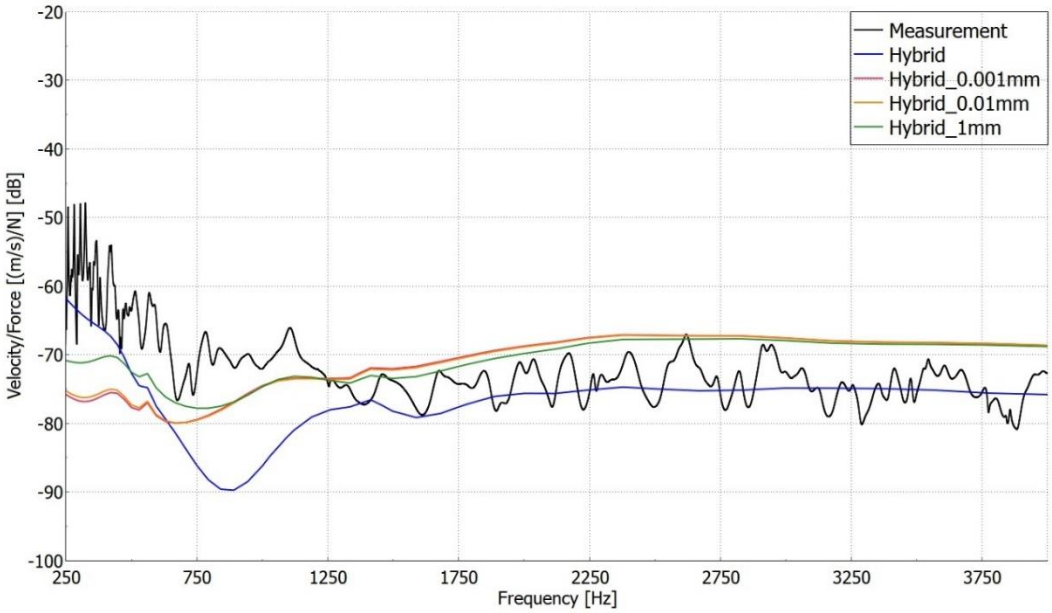

Figure 119: Velocity/Force results of the different airgaps.

As a consequence of the airgaps, the curves have changed, and they were shifted over in frequency as well as in amplitude. The dip around 850 Hz has disappeared but the Hybrid simulations with the airgaps now either underpredict (for 250-1250 Hz) or overpredict (above 1250 Hz) the experiment. All in all, the addition of airgaps rather destroyed the results rather, instead of solving the problematic negative peak.

8.1.6. Conclusions

In this Chapter, a study was built up for a ladder structure representing both strong frame and thin plate elements. Three levels of complexity were considered and compared to the experimental results. All simulations had good correlation with the measured data at the response plate, except for the hybrid foam simulation results. In the latter case, a dip in the graph could be observed as a result of the cumulative damping calculation during the simulation, which was summarized by the plate's damping loss factor and the foam's damping loss factor. The FEM results at the sensor location compared really well to the experiment, while the Hybrid simulations at this location did not match well with the measurements. This study proved that the simulation can be reliable up to 4 kHz, if the model is well built and every parameter is well chosen. In addition, it was proved, that the curvature had not significant effect at higher frequencies, so an idealized flat plate was used during the simulations.

8.2. Hood model: comparison of pure FEM, Hybrid and pure SEA simulation methods

8.2.1. Motivation

This section is unusual in comparison with the rest of the Thesis in that no experimental data was available to validate the simulation model. The examined geometry is a component of a real vehicle, and the three different simulation methods will be compared to each other on it. The purpose is to test the above developed Hybrid methodology on a real vehicle component. Generally, in vehicle NVH the individual subsystems, such as the windshield, firewall, doors, trunk, engine hood, etc., are examined in detail individually too, since they play an important role in the car NVH performance. In this instance, an engine hood was analyzed, but not from NVH performance point of view, but rather from simulation comparison aspect. The geometry consists of a stiffener part and a large panel; thus, it embodies the possibility of a perfect hybrid model as, shown in Fig. 120.

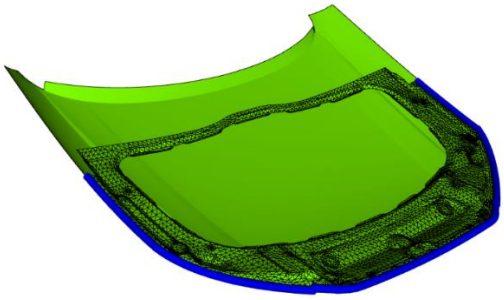

Figure 120: Hood model: the solid green is the large panel, which is ideal for a SEA subsystem, while the meshed stiffener is ideal for FEM.

8.2.2. Simulation models

Three modeling techniques were considered, with various ratios of the FEM and SEA subsystem sizes. The 1st model was a full FEM model, the 2nd a hybrid FEM-SEA model and the 3rd a full SEA model. In all cases the excitation was placed on the stiff parts and the responses were examined on the large panel. The thickness of the model was 1 mm, the material was aluminum with the following properties: density of 2700 kg/m^3, Young's modulus of 69.7 GPa and Poisson's ratio of 0,33. The damping loss factor was 1 % and the excitation force was 1 N. The three different models are represented in Fig. 121.

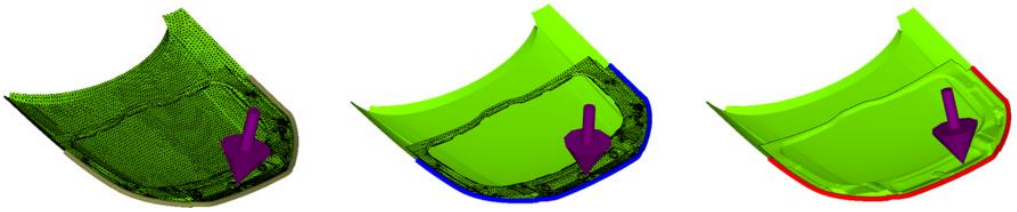

Figure 121: FEM, Hybrid FEM-SEA, and full SEA models of the Hood.

The FEM model was built up from around 20 000 elements and the frequency range between 15 – 2 000 Hz with 1 Hz steps. The Hybrid model was built up from around 9 700 elements and one subsystem. The frequency range was 1/12th octave band between 15.625 – 2 000 Hz. The SEA model consists of a double curved subsystem and a single curved subsystem the frequency range was 1/3th octave band, between 15.625 – 2000 Hz. Simulations were once again completed with the ESI VA One solver. The calculation time of the simulations was quite diverse: the FEM took 3.5 hours, the Hybrid took 5 minutes, while the SEA took only a few seconds.

8.2.3. Results and discussion

Since there is no experimental data regarding the hood model, the FEM results were considered as the reference. As the results show (see Fig. 122) the hybrid simulation matches well the reference results since all main features are well captured in the hybrid simulation. The biggest difference occurs around 1900 Hz. The pure SEA simulation is far from the FEM results in most of the investigated range, both in amplitude and in nature, although over 1700 Hz the two curves are getting closer.

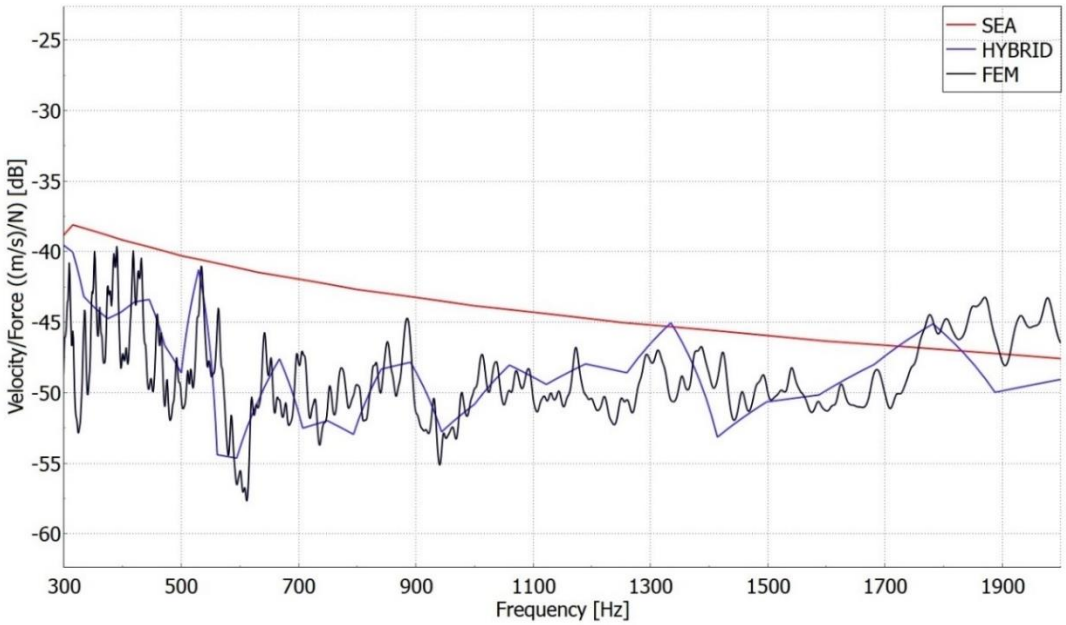

Figure 122: Simulation results of the Hood model. Red curve: SEA simulation; blue curve: Hybrid FE-SEA simulation; black curve: FEM simulation.

In order to validate the SEA model, it is necessary to consider power excitation as well, so instead of the force excitation, a power excitation is employed too. The input power is determined by the injected power of the FEM simulation excitation force, in other words the injected power into the SEA model is equal to the power derived from the 1 N excitation force in FEM. According to Fig. 123, the SEA results match the FEM third octave averaged results perfectly.

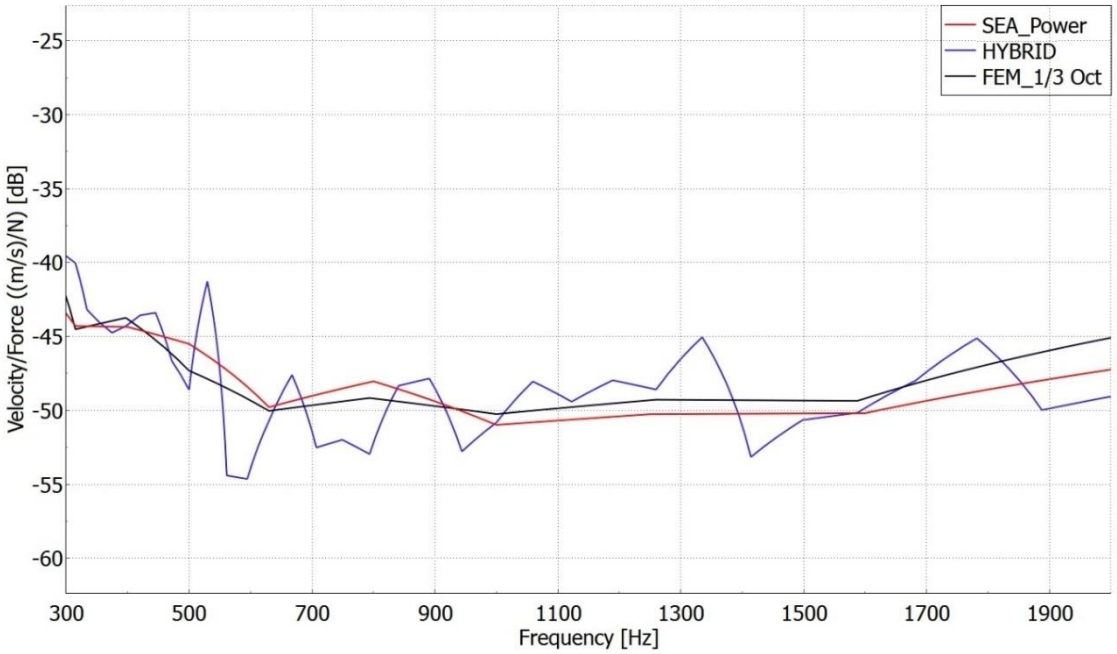

Figure 123: Simulation results of the Hood model. The SEA simulation was excited by the input power that was calculated from the FEM simulation input force.

8.2.4. Conclusions

The current research highlights the advantages of the hybrid simulation and the most important outcome of this study is that the FE-SEA method could be more efficient than pure FEA. The runtime was much less in the Hybrid method, while the results were pretty much the same as the reference results. The pure SEA worked well only at the higher frequencies, over 1700 Hz, or with the corresponding injected power over the entire frequency range resulting from FEM force excitation. This solution was only a demonstration of the validity of SEA, however, in general it is not feasible to run a FEM simulation just for the injected power values.

8.3. Metal cavity

8.3.1. Motivation

In this section, the simulation complexity is further increased by considering a closed frame. A so-called metal cavity, representing a simplified passenger compartment of a vehicle, was considered for the study. The model contains stiff beams and panels in different sizes that affects the modal parameters since it is a function of the panel dimensions.

As a rule of thumb in hybrid simulations, the stiff parts are modeled as FEM while the bigger panels as SEA subsystems. However, in this test apparatus, there are some panels that are not a perfect SEA subsystem in the examined frequency range, so the modelling of them with FEM might be a better choice. The motivation of the study was thus to investigate that what should be the logic behind substructuring of the model, as well as that how the various substructurings affect the simulation results and calculation times.

8.3.2. Measurement setup

The considered test case was a metal box, or a so-called *metal cavity*, that was designed by the MTA-SZE Lendület Vehicle Acoustics Research Group. The test apparatus was made of stainless steel. The main sizes are the following, 1250 × 750 × 850 mm, for the length, width, and height, respectively. The model has around 2000 rivets between the plate connections as well as between the plates and stiffeners. The thickness of the different parts is shown on Fig. 124.

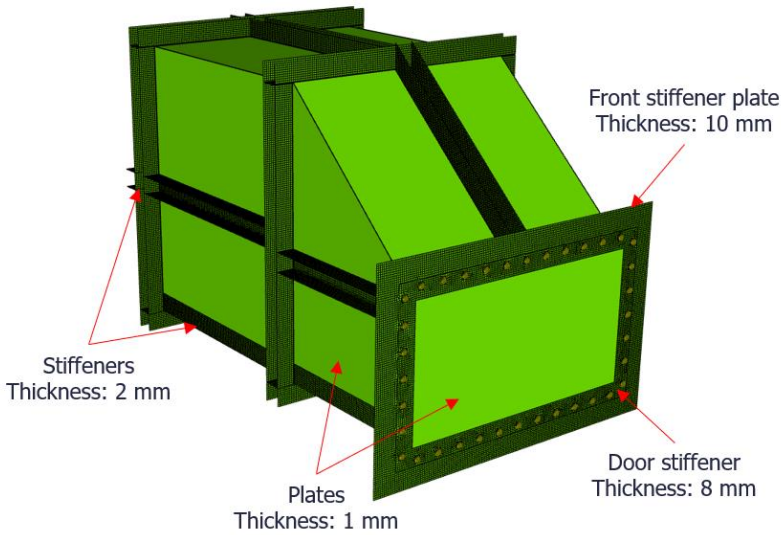

Figure 124: Thickness of the different parts. At the figure only a few plates and stiffeners are signed but all has the same thickness.

During the measurement, the metal cavity was placed on air springs in order to ensure the free-free boundary conditions of the structure. The rigid body modes were under 5 Hz, which was obtained by the adjustment of the pressure in the air springs. Shaker excitation was used with periodic chirp in the frequency range of 100 – 3150 Hz. The frequency resolution was 0.178 Hz and 5 averages were used. The excitation was placed in the right back of the structure. Three response locations were analyzed: a) at the end of a U-shape stiffener so called *Sensor* location, it was measured with a tri-axial accelerometer; b) the *Largest* plate of the structure with 10 response points, which were measured in two waves, with each measurement run with 5 uniaxial accelerometers; c) the second largest panel, the so called *Large* plate, with 10 response points measured twice with 5 uniaxial accelerometers. The schematic image of the measurement setup as well as the excitation and response locations are shown in Fig. 125.

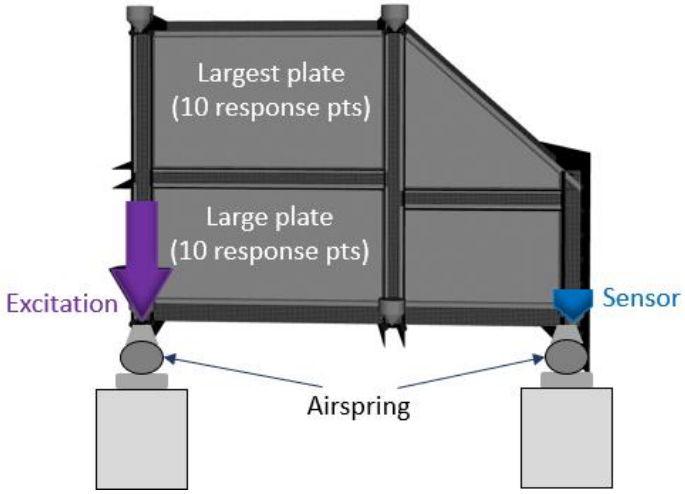

Figure 125: Measurement setup of the metal cavity apparatus as well as the excitation and response locations.

8.3.3. Simulation models

The test apparatus was built up in 6 different versions, in which the ratio of the FEM substructures was varying from 100% to 0%, as illustrated in Fig. 126. Fig. 126 shows with light blue points also the implementation of bolting in the FEM model between the frame and the door stiffener. Table 7 represents the number of elements and the SEA subsystems of the different variations.

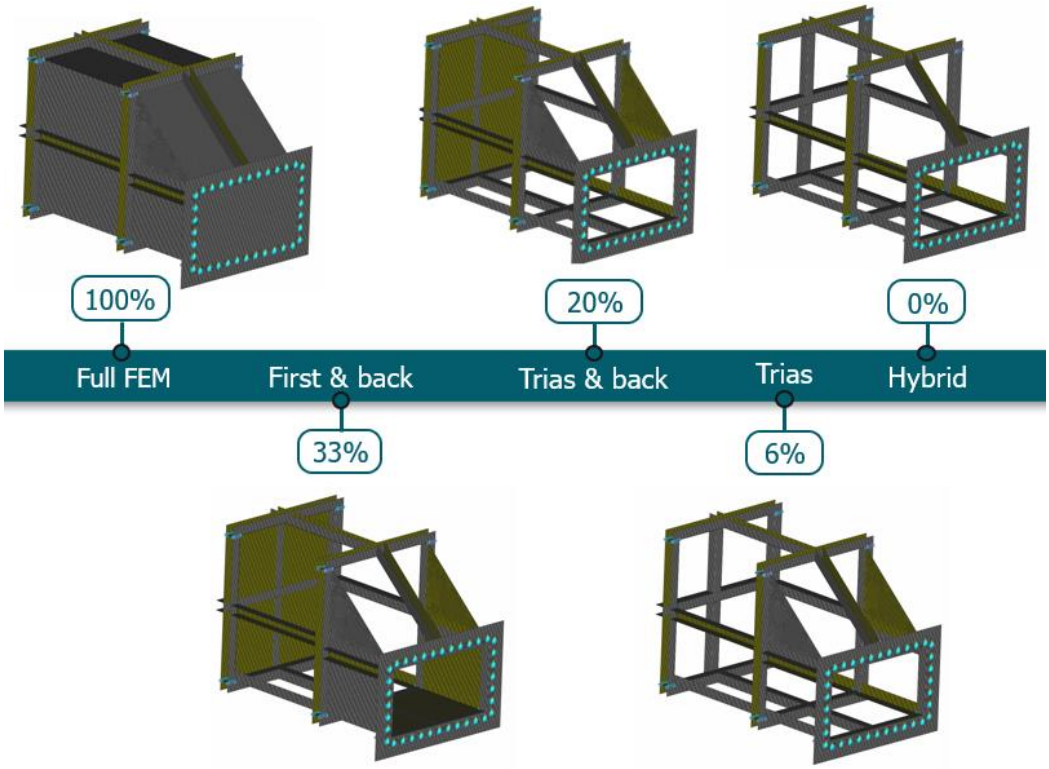

Figure 126: Different versions of the metal cavity, showing the parts, which were modelled by FEM. The parts not shown in the various versions were modelled as SEA subsystems. The light blue points represents the bolting between the frame and door stiffener.

Table 7: Number of finite elements and SEA subsystems of the different model variations of the metal cavity.

Variation	Element numbers	Subsystems
Full FEM	225185	-
First & back	142148	11
Trias & back	125420	15
Trias	107564	19
Hybrid	99824	21

Although the models were built up differently regarding the FEM and SEA subsystem proportions, the simulations themselves were created in exactly the same way. All simulations were run with steel material properties (density of 7850 kg/m^3, Young's modulus of 210 GPa and Poisson's ratio of 0.3) and with constant damping loss factors (0.5 %), the junctions were considered with analytical CLFs. During the simulations, there was no fluid inside the metal cavity. The excitation was 1 N input force, and the frequency range was between 100 – 3 000

Hz with 1/12th octave bandwidth, except the *Full FEM* model, where 1 Hz step was used. The excitation and response points were at the same locations in all model versions. In order to make the simulation more realistic, welding was placed between the top and bottom stiffeners to connect them to the lateral stiffeners, as illustrated in Fig. 127.

The philosophy of the partitions based on the modal parameters of the parts was the following. In Fig. 127 can be seen the modes in 12th octave band of some typical plates, that identified, which plate should represent FE and which remains an SEA subsystem. As it can be seen, for some plates, the fundamental SEA requirement on the modal density (i.e. minimum 3 modes in a frequency band) was achieved only over 1400 Hz. Although the investigated frequency range was broad (200 – 3000 Hz), the main goal of the research remained to reduce the limit between the two methods and to make the hybrid models more accurate at frequencies below ~1000 Hz. So, the plates that had a modal density of 3 or less at higher frequencies were primarily selected as FE subsystems in the various models.

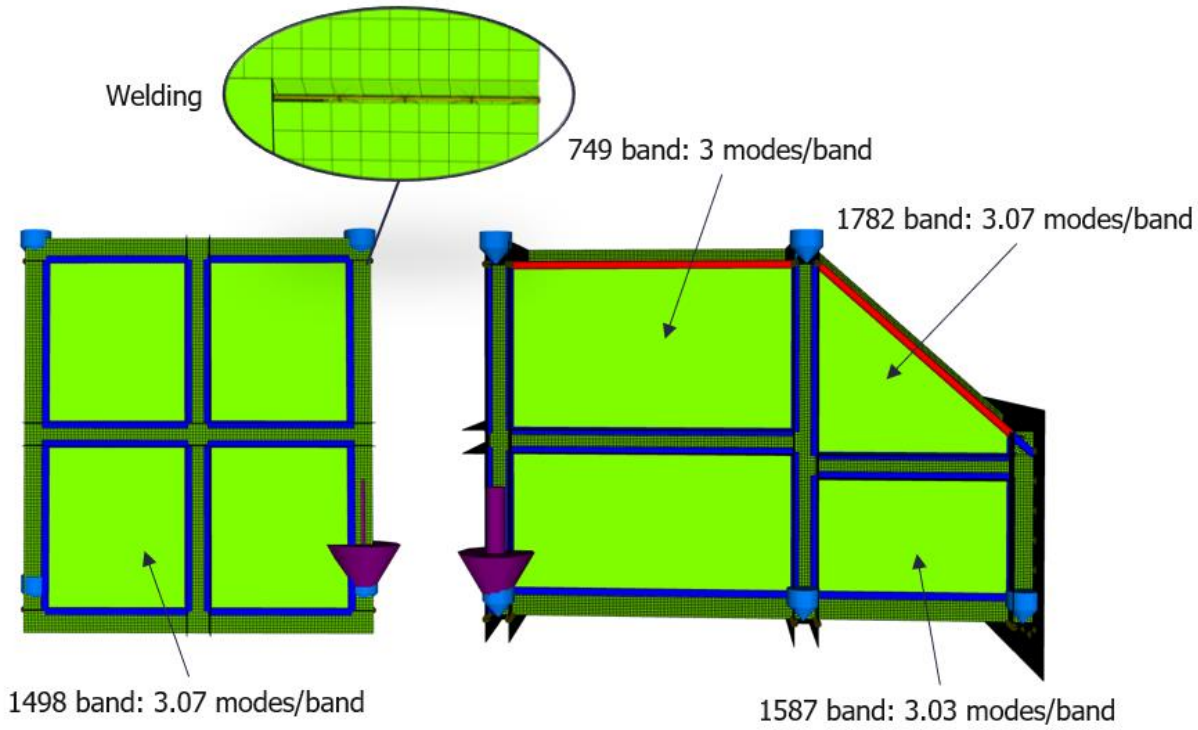

Figure 127: Welding was modelled by solid element and RBE3 (rigid-body-element). The frequency bands where the typical plates of the metal cavity structure are fulfilled the 3 modes in band values; the smallest plate fulfilled in 1782 band, the largest plate fulfilled in 749 band.

The model contained welding and bolting as well, which was represented by rigid body elements (RBEs). These element types are not supported in the simulation software, thus the

modal basis calculation of the FEM parts with the RBEs, beams, solids were solved with Nastran SOL 103. The workflow of the model solution is shown in Fig. 128. Here, The CAD model was built up in Ansa, meshed, and divided into individual properties/each component. The FE parts of every model were solved in Nastran since the RBEs are not supported in VA One. Then the full FEM model was imported into VA One and the components were selected one-by-one to choose, which one is a FEM and an SEA component in the given simulation. In the VA One software the FEM parts – even in the hybrid models – must be agreed with the equivalent Nastran model that was used to calculate the modal basis. Before the frequency response calculation, the Nastran's modal results must be imported into VA One, and then the frequency response simulation is ready to run.

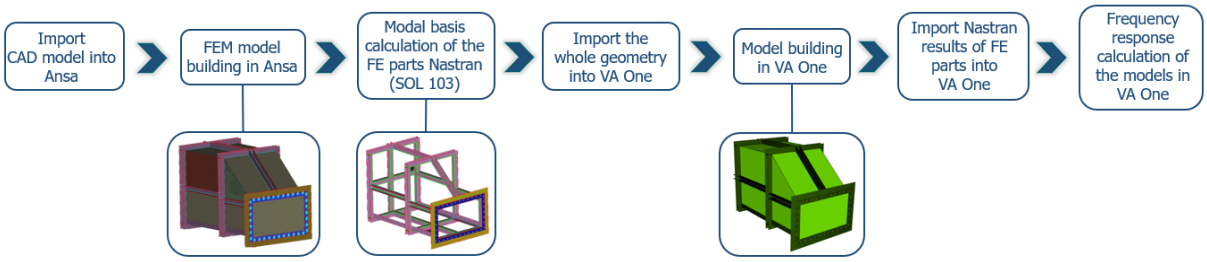

Figure 128: Workflow of the metal cavity except the full SEA model.

8.3.4. Results and discussion

The two goals of this study were to compare the calculation times as well as the simulation results. Firstly, the calculation times will be introduced and then the velocity results. In the comparison of the calculation times, all the important and time-consuming parameters were considered such as the modal basis calculation, the modal results import into VA One, and naturally the frequency response calculation. The frequency response simulation of *Full FEM* model was solved in Nastran (SOL111) as well, but it was not compared to the results since it was not solved by VA One. One of the main goals of the study was to run all model on the same computer and in the same circumstances in order to get a valid comparison about the time data. The simulations were run a computer, which have 98 GB physical memory, 16 CPUs. The calculation times of the different variations are shown in Tab. 8.

Table 8: Calculation time of the different variations.

Variation	Modal basis Nastran SOL 103	Modal results import	VA One frequency response	Total calculation time
Full FEM	1 h 30 min	30 min	168 h	**170 h**
First & back	35 min	20 min	2 h 25 min	**3 h 20 min**
Trias & back	25 min	8 min	1 h 57 min	**2 h 30 min**
Trias	20 min	5 min	1 h 35 min	**2 h**
Hybrid	9 min	4 min	1 h 15 min	**1 h 28 min**

As it can be seen from Table 8, the time data has a huge deviation regarding the various constructions. The *Full FEM* took around one week to solve the frequency response results. The frequency response calculation of the same model in Nastran took only a few hours. The modal basis is reasonable for a model with 225 185 elements and the modal result importing seems as well feasible compared to the other models. One explanation can be the type of the solver in VA One, which is the Cosmic Nastran solver, it either might be a not an up-to-date solver or it did not use the computer efficiently. The frequency step was 1 Hz, and in VA One, one iteration took ~200 sec. The *First & back* variety was computed to 3 hours and 20 minutes, which is much less than the *Full FEM* model. The *Hybrid* case was designed by the theory of Hybrid FE-SEA modelling technique, where the stiff parts are modeled as FE while the panel like components as SEA. As the time data showed, it is much faster compared to *Full FEM*. The second aspect was the comparison of the simulation results to each other. There were three response locations where the results were compared according to Fig. 125: a) blue response sensor at the end of the first stiffener; b) large plate average velocity; c) largest plate average velocity.

First of all, the comparison of the FEM and experiment will be introduced in order to prove the validity of the FEM simulation. The *Full FEM* model will be the reference case during the comparison of the various models, and in the case that it has good correlation with the experimental results. Figs. 129 -131 provide the results for the response locations, for the sensor location on the frame, the large plate and largest plate, respectively.

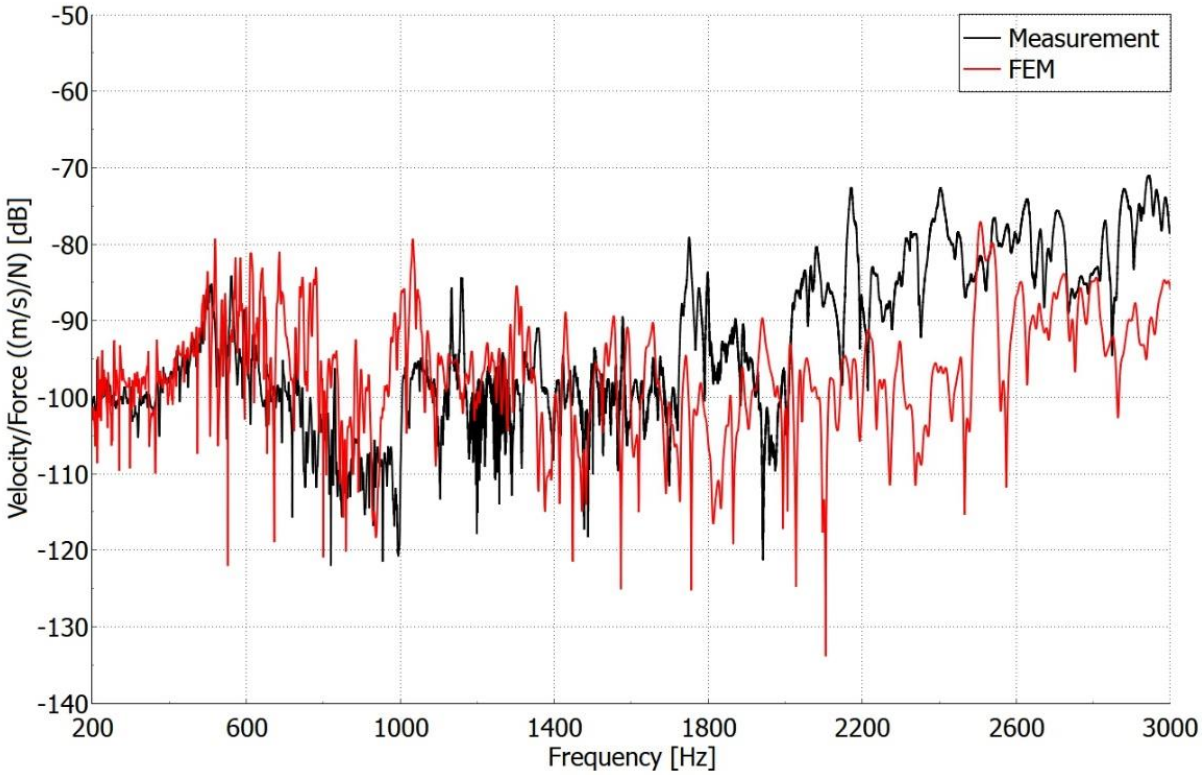

Figure 129: Velocity/Force results of the metal cavity at the right end of the front stiffener so called Sensor location.

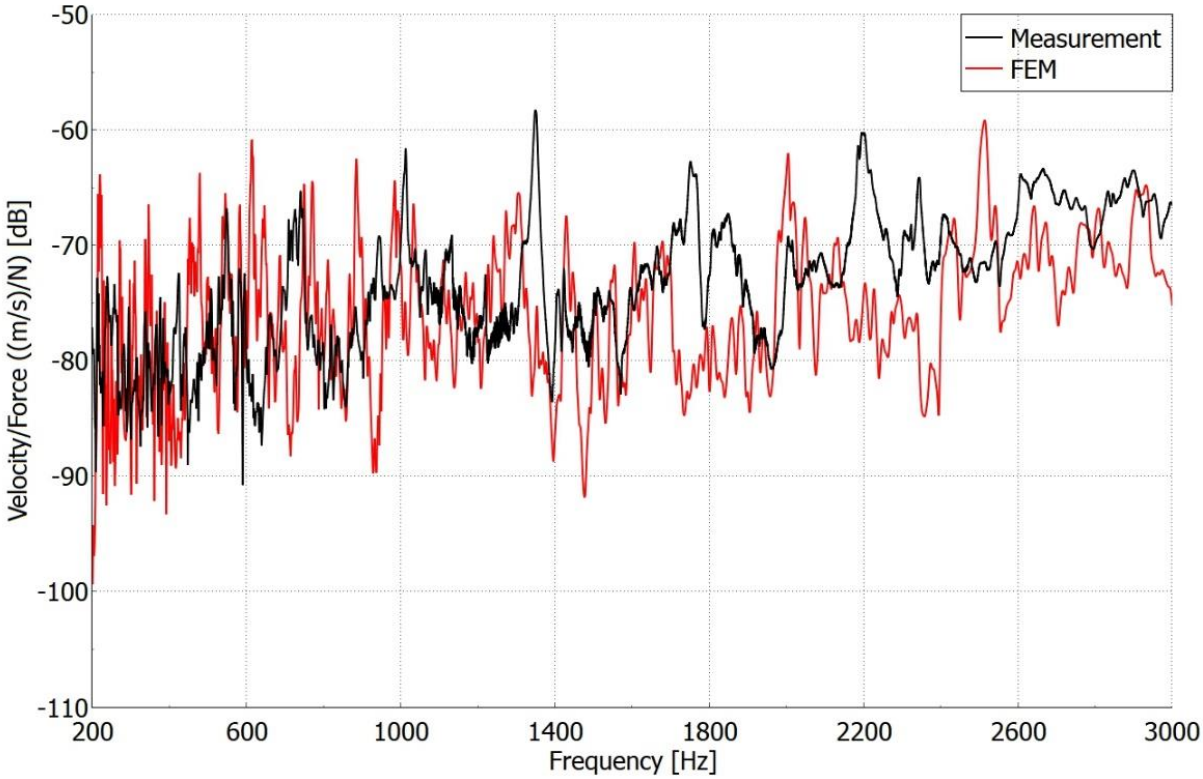

Figure 130: Velocity/Force results of the metal cavity at the Large plate.

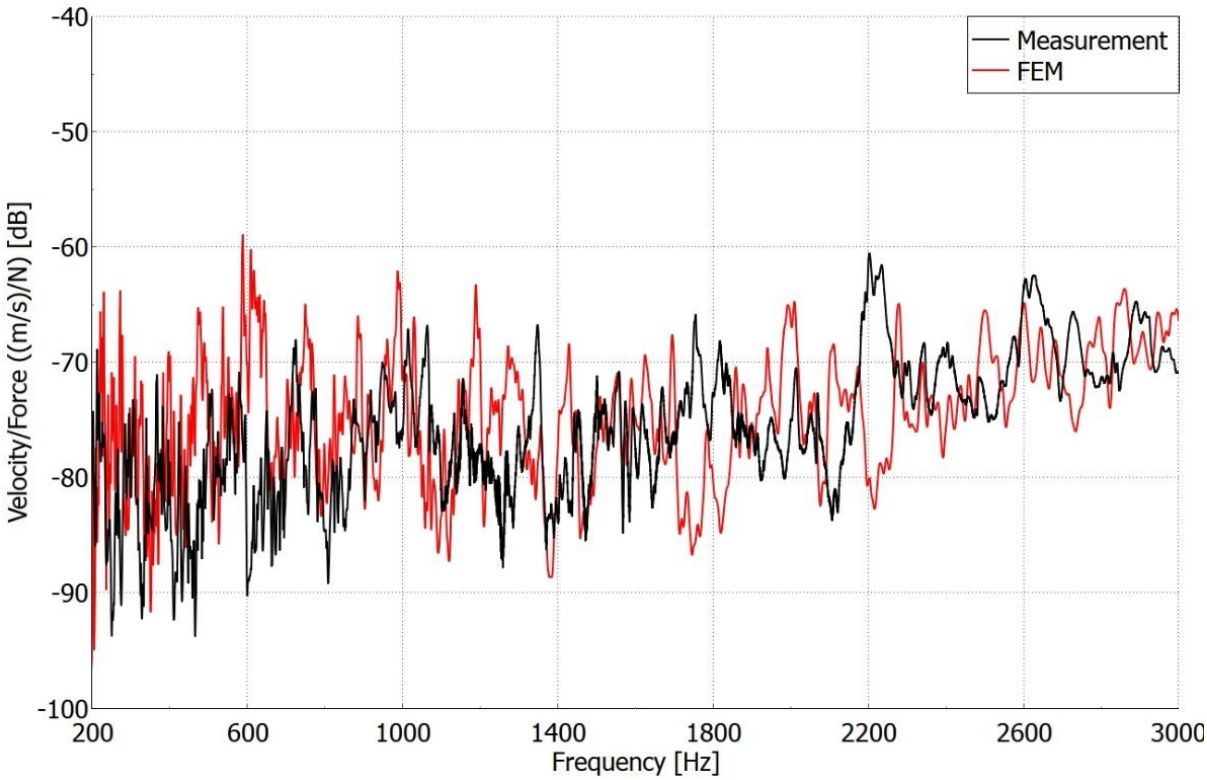

Figure 131: Velocity/Force results of the metal cavity at the Largest plate.

As the comparison shows, the order of magnitude as well as the characteristic of FEM is similar to the experimental results, despite most of the peaks being at different locations. Sufficient deviations occur around 2000-2400 Hz. The differences can be a result of the simplification that was applied during the simulation model, for example, that the plates were overlapped and were riveted at the connections or that the stiffeners were also riveted to the plates. Despite of this, the *Full FEM* variation fulfilled the criteria to be used as a reference during the comparison with the other variations.

Recall, that all simulations were built up with the same material properties and parameters, as well as the excitation and response points were at the same locations. The first comparison point was the sensor location at the right end of the front stiffener, as Fig. 132 represents it.

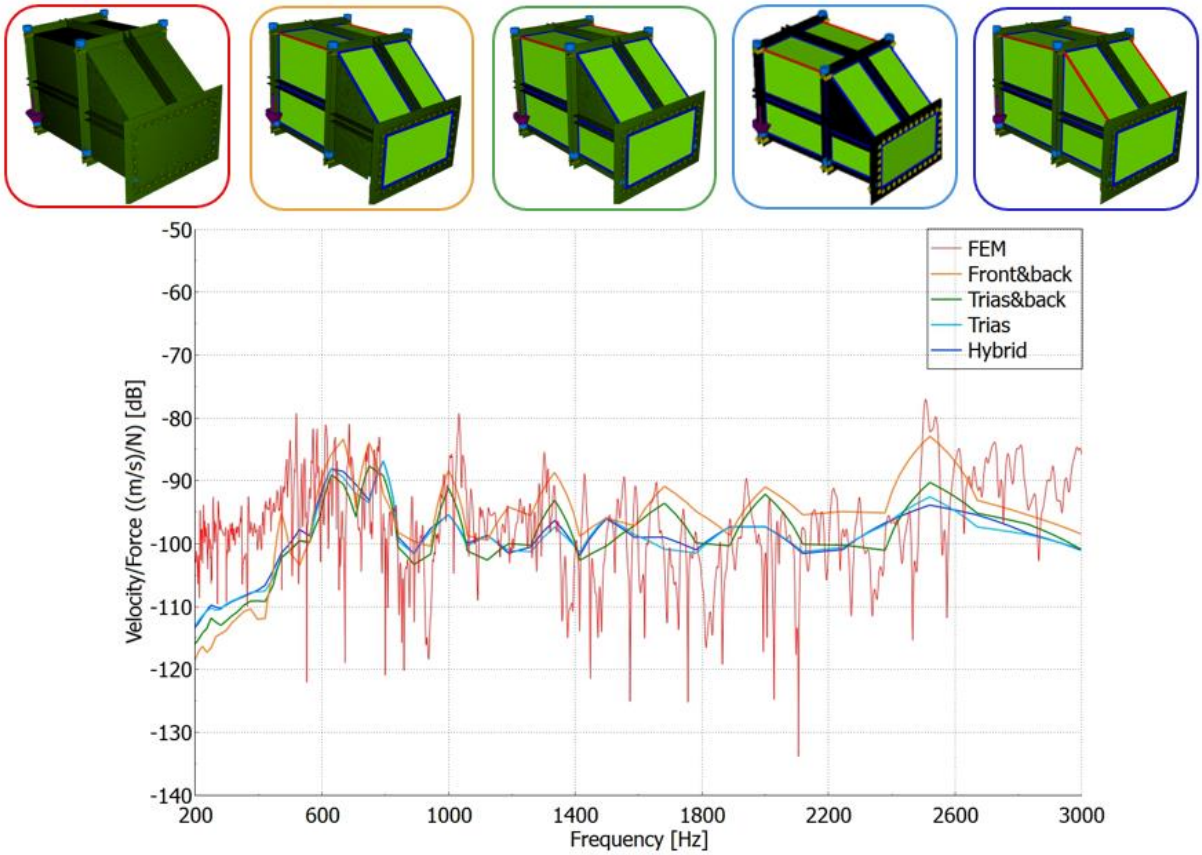

Figure 132: Velocity/Force results of the metal cavity at the Sensor location. The color of the boxes represents the color of the curves.

As the results show in Fig. 132 all the simulations match really well the *Full FEM* results over 500 Hz. At higher frequencies, over 1500 Hz the *Front&Back* variation overestimates a little bit the reference result. The second comparison location was the *Large plate*, for which the results are shown in Fig. 133.

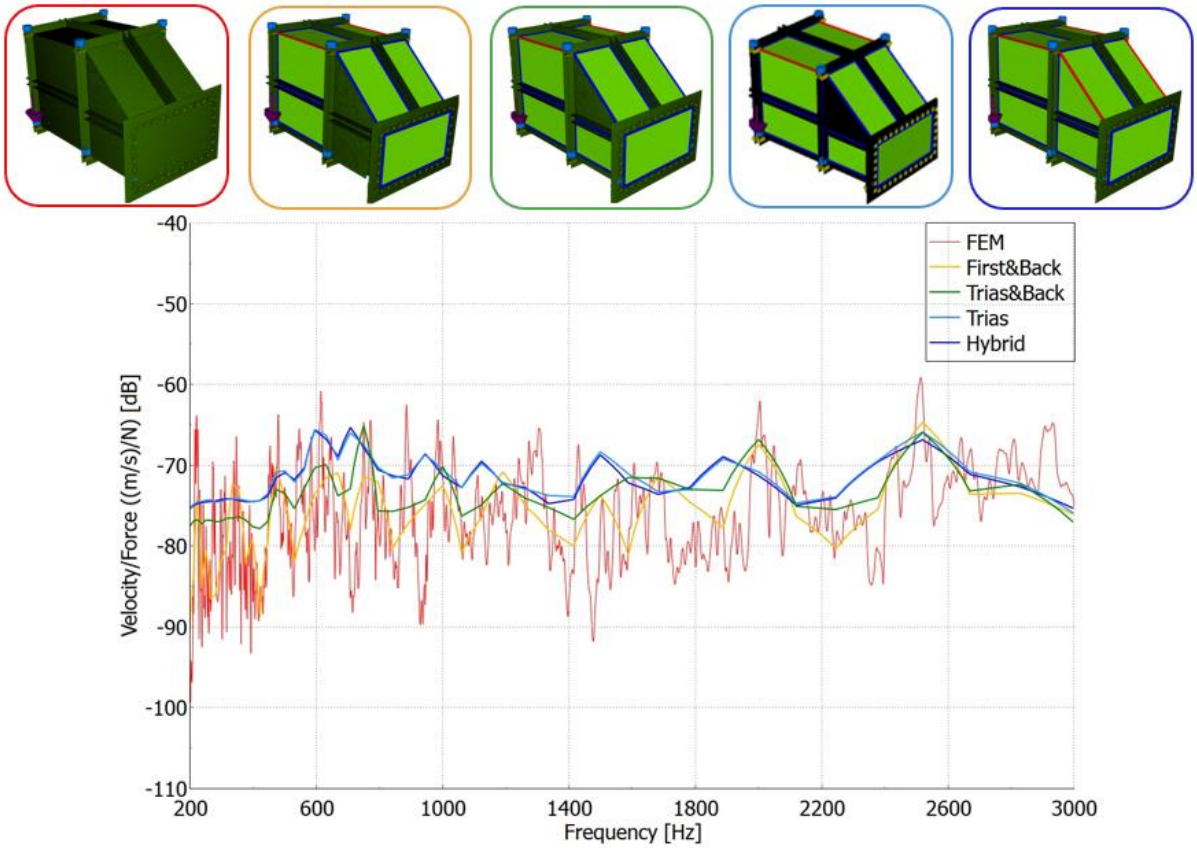

Figure 133: Velocity/Force results of the metal cavity at the Large plate. The color of the boxes represents the color of the curves.

At the *Large plate* location, the *Trias* and *Hybrid* variations were mismatched from the reference results, while the *First&Back* variation had a good agreement with it. The *Trias&Back* variation is not perfect, but in general it captured well the characteristic of the reference *Full FEM* curve, even in the lower frequencies. Lastly, the largest plate results are represented in Fig. 134.

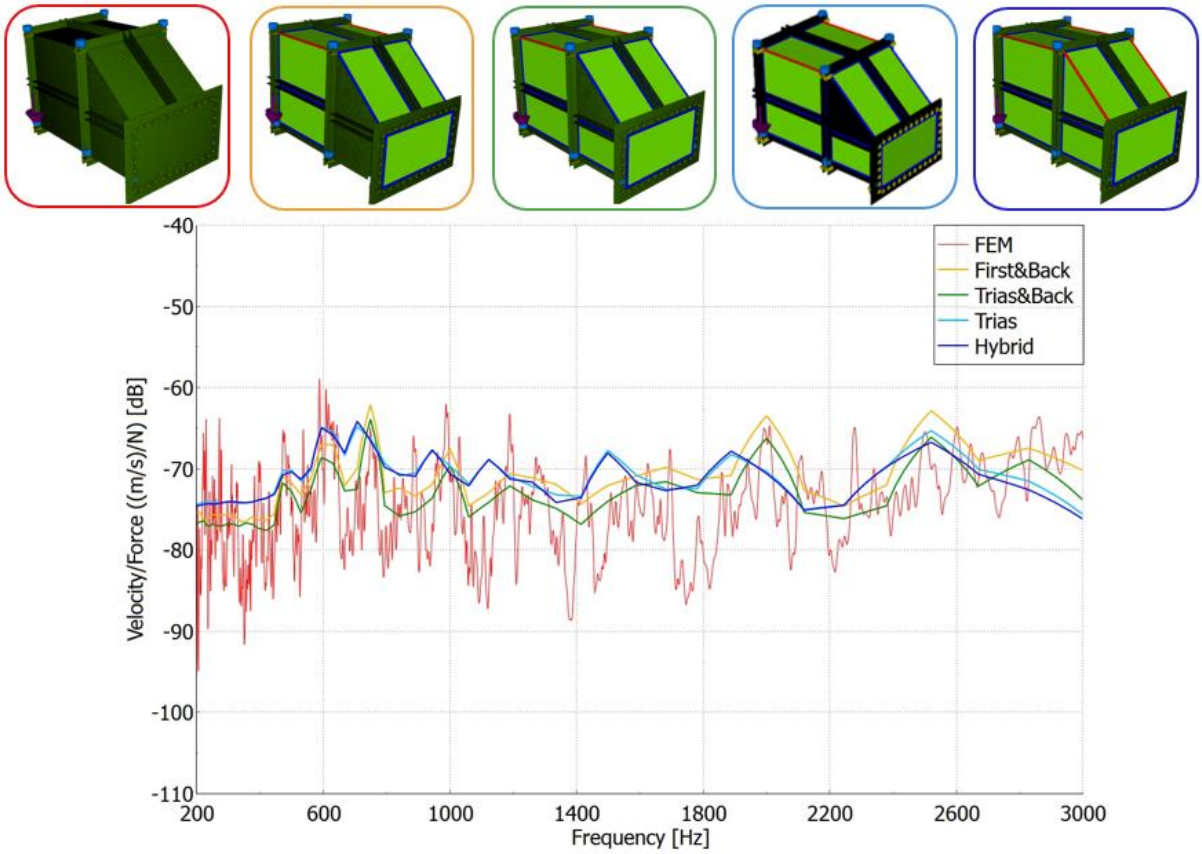

Figure 134: Velocity/Force results of the metal cavity at the Large plate. The color of the boxes represents the color of the curves.

According to the results of Fig. 134, under 1 kHz the *First&Back* and the *Trias&Back* versions captured the reference curve well, but over 1.5 kHz the *First&Back* variation overestimates it. The *Trias* and *Hybrid* results overestimate the *Full FEM* curve up to 2 kHz, then they are a good approximation of it. In terms of the whole frequency range, the *Trias&Back* had a good agreement with the characteristic reference curve.

8.3.5. Conclusions

The goal of this Section was to investigate the effects of the different subdivisions of a hybrid model from calculation time and from velocity response point of view. The geometry of the metal cavity may seem a straightforward hybrid model, with a clear model division, and that which part should be modelled as FEM and which part as an SEA subsystem. The partition was dictated by the modal density value of the plates. Six different variations were built up regarding the proportion of the SEA subsystems to the whole model. A measurement campaign was completed as well in order to validate the *Full FEM* type as the reference model and then compared to all other variations.

According to the time data, the FRF results have significant importance since deviations can occur in the frequency responses in certain bands, but the calculation times were massively less than the reference *Full FEM* simulation was. From one side, the responses of the *Full FEM* simulation showed that it is able to reproduce the experimental results correctly and therefore that variant was used as a reference. On other hand, it was proved, that a proper subdivision of the metal cavity geometry can give good results and save significant calculation time. Consequently, none of the variations were extremely inaccurate, even the *Hybrid* type, and all the models can be used for solving the problem. All in all, the *Trias&Back* model proved to be the best choice for this particular geometry since it is much faster than the *Full FEM* calculation, and it gave good results in every investigated location.

8.3.6. Thesis No. 4

According to the theory of Hybrid FE-SEA, the larger panels should be modeled as SEA subsystems, while the smaller ones and stiff components as FE parts. In complex structures, the determination of the borderline between the FE parts and SEA subsystems is not straightforward, since many components could fit both the FE or SEA methodology.

In relation to this, I proved that [A]:

- The divison of the hybrid model has an impact on the results, namely the proportion of the SEA subsystems related to the FE parts.
- The logic of which parts shall be represented by SEA is driven by the minimum modes in band requirement.
- The divison of the structure massively influences the computational time.

9. CONCLUSIONS AND FUTURE WORKS

This dissertation dealt with Statistical Energy Analysis, with specific focus on the experimental and analytical SEA. The literature review showed that the most important parameters in SEA are the Damping Loss Factor as well as the Coupling Loss Factor, while in Hybrid FE-SEA method it is the subdivision of the model, i.e. that which part should be modelled by FEM and which part by SEA. The research was built up from the simplest geometry (e.g. a flat plate) to more complex structures. This approach allowed to examine the factors influencing the Damping Loss Factors, Coupling Loss Factors and the subdivision. As a conclusion, all test case level yielded simulation results sufficiently accurate when compared to the experiment results. All the listed goals in Section 3 were achieved in the research. Most of them represented original results, since – to the knowledge of the authors - no prior articles have provided such guidelines for measurements, simulations, and results.

Goal 1 was to create guidelines for the experimental determination of the damping. The specific goal was to derive the guideline for an SEA like structure, i.e. an extremely sensitive, lightly damped plate in the frequency range up to about 1000 Hz. Although several papers provide some experimental data in this field, none of them have examined the simultaneous effect of coherence, the driving force, the frequency resolution, and the type of the excitation, nor provided exact guidelines on a methodology on obtaining the DLF's. Without this, the experimental results can differ significantly from author to author. By applying the proposed measurement guideline, the accuracy of SEA simulations could be improved.

Goal 2 was to propose a method for taking into account the spatial distribution of the damping layer on an SEA subsystem. The various spatial distributions of the damping pads influence the DLF values, which directly affect the simulation results. Although this might appear a straightforward relationship, no prior literature examined this phenomenon, and thus this work was the first to systematically address this issue, which is really important for experimental SEA.

Goal 3 was to examine the effect of the applied binding technique between the subsystems on the CLF values. The specific goal was to investigate all binding types occurring in vehicle structures, as well as to investigate the effect of the connection angle between them. The CLF assessment of various joint was investigated by many journal papers, but the combined joints as well the bended structure were examined in this context for the first time. The comparison

of the various joints and bitumen damping layers from vibrational response reduction point of view is an important topic for the vehicle industry, and points beyond just a pure academic purpose study.

Goal 4 was to examine the effect of the relative size of the SEA and FEM-like subsystems for the hybrid FE-SEA method. Currently, this is chosen by the simulation engineer based on experience or intuition, and no systematic study was found in the literature on this very important field. The borderlines between the two methods have a huge importance at larger and more complex structures, where the running time is an issue, and where the engineer must find the optimal ratio between the calculation time and accuracy. Thus, the results of the systematic study presented in this work can be of significant huge help to those dealing with Hybrid FE-SEA simulations.

Future work should include the investigation of the damping pad distributions and to establish a link between the spatial distribution patterns, the area of the damping pads and the variation of the DLF values. Another important step would be to add fluid to the metal cavity test case and to compare the simulation with the experimental results. A further main goal of the research would be to project the know-how and outcomes of this work to actual industrial-size problems, i.e. onto a full vehicle simulation. Different vehicle segments could be examined and the recommended standard subdivision guidelines for each could be determined. Furthermore, the DLF and CLF parameters of earlier vehicle models could be used to generate a databank, on which basis these data for a next generation's virtual model could be determined, in order to increase the accuracy of SEA simulations in the early phase of the development. All in all, SEA could be a powerful tool supporting the early phases of design but requires these systematic guidelines and results to facilitate its acceptance.

10. THESES

10.1. Thesis No. 1

I formulated a novel procedure for the accurate determination of the damping for SEA panels. The procedure was deduced from a systematic approach and appears to provide relatively accurate Damping Loss Factor values in every frequency band, when compared to other method. I investigated the effects of the boundary conditions on the results, such as those of the coherence, the driving force or the type of the excitation. In addition, the method of data processing was also examined with log-normal distribution as well as through arithmetical average. The approach was validated on a rather sensitive, lightly damped flat plate, and the acquired data were implemented in SEA simulations, yielding minimal deviation (less than 1.5 dB) compared to the experiment results [I], [J].

10.1.1. Thesis No. 1.b

In SEA simulations the Noise Control Treatments are considered as a coverage on the surface and there is no information about the spatial distribution of them.

I proved that the different distributions of the damping layers can be taken into account during the SEA simulations if the panel damping is obtained during the measurements [G].

10.2. Thesis No. 2

Different bindings yield different CLF values, that can significantly influence the simulation results. In addition, in the numerical method only a few types of junctions exist and for this reason the reliability of the analytical formulas for CLFs is a key factor from accuracy point of view for complex cases.

In relation to this, I proved that [F]:

- The connection angle has an impact on the CLF values and this might require modification to the analytical CLF formulas to include this effect.
- The type of the adhesive has an impact on the CLF values.
- At combined junctions, such as simultaneous riveting and gluing, the CLF is not a summation of the individual binding CLFs, but rather a combination of them, namely: $CLF_{rivet} + CLF_{glue} \neq CLF_{rivet+glue}$

- Analytical equations can be used with high precision for common cases, if the modelling technique is reliable.

10.3. Thesis No. 3

For vehicle NVH characteristics, the main goal is to reduce the vibration of the panels that radiate noise into the passenger compartment. Traditionally, the vibrational energy of the panel is controlled locally on the panel by adding viscoelastic damping material to it, which in turn adds mass to the system.

I proved that the adhesive binding technique can more effectively reduce the vibrational response of a panel, than a viscoelastic damping layer applied directly on the receiver plate. While this leads to reduced vibration on the plate, the stiffness of the system remains unchanged, while the mass of the system could be reduced in comparison to a classical solution of adding viscoelastic damping layer to the plate [E], [B].

10.4. Thesis No. 4

According to the theory of Hybrid FE-SEA, the larger panels should be modeled as SEA subsystems, while the smaller ones and stiff components as FE parts. In complex structures, the determination of the borderline between the FE parts and SEA subsystems is not straightforward, since many components could fit both the FE or SEA methodology.

In relation to this, I proved that [A]:

- The divison of the hybrid model has an impact on the results, namely the proportion of the SEA subsystems related to the FE parts.
- The logic of which parts shall be represented by SEA is driven by the minimum modes in band requirement.
- The divison of the structure massively influences the computational time.

11. PUBLICATIONS BY THE AUTHOR

A. M. Treszkai, D. Sipos, D. Feszty, Effect of substructuring for a Hybrid FE-SEA simulation for simplified vehicle-like structure, Acoustic Physics journal paper in preparation to be submitted in November 2022

B. A. M. Treszkai, D. Feszty, Reduction of the vibrational response for a coupled plate structure: comparison of viscoelastic damping layer to various binding techniques, JVC/Journal of Vibration and Control, to be submitted in November 2022.

C. D. Sipos, M. F. Treszkai, D. Feszty, Optimization of damping pad distribution on body-in-white car structure. Journal of Vibroengineering, Vol. 24, Issue 2, 2022, pp. 386-393. https://doi.org/10.21595/jve.2021.22158

D. D. Sipos, M. F. Treszkai, D. Feszty, Welding distortion generated uncertainties in the vibrational behavior of a ladder-like structure, NOISE-CON PROCEEDINGS 263 : 2 pp. 4799-4809. , 11 p. (2021)

E. M. F. Treszkai, D. Feszty, Effect of junction type on the vibroacoustic response of a system of plates, NOISE-CON PROCEEDINGS 263 : 2 pp. 3953-3962. , 10 p. (2021)

F. M. F. Treszkai, A. Peiffer, D. Feszty, Power Injection Method-based evaluation of the effect of binding technique on the Coupling Loss Factors and Damping Loss Factors in Statistical Energy Analysis simulations, MANUFACTURING TECHNOLOGY 21 : 4 pp. 544-558. , 18 p. (2021)

G. M. F. Treszkai, B. Vehovszky, D. Feszty, Damping determination by the half power bandwidth method for a rectangular flat plate with bitumen damping layer application, JOURNAL OF VIBROENGINEERING 2021 pp. 1267-1277. , 11 p. (2021)

H. J. Kun, T. Turcsik, M. F. Treszkai, D. Feszty, Methods for improving the mid-frequency acoustic simulation of a lightly damped plate, Inter-Noise 2020, (2020) Paper: 610/17.06

I. M. F. Treszkai, D. Feszty, Alacsony csillapítású lemez, csillapítási veszteség tényezőjének a meghatározása Bevitt Teljesítmény Módszerrel, In: Barabás, István (szerk.) XXVIII. Nemzetközi Gépészeti Konferencia – OGÉT 2020 : 28th International Conference on Mechanical Engineering, Kolozsvár, Románia : Erdélyi Magyar Műszaki Tudományos Társaság (EMT) (2020) 354 p. pp. 182-185. , 4 p.

J. M. F. Treszkai, D. Sipos, D. Feszty, Damping Determination by Half-Power Bandwidth Method for a Slightly Damped Rectangular Steel Plate in the Mid-Frequency Range, ACTA TECHNICA JAURINENSIS 13 : 3 pp. 177-196. , 20 p. (2020)

K. B. Vehovszky, T. Jakubík, M. F. Treszkai, Thermal examination of a simplified exhaust tube-heatshield model, PERIODICA POLYTECHNICA TRANSPORTATION ENGINEERING Onlinefirst pp. 190-195. , 6 p. (2019)

L. M. F. Treszkai, D. Feszty, Review of Hybrid Finite Element – Statistical Energy Analysis methods in vehicle NVH predictions, ACTA TECHNICA JAURINENSIS 12 : 4 pp. 347-370. , 24 p. (2019)

M. M. F. Treszkai, D. Feszty, M. Edgar, B. Vehovszky, J. Kun, Design, Manufacturing and Testing of a Low-Reynolds Number Multi-Element Wing Section for Race Vehicles, In: Ferdynand, Romankiewicz; Remigiusz, Romankiewicz; Robert, Ulewicz (ed.) Advanced Manufacturing and Repair Technologies in Vehicle Industry : Monograph 35th international colloquium, Zielona Góra, Lengyelország : University of Zielona Góra, Faculty of Mechanical Engineering (2018) 394 p. pp. 309-319.

N. B. Vehovszky, T. Jakubík, M. F. Treszkai, Thermal and flow examination of exhaust tube environment, In: Vehovszky, B; Takács, J; Bán, K (ed.) 34th International Colloquium on Advanced Manufacturing and Repairing Technologies in Vehicle Industry, Budapest, Magyarország : Budapest University of Technology and Economics, (2017) pp. 169-172.

O. M. F. Treszkai, T. Jakubík, D. Feszty, B. Vehovszky, Formula Student autó szárnycsomag fejlesztése numerikus áramlástani szimuláció segítségével: Development of Wing Package for a Formula Student Car by Means of CFD Simulation, In: OGÉT 2017: XXV. Nemzetközi Gépészeti Konferencia : 25th International Conference on Mechanical Engineering, Kolozsvár, Románia : Erdélyi Magyar Műszaki Tudományos Társaság (EMT) (2017) 500 p. pp. 428-431. , 4 p.

12. REFERENCES

[1] Siemens AG, “Vibro-Acoustic Engineering Challenges in (Hybrid and) Electric Vehicles,” (2017), [Online].

Available: https://www.researchgate.net/profile/Mohamed-Mourad-Lafifi/post/How-can-vibro-acoustic-analysis-and-its-subdomains-control-theory-dynamics-and-monitoring-be-utilised-in-the-development-of-Electric-Vehicles/attachment/5a738a70b53d2f0bba4f5150/AS%3A589342120611841%401517521519885/download/Vibro-acoustic+engineering+challenges+in+%28hybrid+and%29+electric+vehicles.pdf

[2] W. Desmet, B. Pluymers, O. Atak, "MID-FREQUENCY - CAE Methodologies for Mid-Frequency Analysis in Vibration and Acoustics”, Belgium, (2012), pp. 233-262.

ISBN 978-94-6018-523-6

[3] Audi AG, Audi Mediacenter, (2017), [Online]. Available: https://www.audi-mediacenter.com/en/photos/album/leightweight-construction-240 [01.12.2021]

[4] Audi AG, „Audi Mediacenter”, (2017), [Online].

Available: https://audimediacenter-a.akamaihd.net/system/production/media/43909/images/69626ff49c4be2368432852e5d19011baab53b66/A172352_overfull.jpg?1582331551 [01.12.2021]

[5] J. F. Durand, C. Soize, L. Gagliardini, Structural-acoustic modeling of automotive vehicles in presence of uncertainties and experimental identification and validation, Journal of Acoustic Society of America., 124, 1513, (2008), doi: https://doi.org/10.1121/1.2953316

[6] D. Sipos; M., Brandstetter ; A Guellec ; J. Jacqmot ; D. Feszty, Extended Solution of a Trimmed Vehicle Finite Element Model in the Mid-Frequency Range In: Anon (edited) 11th International Styrian Noise, Vibration & Harshness Congress: The European Automotive Noise Conference (2020) Paper: 2020-01-1549

[7] P. J. Shorter, R. S. Langley, Vibro-acoustic analysis of complex systems, Journal of Sound and Vibration, vol. 288, (2005), pp. 669-699. doi: 10.1016/j.jsv.2005.07.010

[8] R. H. Lyon, R. G. DeJong, Theory and Application of Statistical Energy Analysis, 2nd Edition, 21st November, (1994), ISBN: 978-1483296432

[9] A. Le Bot, Foundation Statistical Energy Analysis in Vibroacoustics, Oxford University Press, 1st Edition, (28 July 2015), ISBN: 978-0198729235

[10] VA One Users' Guide. MECAS ESI Group, (2019)

[11] A. Charpentier, et al., Using the Hybrid FE-SEA Method to Predict Structure Borne Noise Transmission in a Trimmed Automotive Vehicle, "14th International Congress on Sound & Vibration", (9-12 July 2007), Cairns, Australia

[12] R. H. Lyon, G. Maidanik Power flow between linearly coupled oscillators. Journal of Acoustic Society of America 34, (1962), pp. 623–639. doi:10.1121/1.1918177

[13] N. Vladimir, I. Loncar, I. Ancic, I. Senjanovic, Prediction of Noise Performance of Ro-Ro Passenger Ship by the Hybrid Statistical Energy Analysis, "Pomorski zbornik Posebno izdanje", (2018), pp. 29-45. ISSN 0554-6397

[14] J. Parunov, C. Pestelli, S. Rudan, N. Hadzic, I. Senjanovic, Review of Methods for Structure Born Noise Prediction on Ships, Brodogradnja, (2012), pp. 134-139.

[15] F. Sorribes-Palmer, et. Al, Aeroacoustic noise prediction in high speed trains due to attached and detached flow, "International Workshop on Numerical Prediction of Detached Flows", ETSIA-UPM School of Aeronautics, Madrid, Spain, October 23-25 2013, (2013)

[16] Z. Jie, et. Al, SEA and contribution analysis for interior noise of a high speed train, Elsevier, Applied Acoustics, November, (2016), pp. 158-170. doi: 10.1016/J.apacoust.2016.05.019

[17] M. Bustamante, S. N. Y. Gerges, E. F. Vergara, J. P. Arenas, High Damping Characteristics of an Elastomer Particle Damper, International Journal of Acoustics and Vibration, Vol. 21, No. 1, (2016), pp. 112-121. doi: https://dx.doi.org/10.20855/ijav.2016.21.1401

[18] M. Bouhaj, O. Estorff, A. Peiffer, An approach for the assessment of the statistical aspects of the SEA coupling loss factors and the vibrational energy transmission in complex aircraft structures: Experimental investigation and methods benchmark, Journal of Sound and Vibration, 403, (2017), pp. 152-172. doi: http://dx.doi.org/10.1016/j.jsv.2017.05.028

[19] D. Barpanda, J. M. Tudor, Solutions-Based Approach for Noise Reduction in Washing Machines, "27th Conference and Exposition on Structural Dynamics 2009 (IMAC XXVII)", 1 (26), (2009)

[20] R. Zarate, E. Matus, M. Lopez, L. Ballesteros, Design of quieter kitchen appliances: Sound pressure level modeling and validation of a household refrigerator using statistical energy analysis, Proceedings of Meetings on Acoustics, (2017), doi: https://doi.org/10.1121/2.0000632

[21] J. A. Steel, The Prediction of Structural Vibration Transmission Through a Motor Vehicle Using Statistical Energy Analysis, Journal of Sound and Vibration, 193(3), (1996), pp. 691-703.

[22] A. Galasso, G. Di Somma, F. D'Esposito, S. De Rosa, F. Franco, SEA Car Structural and Acoustic Modelling, Proceedings of ISMA2004, (2004), pp. 1473-1485.

[23] J. A. Cordioli, M. Trinches Jr., S. N.Y. Gerges, Applications of the Statistical Energy Analysis to vibro-acoustic modelling of vehicles, SAE Technical Papers, (2004), doi: 10.4271/2004-01-3352

[24] J. Marzbanrad, M. A. Beyg, Vehicle Cabin Noise Simulation due to High-frequencies Simulation, International Journal of Automotive Engineering, 2(2), (2012), pp. 117-123.

[25] C. T. Musser, J. E. Manning, G. C. Peng, Predicting Vehicle Interior Sound with Statistical Energy Analysis, Sound & Vibration, (2012), pp. 8-14.

[26] C. Xin, et al., Simulation on a Car Interior Aerodynamic Noise Control Based on Statistical Energy Analysis, Chinese Journal of Mechanical Engineering, Vol. 25, No. 5, (2012), pp. 1016-1021. doi: 10.3901/CJME.2012.05.1016

[27] A. Putra, et al., Corrected Statistical Energy Analysis Model for Car Interior Noise, Hindawi Publishing Corporation, Advances in Mechanical Engineering, (2014), Article ID 304283

[28] A. Bötke, et al., Modeling and Validation Processes of an Electric Vehicle with Statistical Energy Analysis, EuroNoise 2015, Maastricht, (31 May – 3 June, 2015), ISSN 2226-5147

[29] Y. S. Jang, et al., SEA Modeling and Validation of a Truck Cab for Sound Package Optimization, Inter.Noise Conference 2015., San Francisco, California, USA, (9-12 August 2015)

[30] Y. S. Jang, et al., Optimization of the Sound Package of a Truck using Statistical Energy Analysis, Inter.Noise Conference 2015., San Francisco, California, USA, (9-12 August 2015)

[31] T. Lafont, C. Bertolini, F. Ronzio, T. Courtois, D. Caprioli, Application of Statistical Energy Analysis on a car: from the vehicle modelling to parts targeting, Inter.noise Hamburg 2016, (2016), pp. 7367-7377.

[32] I. Hauer, et al., Prediction of Vehicle Interior Noise in High Frequency Range using Statistical Energy Analysis Hybrid Method, CFA/DAGA'04, Strasbourg, (2004) pp. 11-12.

[33] A. Charpentier, et al., Using the Hybrid FE-SEA Method to Predict Structure-Borne Noise Transmission in a Trimmed Automotive Vehicle, 14th International Congress on Sound & Vibration, Cairns, Australia, (2007)

[34] A. Charpentier, et al., Modeling process and validation of Hybrid FE-SEA method to structure-borne noise paths in a trimmed automotive vehicle, 2008 SAE Brasil Noise and Vibration Conference, Florianopolis, SC, Brazil, (March 30. - April 1. 2008), doi: 10.4271/2008-36-0574

[35] S. M. Chen, et al., Interior Noise Prediction of the Automobile Based on Hybrid FE-SEA Method, Hindawi Publishing Corporation, Mathematical Problems in Engineering, (2011), doi: 10.1155/2011/327170

[36] S. Prasanth, et al., Using the Hybrid FE-SEA Model of a Trimmed Full Vehicle to Reduce Structure Borne Noise from 200 Hz to 1 kHz, SAE International, Symposium on International Automotive Technology, 19-21 January (2011), India, 2011-26-0020

[37] Prasanth S, et al., Modeling process and validation of Hybrid FE-SEA method to structure-borne noise paths in a trimmed automotive vehicle, International Journal of Research in Aeronautical and Mechanical Engineering, Vol.1, Issue.3, July, (2013), pp.: 17-28. ISSN: 2321-3051

[38] Y. Kurosawa, Predicting Automotive Interior Noise Including Wind Noise by Statistical Energy Analysis, International Journal of Mechanical and Mechatronics Engineering, Vol:10, No:3, (2016)

[39] D. Siano, et al., An Hybrid FE/SEA Approach for Engine Cover Noise Assessment, Recent Researches in Mechanical and Transportation Systems, pp. 199-205. ISBN: 978-1-61804-316-0

[40] S. Beigmoradi, et al., Squeak and rattle noise prediction for trimmed door of a car using hybrid statistical energy – Finite element method analysis, The Journal of the Acoustical Society of America, Vol. 19., (June 2013)

[41] F. Wu, et al., Mid-frequency prediction of transmission loss using a novel hybrid deterministic and statistical method, JVE International LTD. Vibroengineering Procedia, Vol. 4, (2014), ISSN 2345-0533

[42] G. Tanner, D.J. Chappell, Comparison of Methods for Modelling Mid-to-High Frequency Vibro-Acoustic Energy Distributions in a Vehicle Floor Structure, SAE International, (2016), doi: 10.4271/2016-01-1853

[43] J. Petrik, R. Fiedler, P. Lepsík, Loss factor estimation of the plywood materials, JVE International LTD. Vibroengineering Procedia, Vol. 7. (2015), pp. 1554-1563.

[44] M. Bustamante, S. N. Y. Gerges, E. F. Vergara, J. P. Arenas, High Damping Characteristics of an Elastomer Particle Damper, International Journal of Acoustics and Vibration, Vol. 21, No. 1, (2016), pp. 112-121. doi: https://dx.doi.org/10.20855/ijav.2016.21.1401

[45] M. B. Mandale, P. Bangarubabu, S. M. Sawant, Damping Loss Factor Estimation by Experimental Method for Plate with Conventional and Composite Materials, International Journal on Design & Manufacturing Technologies, Vol.9 No.2, (July 2015), pp. 6-11.

[46] A. A. Jadhav, S. R. Desai, Estimation of Damping Loss Factor (DLF) for Automotive Glass, Journal of Basic and Applied Engineering Research 2 (6) (2015) pp. 435-438.

[47] R. Cherif, J-D. Chazot, N. Atalla, Damping Loss Factor Estimation of Two-Dimensional Orthotropic Structures from a Displacement Field Measurement, Journal of Sound Vibration, 356 (2015) pp. 61-71.

[48] M. Jaber, H. Schneeweiss, J. Bös, T. Melz, Measurement of the Damping Properties of Carbon Composite Plates by the Power Input Method, Proceedings of ISMA2014 Including USD2014, EMVeM, (2014), pp. 1445-1458.

[49] L. Zoghaib, P-O. Mattei, Damping Analysis of a Free Aluminum Plate, Journal of Vibration and Control, 21 (11), (2015), pp. 2083-2089. doi: https://doi.org/10.1177/1077546313507098

[50] N. Schiller, R. Cabell, F. Grosveld, Impact of Damping Uncertainty on SEA Model Response Variance, Noise-Con 2010, Baltimore, Maryland, (19-21. April 2010)

[51] R. Cabell, N. Schiller, A. Allen, M. Moeller, Loss Factor Estimation Using the Impulse Response Decay Method on a Stiffened Structure, Inter-Noise 2009, Ottawa, Canada, (23-26. August 2009)

[52] N. K. Mandal, R. A. Rahman, M. S. Leong, Experimental Study on Loss Factor for Corrugated Plates by Bandwidth Method, Elsevier, Ocean Engineering, (31) (2004) pp. 1313-1323. doi: https://doi.org//10.1016/j.oceaneng.2003.08.003

[53] M. Iwaniec, Damping Loss Factor Estimation in Plates, Molecular and Quantum Acoustics, (24), (2003), pp. 61-68.

[54] P. R. Mantena, Frequency-Domain Vibration Analysis for Characterizing the Dynamic Mechanical Properties of Materials, 1996 ASEE Annual Conference Proceedings, Session 1626, (1996)

[55] H. W. Wodtke, J. S. Lamancusa, Sound Power Minimization of Circular Plates Through Damping Layer Placement, Journal of Sound and Vibration, 215, (1998), pp. 1145-1163. doi: https://doi.org/10.1006/jsvi.1998.1660

[56] K. Ege, N. B. Roozen, Q. Leclére, R. G. Rinaldi, Assessment of the apparent bending stiffness and damping of multilayered plates; modelling and experiment, Journal of Sound and Vibration, 426, (2018), pp. 129-149. doi: 10.1016/j.jsv.2018.04.013

[57] J. P. Arenas, K. H. Hornig, Sound Power Radiated from Rectangular Plates with Unconstrained Damping Layers, Proceedings of the Ninth International Conference on Computational Structures Technology, Stirlingshire, Scotland, (2008), doi: 10.4203/ccp.88.83

[58] P. R. Beldar, D. V. Kushare, Analytical, Experimental and Numerical Analysis of Passive Damping Treatment of Butyl Rubber, International Research Journal of Engineering and Technology (IRJET), 03(05), (2016), e-ISSN: 2395-0056 doi: https://www.irjet.net/archives/V3/i5/IRJET-V3I504.pdf

[59] R. Fan, G. Meng, J. Yang, C. He, Experimental study of the effect of viscoelastic damping materials on noise and vibration reduction within railway vehicles, Journal of Sound and Vibration, 319(1-2), (2009), pp. 58-76. doi: 10.1016/j.jsv.2008.03.071

[60] K. Y. Sanliturk, Modelling and Validation of a Multilayered Composite Finite Element with Damping Capability, Research Gate, (2013), doi: https://www.researchgate.net/publication/228476351_MODELLING_AND_VALIDATION_OF_A_MULTILAYERED_COMPOSITE_FINITE_ELEMENT_WITH_DAMPING_CAPABILITY#fullTextFileContent

[61] V. D. Cherkasov, Y. V. Yurkin, V. V. Avdonin, Damping Properties of Sandwich Beams with Viscoelastic Layer, ICCATS 2017, Materials Science and Engineering, 262, (2017), doi: 10.1088/1757-899X/262/1/012024

[62] R. Cai, P. Li, Y. Lin, B. Qiu, S. Chen, High frequency noise model based on statistical energy method parameter sensitivity analysis, Vibroengineering PROCEDIA, Vol. 36, (2021), pp. 72-77. doi: https://doi.org/10.21595/vp.2021.21870

[63] Y. Cai, H. Yu, B. Liang, Y. Song, J. Yan, Estimation of statistical energy analysis loss factor for fiber reinforced plastics plate of yachts, Journal of Vibroengineering, Vol. 18, Issue 4, (2016), pp. 2088-2101. Doi: https://doi.org/10.21595/jve.2016.16862

[64] J. Gu, M. Sheng, Improved Energy Ratio Method to Estimate Coupling Loss Factors for Se-ries Coupled Structure, Journal of Mechanical Engineering, Vol. 45, No. 1, (2015), pp. 37-40.

[65] P. P. James, F. J. Fahy, A technique for the assessment of strength of coupling between SEA subsystem: experiments with two coupled plates and two coupled rooms, Journal of Sound and Vibration, 203, (1997), pp. 401-407.

[66] D. A. Bies, D. Hamid, In situ determination of loss and coupling loss factors by the power injection method, Journal of Sound and Vibration, 70, (1980), pp. 187-204.

[67] M. J. Sablik, Coupling Loss Factors at a beam L-joint revisited, Journal of Acoustic Society of America, Vol. 72, No. 4, (1982), pp. 1285-1288.

[68] B. M. Mandale, P. B. Babu, S. M. Sawant, Statistical energy analysis parameter estimation for different structural junctions of rectangular plates, Journal of Mechanical Engineering Science, Vol. 230, No. 15, (2016), pp. 2603-2610. doi: 10.1177/0954406215615628

[69] B. M. Mandale, B. Popuri, Estimation of coupling loss factors for rectangular plates with different materials and junctions, Noise & Vibration Worldwide, 50(9-11), (2019), pp. 306-312. doi: 10.1177/0957456519883264

[70] A. Le Bot, et al. Statistical Energy Analysis, Assumptions and Validity, Medyna 2017: 2nd Euro-Mediterranean Conference on Structural Dynamics and Vibroacoutics, Sevilla, Spain, (25-27 Apr. 2017)

[71] V. H. Patil, D. N. Manik, Sensitivity analysis of a two-plate coupled system in the statistical energy analysis (SEA) framework, Springer, Structural and Multidisciplinary Optimization, 59, (2019), pp. 201-228. doi: https://doi.org/10.1007/s00158-018-2061-9

[72] R. Panuszka, J. Wiciak, M. Iwaniec, Experimental Assessment of Coupling Loss Factors of Thin Rectangular Plates, Archives of Acoustics, Vol. 30, No. 4, (2005), pp. 533-551.

[73] I. Bosmans, P. Mees, G. Vermeir, Structure-borne sound transmission between thin orthotropic plates: analytical solutions, Journal of Sound and Vibration, Vol. 191, No. 1, (1996), pp. 75-90.

[74] M. Cuschieri, J. C. Sun, Use of Statistical Energy Analysis for Rotating Machinery: Determination of Dissipation and Coupling Loss Factors Using Energy Ratios, Journal of Sound and Vibration, Vol. 170, No. 2, (1994), pp. 181-190.

[75] E. C. N. Wester, B. R. Mace, Statistical Energy Analysis of Two Edge-Coupled Rectangular Plates: Ensemble Averages, Journal of Sound and Vibration, Vol. 193, No. 4, (1996), pp. 793-822.

[76] W. Wöhle, T. Beckmann, H. Schreckenbach, Coupling Loss Factors for Statistical Energy Analysis of Sound Transmission at Rectangular Structural Slab Joints, Part I., Journal of Sound and Vibration, Vol. 77, No. 3, (1981), pp. 323-334.

[77] W. Wöhle, T. Beckmann, H. Schreckenbach, Coupling Loss Factors for Statistical Energy Analysis of Sound Transmission at Rectangular Structural Slab Joints, Part II., Journal of Sound and Vibration, Vol. 77, No. 3, (1981), pp. 335-344.

[78] H. Kuttruff, " Room Acoustics", 2nd Ed. Applied Science Publishers Ltd. London (1979)

[79] L. Thibault, N. Totaro, A. Le Bot, A study of the assumptions used in statistical energy analysis, Inter.Noise2014, Melbourne, Australia, (16-19 Nov. 2014).

[80] J. Plunt, Statistical Energy Analysis (SEA) Theory and Applications, International Masters Programme in Sound and Vibration Course: Technical Acoustics II., Chalmers Thekniska Högskola, Göteborg, (April 1998), http://www.gothenburgsound.se/downloads/pdf/SEAkompEng.pdf

[81] T. Lafont, N. Totaro, A. Le Bot. Review of statistical energy analysis hypotheses in vibroacoustics. Proceedings of the Royal Society A: Mathematical, Physical and Engineering Sciences, Royal Society, 470, (2014)

[82] R. S. Langley, K. H. Heron, Elastic wave transmission through plate/beam junctions, Journal of Sound and Vibration, Vol. 143, No. 2, (1990), pp. 241–253.

[83] R. Lyon, G. Maidanik, Power flow between linearly coupled oscillators, Journal of Acoustical Sociate of America, 34, (1962), pp. 623–639.

[84] L. Cremer, M. Heckl, E. E. Ungar, Structure-borne sound, Spring-Verlag, Berlin, (1988)

[85] B. B. Muller, Statistische Energie Analyse, Grundlangen und anwendungen, 28–29Marz, Planneg/Munchen, Germany (1995)

[86] A. Cummings, Low frequency acoustic radiation from duct walls, Journal of Sound and Vibration. 71 (2), (1980), pp. 201-226.

[87] MSC Nastran, Dynamic Analysis User's Guide, (2019)

[88] Siemens AG., What is a Frequency Response Function FRF, [Online], Available: https://community.sw.siemens.com/s/article/what-is-a-frequency-response-function-frf [10.03.2022]

[89] A. Presas, D. Valentin, E. Egusquiza, C. Valero, M. Egusquiza, M. Bossio, Accurate Determination of the Frequency Response Function of Submerged and Confined Structures by Using PZT-Patches, Sensors 2017, No.17 Vol: 660, (2017), doi: 10.3390/s17030660

[90] Siemens AG., Windows and Spectral leakage, [Online], Available: https://community.sw.siemens.com/s/article/windows-and-spectral-leakage [10.03.2022]

[91] LMS Test.Lab User's Guide 2022, 16A Functions

[92] J. Kun, T. Turcsik, D. Feszty, Design of acoustic cavity test apparatus for validation of mid-frequency response of a plate-cavity system, In: Jeon, J.Y. (edit), Korean Society of Noise and Vibration Engineering Paper: 615/17.08 (2020)

[93] N. H. Baharin, R. A. Rahman, Effect of accelerometer mass on thin plate vibration, Jurnal Mekanikal, (29), (2009), pp. 100–111.

[94] F. F. Yap, J. Woodhouse, Investigation of Damping Effects on Statistical Energy Analysis of Coupled Structures, Journal of Sound and Vibration, 197(3), (1996), pp. 351-371.

[95] Henkel „Technical Data Sheet of Loctite® 454™" (2012), [Revised Nov. 2020] Available: http://tds.henkel.com/tds5/Studio/ShowPDF/243%20NEW-EN?pid=454-2012%20NEW&format=MTR&subformat=REAC&language=EN&plant=WERCS

[96] Henkel, „ Technical Data Sheet of Loctite® EA 3450™”, (2014), [Revised Nov. 2020] Available: http://tds.henkel.com/tds5/Studio/ShowPDF/243%20NEW-EN?pid=EA%203450&format=MTR&subformat=REAC&language=EN&plant=WERCS

[97] J. Pang, Noise and Vibration Control in Automotive Bodies, Wiley & Sons Ltd., (2019), ISBN: 9781119515494

[98] M. F. Treszkai, D. Sipos, D. Feszty, Damping Determination by Half-Power Bandwidth Method for a Slightly Damped Rectangular Steel Plate in the Mid-Frequency Range, Acta Technica Jaurinensis, Vol. 13, No. 3, (2020), pp. 177-196. doi: 10.14513/actatechjaur.v13.n3.545

[99] M. Tatari, M. Mahjoob, N. Nasrollahzadeh, Nonlinear Vehicle Seat BSR Characterization Using CAE Methodology, Springer Science+Business Media New York 2014, (July 2014), pp.: 231-256, doi 10.1007/978-1-4614-6877-6 8

[100] D. Sipos, M. F. Treszkai, D. Feszty, Welding distortion generated uncertainties in the vibrational behavior of a ladder-like structure, Noise-Con Proceedings 263, 2 (2021), pp. 4799-4809.